



**US Army Corps
of Engineers®**
Engineer Research and
Development Center

Combined Wave and Surge Overtopping of Levees: Flow Hydrodynamics and Articulated Concrete Mat Stability

Steven A. Hughes

August 2008

Combined Wave and Surge Overtopping of Levees: Flow Hydrodynamics and Articulated Concrete Mat Stability

Steven A. Hughes

*Coastal and Hydraulics Laboratory
U.S. Army Engineer Research and Development Center
3909 Halls Ferry Road
Vicksburg, MS 39180-6199*

Final report

Approved for public release; distribution is unlimited.

Prepared for U.S. Army Engineer District, New Orleans
P.O. Box 60267
New Orleans, LA 70160-0267

Abstract: A 1-to-25 scale physical model of a typical cross section of the levee along the Mississippi River Gulf Outlet (MRGO) was constructed at the U.S. Army Engineer Research and Development Center's Coastal and Hydraulics Laboratory in Vicksburg, MS. The purpose of the physical model was to obtain hydrodynamic measurements of unsteady flow conditions caused by combined wave and surge overtopping of the levee, and to examine the feasibility of using articulated concrete mats (ACMs) for levee protection during this type of overtopping event. Specifically, the U.S. Army Engineer District, New Orleans, was interested in determining whether the same ACMs used by the Corps' Mat Sinking Unit to protect river banks could be used to protect the MRGO levee against surge and wave overtopping.

When the storm surge elevation was 0.75 ft above the levee crest, the stability tests indicated the ACMs were prone to uplift on the lower portion of the levee protected-side slope for even relatively mild wave overtopping. An increase in wave height created mat roll-up instability at the toe of the flood-side levee slope, indicating the need to bury or anchor the leading and tailing edges of the mats. Mat stability could be increased with additional anchoring or increasing mat thickness.

Tests were also conducted to document the hydrodynamics associated with combined wave and surge overtopping. The primary parameters were three overtopping surge levels (+1, +3, and +5 ft); three significant wave heights (3, 6, and 9 ft); and three peak wave periods (6, 10, and 14 sec) for a total of 27 unique conditions. Measurements included the incident irregular waves and time series of water elevations at seven locations on the crest and protected-side slope of the levee. Horizontal flow velocity was recorded near the leeward levee crest shoulder, and the velocity was then combined with water elevation to estimate the unsteady instantaneous discharge over the levee. Discharge cumulative probability distributions were determined using the Weibull probability distribution, and a predictive equation was developed for the distribution of overtopping discharge as a function of wave and surge parameters.

DISCLAIMER: The contents of this report are not to be used for advertising, publication, or promotional purposes. Citation of trade names does not constitute an official endorsement or approval of the use of such commercial products. All product names and trademarks cited are the property of their respective owners. The findings of this report are not to be construed as an official Department of the Army position unless so designated by other authorized documents.

DESTROY THIS REPORT WHEN NO LONGER NEEDED. DO NOT RETURN IT TO THE ORIGINATOR.

Contents

Figures and Tables.....	vi
Preface.....	x
Unit Conversion Factors.....	xii
1 Introduction.....	1
Background	1
Levee overtopping physical model	5
Physical model study tasks.....	5
Report organization and content.....	6
Units of measure	6
2 Estimation of Overtopping Flow	7
Levee armoring design physical parameters.....	7
Estimation of wave overtopping flow parameters	8
<i>Flow parameters at flood-side levee crest edge.....</i>	<i>11</i>
<i>Estimation of friction factor</i>	<i>14</i>
<i>Flow parameters on the protected-side levee slope</i>	<i>16</i>
<i>Discharge and critical velocity.....</i>	<i>18</i>
<i>Protected-side slope supercritical flow</i>	<i>21</i>
Combined wave and surge overtopping.....	23
3 Principles of Physical Modeling.....	26
Principles of similitude.....	26
<i>Hydraulic similitude.....</i>	<i>27</i>
<i>Wave force and armor weight similitude</i>	<i>29</i>
Physical model advantages	30
Physical model disadvantages	31
<i>Physical model scale effects</i>	<i>31</i>
<i>Physical model laboratory effects</i>	<i>32</i>
<i>Other physical model disadvantages.....</i>	<i>33</i>
Physical model appropriateness	33
4 Physical Model Design.....	35
Model facility	35
Model scale selection	36
<i>Model purpose and layout</i>	<i>37</i>
<i>Hydrodynamic similitude criteria.....</i>	<i>38</i>
<i>Wave generation capability</i>	<i>38</i>
<i>Overtopping surge flow</i>	<i>39</i>
<i>Force and ACM weight.....</i>	<i>40</i>
<i>Summary of model scaling.....</i>	<i>41</i>

Model design and construction	42
<i>Levee cross section</i>	42
<i>Surge flow generator</i>	45
<i>Model articulated mats</i>	46
Potential scale and laboratory effects	49
<i>Scale effects in levee overtopping physical model</i>	50
<i>Laboratory effects in levee overtopping physical model</i>	51
5 Experiment Setup and Operating Procedures	52
Experiment instrumentation	52
<i>Water levels</i>	52
<i>Flow discharge</i>	53
<i>Waves</i>	53
<i>Water pressure</i>	54
<i>Flow velocity</i>	55
Storm surge and wave calibration	55
<i>Wave calibration</i>	57
Operating procedures	58
<i>Combined wave and surge overtopping experiments</i>	59
Data collection and initial analyses	60
6 Articulated Concrete Mat Stability	63
Stability experiments	64
<i>Tests with 1-ft surge, 3-ft waves</i>	65
<i>Tests with 1-ft surge, 6-ft waves</i>	66
<i>Tests with 3-ft surge, 3-ft waves</i>	67
Summary of ACM stability testing	71
<i>Testing results</i>	71
<i>Suggestions</i>	72
7 Hydrodynamics of Combined Wave and Surge Overtopping	74
Summary of experiments	74
Typical measured results	76
<i>Time series measurements</i>	76
<i>Water surface profile measurements</i>	79
Average overtopping discharge	85
Overtopping flow discharge distributions	87
<i>Overtopping distribution variation with wave and surge parameters</i>	89
<i>Weibull probability distribution</i>	93
<i>Prediction of combined wave and surge overtopping probability</i>	95
Summary of combined wave and surge overtopping hydrodynamics	106
8 Summary and Conclusions	108
Summary	108
<i>Physical model</i>	108
<i>Stability of articulated concrete mats</i>	109
<i>Hydrodynamics of combined wave and surge overtopping</i>	109

Conclusions	110
<i>Stability of articulated concrete mats</i>	110
<i>Hydrodynamics of combined wave and surge overtopping</i>	111
Suggestions for future research	112
References	114
Appendix A: Data Plots	116
Time series plots	116
Overtopping probability distributions	143
Report Documentation Page	

Figures and Tables

Figures

Figure 1. Minor erosion due to overtopping on the Citrus Back levee.	1
Figure 2. Crown erosion along MRGO levee in St. Bernard Parish.	2
Figure 3. Demonstration deployment of ACMs.	3
Figure 4. Overtopping of earthen levees.	8
Figure 5. Wave overtopping definition sketch.	9
Figure 6. Surge overtopping design parameters.	17
Figure 7. Discharge versus upstream head h_1	20
Figure 8. Critical velocity on crest versus upstream head h_1	20
Figure 9. Backside slope velocity versus upstream head h_1	23
Figure 10. Backside slope flow thickness versus upstream head h_1	24
Figure 11. Photograph showing the 3-ft flume.	36
Figure 12. MRGO levee cross section replicated in physical model.	37
Figure 13. Levee model being carved out of high-density foam.	43
Figure 14. Finished section of levee model.	43
Figure 15. Mounting hardware for dynamic pressure gauges.	44
Figure 16. Isometric view of levee model placed in flume.	44
Figure 17. Cross section sketch of levee overtopping model in 3-ft flume.	45
Figure 18. Model blocks used to fabricate articulated mats.	47
Figure 19. Approximately 1,000 model blocks.	47
Figure 20. Articulated mat assembly jig.	48
Figure 21. Mesh glued to underside of block mattress.	48
Figure 22. Final assembled model articulated mat.	49
Figure 23. Steady surge overtopping water surface profiles.	54
Figure 24. Stacks of ACMs at fabrication yard.	63
Figure 25. Portion of casting yard in St. Francisville, LA.	64
Figure 26. Articulated mat uplift during wave overtopping (1-ft surge, 3-ft wave).	66
Figure 27. Video capture sequence showing mat roll up at seaward toe of levee.	67
Figure 28. Articulated mat fluttering during 3-ft surge and 3-ft, 10-sec wave.	68
Figure 29. Video capture sequence showing wave overtopping (1 of 2).	69
Figure 30. Video capture sequence showing wave overtopping (2 of 2).	70
Figure 31. Test R104: Surge = +1 ft, H_{m0} = 3.3 ft, T_p = 10.5 sec.	77
Figure 32. Test R104 (extract): Surge = +1 ft, H_{m0} = 3.3 ft, T_p = 10.5 sec.	78
Figure 33. Test R115: Surge = +3 ft, H_{m0} = 8.7 ft, T_p = 10.5 sec.	80
Figure 34. Test R115 (extract): Surge = +3 ft, H_{m0} = 8.7 ft, T_p = 10.5 sec.	81
Figure 35. Pressure head (model feet) output from gauge P4.	82

Figure 36. Single wave overtopping time-history.....	83
Figure 37. Water surface profiles for 1830-1837 data interval.....	84
Figure 38. Water surface profiles for 1840-1845 data interval.....	84
Figure 39. Dimensionless combined average discharge versus relative freeboard.....	87
Figure 40. Discharge distribution for surge = +1 ft, $H_{m0} = 6.2$ ft, $T_p = 10.5$ sec.....	88
Figure 41. Exceedance probability variation with storm surge (medium waves).	90
Figure 42. Exceedance probability variation with storm surge (large waves).	90
Figure 43. Exceedance probability variation with wave height (+1-ft surge).....	91
Figure 44. Exceedance probability variation with wave height (+5-ft surge).....	91
Figure 45. Exceedance probability variation with wave period (+1-ft surge).....	92
Figure 46. Exceedance probability variation with wave period (+3-ft surge).....	92
Figure 47. Example best fit of Weibull distribution to measured data.	94
Figure 48. A good fit of Weibull distribution to measured data.	96
Figure 49. A mediocre fit of Weibull distribution to measured data distribution tail.	96
Figure 50. Measured average discharge versus discharge from Weibull distribution.	99
Figure 51. Correlation of shape factor b with wave and surge parameters.....	100
Figure 52. Predicted versus actual exceedance probability ($H_{m0} = 3$ ft, $T_p = 6$ sec).	102
Figure 53. Predicted versus actual exceedance probability ($H_{m0} = 6$ ft, $T_p = 6$ sec).	102
Figure 54. Predicted versus actual exceedance probability ($H_{m0} = 9$ ft, $T_p = 6$ sec).	103
Figure 55. Predicted versus actual exceedance probability ($H_{m0} = 3$ ft, $T_p = 10$ sec).	103
Figure 56. Predicted versus actual exceedance probability ($H_{m0} = 6$ ft, $T_p = 10$ sec).	104
Figure 57. Predicted versus actual exceedance probability ($H_{m0} = 9$ ft, $T_p = 10$ sec).....	104
Figure 58. Predicted versus actual exceedance probability ($H_{m0} = 3$ ft, $T_p = 14$ sec).	105
Figure 59. Predicted versus actual exceedance probability ($H_{m0} = 6$ ft, $T_p = 14$ sec).	105
Figure 60. Predicted versus actual exceedance probability ($H_{m0} = 9$ ft, $T_p = 14$ sec).	106
Figure A1. Run 128 time series plots (surge = +1 ft, $H_{m0} = 3$ ft, $T_p = 6$ sec).	116
Figure A2. Run 129 time series plots (surge = +1 ft, $H_{m0} = 6$ ft, $T_p = 6$ sec).	117
Figure A3. Run 130 time series plots (surge = +1 ft, $H_{m0} = 9$ ft, $T_p = 6$ sec).	118
Figure A4. Run 104 time series plots (surge = +1 ft, $H_{m0} = 3$ ft, $T_p = 10$ sec).	119
Figure A5. Run 105 time series plots (surge = +1 ft, $H_{m0} = 6$ ft, $T_p = 10$ sec).	120
Figure A6. Run 131 time series plots (surge = +1 ft, $H_{m0} = 9$ ft, $T_p = 10$ sec).	121
Figure A7. Run 107 time series plots (surge = +1 ft, $H_{m0} = 3$ ft, $T_p = 14$ sec).	122
Figure A8. Run 108 time series plots (surge = +1 ft, $H_{m0} = 6$ ft, $T_p = 14$ sec).	123
Figure A9. Run 109 time series plots (surge = +1 ft, $H_{m0} = 9$ ft, $T_p = 14$ sec).	124
Figure A10. Run 110 time series plots (surge = +3 ft, $H_{m0} = 3$ ft, $T_p = 6$ sec).	125
Figure A11. Run 111 time series plots (surge = +3 ft, $H_{m0} = 6$ ft, $T_p = 6$ sec).	126
Figure A12. Run 112 time series plots (surge = +3 ft, $H_{m0} = 9$ ft, $T_p = 6$ sec).	127
Figure A13. Run 113 time series plots (surge = +3 ft, $H_{m0} = 3$ ft, $T_p = 10$ sec).	128
Figure A14. Run 132 time series plots (surge = +3 ft, $H_{m0} = 6$ ft, $T_p = 10$ sec).	129
Figure A15. Run 115 time series plots (surge = +3 ft, $H_{m0} = 9$ ft, $T_p = 10$ sec).	130

Figure A16. Run 116 time series plots (surge = +3 ft, H_{m0} = 3 ft, T_p = 14 sec).....	131
Figure A17. Run 117 time series plots (surge = +3 ft, H_{m0} = 6 ft, T_p = 14 sec).....	132
Figure A18. Run 118 time series plots (surge = +3 ft, H_{m0} = 9 ft, T_p = 14 sec).....	133
Figure A19. Run 119 time series plots (surge = +5 ft, H_{m0} = 3 ft, T_p = 6 sec).....	134
Figure A20. Run 120 time series plots (surge = +5 ft, H_{m0} = 6 ft, T_p = 6 sec).....	135
Figure A21. Run 121 time series plots (surge = +5 ft, H_{m0} = 9 ft, T_p = 6 sec).....	136
Figure A22. Run 122 time series plots (surge = +5 ft, H_{m0} = 3 ft, T_p = 10 sec).....	137
Figure A23. Run 123 time series plots (surge = +5 ft, H_{m0} = 6 ft, T_p = 10 sec).....	138
Figure A24. Run 124 time series plots (surge = +5 ft, H_{m0} = 9 ft, T_p = 10 sec).....	139
Figure A25. Run 125 time series plots (surge = +5 ft, H_{m0} = 3 ft, T_p = 14 sec).....	140
Figure A26. Run 126 time series plots (surge = +5 ft, H_{m0} = 6 ft, T_p = 14 sec).....	141
Figure A27. Run 127 time series plots (surge = +5 ft, H_{m0} = 9 ft, T_p = 14 sec).	142
Figure A28. Run 128 overtopping distribution plots (surge = +1 ft, H_{m0} = 3 ft, T_p = 6 sec).....	143
Figure A29. Run 129 overtopping distribution plots (surge = +1 ft, H_{m0} = 6 ft, T_p = 6 sec).....	144
Figure A30. Run 130 overtopping distribution plots (surge = +1 ft, H_{m0} = 9 ft, T_p = 6 sec).....	145
Figure A31. Run 104 overtopping distribution plots (surge = +1 ft, H_{m0} = 3 ft, T_p = 10 sec).....	146
Figure A32. Run 105 overtopping distribution plots (surge = +1 ft, H_{m0} = 6 ft, T_p = 10 sec).....	147
Figure A33. Run 131 overtopping distribution plots (surge = +1 ft, H_{m0} = 9 ft, T_p = 10 sec).....	148
Figure A34. Run 107 overtopping distribution plots (surge = +1 ft, H_{m0} = 3 ft, T_p = 14 sec).....	149
Figure A35. Run 108 overtopping distribution plots (surge = +1 ft, H_{m0} = 6 ft, T_p = 14 sec).....	150
Figure A36. Run 109 overtopping distribution plots (surge = +1 ft, H_{m0} = 9 ft, T_p = 14 sec).....	151
Figure A37. Run 110 overtopping distribution plots (surge = +3 ft, H_{m0} = 3 ft, T_p = 6 sec).....	152
Figure A38. Run 111 overtopping distribution plots (surge = +3 ft, H_{m0} = 6 ft, T_p = 6 sec).....	153
Figure A39. Run 112 overtopping distribution plots (surge = +3 ft, H_{m0} = 9 ft, T_p = 6 sec).....	154
Figure A40. Run 113 overtopping distribution plots (surge = +3 ft, H_{m0} = 3 ft, T_p = 10 sec).....	155
Figure A41. Run 132 overtopping distribution plots (surge = +3 ft, H_{m0} = 6 ft, T_p = 10 sec).....	156
Figure A42. Run 115 overtopping distribution plots (surge = +3 ft, H_{m0} = 9 ft, T_p = 10 sec).....	157
Figure A43. Run 116 overtopping distribution plots (surge = +3 ft, H_{m0} = 3 ft, T_p = 14 sec).....	158
Figure A44. Run 117 overtopping distribution plots (surge = +3 ft, H_{m0} = 6 ft, T_p = 14 sec).....	159
Figure A45. Run 118 overtopping distribution plots (surge = +3 ft, H_{m0} = 9 ft, T_p = 14 sec).....	160
Figure A46. Run 119 overtopping distribution plots (surge = +5 ft, H_{m0} = 3 ft, T_p = 6 sec).....	161
Figure A47. Run 120 overtopping distribution plots (surge = +5 ft, H_{m0} = 6 ft, T_p = 6 sec).....	162
Figure A48. Run 121 overtopping distribution plots (surge = +5 ft, H_{m0} = 9 ft, T_p = 6 sec).....	163
Figure A49. Run 122 overtopping distribution plots (surge = +5 ft, H_{m0} = 3 ft, T_p = 10 sec).....	164
Figure A50. Run 123 overtopping distribution plots (surge = +5 ft, H_{m0} = 6 ft, T_p = 10 sec).....	165
Figure A51. Run 124 overtopping distribution plots (surge = +5 ft, H_{m0} = 9 ft, T_p = 10 sec).....	166
Figure A52. Run 125 overtopping distribution plots (surge = +5 ft, H_{m0} = 3 ft, T_p = 14 sec).....	167
Figure A53. Run 126 overtopping distribution plots (surge = +5 ft, H_{m0} = 6 ft, T_p = 14 sec).....	168
Figure A54. Run 127 overtopping distribution plots (surge = +5 ft, H_{m0} = 9 ft, T_p = 14 sec).....	169

Tables

Table 1. Empirical coefficients for flood-side crest edge flow parameters.	12
Table 2. Prototype and model wave and surge parameter values.	39
Table 3. Prototype and model ACM parameters.....	41
Table 4. Model scale ratios and prototype equivalence.	41
Table 5. Water surface elevations for steady surge overtopping.....	56
Table 6. Summary of experiments and hydrodynamic forcing.....	75
Table 7. Parameters from best fit of Weibull probability distribution.....	97

Preface

This technical report describes small-scale physical model tests simulating combined wave and storm surge overtopping of a typical levee cross section of the Mississippi River Gulf Outlet (MRGO). The study was conducted by the U.S. Army Engineer Research and Development Center (ERDC), Coastal and Hydraulics Laboratory (CHL), Vicksburg, MS, for the U.S. Army Engineer District, New Orleans (MVN). The purpose of this physical model was to obtain measurements of key hydrodynamic parameters associated with unsteady flow overtopping, and to examine the feasibility of using articulated concrete mats for levee protection during combined wave and surge overtopping. Initial funding authority was provided by the New Orleans District to CHL on 3 August 2006, and a review draft of this report was submitted to MVN on 18 May 2007. Review comments from MVN were incorporated into the report on 27 November 2007.

Michelle C. Daigle, CEMVN-OD-G, Program Manager, Operations Division, was the point of contact for the sponsoring New Orleans District, and she provided study oversight and review. Dr. Harley Winer, CEMVN-ED-HC advised on the range of surge and wave parameters.

The physical model study was directed by Dr. Steven A. Hughes, Navigation Division (HN), CHL. Julie A. Cohen and Hugh F. Acuff, HN-HH, CHL, were instrumental in the design, construction, and operation of the physical model. The physical model levee cross section and scaled articulated concrete mats were constructed by craftsmen from the ERDC Department of Public Works (DPW) under the supervision of Mitchell Simmons, Model Shop foreman. David Daily and Timothy Nisley, Instrumentation Support Division, supported the instrumentation and wave machine requirements. J. Holley Messing, Coastal Engineering Branch, Navigation Division, completed word processing and formatting of the draft report.

This study was conducted during the period August 2006 through May 2007 under the direct supervision of Jose E. Sanchez, Chief, Harbors, Entrances, and Structures Branch, Navigation Division, CHL. Administrative supervision was provided by Thomas W. Richardson, Director,

CHL; William D. Martin, Deputy Director, CHL; and Dr. M. Rose Kress, Chief, Navigation Division, CHL.

COL Gary E. Johnston was Commander and Executive Director of ERDC. Dr. James R. Houston was Director.

Unit Conversion Factors

Multiply	By	To Obtain
cubic yards	0.7645549	cubic meters
feet	0.3048	meters
inches	2.54	centimeters
miles (U.S. statute)	1.609347	kilometers
square miles	2.589998 E+06	square meters
tons (2,000 pounds, mass)	907.1847	kilograms

1 Introduction

Background

Ideally, all levees would have a crown elevation with ample freeboard to prevent wave and/or surge overtopping for any conceivable storm scenario. However, economics dictate more practical levee designs having lower crown elevations, but with the risk that some wave/surge overtopping will occur during extreme events. Earthen levees constructed without slope protection or armoring must rely on the erosion resistance of the outer soil layer during episodes of wave and/or storm surge overtopping.

Post-Katrina investigations revealed that most earthen levee damage due to storm surge and wave overtopping occurred on the levee protected-side slope. Figure 1 illustrates typical minor damage from overtopping where weaker, unprotected soil was eroded on the levee backside slope (right side of photograph). In this case, overtopping was probably not severe or the duration of overtopping was relatively short.



Figure 1. Minor erosion due to overtopping on the Citrus Back levee.

If the surge level continues to rise, and greater volumes of water overtop the levee for an extended period, the initial erosion areas will expand until eventually the levee crown and portions of the flood side are eroded as shown in Figure 2. Once the levee crown or grass covering on the protected side is lost, there is a higher risk of levee breaching and catastrophic flooding.

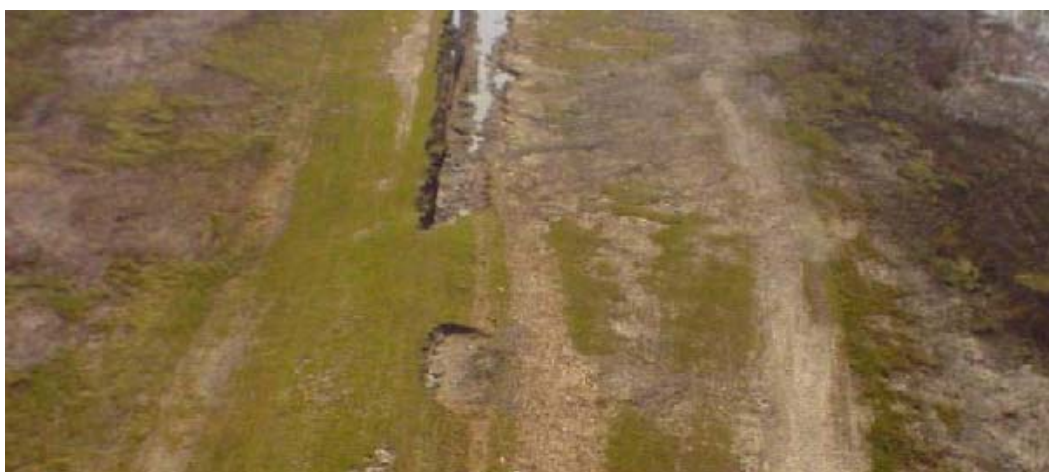


Figure 2. Crown erosion along MRGO levee in St. Bernard Parish.

Usually erosion resistance for wave or surge overtopping is most needed on the levee crown and down the rear slope on the protected side of the levee as evidenced in Figures 1 and 2. Levees constructed with a top layer of good clay and well-established vegetation with a healthy root system have much better erosion resistance than top layers of sandy soil with sparse or unhealthy vegetation. Where expected overtopping rates are within permissible ranges, the crown and protected-side slope clay layer can be adequately protected with good quality grass having a well-established root system, but continual maintenance is needed to assure the grass covering remains in top condition. At locations where the levee crest elevation cannot be raised to the elevation associated with permissible overtopping for grass-covered slopes, it will be necessary to protect the levee soil with some type of armoring system that can withstand the forces of the anticipated hydrodynamic loading. Figure 3 shows a demonstration deployment of articulated concrete mats (ACMs) on an earthen slope. The mats were designed for use as riverbank protection.

At the initiation of this study, the U.S. Army Corps of Engineers was proposing to use ACMs or turf reinforcement mats (TRMs) to armor the backside (protected side) slopes along selected reaches of the Mississippi River Gulf Outlet (MRGO). With the levees at present design crest elevations, portions of the MRGO levee will be overtopped by both waves and storm surge associated with hurricanes comparable to Hurricane Katrina. Armoring of the backside slope will prevent (or significantly hinder) erosion of levee soil by head cutting that ultimately could lead to breaching and large-scale flooding of the protected region if the earthen levees are not protected.



Figure 3. Demonstration deployment of ACMs.

The excessive wave and surge overtopping dilemma is not unique to MRGO, and there are numerous locations within the Southeastern Louisiana levee system that will either need to be raised to prevent overtopping or armored to prevent excessive erosion of levee soil that could lead to catastrophic breaching.

During the preparation of this report the fate of the MRGO was still being debated, so it remains uncertain whether or not portions of the MRGO will need to be armored. Nevertheless, the research and findings described in this report are applicable at any location in the levee system that could be exposed to surge and wave overtopping, provided the levee cross section does not differ significantly from that of the representative MRGO levee used in this physical model study.

A critical aspect of any design project related to levee armoring is availability of design guidance specific to the flow conditions and failure modes associated with wave and surge overtopping of levees. Recognized failure modes for ACMs include the following, either singularly or in combination.

- *Uplift of mats.* The ACMs must be stable without movement when subjected to flows generated by combined wave and surge overtopping.

- *Roll up of mats.* The leading edge of the ACM must be securely anchored at the levee crest or somewhere on the flood-side slope to prevent roll up of the mat as high-velocity flows pass over the levee crest and down the backside slope.
- *Loss of underlying soil.* The underlying soil (typically compacted clay) must not be eroded when the levee backside slope is subjected to design flow conditions.
- *Erosion at mat toe.* The downslope toe of the mats must be terminated in such a manner to prevent head cutting as the flow passes over the toe. This may include protection against turbulence caused by formation of a hydraulic jump where the supercritical flow enters standing tailwater.
- *Erosion between adjacent mats.* Erosion of levee soil through gaps between adjacent mats must be prevented.

The above failure modes do not include failure of the ACM itself, such as separation of inter-block connectors, breakage of individual blocks, etc.

A number of proprietary ACM and TRM systems have been tested for uplift stability and erosion protection during previous laboratory experiments conducted at full scale. However, design guidance based on these tests is limited to the case of steady storm surge overflow without waves, and the guidance is specific to the particular protection products tested when placed at the same slopes as replicated in the physical model. In addition some aspects of the failure modes listed above may not have been addressed in previous tests.

Design guidance appropriate for the protection alternatives proposed by the Corps of Engineers for the MRGO armoring did not exist prior to this study. Whereas it might be possible to transfer full-scale stability results from proprietary ACM and TRM tests to the Corps' design as a first approximation, this would cover only the case of surge overflow, and not the more problematic situation where overtopping waves create additional stress on the levee backside slope protection. In other words, accurate design guidance specific to the storm climatology and particular solutions proposed for armoring the MRGO and other levees is needed to assure the as-built project can withstand the expected wave and storm surge overtopping.

Levee overtopping physical model

A small-scale physical model of a typical MRGO levee cross section was constructed and installed in a 3-ft-wide wave flume at the U.S. Army Engineer Research and Development Center (ERDC), Coastal and Hydraulics Laboratory (CHL), in Vicksburg, MS. Funding for model construction and operation was provided to CHL by the U.S. Army Engineer District, New Orleans (hereafter, the New Orleans District).

The physical model featured fixed-bed bathymetry seaward of the levee, and the levee cross section was fabricated out of high-density foam. Because of scaling effects, no attempt was made to construct the levee using erodible soil. Thus, aspects related to erodibility of the underlying soil were not simulated in these tests. In addition to the wave generation capacity, a recirculation system was installed to simulate steady surge overflow of the levee combined with wave propagation and overtopping. Thus, the physical model was capable of simulating steady storm surge overflow, wave overtopping when the surge level was lower than the levee crest elevation, and wave overtopping when the surge elevation exceeded the levee crest elevation.

The objectives of this study were (1) to examine the feasibility of armoring portions of the MRGO levees with a specific type of ACMs, and (2) to provide the New Orleans District with design information related to dynamic pressures and unsteady flow velocities associated with a broad range of combined wave and surge overtopping parameters.

Physical model study tasks

The testing program for the small-scale physical model of the representative MRGO levee was designed to provide necessary information relevant to the following study tasks.

- Determine stability criteria for the ACMs normally used for riverbank protection when subjected to combined wave and storm surge overtopping.
- Quantify the unsteady hydrodynamic flow parameters associated with combined wave and storm surge overtopping of the MRGO levees and develop appropriate estimation techniques.

Report organization and content

This report focuses on design and construction of the small-scale levee physical model, model calibration and operation, and description and analysis of results. The chapters of this report are organized in chronological order from initial design of the model through to interpretation of final results.

Chapter 2 reviews existing methodologies for estimating hydrodynamic parameters associated with wave-only and surge-only levee overtopping. Chapter 3 overviews the principles of physical modeling, points out the advantages and disadvantages of the technology, and discusses known scale and laboratory effects and how these effects might influence model results. Chapter 4 covers design and construction of the levee overtopping physical model including the surge overtopping generator and fabrication of the model ACMs. Chapter 5 details the selected key model parameters and operating procedures including instrumentation, measurements, and data analyses.

Chapter 6 presents results from stability tests of the ACMs along with suggestions for possible performance improvements. Analyses of flow hydrodynamics associated with combined storm surge overflow and wave overtopping are presented in Chapter 7 along with engineering methods for estimating parameters of the overtopping discharge distribution. Finally, Chapter 8 presents the summary and conclusions from this study.

Units of measure

Most dimensional parameters and values cited in this report are given in non-SI units of measurement. Conversion to equivalent SI units can be made using the conversion factors listed on page xiv of this report. Usually, the values of measured model parameters have been scaled to equivalent prototype values so readers can better understand the model response. In most cases the distinction is made between model and prototype scale. However, there are instances where values are reported without specifically stating whether the units are model- or prototype-scale units. In these cases, the context and/or parameter magnitude will usually reveal whether the value is in model dimensions or equivalent prototype dimensions.

2 Estimation of Overtopping Flow

Levee armoring design physical parameters

Physical parameters important for the design of armor and protection systems placed on the protected-side slope of earthen levees are the levee geometry, properties of the earthen material comprising the levees, and the hydrodynamic forces acting on the backside slope. The geometric parameters of most importance are levee crest elevation and slope of the protected side. Levee crest width has relatively minor influence.

The key geotechnical design parameters are those related to soil type, compaction, strength, and erosion resistance. Where levees are to be armored or otherwise protected to prevent erosion of the levee material, the main function of the underlying soil/clay layer is to help prevent leeching of levee core material and to support the weight of the armoring without undue settlement. The load-bearing requirement varies with the particular levee protection system.

Backside slope armoring systems must resist the forces of fast-flowing, turbulent water that has overtopped the levee crest. Figure 4 illustrates the three overtopping cases that might occur. Wind generated waves will overtop levees facing larger bodies of water before the still-water level reaches the elevation of the crest as shown in Figure 4(a). Levees not exposed to wave activity (e.g., river levees) will not be overtopped until the still-water level exceeds the levee crest elevation as illustrated by Figure 4(b). However, the water level may vary slowly in time due to tide, a time-varying surge hydrograph, or long-period seiching (the formation of standing waves in water) of a lake or basin. The third, and most problematic, overtopping is shown in Figure 4(c). The still-water level exceeds the levee crest elevation, and hurricane waves provide a pulsing, unsteady component to the overtopping flow.

The remainder of this chapter discusses these three overtopping situations and summarizes existing engineering methods for estimating various representative parameters of the overtopping flow hydrodynamics. This review is not intended to be a complete and thorough investigation of the literature; but instead it provides a few simple, established methods for estimating flow parameters.

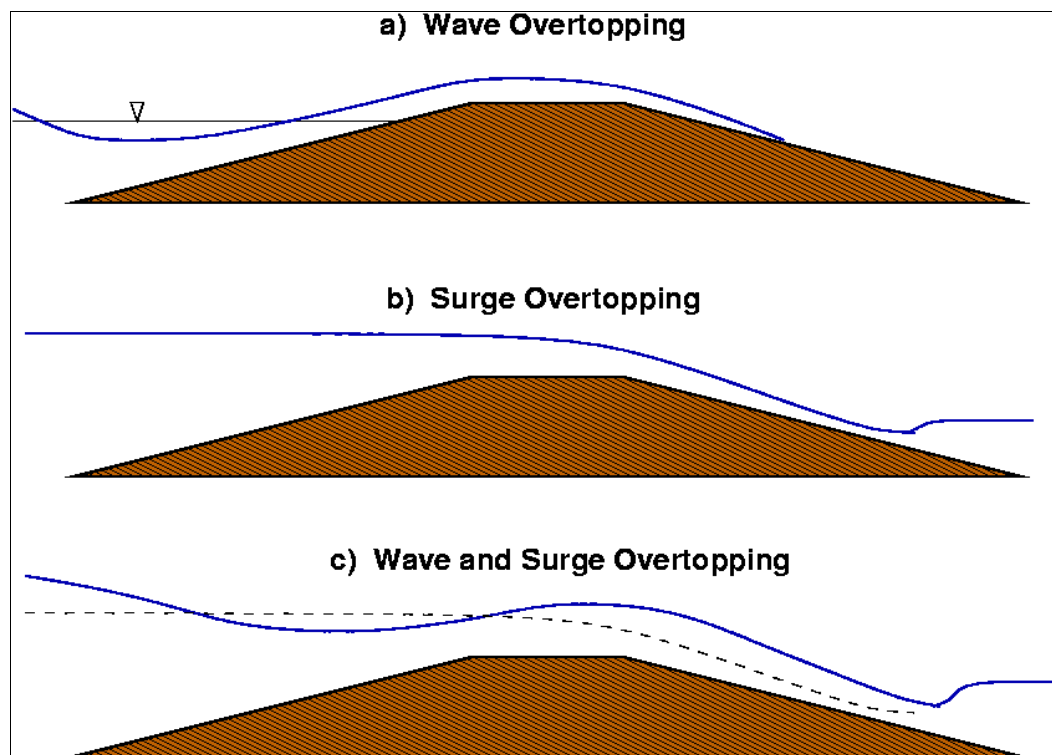


Figure 4. Overtopping of earthen levees.

Estimation of wave overtopping flow parameters

Few (if any) armoring or slope protection products have been tested at large scale for effectiveness when subjected to wave overtopping as illustrated by Figure 4(a). The main difference between wave overtopping and steady flow overflow (Figure 4(b)) is the periodic nature of the unsteady wave overtopping. As each wave overtops, it has a forward velocity across the levee crest that exceeds the crest velocity of comparable surge overtopping. Thus, unprotected soil on the levee crest that is stable for low levels of surge overtopping may erode if waves overtop.

For most levee protected-side slopes, critical flow conditions will exist at the leeward edge of the levee crest causing the wave overtopping flow to be supercritical on the backside slope. However, this flow condition is unsteady and peak velocities are sustained for only a brief time. In addition, the unsteady discharge over the crest results in a limited overtopping volume. Consequently, any erosion on the backside slope due to wave overtopping is intermittent, and the erosion rate will vary with overtopping intensity.

Experiments have been conducted in Europe at small and large scale with the aim of quantifying the wave overtopping flow parameters on the inner slope of dikes and levees (Schüttrumpf et al. 2002; van Gent 2002; Schüttrumpf and van Gent 2003; Schüttrumpf and Oumeraci 2005). These authors developed analytical expressions to represent the velocity and flow depths at the edge of the crest on the flood side, at the edge of the crest on the protected side, and down the backside slope as illustrated in Figure 5.

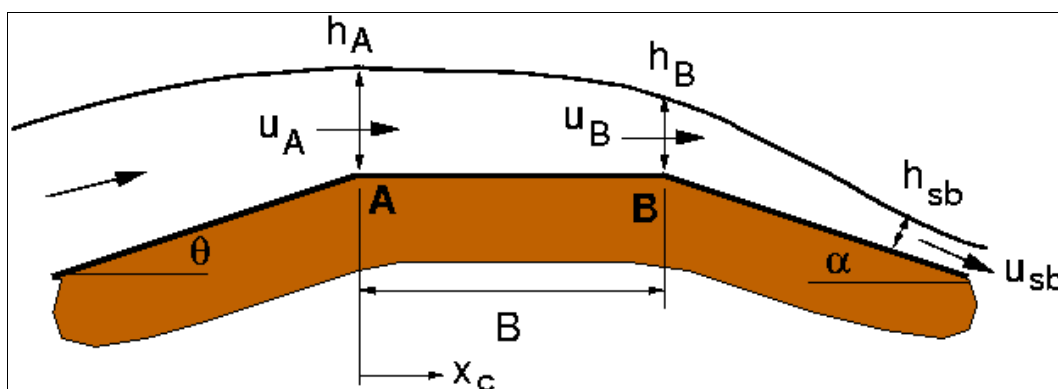


Figure 5. Wave overtopping definition sketch (after Schüttrumpf and Oumeraci 2005).

The key parameters necessary for estimating the flow velocities and depths are the levee freeboard R_c , the run-up elevation exceeded by 2 percent of the waves $R_{u2\%}$, and a friction factor f_F that accounts for frictional energy loss as the overtopping wave travels across the crest and down the protected-side slope.

Independent laboratory experiments were conducted in The Netherlands (van Gent 2002) and in Germany (Schüttrumpf et al. 2002). These two studies produced very similar estimation analysis techniques with only minor differences in the details. A joint paper (Schüttrumpf and van Gent 2003) reconciled the differences to the extent possible.

Van Gent's (2002) small-scale experiments had a 1:100 foreshore slope with a 1:4 slope on the flood side of the dike. Two levee crest widths (0.2 and 1.1 m) were combined with two protected-side slopes (1:2.5 and 1:4) to give four different dike geometries using a smooth dike surface. A fifth test series was conducted with a rough surface. Velocity and flow thickness were measured at the edges of the crest and at three locations spaced down the protected-side slope. Micro-impellers were used to measure velocity. Eighteen irregular wave tests were performed for the different dike

geometries, ten with single-peaked spectra and eight with double-peaked spectra. Incident wave conditions were determined by measuring the generated waves without the structure in place, and applying the Mansard and Funke (1980) frequency-domain method to remove reflection caused by the dissipating beach profile. Van Gent (2002) used the wave parameter $H_{1/3}$ in the analysis, but did not indicate how this time-domain parameter was determined from the frequency-domain value of H_{mo} found from the reflection analysis. Wave period was specified as mean period $T_{m-1.0}$, and it was estimated from the moments of the incident wave frequency spectra. The mean period is reported to better represent double-peaked spectra.

Schüttrumpf et al.'s (2002) experiments included both small- and large-scale tests. The small-scale tests utilized three flood-side slopes (1:3, 1:4, and 1:6), a crest width of 0.3 m, and five protected-side slopes (1:2, 1:3, 1:4, 1:5, and 1:6). A total of 270 tests were run using regular waves and irregular waves conforming to the JONSWAP spectrum. Flow depths were measured with resistance wave gauges, and overtopping flow velocity was recorded using micro-impellers. For the large-scale tests the flood-side slope was 1:6, the crest width was 2 m, and the protected-side slope was 1:3. A total of 250 model tests were run using some regular waves, but mostly irregular waves. Flow depth and velocity were measured using wave gauges and micro-impellers.

Wave data from Schüttrumpf et al.'s (2002) tests were analyzed in the frequency domain using the reflection method of Mansard and Funke (1980). The time-domain wave height parameter $H_{1/3}$ was used in their overtopping analysis with the conversion from the frequency domain wave height given as $H_{1/3} = 0.94 H_{mo}$ (Schüttrumpf 2006, personal communication). This conversion may have been a typographical error because we should expect $H_{1/3}$ to be greater than H_{mo} for shallow water waves. Also, the conversion is strictly valid only for these tests and not in general because it was determined for wave flume data with a constant water depth for all tests. The wave period was specified as the mean wave period, and it was determined from the calculated incident wave spectra by the simple relationship $T_m = 0.88 T_p$ (Schüttrumpf 2006, personal communication).

Flow parameters at flood-side levee crest edge

At the flood-side edge of the levee crest (denoted by the subscript letter *A* in this report) the flow parameters are given by Equations 1 and 2:

$$\frac{h_{A2\%}}{H_s} = C_{Ah2\%} \left[\frac{R_{u2\%} - R_c}{H_s} \right] \quad (1)$$

and

$$\frac{u_{A2\%}}{\sqrt{gH_s}} = C_{Au2\%} \sqrt{\frac{R_{u2\%} - R_c}{H_s}} \quad (2)$$

where:

$h_{A2\%}$ = peak flow depth exceeded by 2 percent of the waves

H_s = significant wave height [= H_{mo}]

$C_{Ah2\%}$ = empirical depth coefficient determined from test data

$R_{u2\%}$ = run-up elevation exceeded by 2 percent of the waves

R_c = crest freeboard [= crest elevation minus still-water elevation]

$u_{A2\%}$ = flow depth-averaged peak velocity exceeded by 2 percent of the waves

g = acceleration of gravity

$C_{Au2\%}$ = empirical velocity coefficient determined from test data.

The values of $h_{A2\%}$ and $u_{A2\%}$ were determined from the peaks of the overtopping wave time series, and these parameters represent the levels exceeded by only 2 percent of the total waves during the tests. For example, if a test had 1,000 waves, perhaps only 200 waves overtopped the crest. The 2 percent exceedance level would be the level exceeded by 20 of the 1,000 waves ($0.02 \times 1,000$), but this is 10 percent of the overtopping waves. Schüttrumpf et al. (2002) also provided coefficients for the average overtopping parameters $h_{A50\%}$ and $u_{A50\%}$. All of the equations pertain to the maximum velocity at the leading front of the overtopping wave. Flow velocities and depths associated with a single wave decrease after passage of the wave front.

Note in Equations 1 and 2 that significant wave height H_s in the denominator cancels on both sides of the equations. Thus, the flow depth is directly proportional to the difference between the 2-percent run-up and

levee freeboard, and the depth-averaged flow velocity is proportional to the square root of this difference. Wave parameters enter into the estimation of flow depth and velocity at the flood-side crest edge through the estimation of the 2-percent run-up parameter $R_{u2\%}$. As noted by van Gent (2002), the calculated $R_{u2\%}$ is a fictitious value in cases where run-up exceeds the structure freeboard. It is the level that would be exceeded by 2 percent of the waves if the front slope were continued upwards indefinitely.

The values of the empirical coefficients determined for the two studies are given in Table 1.

Table 1. Empirical coefficients for flood-side crest edge flow parameters.

Coefficient	Schüttrumpf	van Gent
$C_{Ah2\%}$	0.33 ^{2,3} and 0.22 ⁴	0.15 ^{1,3}
$C_{Au2\%}$	1.55 ² and 1.37 ³	1.30 ^{1,3}
$C_{Ah50\%}$	0.17 ^{2,4}	-
$C_{Au50\%}$	0.94 ^{2,4}	-
¹ van Gent (2002). ² Schüttrumpf et al. (2002). ³ Schüttrumpf and van Gent (2003). ⁴ Schüttrumpf and Oumeraci (2005).		

The coefficient $C_{Ah2\%}$ is a constant that is actually equal to a slope-dependent constant C_2 divided by $\tan \theta$, where θ is the flood-side structure slope. Values of C_2 given in the various papers are used in an equation slightly different than Equation 1. The value for $C_{Ah2\%}$ given by Schüttrumpf was revised from 0.33 to 0.22 in the most recent paper (Schüttrumpf and Oumeraci 2005), and this probably represents a better value as shown by the data plot given in the 2005 paper and the fact it is closer to the value obtained by van Gent. The value of $C_{Au2\%} = 1.55$ is derived from a table in Schüttrumpf et al. (2002) that associated this coefficient with large-scale tests. A coefficient associated with the 10 percent exceedance level can also be derived from the same table as $C_{Au10\%} = 1.37$ for large-scale tests. In Schüttrumpf and van Gent (2003) the value of $C_{Au2\%} = 1.37$ was reported, and this is thought to be a typographical error. The correct value should have been $C_{Au2\%} = 1.55$.

Schüttrumpf and van Gent (2003) attribute differences in empirical coefficients to different dike geometries and instruments, but they noted the

differences are not too great. Van der Meer et al. (2006) suggested an error in measurement or analysis might have caused the factor-of-two difference seen for the coefficient $C_{Au2\%}$, but the revised value of 0.22 brings the results closer. A more probable cause for variation might be in the method each investigator used to estimate the value of 2 percent run-up $R_{u2\%}$.

Van Gent (2002) estimated $R_{u2\%}$ using a formula he developed earlier (van Gent 2001) that uses $H_{1/3}$ and $T_{m-0.1}$ as the wave parameters. Schüttrumpf estimated $R_{u2\%}$ using the equations of de Waal and van der Meer (1992) with wave height $H_{1/3}$ and wave period T_m instead of spectral peak period T_p . Both formulas give reasonable estimates that fall within the scatter of the 2 percent run-up data, so whichever formula is selected for calculating $R_{u2\%}$ the estimates for overtopping flow parameters should be reasonable.

Until further clarification becomes available, it is recommended that values of $C_{Ah2\%} = 0.22$ and $C_{Ah2\%} = 1.55$ be used to estimate the overtopping flow parameters associated with the flow depth and velocity exceeded by 2 percent of the incoming waves.

Flow parameters at the protected-side levee crest edge

Overtopping waves flowing across the dike or levee crest decreases in height, and the velocity decreases as a function of the surface friction factor f_F . The flow depth (or thickness) can be estimated at any location on the crest with the equation:

$$h_{B2\%} = h_{A2\%} \exp \left(-C_3 \frac{x_c}{B} \right) \quad (3)$$

where:

B = crest width

x_c = distance along the crest from the flood-side edge

C_3 = an empirical coefficient.

The flow thickness at the protected-side crest edge (denoted by the subscript letter B in this report) is given when $x_c = B$. Different values of the coefficient were given in the various publications, i.e., based on the

2 percent exceedance levels $C_3 = 0.89$ for TMA spectra and $C_3 = 1.11$ for natural spectra (Schüttrumpf et al. 2002); $C_3 = 0.40$ and 0.89 (Schüttrumpf and van Gent 2003); and $C_3 = 0.75$ for irregular and regular waves (Schüttrumpf and Oumeraci 2005). The factor-of-two difference between van Gent and Schüttrumpf was attributed to the difference in estimating wave run-up.

For levee calculations it is recommended that a value of $C_3 = 0.75$ be used on the assumption that earlier values had been corrected by publication of the journal article. The 2 percent run-up elevation should be estimated using the run-up formulas of de Waal and van der Meer (1992) or Hughes (2004). If van Gent's (2001) method for estimating wave run-up is used, it would be more appropriate to use a value of $C_3 = 0.40$. Note that Equation 3 is applicable for estimating $h_{B50\%}$ if the flow depth $h_{A50\%}$ is used instead of $h_{A2\%}$. In fact, Schüttrumpf and Oumeraci (2005) presented only the 50 percent exceedance values.

Flow velocity along the dike crest exceeded by 2 percent of the waves is given by a similar equation:

$$u_{B2\%} = u_{A2\%} \exp \left(- \frac{x_c}{2} \frac{f_F}{h_{B2\%}} \right) \quad (4)$$

where:

f_F = Fanning friction factor appropriate for the levee crest surface
 $h_{B2\%}$ = flow depth at that location on the crest obtained via Equation 3.

At the protected-side crest edge, evaluate Equation 4 with $x_c = B$. Van Gent (2002) had a different expression for $u_{B2\%}$, but in Schüttrumpf and van Gent (2003) both authors agreed on Equation 4. A theoretical derivation for Equation 4 is given in Schüttrumpf and Oumeraci (2005).

Estimation of friction factor

The Fanning friction factor has a significant influence on flow velocity across the crest and down the backside slope. The small-scale experiments of Schüttrumpf et al. (2002) had a structure surface constructed of wood fiberboard, and the friction factor was determined experimentally to be

$f_F = 0.0058$ (Schüttrumpf and Oumeraci 2005). The structure in the companion large-scale experiments was constructed with a bare, compacted clay surface; and experimental results gave the friction factor as $f_F = 0.01$ (Schüttrumpf et al. 2002). Schüttrumpf and Oumeraci (2005) also list the following representative values for friction factor on the protected-side slope: $f_F = 0.02$ (smooth slopes), and from Cornett and Mansard (1994) $f_F = 0.1 - 0.6$ (rough revetments and rubble-mound slopes). Grass-covered slopes would probably have a friction coefficient not much above $f_F = 0.01$.

Determination of an appropriate value of friction factor for various armor-ing alternatives may be difficult because of the lack of published values. As a first approximation an estimate can be made if a representative value of Manning's n is known for a particular surface slope or armor-ing product. Manning's n can be related to the Chezy coefficient C_z by the expression (e.g., Henderson 1966)

$$C_z = \frac{R^{1/6}}{n} \quad (5)$$

where:

R = hydraulic radius
 n = given in metric units.

For wide channels, R is essentially the same as the depth h . The Chezy coefficient can be given in terms of the Darcy friction factor f_D . Because the Fanning friction factor is one-fourth of the Darcy friction factor, i.e., $f_D = f_F/4$, the Chezy coefficient can also be given in terms of the Fanning friction factor as (Henderson 1966)

$$C_z = \sqrt{\frac{8g}{f_D}} = \sqrt{\frac{2g}{f_F}} \quad (6)$$

Combining Equations 5 and 6, substituting h for R , and rearranging yields Equation 7 (in metric units) for f_F in terms of Manning's coefficient and flow depth h in meters, i.e.,

$$f_F = \frac{2g n^2}{h^{1/3}} \quad (7)$$

The validity of Equation 7 has not been proven, and it is based on the assumption that friction factors and Manning's n associated with steady supercritical overflow that has reached equilibrium (e.g., Chezy or Manning equation) will be the same for unsteady, rapidly varying flows due to wave overtopping. Therefore, caution must be exercised when applying Equation 7.

Flow parameters on the protected-side levee slope

Both European investigators (Schüttrumpf and van Gent) derived theoretical expressions for the wave front depth-averaged, slope-parallel flow velocity down the protected-side slope by simplification of the momentum equation. Schüttrumpf and Oumeraci (2005) presented an iterative solution, whereas van Gent (2002) derived an explicit formula. A comparison between the two solutions revealed only small differences in the result, and both formulations approached the same equation in the limit as distance down the slope becomes large (Schüttrumpf and van Gent 2003). For ease of application, van Gent's formula is preferred, and it was given as

$$u_{sb2\%} = \frac{K_2}{K_3} + K_4 \exp \left(-3 K_2 \cdot K_3^2 \cdot s_b \right) \quad (8)$$

with

$$K_2 = (g \sin \alpha)^{1/3} \quad (9)$$

$$K_3 = \left[\frac{f_F}{2} \frac{1}{h_{B2\%} \cdot u_{B2\%}} \right]^{1/3} \quad (10)$$

$$K_4 = u_{B2\%} - \frac{K_2}{K_3} \quad (11)$$

and α is the angle of the protected-side slope, s_b is the distance down the slope from the crest edge, and $h_{B2\%}$ and $u_{B2\%}$ are the flow depth and flow velocity, respectively, at the protected-side crest edge. For long distances downslope, the exponential term in Equation 8 becomes insignificant, and the velocity equation reduces to

$$u_{sb2\%} = \frac{K_2}{K_3} = \left[\frac{2 g \cdot h_{B2\%} \cdot u_{B2\%} \cdot \sin \alpha}{f_F} \right]^{1/3} \quad (12)$$

Flow thickness perpendicular to the slope at any point down the protected-side slope is found from the continuity equation as

$$h_{sb2\%} = \left[\frac{h_{B2\%} \cdot u_{B2\%}}{u_{sb2\%}} \right] \quad (13)$$

Equations 1–13 can be used to estimate the wave overtopping peak velocity and associated flow depth over a levee that is exceeded by only 2 percent of the incoming waves.

Estimation of surge overtopping flow parameters

For the case of water overflowing a levee as illustrated in Figure 6, sub-critical flow exists on the high-water side of the levee (left side in Figure 6), critical flow occurs somewhere on the levee crest, and the flow down the backside slope is supercritical unless the backside slope is very mild. At the toe of the levee, or when the downward flowing water joins with the tailwater (i.e., ponding flood water), a hydraulic jump is formed as the flow returns to subcritical. Erosive turbulence occurs at the location of the hydraulic jump. For the flow situation depicted in Figure 6, discharge is determined by the upstream head h_1 .

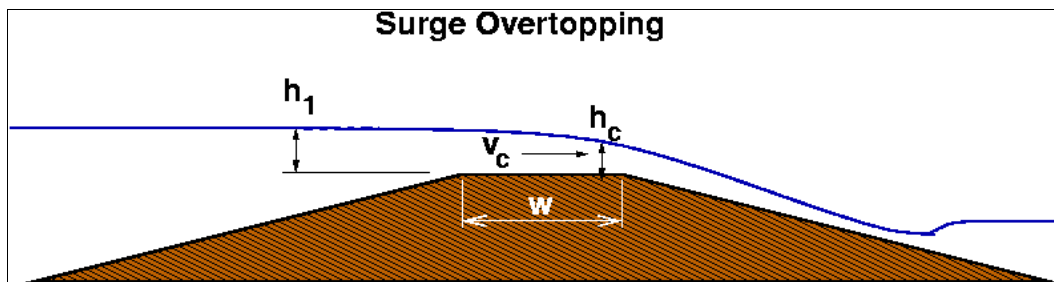


Figure 6. Surge overtopping design parameters.

As the tailwater continues to rise in the flooded area, the hydraulic jump moves up the slope. Eventually, the tailwater reaches an elevation above the levee crest and near that of the upstream flow, and discharge is controlled by upstream head and the tailwater. This flow condition has importance for roadway embankments, but it is not relevant for levees

because tailwater at this elevation indicates complete inundation on the protected area (polder) behind the levee system.

Discharge and critical velocity

If the levee crest for the surge overtopping case shown in Figure 6 is sufficiently long to maintain a hydrostatic pressure distribution, critical flow (transition between subcritical and supercritical flow) will occur somewhere along the levee crest. Assuming minimal frictional energy losses along the crest, the discharge per unit width of levee is computed by the generally accepted equation for flow over a broad-crested weir given by open channel flow texts (e.g., Henderson 1966) as

$$q = \left(\frac{2}{3} \right)^{3/2} \sqrt{g} h_1^{3/2} = 0.5443 \sqrt{g} h_1^{3/2} \quad (14)$$

where:

- q = discharge per unit length
- g = gravitational acceleration
- h_1 = upstream head (difference between surge elevation and levee crest elevation as shown in Figure 6).

Note that surge elevation includes effects of slowly varying tides. Equation 14 is dimensionally homogeneous and can be applied using any consistent set of units because the numerical coefficient is dimensionless. Often in hydraulics the gravitational constant is substituted using inch/pound units, the resulting coefficient becomes 3.09, and it has units of 0.5 ft per second.

Kindsvater (1964) investigated flows over roadway embankments, and he presented an empirical form of the broad-crested weir discharge formula that compensates for frictional losses across the paved crest, i.e.,

$$q = C_f \sqrt{g} h_1^{3/2} \quad (15)$$

where $C_f \leq 0.5443$. The empirical coefficient was given in design nomograms (Chen and Anderson 1987) as a function of the ratio of upstream head over embankment width h_1/w . However, the decrease in C_f is rather insignificant until the upstream head becomes small (less than 0.5 ft). For

example, with $h_1/w < 0.15$ and $h_1 = 0.5$ ft, $C_f = 0.5322$ which is only about a 2 percent reduction due to frictional losses. Grass-covered or rock-armored crests would provide a greater reduction. As a first approximation, it seems appropriate to use the slightly conservative Equation 14 to estimate discharge due to surge overflow.

Discharge per unit length of levee can also be represented in terms of the flow Froude number F_R by the expression

$$q = \sqrt{g h^3} F_R \quad (16)$$

For critical flow $F_R = 1$, and

$$q_c = \sqrt{g h_c^3} \quad (17)$$

where h_c is the critical depth (Figure 6). For steady flow, mass continuity yields constant discharge at every location so Equations 14 and 17 are equivalent, and the critical depth can be found from the two equations as

$$h_c = \frac{2}{3} h_1 \quad (18)$$

When the Froude number is unity, the critical velocity v_c is given by

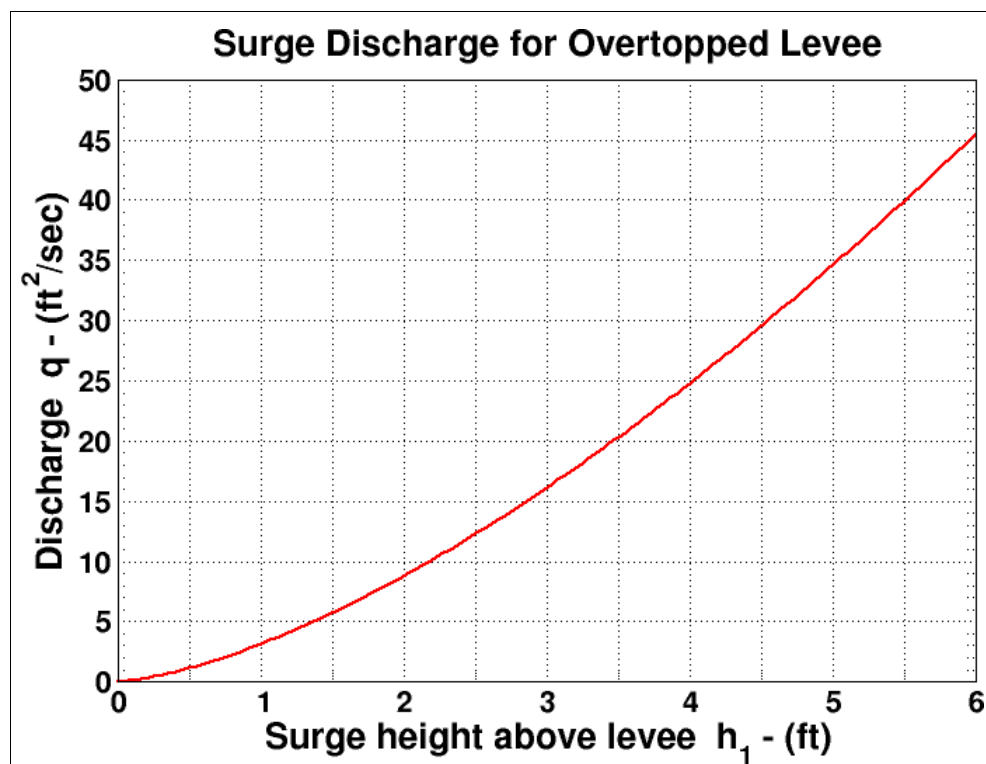
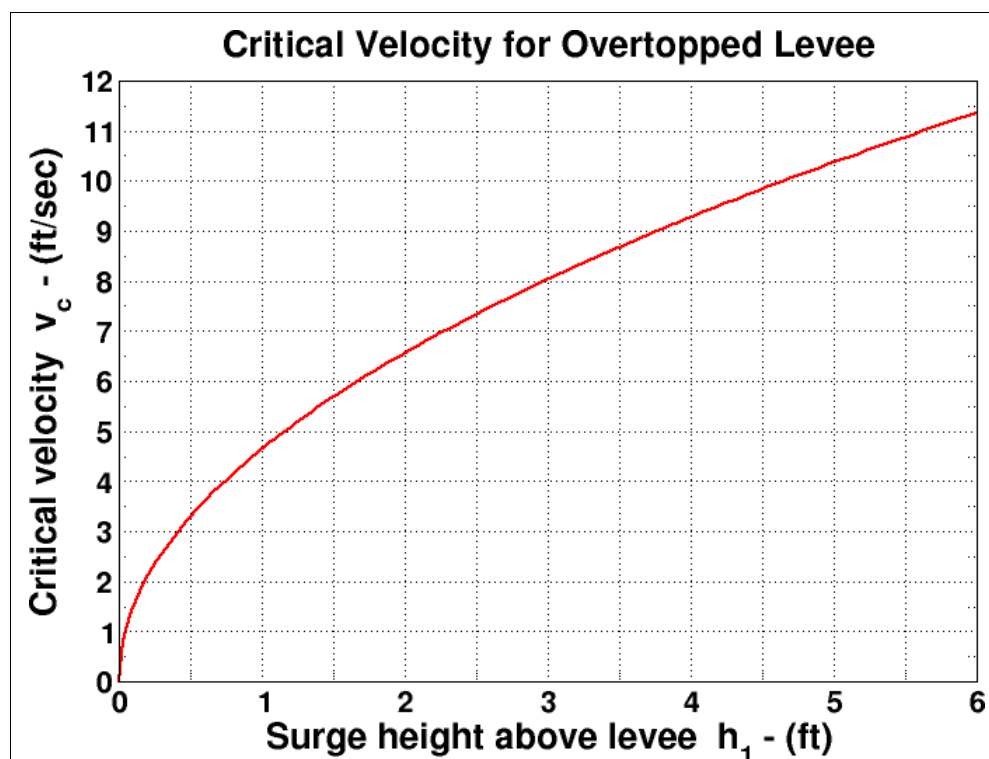
$$v_c = \sqrt{g h_c} \quad (19)$$

or

$$v_c = \sqrt{\frac{2}{3} g h_1} \quad (20)$$

when Equation 18 is substituted for h_c .

Figures 7 and 8 show discharge per unit length and critical velocity on the crest, respectively, plotted as a function of surge elevation above the levee crest h_1 .

Figure 7. Discharge versus upstream head h_1 .Figure 8. Critical velocity on crest versus upstream head h_1 .

Protected-side slope supercritical flow

Levee surge overflowing water transitions from critical to supercritical flow as it continues over the rear edge of the levee crest and flows down the protected-side slope. If the slope were frictionless, water would continue to accelerate under the force of gravity. However, slope surface roughness resists the flow by forming a turbulent boundary layer, and a balanced steady flow condition is established. Flows of this type can then be analyzed using a flow resistance equation.

The mean velocity for a fully developed resistance flow where the boundary layer is turbulent in the fully rough range (independent of Reynolds number) is given by the Chezy equation as

$$v = C_z \sqrt{R S_f} \quad (21)$$

where:

- C_z = Chezy coefficient (determined empirically)
- R = hydraulic radius [$R = A/P$]
- A = channel cross-sectional area
- P = channel wetted perimeter
- S_f = slope of the total energy line (or friction slope).

The Chezy flow resistance equation is dimensionally nonhomogeneous because the Chezy coefficient has dimensions of square root of length divided by time. Thus, care must be exercised when applying this equation.

For very wide channels (e.g., flow over a levee having constant crest elevation), the hydraulic radius R is equal to the flowing water thickness h_o taken perpendicular to the slope. If the protected-side slope is linear with nearly similar roughness along its length, the flow becomes uniform at some downslope location; and the water free surface is parallel to the levee slope. For this condition of steady, uniform flow (and mild slopes) the slope of the total energy line is the same as the levee slope so $S_f = S_o = \sin \theta$ where θ is the angle of the protected-side slope relative to the horizontal. Substituting $R = h_o$ and $S_f = \sin \theta$ into Equation 21, and representing the Chezy coefficient by Equation 6 yields

$$v_o = \sqrt{\frac{8g}{f_D}} \sqrt{h_o \sin \theta} \quad (22)$$

where v_o represents the slope-parallel mean velocity for fully-developed, steady, uniform flow.

Hartung and Scheuerlein (1970) presented the formula given by Equation 22. They gave a function for the friction factor f_D that accounted for slope roughness due to armoring stone sizes, a stone packing factor, flow thickness perpendicular to the slope, and an aeration factor related to the amount of air entrained into the flow. An iterative solution of the Hartung and Scheuerlein equation is required, and it applies primarily to rock-armored slopes.

Perhaps the most popular flow resistance equation is the Manning formula. Systematic observations in natural rivers by earlier researchers led to a relationship for Chezy coefficient expressed in metric units as

$$C_z = \frac{R^{1/6}}{n} \quad (23)$$

where n is characteristic of only the surface roughness. (In 1891, the Frenchman Flamant wrongly attributed this relationship to the Irishman Manning (Henderson 1966).) Substituting Equation 23 into Equation 21 and converting the equation to the inch/pound system of units gives the usual form of the Manning equation with v having units of feet per second and R given in units of feet.

$$v = \frac{1.49 R^{2/3} S_f^{1/2}}{n} \quad (24)$$

For steady, uniform flow $R = h_o$, $S_f = \sin \theta$, and $h_o = q_o / v_o$. Making these substitutions into Equation 24, and solving for v_o gives the following equation for the mean flow velocity in units of feet per second.

$$v_o = \left[\frac{1.49 \sqrt{\sin \theta}}{n} \right]^{3/5} q_o^{2/5} \quad (25)$$

where q_o in units of square feet per second equals the critical discharge q_c , and Manning's n is given in metric units. Care must be taken when applying the Manning equation because the variables must be given in specific units.

Typical values for Manning's n are 0.025 for earth with some rocks and weeds up to 0.150 for very weedy, winding, and overgrown natural rivers. Figure 9 shows the variation of backside slope velocity as a function of levee slope and the elevation difference between the surge and levee crest for two values of Manning's n . Figure 10 plots the corresponding values of flow thickness down the levee backside slope.

Combined wave and surge overtopping

The most devastating flow condition on the backside levee slope will occur when the surge level is above the levee crest, and the levee is exposed to hurricane-force waves as illustrated in Figure 4(c). If the levee crest remains intact, some incident waves will break before reaching the crest and continue to propagate across the crest as a broken wave form resembling a strong turbulent bore. This bore will cascade down the backside

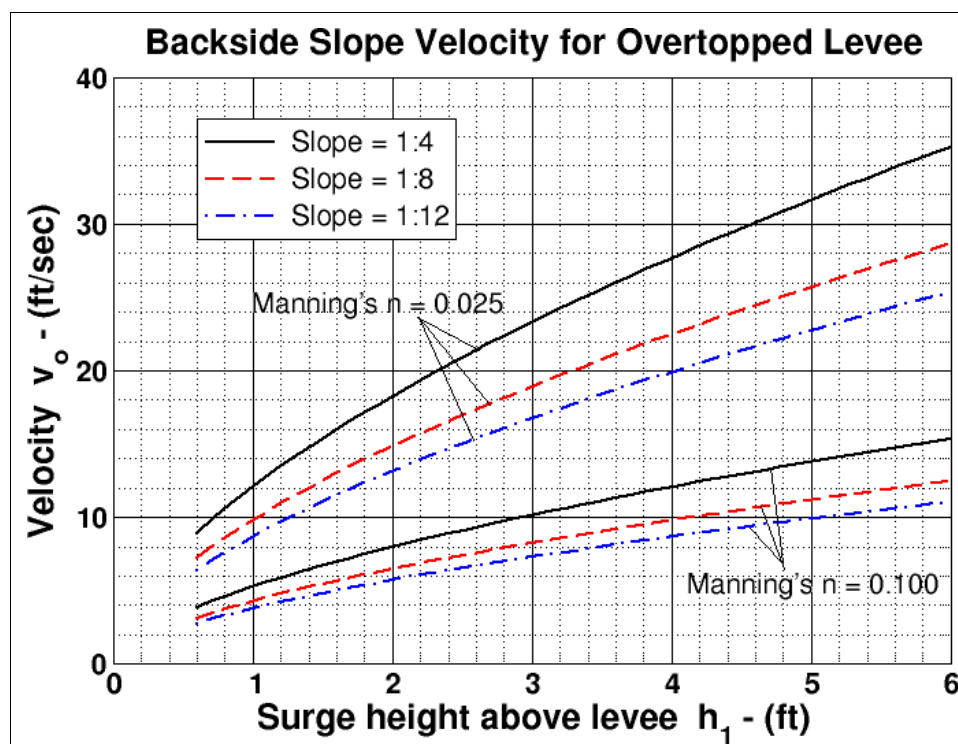


Figure 9. Backside slope velocity versus upstream head h_1 .

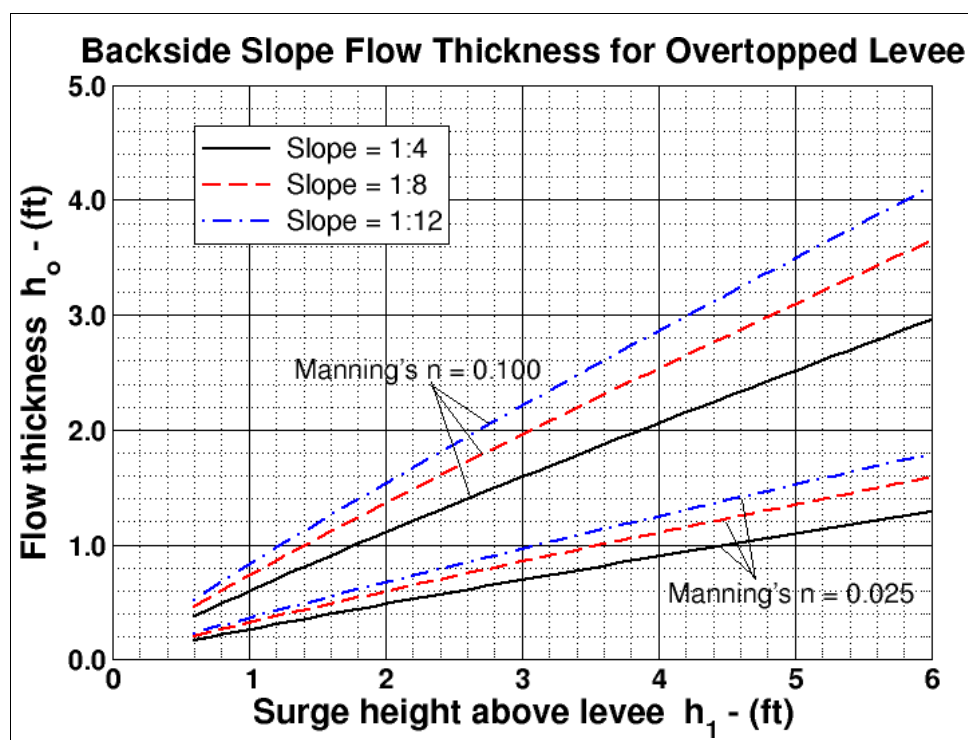


Figure 10. Backside slope flow thickness versus upstream head h_1 .

slope adding its mass to the steady overtopping discharge as a discharge pulse. The resulting flow condition is unsteady in time and nonuniform over the slope with varying acceleration.

There are no simple analytical techniques suitable for obtaining approximate values of the pertinent flow parameters, and little (if any) laboratory data exist for this overtopping condition. Numerical modeling holds promise for analyzing the hydrodynamics of combined wave and storm surge overtopping; but even if the hydrodynamic results correspond well to laboratory measurements, it will be difficult to apply the information to evaluating stability of armoring and protection systems because of the complete lack of large-scale product testing for this combined wave and surge flow condition.

A reasonable engineering expectation would be that armoring products capable of withstanding a given steady flow velocity or shear stress magnitude caused by surge overtopping should also withstand the same magnitude arising from wave overtopping. Possible factors that may negate this hypothesis include the effect of flow acceleration/deceleration that occurs with wave overtopping and the varying water depth on the backside slope. In other words, protection systems that have proven stable under

steady flow conditions may not respond well in an unsteady flow that is constantly accelerating and decelerating.

This study focused on documenting the hydrodynamic flow parameters associated with unsteady flow on the levee protected-side slope when subjected to combined wave and surge overtopping. This is the first step toward being able to relate full-scale armor stability test results from steady flow overtopping to an equivalent unsteady flow condition arising from combined wave and surge overtopping.

3 Principles of Physical Modeling

This chapter overviews the principles that govern the design and operation of small-scale, fixed-bed physical models of free-surface flow phenomena. Included is a discussion of the advantages and disadvantages of physical models, along with a description of how the modeling technology can be best applied to investigate wave and storm surge overtopping of earthen levees along MRGO.

Principles of similitude

The basis of all physical modeling is the idea that the model behaves in a manner similar to the prototype it is intended to emulate. Thus, a properly validated physical model can be used to predict the prototype (real world) under a specified set of conditions. However, there is a possibility that physical model results may not be indicative of prototype behavior due to scale effects or laboratory effects. The role of the physical modeler is to minimize scale effects by understanding and applying proper similitude relationships and to minimize laboratory effects through careful model operation.

Similarity between the real world (prototype) and a small-scale replica (model) of a coastal project area is achieved when all major factors influencing reactions are in proportion between prototype and model while those factors that are not in proportion throughout the modeled domain are so small as to be insignificant to the process. For coastal short-wave models, three general conditions must be met to achieve model similitude:

1. *Geometric similarity* exists between two objects or systems if the ratios of all corresponding linear dimensions are equal. This relationship is independent of motion of any kind and involves only similarity in form (Warnock 1950). Geometrically similar models are also known as geometrically undistorted models because the horizontal and vertical length scales are the same. (Departure from geometric similarity is restricted to hydrodynamics of long waves and unidirectional flows.)
2. *Kinematic similarity* indicates a similarity of motion between particles in model and prototype. Kinematic similarity is achieved when the ratio between the components of all vectorial motions for the prototype and model is the same for all particles at all times (Hudson et al. 1979). In a

- geometrically similar model, kinematic similarity gives particles paths that are geometrically similar to the prototype. Kinematic similarity assures the flow velocities and pressures associated with water overtopping the levees is correctly replicated in the physical model.
3. *Dynamic similarity* between two geometrically and kinematically similar systems requires that the ratios of all vectorial forces in the two systems be the same (Warnock 1950). This means that there must be constant prototype-to-model ratios of all masses and forces acting on the system. The requirement for dynamic similarity arises from Newton's second law that equates the vector sum of the external forces acting on an element to the element's mass reaction to those forces. Dynamic similitude is required when the model is used to determine the capability of ACMs to remain stable while resisting water velocities and accelerations.

Perfect similitude requires that the prototype-to-model ratios of the inertial, gravitational, viscous, surface tension, elastic, and pressure forces be identical. In practice, perfect similitude is impossible at reduced model scale. Fortunately, many coastal problems and flow regimes are adequately modeled by an imperfect similitude where inertial and gravitational forces dominate while all other forces are small in comparison.

For convenience, physical modeling similitude requirements are expressed in terms of scale ratios, defined as the ratio of a parameter in the prototype to the value of the same parameter in the model. The scale ratio is represented by the notation

$$N_X = \frac{X_p}{X_m} = \frac{\text{value of } X \text{ in prototype}}{\text{value of } X \text{ in model}} \quad (26)$$

where N_X is the prototype-to-model scale ratio of the parameter X . For example, the length scale is usually denoted as N_L and the velocity scale is N_V .

Hydraulic similitude

Hydraulic similitude requirements for coastal hydrodynamic short-wave models can be derived (e.g., Hughes 1993) from the continuity and Navier-Stokes equations governing incompressible, free-surface flows. The resulting similitude conditions are listed here. In Equations 27-29 the expressions on the left side give the similitude criteria, which are also given in terms of scale ratios on the right side (Hughes 2003).

1. The model must be geometrically undistorted, i.e., horizontal and vertical length scales are the same.
2. The Froude number, which is the ratio of inertial to gravitational forces, must be the same in the model as in the prototype, i.e.,

$$\left(\frac{V}{\sqrt{gL}} \right)_p = \left(\frac{V}{\sqrt{gL}} \right)_m \quad \text{or} \quad \frac{N_V}{\sqrt{N_g N_L}} = 1 \quad (27)$$

3. The Strouhal number, which is the ratio of temporal to convective inertial forces, must be the same in the model as in the prototype, i.e.,

$$\left(\frac{L}{Vt} \right)_p = \left(\frac{L}{Vt} \right)_m \quad \text{or} \quad \frac{N_L}{N_V N_t} = 1 \quad (28)$$

4. The Reynolds number, which is the ratio of inertia to viscous forces, must be the same in the model as in the prototype, i.e.,

$$\left(\frac{\rho LV}{\mu} \right)_p = \left(\frac{\rho LV}{\mu} \right)_m \quad \text{or} \quad \frac{N_\rho N_L N_V}{N_\mu} = 1 \quad (29)$$

where:

V = characteristic velocity
 g = gravitational acceleration
 L = characteristic length
 t = time
 ρ = fluid density

and the subscripts p and m represent prototype and model, respectively.

The geometric similarity criterion (condition 1) coupled with the Froude criterion (condition 2) assure that all terms in the governing flow equations are in similitude with the exception of the viscous terms. Froude similarity includes the turbulent Reynolds shear stress terms; thus, macro features of turbulent dissipative processes are also in similitude.

Viscous effects can only be modeled if the Reynolds criterion (condition 3) is met along with the Froude criterion in a geometrically similar model. In general this is practical only at prototype scale (full-size scale).

Consequently, coastal short-wave models can be either nondissipative where viscous and capillary effects are negligible, such as waves prior to breaking; or the model can have highly turbulent flow dissipation over a relatively short distance, such as during wave breaking on a structure or a beach (Le Méhauté 1976). In reality, there will always be a small amount of wave attenuation due to viscous frictional losses and surface tension effects, but these scale effects can be minimized to the point of insignificance.

The hydrodynamic time scale for Froude-scaled hydrodynamic models is obtained by solving Equation 27 for N_V and substituting into Equation 28 to give

$$N_t = \sqrt{\frac{N_L}{N_g}} \quad (30)$$

Because the gravitational force will be the same in the model as in the prototype, the ratio N_g will be unity, and N_g is usually not included in the scaling criteria. Other scale ratios derived from Froude and Reynolds scaling are given in most similitude texts (e.g., Hughes 1993).

Wave force and armor weight similitude

Scaling of wave forces and ACM weight must also follow the Froude scaling criterion. Given in terms of prototype-to-model scale ratios, the general force scale is as follows:

$$N_F = N_V N_L^3 \quad (31)$$

where $N_V = \gamma_p/\gamma_m$ and $\gamma = \rho g$ is specific weight. The value of γ depends on the forcing. Wave force scaling uses the specific weight of water, whereas forces due to the weight of ACMs use a value of specific weight that accounts for the concrete material and the steel wires that connect the concrete blocks into a mat.

Stability of ACMs requires that the hydrodynamic forces induced by the flowing water be less than the resistance force due to the concrete mat's self-weight. The upward buoyancy force when the mats are submerged acts to decrease the stability, and this important aspect is taken into

account by requiring the immersed specific weight of the mats in the model to be the same as the mats in the prototype, i.e.,

$$\left(\frac{\gamma_a}{\gamma_w} \right)_p = \left(\frac{\gamma_a}{\gamma_w} \right)_m \quad \text{or} \quad N_{\gamma_a} = N_{\gamma_w} \quad (32)$$

where γ_a is specific weight of the ACM, and γ_w is specific weight of water. Nearly all scale model experiments use fresh water. If the prototype is situated in denser salt water, the scale ratio of concrete mat specific weight is approximately 1.025. Thus, the material used for the model mats must be slightly less dense than the material used in the prototype. This adjustment compensates for the increased buoyancy of the mats in salt water.

In cases where suitable model material having the exact required density cannot be found, other methods are used to achieve approximate similitude using materials with densities reasonably close to the target density. This may involve slight changes in model unit dimensions to get the correct scaled weight of the mat unit, or it may involve similitude of the Hudson stability equation (Hughes 2003) in cases of rubble-mound stability.

Strict dynamic similitude of ACM stability would require that the mass distribution of the mats be faithfully reproduced in the model. However, because the mats are constructed of uniform material to uniform dimensions with only minor steel wire, it is reasonable to assume that the mass of the mats is uniformly distributed and consistent between mats.

Physical model advantages

Small-scale physical models are essentially analog computers of all the physical processes being simulated with the model. Nonlinearities and complex physical interactions between fluid and solid boundaries are faithfully reproduced without compromise provided the model has been scaled correctly and laboratory effects are controlled. For this reason, small-scale physical models offer an opportunity to examine those processes that are beyond theoretical understanding or are too complicated to represent adequately with simplified analytical or numerical modeling tools. The following is a list of advantages associated with physical models (Hughes 1993).

1. Physical models incorporate and integrate the fully nonlinear governing equations of the modeled process without simplifying assumptions.
2. Complex boundaries and bathymetry can be included without difficulty.
3. The small size of the model permits easy data collection.
4. Model forcing conditions can be easily simulated and controlled.
5. Similitude requirements for many problems are well understood and easily implemented.
6. Visual feedback from a physical model often reveals aspects of the physical process that had not been considered previously. Observations also help researchers to understand the differences that arise from changing the forcing conditions, and they often stimulate new ideas or alternative solutions.
7. Engineering solutions can be optimized in a physical model to achieve improved project functionality at minimum expense.
8. Often physical models are a cost-effective option relative to alternate study methods.

The benefits arising from physical model studies depend largely on the careful operation of the model coupled with a full understanding of the potential problems and shortcomings that may exist because of scale or laboratory effects.

Physical model disadvantages

The major disadvantages associated with small-scale physical models relate to either scale effects or laboratory effects.

Physical model scale effects

Scale effects in coastal hydrodynamic models result primarily from the Froude scaling assumption that gravity is the dominant physical force balancing the inertial forces. The other physical forces of viscosity, elasticity, and surface tension are incorrectly scaled with the belief that these forces contribute little to the physical processes. Scale effects in physical models are analogous to decreased accuracy that occurs in numerical models when complex physical processes are represented by simplified mathematical formulations (Kamphuis 1991).

In fixed-bed models the primary scale effect occurs wherever flows in the model become so slow that the flow regime might transition from turbulent to laminar flow conditions, whereas such a transition would not occur

in the prototype. In this case the viscous forces in the model would not be in similitude. An example of this scale effect is flow through a rubble-mound structure where the flow regime is always considered to be turbulent in the prototype but might be laminar in a small-scale physical model.

Surface friction is another potential scale effect. Surface roughness affects water flow, and it provides contact friction between adjacent solid objects. However, it is difficult to scale surface roughness of ACMs according to the model length scale. In this situation it is best to error on the conservative side by making the model mats smooth. This will allow slightly higher flow velocities adjacent to the blocks, and smooth blocks will have relatively less frictional resistance where they are in contact with adjacent blocks.

Finally, it is not possible to scale the levee soils to model size and expect similar erosive behavior of the earthen levee under the ACMs. Erosion of levee soils, particularly vegetated surfaces, can be modeled only at full scale, which is the only way to assure there are no scale effects.

Physical model laboratory effects

Laboratory effects in coastal physical models are primarily related to the following:

1. Physical constraints on flow in the model are caused by the need of representing a portion of the prototype in a finite amount of space. Model boundaries may exist where there is no boundary in the prototype. Waves reflect off model boundaries and introduce reflected wave trains back into the simulated wave field. This problem is partially solved using energy dissipating beaches composed of gentle slopes and rubberized horsehair mats that can minimize reflection to less than 5 percent.
2. Mechanical means of wave and current generation may introduce unintentional nonlinear effects. The most common example is incorrect reproduction of bound long waves that sometimes cause problems for harbor basins. The model engineer must attempt to make the mechanical waves resemble reasonably well the waves observed in nature.
3. Prototype forcing conditions are simplified, and only a subset of all possible conditions can be selected for testing. A common laboratory effect in wave basins is when long-crested unidirectional waves are generated to approximate directional waves that occur in nature. This compromise is not considered serious if the testing covers multiple approach angles, but the engineer must assess the approximation to determine whether it is

reasonable. Another example is simulating a storm using a constant water level as opposed to a time-varying surge hydrograph.

Laboratory effects in physical models are analogous to problems in numerical models caused by numerical approximation to the equations, roundoff and truncation errors, and computer speed, memory, and availability (Kamphuis 1991).

Other physical model disadvantages

Cost of physical model construction and operation is an important factor to consider. Construction costs increase directly with the model size, so the reduction in potential scale effects that arises from larger models will come at higher costs. Operation of a physical model requires skilled engineers and technicians, and significant time and effort is spent minimizing laboratory effects and assuring quality measurements. Also, time scales in physical models are determined by the similitude relationships so some time-dependent simulations make take a long time to complete (when compared to numerical modeling).

Even though data acquisition in a physical model is much easier than field data collection, there are inherent limitations. The number of measurement locations in the model is limited by available instrumentation and data channels. Therefore, careful consideration must be given about what to measure and where to place the instruments.

Physical model appropriateness

In many cases, a coastal problem can be examined by several different methods including numerical models, physical models, analytical techniques, statistical analyses, and desktop studies. Selecting which techniques are most suited to a particular problem requires the following: (1) knowledge of the primary forcing and responses that shape the coastal processes in the problem area, and (2) an understanding of how well the forcing and response are replicated by the alternative technologies. Often multiple technologies are employed with each providing part of the answer.

Physical models are appropriate where the hydrodynamic physical processes are complex (wave nonlinearities, wave/current interactions, complex bathymetry, numerous boundaries), and where the response to

the hydrodynamics is not well understood or quantified. In addition, the similitude relationships for the dominant processes must be known, and the potential scale and laboratory effects are thought to be surmountable.

Combined wave overtopping and storm surge overflow of earthen levees qualifies as a complicated hydrodynamic physical process. The hydrodynamic regime for this situation is complicated by a number of physical processes. For the case of wave overtopping where the still-water level is below levee crest elevation, the processes include wave reflection by the levee, wave run-up on the flood-side slope, flow across the levee crown, and unsteady flow down the protected-side slope. When the surge level exceeds the levee crest elevation, water flows across the levee crown, passes through the critical flow threshold, and flows down the protected-side slope as supercritical flow. If there is standing water farther down the slope, a hydraulic jump occurs where the supercritical flow meets the standing water. If waves propagate on an overflowing storm surge, the flow processes become unsteady with sudden increases of overtopping water as the wave crests propagate over the levee crown. This causes rapid changes in pressure on the protected-side slope, and flow accelerations will be important. Depending on the surge elevation relative to the levee crest, some waves may break directly on the levee crown or propagate across the crown as broken waves.

Physical models have proven in the past to be reliable for determining stability of slope armoring alternatives such as ACMs. Mat stability in wave/flow environments is a complex physical process that presently defies analytical or numerical analyses. Flow patterns over and around the mats are complicated, and the lifting forces exerted on the mats are unsteady in time.

4 Physical Model Design

This chapter describes the design of the levee wave and surge overtopping physical model. Included in the chapter are descriptions of the modeling facility, the rationale for scale selection, details of design and construction of the levee model and ACMs, and a summary of potential scale effects and how they might influence model results.

Model facility

Surge overtopping of earthen levees is primarily a two-dimensional physical process, and the worst case for wave overtopping is where the wave crests are parallel to the levee centerline (normal wave incidence). Therefore, except for rare exceptions, the physical processes involved in combined wave and storm surge overtopping of earthen levees can be considered two-dimensional. This allowed the overtopping study to be conducted in a two-dimensional wave flume rather than a three-dimensional wave basin.

The purpose of the model was to measure hydrodynamic parameters of the flow associated with combined wave and storm surge overtopping for 27 combinations of surge elevation and wave conditions. Irregular waves were used in the study. In addition to measuring hydrodynamic parameters, ACMs were tested for stability within this range of wave and surge combinations.

Several wave flumes were available at CHL, and these facilities were evaluated in terms of study requirements. The primary flume requirements included the following: (1) large enough to conduct the study at a size that minimized potential scale effects, (2) regular and irregular wave generating capability, (3) existing or easily added capability to pump sufficient water for creating overtopping storm surge levels, (4) a test section with glass side walls for video and acquiring velocity measurements with a laser Doppler velocimeter (LDV), and (5) existing or easily added electrical wiring (440 volts, three-phase) for operating the LDV system.

A wave flume at CHL known as the 3-ft flume met all the above criteria, and it was dedicated to the levee overtopping study. A photograph of the

3-ft flume is shown in Figure 11. The flume measures appropriately 150 ft in length, 3 ft in width, and 3 ft in depth.

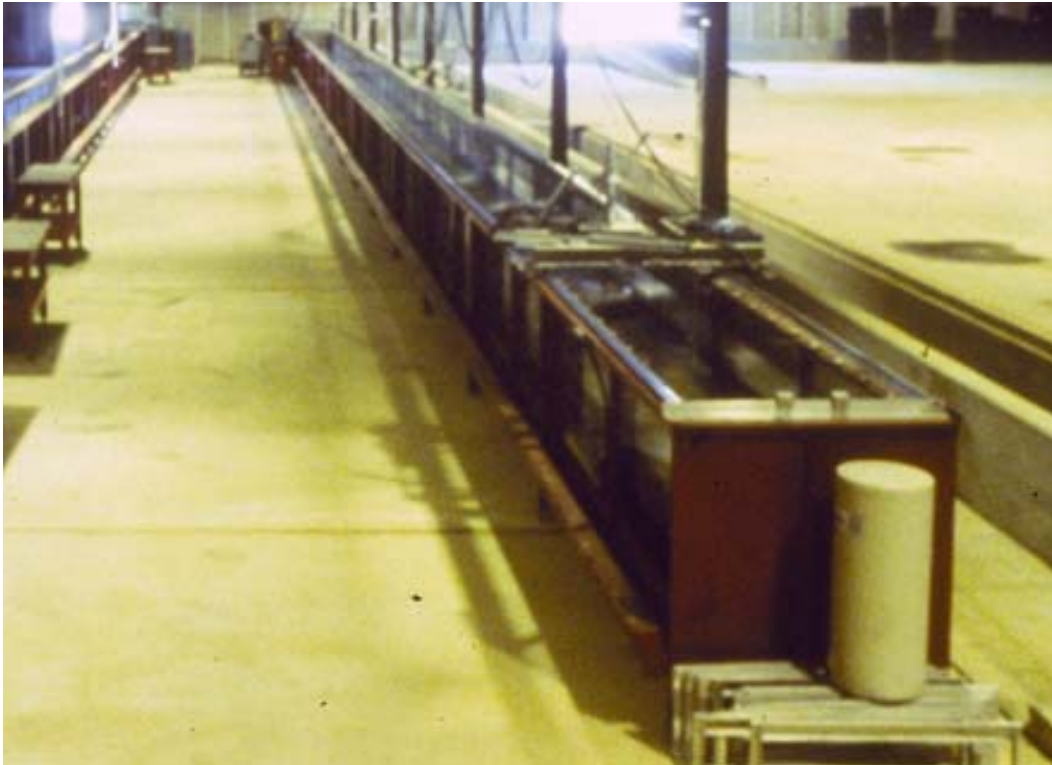


Figure 11. Photograph showing the 3-ft flume.

Model scale selection

Selecting physical model scale ratios requires consideration and assessment of multiple requirements and limitations. The model must include as much of the levee cross section as needed to simulate the physical forcing. This includes a suitable approach slope for the waves on the flood side of the levee and sufficient reproduction of the mild-sloped berm on the protected side. Those physical processes identified as being the dominant forcing in the levee overtopping phenomenon must be scaled according to established similitude criteria at a scale as large as can be accommodated in the model facility in order to minimize potential scale effects. Existing wavemakers must be able to reproduce the maximum waves to be used in testing at the selected scale. If the wavemaker is insufficient in this regard, either new equipment must be sought, or the model scale must be reduced to meet the requirement. Known scale effects, laboratory effects, and other limitations must be assessed to determine possible impacts on model results. The following sections detail the scale section processes for the MRGO levee wave and surge overtopping physical model.

Model purpose and layout

The physical model was constructed to support the New Orleans District. The primary purpose of the physical model was to quantify the flow hydrodynamics associated with combined wave and storm surge overtopping and to determine stability of ACMs placed on the levee as soil protection. All subsequent model design decisions were based on fulfilling this purpose.

Figure 12 shows the MRGO levee cross section that was selected by the New Orleans District to be replicated in the physical model. The flood side is on the left side of the figure. In order to assure correct wave transformation of incident waves, it was necessary to reproduce the entire seaward portion of the levee including the 1-on-5 toe slope, the 1-on-24 berm, and the 1-on-4.25 flood-side levee slope. The 10-ft-wide levee crown, the protected-side 1-on-3 slope, and most of the protected-side 1-on-24 slope were also included in the physical model.

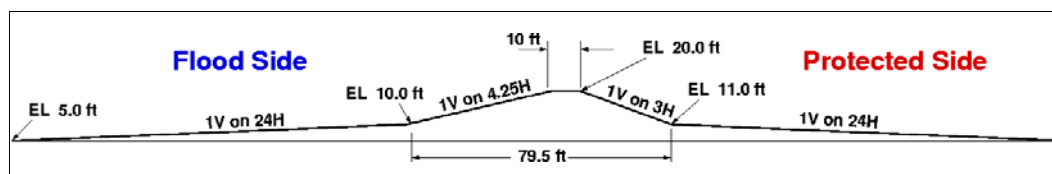


Figure 12. MRGO levee cross section replicated in physical model.

The 3-ft flume had an existing concrete 1-on-100 concrete slope on which the levee model was placed. The position of the levee model on the slope was optimized after considering three criteria. First, the elevation of the levee crest had to be as high as possible to maximize water depth at the wave board. However, the water depth must allow enough freeboard in the wave flume to contain waves propagating on the maximum surge level. Second, the model had to be positioned so that all the locations at which flow velocity might be measured were not obscured by column supports, and the LDV system could project the laser beams through the flume glass side walls. Finally, there needed to be enough flume volume behind the levee model to serve as a water reservoir. This reservoir had to hold the volume needed to create the overtopping surge at the start of each experiment, and it had to receive the overtopping flow without creating a back-water condition on the protected side of the levee.

The above considerations, along with an initial estimate of required wave and flow generation needs, indicated the model length scale N_L would need to be between 20 and 30, and the value of $N_L = 25$ was selected. The next step was to determine the corresponding similitude criteria for waves, storm surge, and ACMS; and to evaluate the capability of the 3-ft flume wavemaker to assure the desired wave conditions could be generated in the physical model.

Hydrodynamic similitude criteria

Small-scale model simulation of all free-surface flow phenomena, such as waves, must adhere to the Froude scaling, which means simply that the model must be geometrically undistorted (horizontal and vertical length scales are the same), and the model velocity scale and time scale must conform to the scaling relationships given by Equations 27 and 30, respectively. For a model length scale of $N_L = 25$, the required velocity scale is given by

$$N_V = \sqrt{N_g N_L} = \sqrt{(1)(25)} = 5.0 \quad (33)$$

and the hydrodynamic time scale (wave period scale) becomes

$$N_T = \sqrt{\frac{N_L}{N_g}} = \sqrt{\frac{(25)}{(1)}} = 5.0 \quad (34)$$

where the gravitational scale ratio N_g is unity.

Wave generation capability

Estimates of key storm surge, wave height, and wave period testing parameters were determined through discussions with the New Orleans District, and the parameters were selected to bracket, within reason, probable overtopping conditions. These parameters (nominal values) are shown in Table 2 with the model equivalents determined using the length scale ratio of $N_L = 25$ and time scale ratio of $N_T = 5$. The water depth at the wave board was a limitation of the model facility, so that value was scaled up to prototype to assure water depth at wave generation would be sufficient.

Table 2. Prototype and model wave and surge parameter values.

Parameter	Prototype Values	Model Values
Surge elevation above levee crest	+1, +3, and +5 ft	+0.48, +1.44, +2.40 in.
Significant wave height range	3, 6, and 9 ft	1.44, 2.88, and 4.32 in.
Peak wave period range	6, 10, and 14 sec	1.2, 2.0, and 2.8 sec
Water depth at wave board	51, 53, 55 ft	24.48, 25.44, and 26.40 in.

Because of the random character of natural sea states, irregular waves more closely replicate nature and are preferred in the physical model. However, it requires more capability to generate irregular significant wave heights (H_{mo}) than it does to generate regular waves of the same height. The existing piston-type wavemaker installed in the 3-ft flume had sufficient capability to meet or exceed the wave generation requirements given for the model experiments. The wave board is programmable, and it can produce either regular or irregular waves. Thus, the wavemaker was considered adequate and appropriate for generating the necessary wave conditions at the chosen length scale.

Overtopping surge flow

The overtopping discharge per unit levee length associated with a storm surge having an elevation 5 ft (prototype scale) over the elevation of the levee crest can be estimated using the wide-crest weir formulation given by Equation 14, i.e.,

$$q = 0.5443\sqrt{g}(h_1)^{3/2} = 0.5443\sqrt{32.2\text{ ft/sec}^2}(5\text{ ft})^{3/2} = 34.5\text{ ft}^2/\text{sec} \quad (35)$$

The 3-ft flume width corresponds to a prototype-scale levee reach length of 75 ft, so the total volumetric surge overtopping discharge for this width is determined as

$$Q_p = 34.5\text{ ft}^2/\text{sec} (75\text{ ft}) = 2,588\text{ ft}^3/\text{sec} \quad (36)$$

The Froude scale ratio for volumetric discharge is simply the scale ratio for area times the scale ratio for velocity, or

$$N_Q = (N_L)^2 N_V = (N_L)^{5/2} = (25)^{5/2} 3,125 \quad (37)$$

Thus, the required maximum pumping capacity needed to maintain the equivalent of a 5-ft overtopping surge in the physical model was

$$Q_m = \frac{Q_p}{N_Q} = \frac{2,588 \text{ ft}^3/\text{sec}}{3,125} = 0.83 \text{ ft}^3/\text{sec} = 373 \text{ gal/min} \quad (38)$$

Force and ACM weight

Correct similitude for testing ACMs at small scale requires (1) the mat dimensions be reduced according to the geometric length scale, and (2) the mats in the model must have the same relative density as in the prototype. These requirements assure that the mats will respond to hydrodynamic forces in a manner similar to what would occur in nature at full scale.

The importance of preserving the ratio of mat material relative density between model and prototype is related to the uplift buoyancy of the mats when submerged. This buoyancy force differs slightly between fresh and salt water. For practical reasons fresh water is used in the physical model. If the prototype condition was also fresh water, then the relative density criterion simply requires the model mat material to have the same mass density as the concrete used to fabricate the full-scale mats. However, for this study it was assumed that the prototype condition would be salt water, and it was necessary to determine the required mass density for the model mat material using Equation 32.

The specific weight of concrete used to fabricate the ACMs used by the Corps of Engineers for protecting riverbanks was estimated to be $(\gamma_a)_p = 148.3 \text{ lb/ft}^3$ where the subscript “p” represents “prototype.” This estimate was obtained by dividing the weight of an individual ACM block by the volume of the block. The specific weight of salt water is $(\gamma_w)_p = 64.0 \text{ lb/ft}^3$, and the specific weight of fresh water is $(\gamma_w)_m = 62.4 \text{ lb/ft}^3$ where the subscript “m” represents “model.” Solving Equation 32 for the model mat material specific weight and substituting the above values yielded

$$(\gamma_a)_m = (\gamma_a)_p \frac{(\gamma_w)_m}{(\gamma_w)_p} = 148.3 \text{ lb/ft}^3 \frac{(62.4 \text{ lb/ft}^3)}{(64.0 \text{ lb/ft}^3)} = 144.6 \text{ lb/ft}^3 \quad (39)$$

The corresponding prototype-to-model force (weight) scale for the mats is found from Equation 31 as

$$N_F = N_{\gamma_a} N_L^3 = \frac{(148.3 \text{ lb/ft}^3)}{(144.6 \text{ lb/ft}^3)} (25)^3 = 16,025 \quad (40)$$

The scale ratio for specific weight of mat material is identical to the scale ratio of water specific weight, so both the hydrodynamic forcing and mat resistance conform to the same similitude requirement. Table 3 lists the primary geometry and weight parameters for the ACMs in both prototype-scale and model-scale units.

Table 3. Prototype and model ACM parameters.

Parameter	Prototype Value	Model Value
ACM block length	3.85 ft	1.85 in.
ACM block width	1.48 ft	0.71 in.
ACM block thickness	3.0 in.	1/8 in.
Length of 16-block mat	25 ft	1 ft
Gap width between blocks	1 – 2 in.	1 – 2 mm
ACM block weight	209 lb	0.21 oz (92 g)

Summary of model scaling

The important model scale ratios (value in the prototype divided by the equivalent value in the model) are summarized in Table 4. The fundamental scaling parameter is the length scale, $N_L = 25$, which can be interpreted as 1 ft in the model equals 25 ft in the real world.

Table 4. Model scale ratios and prototype equivalence.

Scale	Scale Value	Model-to-Prototype Equivalence
Length scale	$N_L = 25$	1 ft = 25 ft
Time scale	$N_T = 5.0$	1 sec = 5.0 sec
Velocity scale	$N_V = 5.0$	1 ft/sec = 5.0 ft/sec
Discharge scale	$N_Q = 3,125$	1 gal/sec = 418 ft ³ /sec
Force/weight	$N_F = 16,025$	1 oz = 1,002 lb

Model design and construction

Once model scale ratios were determined, focus turned to designing and fabricating all the components of the model. This included the levee cross section, flow recirculation system, model ACMs, and accommodation for instrumentation within the physical model. The following subsections provide details.

Levee cross section

The MRGO levee cross section shown in Figure 12 was scaled to model dimensions, and a three-dimensional rendering of the model was created in AutoCAD. The ERDC Model Shop converted the AutoCAD drawing into computer commands to drive the 5-degree-of-freedom automated router. The router carved the model out of high-density foam (30 lb/ft³). The model was constructed in several sections to facilitate placement in the flume and to allow installation of pressure gauges. Figure 13 shows the levee model being carved, and Figure 14 shows a section of the finished cross section.

The instrumentation plan included seven flush-mounted dynamic pressure gauges on the levee crest and down the levee protected-side slope. The router was programmed to rebate for the pressure gauge mounts, and provision was made for running the gauge cables under the levee model and out the rear side during installation. This allowed for exchanging gauges in case of problems. Figure 15 shows the mounting holes for the pressure gauges.

After completion of model fabrication, the model was test fitted in the flume before final installation. The model material is lighter than water, so it would float if not securely affixed to the flume boundaries. Strong glue was used to secure the model to the flume bottom, and sealant was placed along all edges where water might seep under the foam blocks. As long as water is prevented from getting beneath the model, the foam will not experience uplift due to hydrodynamic buoyancy.

Figure 16 shows an isometric view of the fabricated levee model placement in the 3-ft flume. The flood side of the levee is toward the upper left corner in Figure 16. Levee model positioning in the flume was selected so the main areas of interest on the flood side and protected side of the levee

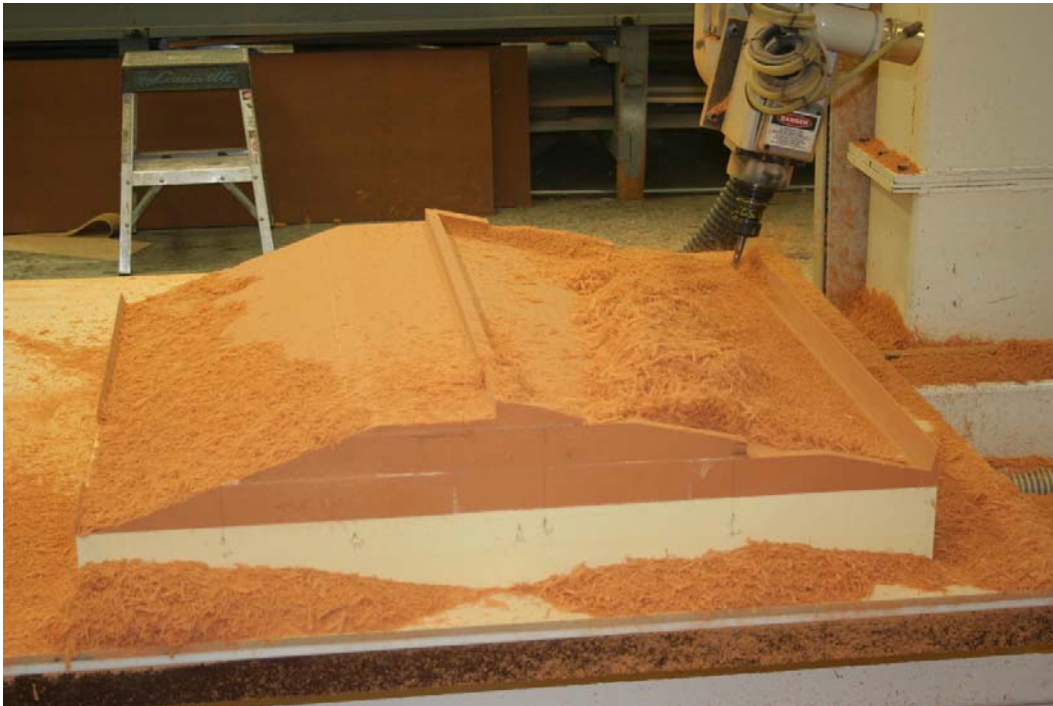


Figure 13. Levee model being carved out of high-density foam.

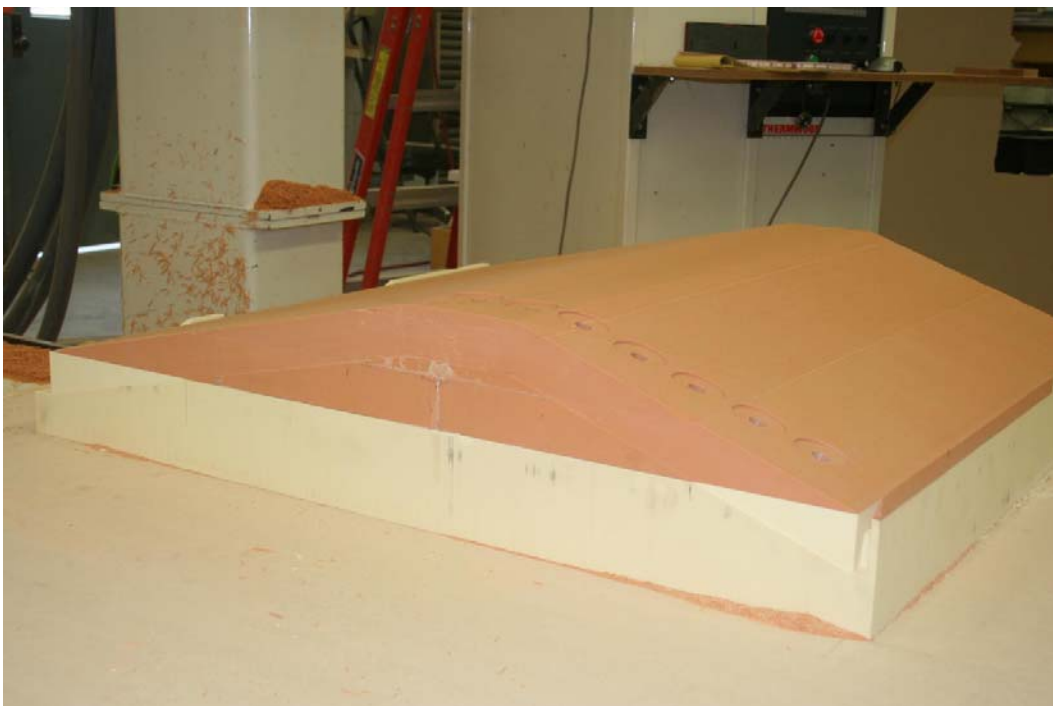


Figure 14. Finished section of levee model.

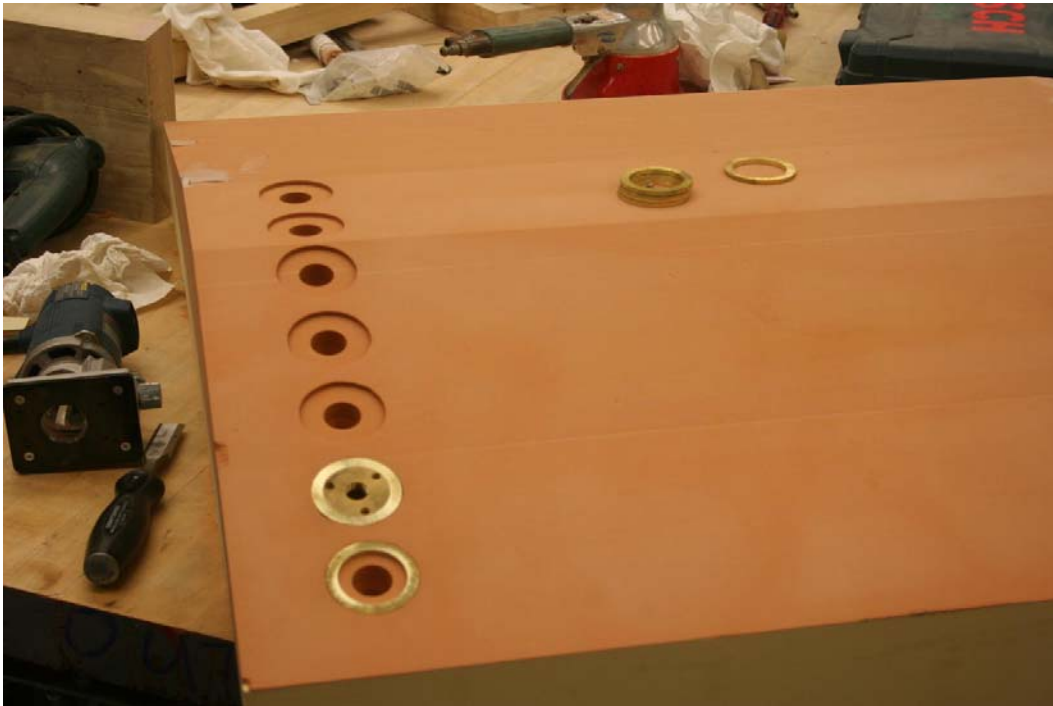


Figure 15. Mounting hardware for dynamic pressure gauges.

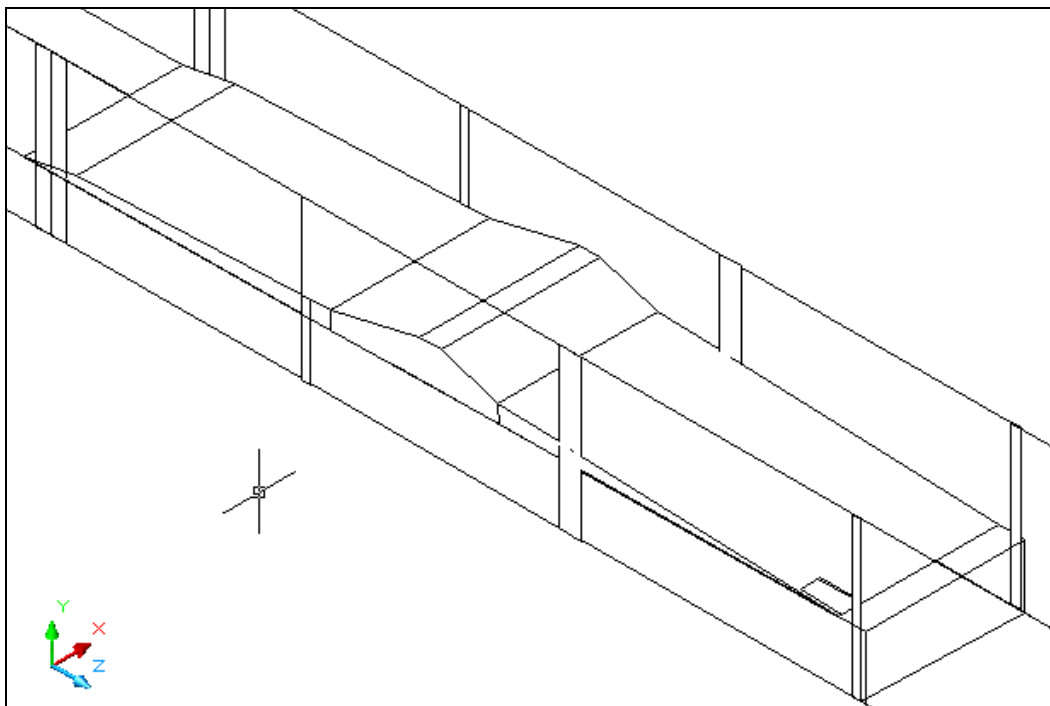


Figure 16. Isometric view of levee model placed in flume.

could be seen through the glass side wall without being obstructed by the flume's vertical columns. This allowed a clear view for video/photo imaging and for using the LDV for measuring overtopping flows.

Figure 17 shows the relative location of the levee model in the 3-ft flume. The levee crest is approximately 106 ft from the wave board (left end of Figure 17) with the crest elevation 2 ft above the wave flume bottom. Seaward of the levee model section is a long 1:100 approach slope and a shorter 1:20 slope transition to the bottom of the flume. Surge and waves that overtop the levee flow into the reservoir (right end of Figure 17) and a pump recirculates the water to the seaward end of the flume. Four wave gauges were mounted in the wave flume in the positions indicated on the sketch.

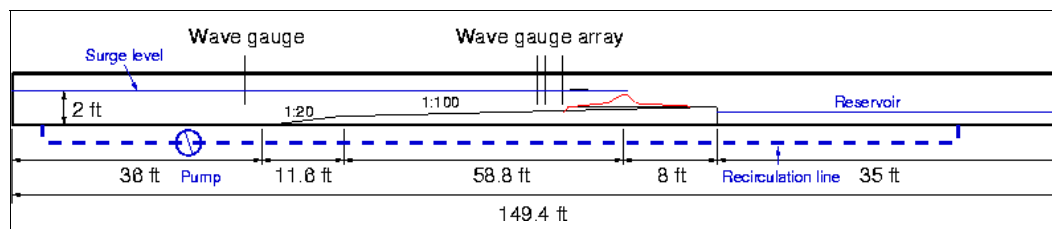


Figure 17. Cross section sketch of levee overtopping model in 3-ft flume.

Surge flow generator

Plumbing was added to the 3-ft flume to create the capability of generating steady overtopping surge flows. A large pipe was installed connecting the outflow drain in the reservoir section of the flume to the inflow manifold near the wave board. This pipe is indicated by the dashed line in Figure 17. A large pump with a 5 ft³/sec rating was placed in the pipeline, and this pump easily met the 0.83 ft³/sec requirement given by Equation 38. A control valve was also placed in the line near the pump. Flow rate was monitored using an ultrasonic flow meter on the pipeline.

Rubberized “horsehair” mats were used in the reservoir end of the flume near the outflow port to prevent vortex formation and air entrainment into the pipe. A horizontal deflector plate was placed above the bottom-mounted inflow port near the wave board to minimize disturbances to the free surface and to prevent a vertical jet from hitting the ceiling of the model shelter. The surge flow generator produced smooth, steady overtopping flows over the levee crest.

Model articulated mats

Several different materials were considered for use in fabricating the ACMs. Matching the derived material specific weight of 144.6 lb/ft³ was the primary objective, but other material factors such as availability, robustness, and ease of fabrication were also considered. The best material turned out to be fire brick that had a calculated specific weight of $(\gamma_a)_m = 136 \text{ lb/ft}^3$. Because the selected model material specific weight was 6 percent lighter than required for perfect similitude, it was necessary to increase the model block thickness slightly so that each block would have the correct scaled weight as listed in Table 3. This increase in block thickness amounted to approximately 0.2 in. at prototype scale.

The model blocks were cut from fire bricks using a precision, computer-controlled water jet. Before beginning full production, sample blocks were cut and weighed to assure model block weight was correct. Thirty-two blocks were cut, and random groups of 16 blocks were selected and weighed as a group to give an average block weight. Based on the results of the first set of tests, a slight block thickness decrease was implemented, and the testing was repeated. The resulting average block weights from four random groups were 91.75, 92.14, 92.15, and 91.68 g. This was considered a good match to the target weight of 92 g given in Table 3. Fire brick absorbs considerably more water than concrete, so the weights given above were for wet model blocks, which was the condition during stability testing. Dry weight tests produced average weights of about 87.3 g. Figure 18 shows several of the model blocks cut from fire brick.

Approximately 1,000 model blocks were fabricated. This was estimated to be the number of blocks required to cover the model levee from the toe of the flood-side 1:4.25 slope, over the levee crown, and all the way down the protected-side 1:3 slope with a little left over to transition onto the 1:24 berm. Figure 19 shows all the fabricated blocks prior to assembly into mats.

Two mats having a width of about 1.5 ft and a length to cover the levee were fabricated using the jig shown on Figure 20. This jig was also cut using the precision water jet, and it held the blocks with the necessary gap distance to replicate the prototype.



Figure 18. Model blocks used to fabricate articulated mats.



Figure 19. Approximately 1,000 model blocks.

Once a section of blocks was placed in the grid, a nylon mesh was glued to the surface of the blocks using a waterproof adhesive as shown in the close-up image of Figure 21. The mesh offered no bending stiffness to the mats, and this was thought to be similar to the minimal stiffness of the thin stainless steel wires used to articulate the full-sized concrete mats.

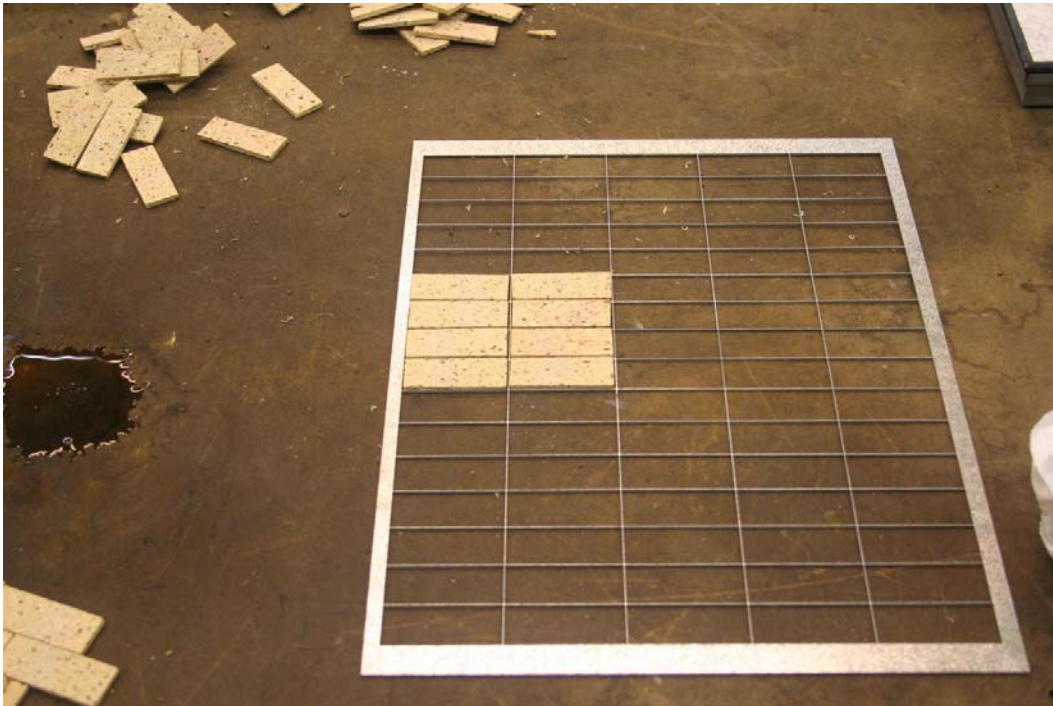


Figure 20. Articulated mat assembly jig.



Figure 21. Mesh glued to underside of block mattress.

One minor difference between the model and prototype mats is the model mats are tied together at the underside of the blocks whereas the full-size mats are tied through the center of the block thickness. Figure 22 shows a portion of an assembled mat looking down on the topside mat surface.

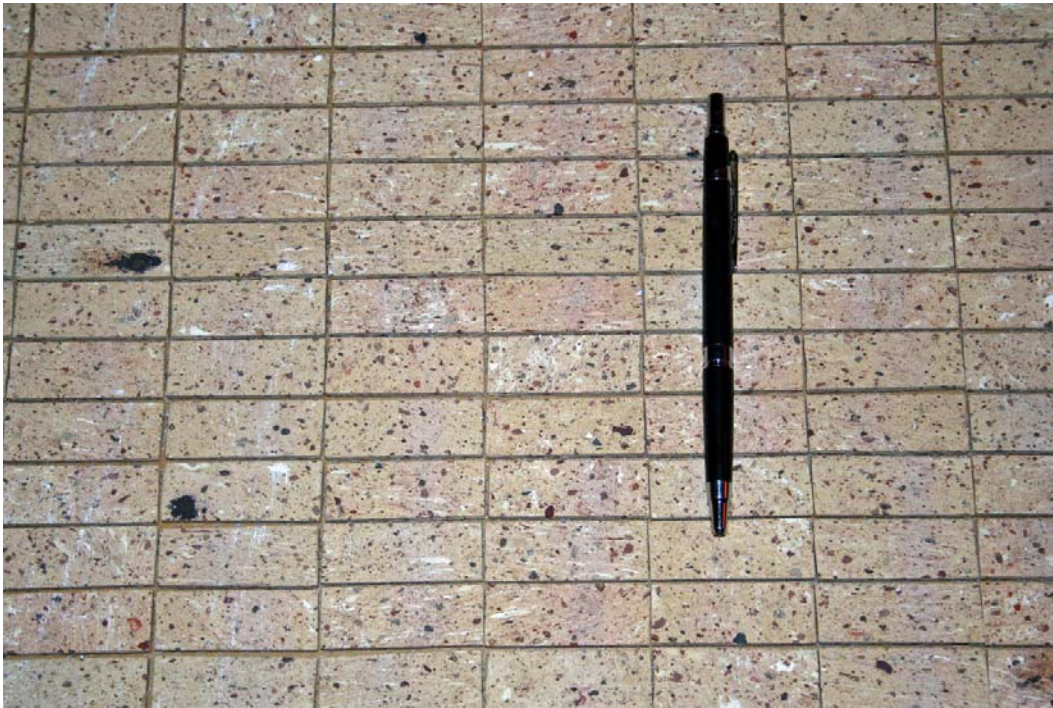


Figure 22. Final assembled model articulated mat (looking down at the topside mat surface).

Prior to testing the mats were placed on top of the installed model levee cross section without any anchoring or securing. Thus, the only thing preventing mat uplifting during hydrodynamic flow was the mat self weight. Lateral sliding of the mats was resisted somewhat by friction between the mat nylon mesh and the smooth surface of the model levee, but this frictional resistance was not considered to be similar to what would be experienced by the full-size mats.

The 10-ft levee crown dimension was not an even multiple of block width. Thus, in order to cover both levee slopes and the crown with a continuous mat, it was necessary to install a half-width block in the mattress on the levee crown.

Potential scale and laboratory effects

Scale effects and laboratory effects were summarized in general terms in Chapter 3. An assessment of how scale and laboratory effects might influence results obtained from the MRGO levee wave and surge overtopping physical model is given in the following paragraphs.

Scale effects in levee overtopping physical model

At the selected model length scale, hydrodynamics are in similitude so there is no appreciable scale effect related to the hydrodynamics. All wave-related phenomena such as wave shoaling, reflection by the levee, and wave breaking will be in similitude with the prototype. All phenomena related to steady and unsteady subcritical, critical, and supercritical flow will be simulated correctly, and all nonlinear aspects of the wave motion and interaction of waves with the steady surge overflow discharge also will be correct. There has been suggestion in the literature of a slight scale effect associated with wave overtopping, but this pertains mainly to the case where waves run up the slope, and the surface friction is not correctly scaled in the model. However, any such scale effect would probably be less in the case of waves combined with steady flow overtopping. Flow over and through the ACMs will be in similitude because the mats are large enough to preclude any scale effects related to laminar flow conditions within the mattress gaps.

The physical model was conducted using fresh water to simulate the salt water environment at the MRGO. This is a practical compromise to avoid corrosion of laboratory facilities and delicate instrumentation. The slight difference in water density between model and prototype has virtually no impact on hydrodynamics as proven by many studies over the past 50 years (Hughes 1993), and the buoyancy scale effect related to ACM stability was corrected.

The response of the model ACM will be in similitude because the mat weight and material density have been scaled with reasonable accuracy. The model ACM blocks have a smoother surface than the equivalent prototype. This will allow slightly faster supercritical flow down the levee protected-side slope, and it could promote an uplift instability in the model at slightly slower velocities than would occur at full scale.

Another aspect of the mat installation that could introduce a scale effect is the direct placement of the mats on the solid levee surface. The model mats rest on the nylon mesh, and this leaves a small gap in which water can reside during overtopping. This would be similar to the situation in the prototype where the mats are placed on top of a gravel filter layer. However, if ACMs in the prototype are placed directly on the levee soil, water will not as readily seep under the blocks. Thus, uplift of the mattresses in the real world might be delayed until such time that the suction bond

between the underlying soil and the mattress blocks is broken. For this situation the model response is conservative, i.e., the mats will lift in the model a little easier than in the prototype. If there has to be a scale effect related to ACM stability, it is better to error on the conservative side.

Laboratory effects in levee overtopping physical model

The key laboratory effects in the MRGO levee overtopping physical model were related to wave generation and maintaining correct storm surge elevation. Because the levee overtopping model was two-dimensional, the only model boundary of concern was the vertical piston-type wave board. Waves reflected by the levee model were re-reflected perfectly by the wave board back toward the model. The wavemaker was not equipped with active wave absorption capability, so this laboratory effect could not be corrected. However, the re-reflected waves became part of the incident wave spectrum, and the measured wave data were processed to estimate the total incident wave energy spectrum.

The pumping system recirculated water in the wave flume to create a constant surge level above the levee crest. With just steady flow overtopping, the system could be adjusted to maintain the correct level without any further intervention. However, when waves were added to the steady overflow, the overtopping rate became unsteady with a larger amount of overtopping occurring with large waves and less overtopping with smaller waves. In time, the mean surge level seaward of the levee would slightly decrease if overtopping volume due to waves was not reintroduced into the wave flume in the same manner as was done with surge overflow. This is a result of having a relatively small volumetric capacity in the wave flume. Such a decrease does not occur in nature because of the vast volume of water at the surge elevation. The levee model was placed as far from the wave board as practical to maximize the volumetric storage seaward of the levee; and during tests the return flow rate was manually manipulated to compensate for wave overtopping losses. Additional details are provided in Chapter 5.

5 Experiment Setup and Operating Procedures

A physical model is similar in ways to an analog computer because reactions in the model are governed by the physical forces generated by waves and flowing water. If the model is not properly configured, or if the model is not properly operated, model results can be negatively influenced or even incorrect. Thus, care is needed in setting up the experiments and assuring that correct operating procedures are followed.

This chapter describes the instrumentation used to record model response, overviews the wave and surge calibration, discusses the procedures followed when operating the physical model, and describes the data collection and initial data analyses.

Experiment instrumentation

Physical parameters that were measured during the levee overtopping physical model study included water levels, flow discharge, waves, water pressure, and flow velocity. The following sections briefly describe the instrumentation used to acquire measurements of these parameters.

Water levels

Static water levels such as the steady storm surge elevation, water level in the reservoir portion of the flume, and steady flow over the levee model were measured using standard point gauges referenced to a common vertical datum. Several point gauges were placed at fixed locations, and one point gauge was mounted on a carriage that could be moved on rails along the length of the wave flume.

During the overtopping experiments the water surface in the receiving reservoir was generally agitated, so a point gauge was not a practical solution. Instead, a stilling well with graduated markings was used to monitor the quasi-static water level in the reservoir.

Flow discharge

An ultrasonic flow meter was placed on the recirculation pipe to monitor the flow rate. The main purpose of this instrument was to make the initial valve setting while bringing the overtopping surge elevation up to the level required for each experiment. Final valve adjustment was achieved by referring to a nearby point gauge. Steady flow discharge indicated by the flow meter for an established overtopping surge elevation was compared to theoretical discharge estimates using Equation 14, and good agreement was found.

Waves

Four capacitance-type wave gauges were placed at the locations shown in Figure 17. Gauge 1 was located over the horizontal bottom of the wave flume closest to the wave board. Gauges 2-4 were placed as a three-gauge array near the toe of the levee model. The gauges work by sensing the change in capacitance in a thin insulated vertical wire as the water elevation varies on the wire. Each gauge captures a time series of information that can be converted into water surface elevations at that location. The time series can then be analyzed to obtain wave information.

All wave gauges were mounted on remotely controlled stepping motors that permitted the gauges to be raised and lowered precise vertical distances for calibration. Wave gauges were calibrated daily with the water motionless and at a depth equal to the model levee crest. The gauges were first raised 10 equal increments, then lowered 20 equal increments, and finally raised 10 equal increments to bring the gauges back to their original vertical positions. Data collected at each stopping point were analyzed to establish the relationship (usually linear) between water elevation at the gauge and frequency output by the gauge. Provided all gauges exhibited the expected calibration, the calibration relationships were saved in a file for later application to the measured raw wave data collected the same day as the calibration.

For all experiments wave data collection started at the same instant the wavemaker was activated and continued until the wave board stopped. Time series sea surface elevation data were collected at a 50-Hz rate. Wave data were transmitted into the main control room and recorded on a computer for post-experiment processing.

Water pressure

Seven Druck PDCR-200 pressure cells were installed in the levee cross section with the surface of the pressure cells flush with the levee surface. Two of the instruments were located on the levee crest, and the remaining five gauges were evenly spaced down the protected-side slope. Figure 23 shows the locations of the pressure cells with coordinates given in units of model feet. The flood-side levee crest edge is at location (1.000, 2.000). The purpose of the pressure cells was to measure water depth variations over the levee as a function of time.

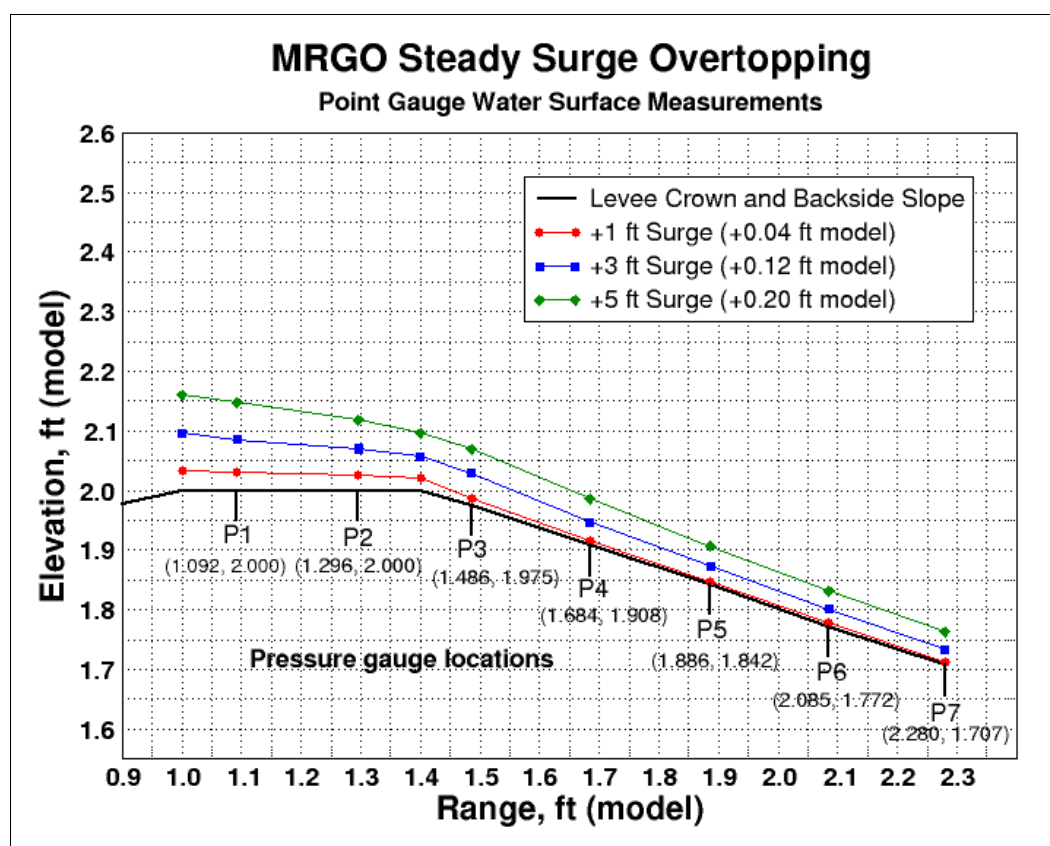


Figure 23. Steady surge overtopping water surface profiles.

The pressure cells were initially calibrated before placement in the model, and the calibration was checked by flooding the levee model to known static levels and confirming the water depth over each gauge (as measured with a point gauge) corresponded to the gauge output.

Pressure data were collected at a 50-Hz rate concurrent with wave data. Data collection began when the wavemaker commenced operation, and collection ended when the wave generation ceased. Prior to each

experiment, all the pressure cells were adjusted to read zero when no water was present over the instrument, i.e., when the crest and protected-side levee slope were dry.

Flow velocity

A fiber-optic LDV was used to measure two orthogonal components of flow velocity at locations in the vicinity of the rearward crest edge. The LDV was mounted outside the flume, and it operated in the backscatter mode. Water velocities were obtained at the laser beam crossing point located approximately 3 in. from the inside face of the glass flume wall. This cross-flume location corresponded to the line of pressure cells shown on Figure 15.

Velocity data were collected at a 50-Hz rate concurrent with the wave and pressure data. The LDV system required no calibration because equations are available to relate the sensed Doppler shift frequency directly to velocity as a function of laser light velocity and the applied frequency shift. However, checks were made to confirm accurate LDV velocity readings by creating a steady flow overtopping condition and measuring the velocity in the direction of principle flow near the location of critical flow transition on the levee crest. The measured velocity was compared to the theoretical estimate given by Equation 20 and good agreement was found.

The LDV system required that water in the wave flume be seeded with small particles of titanium dioxide (latex paint without hardening agent), and a series of systematic tests was conducted to determine an appropriate amount of seeding to assure consistent velocity readings. The seeding material stayed in suspension for extended time periods, but prior to each day's testing, energetic wave conditions were run in the flume to help stir up particles that had settled on the bottom of the tank.

Storm surge and wave calibration

In addition to calibrating individual instruments to measure faithfully the physical parameters, it was necessary to calibrate the mechanical systems to reproduce the storm surge elevations and wave characteristics specified for each test. The calibration procedures are described briefly below.

Storm surge level calibration

For a large model basin or the open ocean, the storm surge still-water level will be relatively constant in the vicinity of the levee except close to where the flow overtops the levee crest. Near the crest the water elevation drops as the water flows across the crest, reaches a critical depth, and then becomes supercritical. The target surge elevation was simulated within the confines of the narrow wave flume by constantly recirculating water from the receiving reservoir back to the input port near the wave board. This process could introduce a laboratory effect by creating a noticeable slope in the water surface over the length of the flume.

Water surface elevation measurements were recorded at points along the wave flume seaward of the levee crest to document any pronounced slope in the water surface. Results are shown in Table 5 for several different elevations of overtopping surge. The values in Table 5 are in units of model feet above the elevation of the levee crest. These measurements revealed a reasonable horizontal water surface seaward of the levee similar to what is expected in the prototype. Thus, it was concluded that the wave flume was accurately replicating the hydrodynamics of overtopping surge.

Table 5. Water surface elevations for steady surge overtopping.

Location	2-ft Surge (0.08-ft model)	5.5-ft Surge (0.22-ft model)	9.25-ft Surge (0.37-ft model)
Protected-side crest edge	0.040	0.110	0.200
Flood-side crest edge	0.075	0.180	0.285
Toe of 1:4.25 slope	0.080	0.210	0.360
Toe of levee model	0.075	0.210	0.360
10 ft seaward of levee model toe	0.080	0.215	0.368
20 ft seaward of levee model toe	0.078	0.215	0.363
30 ft seaward of levee model toe	0.080	0.220	0.370
40 ft seaward of levee model toe	0.078	0.220	0.370
Point gauge	0.088	0.225	0.380
50 ft seaward of levee model toe	0.078	0.220	0.370
60 ft seaward of levee model toe	0.083	0.220	0.372
70 ft seaward of levee model toe	0.073	0.215	0.365
Measured discharge	107 gal/min	460 gal/min	972 gal/min

The three surge overtopping elevations selected for the tests (+1, +3, and +5 ft) were simulated in the flume and run in a steady flow state without waves. The movable point gauge was used to measure the overtopping flow water surface elevation above the levee crest and at the location of each pressure gauge. The water surface profiles for the three surge levels are shown on Figure 23. These measurements were used to adjust the pressure gauge output to compensate for incorrect gauge zeroing. Comparison of the measured depths on the protected-side slope with theoretical estimates using Manning's equation (Equation 25) gave estimates of the Manning's coefficient for the model levee slope surface of $n = 0.012$ (1-ft surge), $n = 0.026$ (3-ft surge), and $n = 0.038$ (5-ft surge). The increase of Manning's n with surge level is possibly due to the flow not having sufficient distance along the slope to reach the steady-state condition where the energy slope line equals the levee slope.

Wave calibration

Wave and surge parameters for testing were determined in consultation with the New Orleans District. As noted in Table 2, Chapter 4, there were three surge elevations ($S = +1, +3$, and $+5$ ft above levee crest), three significant wave heights ($H_{mo} = 3, 6$, and 9 ft), and three peak wave periods ($T_p = 6, 10$, and 14 sec). This gave a total of 27 unique conditions for combined wave and surge overtopping.

Idealized spectral representations of wave conditions characterized by the TMA spectrum were scaled to model-size spectra. A computer program created time series realizations of sea surface elevations that matched the spectral description. A theoretical relationship for converting from sea surface elevation time series to equivalent wave board stroke time series for piston-type wavemakers was used to develop a first approximation for the wave board signal. However, the theory does not include provision for a steady current generated by flow recirculation in the wave flume, or wave shoaling as the waves approach the levee. Therefore, it was necessary to calibrate the wave machine following a standard procedure used at CHL.

The initial wave board signal was run in the flume at the designated surge elevation water level, and measurements were made at all wave gauges. Results from the three-gauge array were analyzed, and a gain factor was calculated that would uniformly increase or decrease the wave board stroke signal to match the target spectrum. Then the test was repeated with the new board signal. Once the measured spectra matched the target

spectra, the command signals were saved for future use in tests specifying that particular combination of wave parameters and surge elevation.

Operating procedures

Generally, the following standard procedures were followed during testing of the MRGO levee overtopping physical model.

ACM stability experiments

Stability testing of ACMs was relatively straightforward. Below are the steps followed for each experiment.

1. Wave gauges were calibrated in the morning with the water level at the elevation of the levee crest. After calibration the wave gauges were moved vertically (via remote-controlled stepping motors) so the midpoint of the gauge would correspond with the target steady surge level for the experiment.
2. Pressure measurements were not acquired during ACM stability experiments. In order to protect the sensitive surface of the pressure cells, the instruments were manually recessed into the brass mounting collars so the mats would not touch the pressure cells.
3. The model ACMs were carefully lifted into the wave flume and placed directly on the levee model. The mats were held in place only by their self-weight. Each of the two mats extended continuously from the flood-side toe of the 1:4.25 slope, across the levee crown, and down the protected-side slope. About 3 in. of mat continued along the mild 1:24 berm. The two mats provided coverage of the entire 3-ft width of the wave flume.
4. The main documentation for the ACM stability experiments was video footage. Prior to testing, various floodlighting options were tested to provide suitable video images. The video camera was placed on a tripod, and the lens was zoomed in and out to make sure the region of interest was in the frame.
5. The pump was activated and water from the reservoir was pumped into the seaward portion of the flume. The pipe valve was adjusted until the correct overflowing surge level was obtained at the nearby point gauge.
6. Once everything was ready, the flow discharge reading was noted, and the computer operator was informed by handheld radio to begin running waves in the flume. At the same time the video camera was activated.
7. During the tests the engineer made observations of the ACM response and noted any instability in a notebook.

8. Wave generation continued for a total of 5 min. At the end of wave generation the pump was shut down, and the residual surge elevation was allowed to drain over the levee into the overtopping reservoir.

Combined wave and surge overtopping experiments

Tests aimed at documenting the hydrodynamic parameters of combined wave and surge overtopping followed many of the same procedures listed above, along with a few additional steps.

1. Wave gauges were calibrated in the morning with the water level at the elevation of the levee crest. After calibration the wave gauges were moved vertically (via remote-controlled stepping motors) so the midpoint of the gauge would correspond with the target steady surge level for the experiment.
2. Pressure gauges were set to zero (atmospheric pressure) prior to any water overtopping the levee crest.
3. The LDV system was activated, and the laser beam intensity was adjusted to maximum strength using a power meter. A test reading was made to assure the particle seeding in the water was sufficient for receiving a high-quality backscatter signal.
4. The pump was activated and water from the reservoir was pumped into the seaward portion of the flume. The pipe valve was adjusted until the correct overtopping surge level was obtained at the nearby point gauge.
5. The LDV fiber-optic probe was moved using its motorized support traverse to a position where the laser beam crossing point was directly over the location of pressure gauge P2 (Figure 23). The elevation of the beam crossing above the surface of the levee crown was set to approximately one-half of the steady flow depth at that location for the specified overtopping surge. The LDV probe was rotated so the x-component of velocity was parallel to the levee crest surface.
6. With the LDV probe in place, the output voltage was monitored, and root-mean-square estimates of voltage were manually converted to velocity for comparison with theoretical estimates of what the critical velocity would be for this condition. This comparison was only to assure the LDV was functioning properly.
7. Once everything was ready, the flow discharge reading was noted, and the computer operator was informed by handheld radio to begin running waves in the flume. Data collection was begun at the same time as wave generation. Fifteen channels of data were collected at a 50-Hz rate. The

- channels collected were wave board control, wave board feedback, four wave gauges, seven pressure gauges, and two velocity channels.
8. During the tests the engineer made observations of any unusual overtopping phenomena in a notebook.
 9. The water level in the reservoir remained at a constant level during steady flow overtopping. However, once waves started to push additional water over the levee, the level in the reservoir rose. This equated to a decrease in the surge level seaward of the levee. To minimize this effect, the water level in the reservoir was monitored at the stilling basin gauge, and when the level increased, an observer signaled the pipe valve operator to increase the flow rate slightly. If the flow rate was increased too much, or overtopping decreased, the opposite signal was given. This process helped maintain a reasonably constant surge level throughout the experiment. The valve operator noted the changes in flow rate given by the flow meter, along with approximate duration at each rate. However, the data are not sufficient for estimating the wave-related component of overtopping during combined wave and surge overtopping tests.
 10. Wave generation and data collection continued for a total of 5 min. At the end of wave generation the pump was left running, and the water surface rapidly settled into steady-state surge overtopping. After a short time, the next wave condition was run in the flume. If the surge level needed to be changed, these steps were taken before commencing with the next test.
 11. At the end of testing for the day, the pump was shut down, and the residual surge elevation was allowed to drain over the levee into the overtopping reservoir.

Data collection and initial analyses

At the completion of each experiment, the collected data were immediately converted into engineering units and stored in a computer file containing the necessary identifying information. Data channels from the wave gauges were converted into model units of meters by applying the calibration factors determined at the start of testing for that day. Pressure data were converted to pressure head of water in units of model feet, and the voltage output from the two channels of LDV velocity was left in units of volts for later conversion to velocity.

As mentioned all data were collected for a total of 5 min (300 sec) at a 50-Hz rate giving time series of 15,000 points for each data channel. The first 500 to 800 points of the time series measured just the steady flow

overtopping until waves arrived at the levee. The length of steady flow measurement depended on the wave period being generated in the flume.

Standard post-test analysis of the recorded wave gauge signal included time series analysis for representative statistics such as significant wave height $H_{1/3}$ and mean wave period T_m , and the wave height distribution. Frequency-domain analysis decomposed the measured irregular wave time series under the assumption that the measurement can be represented by the summation of many sine waves of differing amplitudes and periods. The main result from frequency-domain analysis was a wave energy spectrum indicating the distribution of wave energy over the range of wave frequencies (inverse period). The square root of the area under the spectrum times four is known as the zeroth-moment wave height, or H_{mo} . This parameter is often called significant wave height, because for narrow-banded spectra in deep water, H_{mo} is approximately equal to $H_{1/3}$. The other key parameter taken from frequency-domain analysis is the wave period associated with the spectral peak T_p . This standard analysis was for quality control purposes.

Time series from the three-gauge array closest to the model levee were analyzed for incident and reflected wave energy using the method of Goda and Suzuki (1976), and the results were expressed in terms of significant wave height H_{mo} . The analysis looked at gauge pairings 2-3 and 2-4 that had separation distances of 8 in. and 23.5 in., respectively. Whereas the analysis was automated, the engineer manually specified the frequency range over which the analysis was to be applied for each case. Analyzing beyond the range of appreciable spectral energy (region of reduced coherence) introduces significant error into the estimates of wave reflection.

Post-processing of the pressure and velocity data was accomplished using a custom MatLab script. The script converted the time series data into consistent units (either model or prototype scale), plotted time series and outcomes of various computations, and created animations of the unsteady water surface elevations over the levee. Voltages output from the LDV system were converted to velocities using the equation

$$V = \left[\frac{f_{\max}}{10 \text{ volts}} (\text{volt})_{out} - f_s \right] \cdot C \quad (41)$$

where:

f_{max} = maximum frequency in the tracker range

f_s = channel shift frequency

C = conversion factor based on laser color and fiber-optic probe geometry.

For these tests and probe the following values were selected for use in Equation 41: $f_{max} = 333,000$ Hz, $f_s = 20,000$ Hz, and $C = 5.3678 (10)^{-6}$ m/sec/Hz for the green laser light channel that was oriented in the direction of principal flow.

Finally, the MatLab script optionally outputted selected time series of the data in either inch/pound or metric units at model or prototype scale for external analyses or plotting using other software. Analysis was performed on a standard PC workstation running the Linux operating system.

6 Articulated Concrete Mat Stability

One of the principal goals of the levee overtopping model was to investigate the feasibility of protecting earthen levees from overtopping flow erosion using ACMs. The particular ACMs of interest were the same mats used by the Corps of Engineers Mat Sinking Unit to armor the banks of the Mississippi River. This chapter describes the mat stability testing conducted in the small-scale physical model and presents stability results.

The ACMs are constructed of 3-in.-thick concrete blocks weighing 209 lb each and held together by stainless steel wire into mattresses as shown in Figure 24. Block dimensions are given in Table 3 (Chapter 4), and Figure 3 (Chapter 1) shows a test deployment of the mats.



Figure 24. Stacks of ACMs at fabrication yard.

The advantages of using these particular ACMs include availability, Corps' experience deploying the mats, and off-site fabrication with easy transport by either barge or truck. Figure 25 shows a portion of the existing stock of ACMs at the St. Francisville, LA, casting yard.



Figure 25. Portion of casting yard in St. Francisville, LA.

Stability experiments

The usual stability criteria for ACMs is no movement of the mat blocks in uplift, no sliding of the mats over the underlying material, and no erosion of the underlying soil. For some ACM systems, the usual practice is to place the mats over some type of filter layer (geotextile or stone filter) that prevents the levee or embankment soil from leeching out between the block gaps. Movement of the blocks by uplift may damage the filter layer and possibly result in loss of filter material or puncture of the geosynthetic cloth. Block uplifting could also “pump” water and promote erosion. Thus, movement of the blocks is often considered to be a failure of the installation.

Fabrication of the articulated mats used in the physical model is described in Chapter 4, and the testing procedures are given in Chapter 5. Simulation of ACM stability in the physical model was a reasonable representation of ACM stability in the prototype of mats placed atop a gravel filter layer. In this case, overtopping water can infiltrate the gravel layer, and an uplift force on the blocks can be created when the water flowing over the blocks has a lower pressure than the water underneath the blocks (Bernoulli effect). In the model, the blocks were held slightly above solid levee by mesh fabric attached to the underside of the blocks, and thus, water was present underneath the blocks during wave and surge overtopping.

The physical model tests do not represent as well the situation where the ACMs are placed directly on the levee soil without any filter layer or geotextile erosion protection. Without the protection of a filter layer, overtopping water will first begin to erode soil in the gaps between ACM blocks, and that opens up pathways for undercutting the edges of the

blocks and eventual erosion of soil beneath the blocks. However, uplift forces on the blocks will initially be less because water will not penetrate beneath the blocks until some time after overtopping commences (or when storm rains saturate the levee soil). The interface between the blocks and levee soil may provide additional resistance to uplift similar to boots sticking in mud. However, once the mats experience uplift, there is little to prevent erosion of the bare levee soil that has little vegetative root system to hold it together.

Tests with 1-ft surge, 3-ft waves

Five tests were conducted with a nominal 1-ft steady overflowing surge combined with waves with a nominal significant wave height of 3 ft. The 1-ft steady overflowing surge was established relative to the crest of the levee without mats in place. Accounting for the 3-in. mat thickness, the actual surge elevation above the top of the mats was 0.75 ft (prototype scale). With just the steady surge overflow there was a slight movement of the blocks at the landward-most end of the mat just past the transition of the 1:3 protected-side slope and the 1:24 berm slope. Test setup and operating procedures are detailed in Chapter 5.

The first test (NOLAS1H3To6Roo2) was the mildest wave condition in the proposed testing suite. Actual wave height and period (prototype scale) determined from the incident wave analysis were $H_{mo} = 2.7$ ft and $T_p = 6.1$ sec. Most of the overtopping waves managed to lift the mat slightly near the bottom of the 1:3 protected-side slope. The supercritical flow accelerated as it came down the slope with the velocities toward the down-slope end. Additional flow acceleration occurred where the flow was redirected onto the milder 1:24 berm slope. Larger waves in the overtopping wave train lifted the mat farther up the slope but not as far as the midpoint between the levee crest and the terminus of the 1:3 slope. The gap between the underside of the lifted mat and the surface of the model levee was estimated to be approximately 1 mm or about 1 in. at prototype scale. Figure 26 shows mat uplift with the passage of an overtopping wave. Burial of the mat in a trench at the transition between the 1:3 slope and the 1:24 berm slope would have lessened the mat uplift at that transition point, but mat uplift would still occur farther up the slope.



Figure 26. Articulated mat uplift during wave overtopping (1-ft surge, 3-ft wave).

Similar stability results were found when the wave period was increased while maintaining the same nominal wave height and steady surge levels. The analyzed wave parameters were $H_{mo} = 3.3$ ft and $T_p = 10.5$ sec for test NOLAS1H3T10R003 and $H_{mo} = 2.6$ ft and $T_p = 13.7$ sec for test NOLAS1H3T14R004. For longer periods the duration of mat uplift was a little longer. The key point was the mat instability for a relatively minor surge overtopping and wave condition.

Tests with 1-ft surge, 6-ft waves

Two more ACM stability tests were conducted at the same surge level (0.75 ft) but with increased wave heights. Test NOLAS1H6T06R005 had values of $H_{mo} = 5.5$ ft and $T_p = 5.9$ sec. Mat uplift was observed at least half way up the protected-side 1:3 slope for many of the overtopping waves. The mats also lifted slightly on the flood-side 1:4.25 slope at a location between 2 blocks and 5 blocks down the slope from the seaward levee crest. At the seaward terminus of the mat at the base of the flood-side levee slope, the mats curled up slightly with passage of larger waves. In actual deployments the seaward ends of the mats would be securely held either by burial in a trench, by anchoring to piles, or by some other means. One large wave actually shifted the mats landward a distance equivalent to two block widths. However, sliding resistance was not correctly simulated in the physical model, and sliding would not occur if the mats are properly anchored.

The most dramatic instability occurred during test NOLAS1H6T10R006 with wave parameters of $H_{mo} = 6.2$ ft and $T_p = 10.5$ sec. In addition to extensive uplift on the protected-side slope, the mats experienced severe

roll up at the seaward end. Eventually the mats were swept entirely off the model levee proving once again that anchoring of the mats at the seaward and shoreward ends is critical. Figure 27 shows one sequence of frames captured from the video. Even with steady surge elevation above the crest, overtopping was temporarily stalled with the arrival of the wave trough. As the wave crest passed over the toe of the mat, roll up was initiated, and the wave momentum continued to roll the mat after the wave crest overtopped the levee. Proper anchoring would prevent this from occurring.

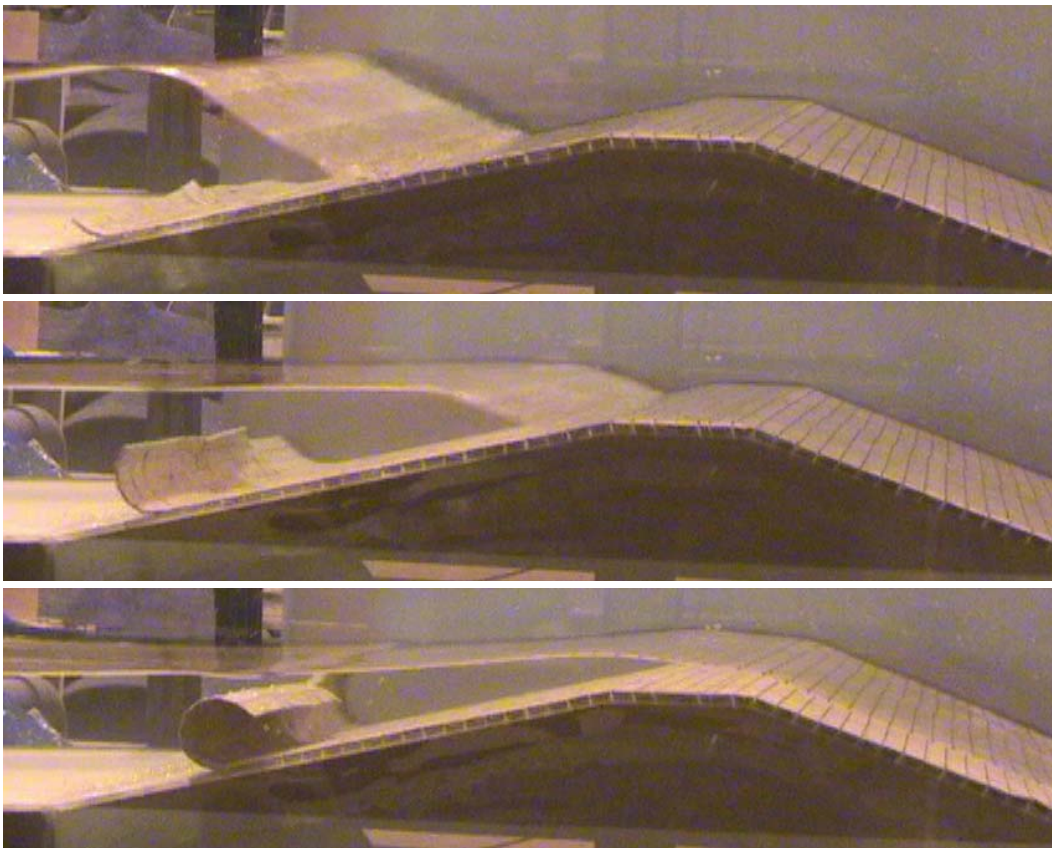


Figure 27. Video capture sequence showing mat roll up at seaward toe of levee.

Tests with 3-ft surge, 3-ft waves

With the steady overtopping surge elevation increased to a nominal 3 ft (2.75 ft actual) above the levee crest, the landward end of the mats on the levee protected side maintained a steady fluttering motion near the transition between the 1:3 protected-side slope and the mild slope berm, even without waves. Part of this was caused by the mats not being securely anchored, but even if the mats were anchored, some uplift would likely occur due to the high steady overtopping flow velocity.

Three tests were conducted with a nominal wave height of 3 ft. The first test was the mildest wave condition with $H_{mo} = 2.6$ ft and $T_p = 5.7$ sec (NOLAS3H3To6R007). Addition of mild wave action to this higher surge level resulted in a time-varying water level on the protected-side slope because the wave troughs were not low enough to cause overtopping to cease temporarily. The landward end of the mats remained in constant motion for a distance of about six block widths up the 1:3 slope. Additional lifting occurred with passage of each wave down the protected-side slope. There was no sign of mat uplift on the levee crest or on the flood-side slope.

Similar response was seen for test NOLAS3H3T10R008 ($H_{mo} = 2.9$ ft and $T_p = 10.1$ sec) with an increased wave period. Figure 28 illustrates the energetic mat movement during this test, and Figures 29 and 30 show a sequence of video images of a single wave overtopping event for this test.

Test NOLAS3H3T14R009 increased the wave period while keeping the wave height similar to previous tests ($H_{mo} = 2.5$ ft and $T_p = 14.4$ sec). The longer wave periods resulted in the protected side being nearly free of flow during some wave troughs. Mat lifting was confined more to the lower half of the protected-side slope during this test. Vibration of the unsecured landward end of the mats was starting to damage the model mats.



Figure 28. Articulated mat fluttering during 3-ft surge and 3-ft, 10-sec wave.

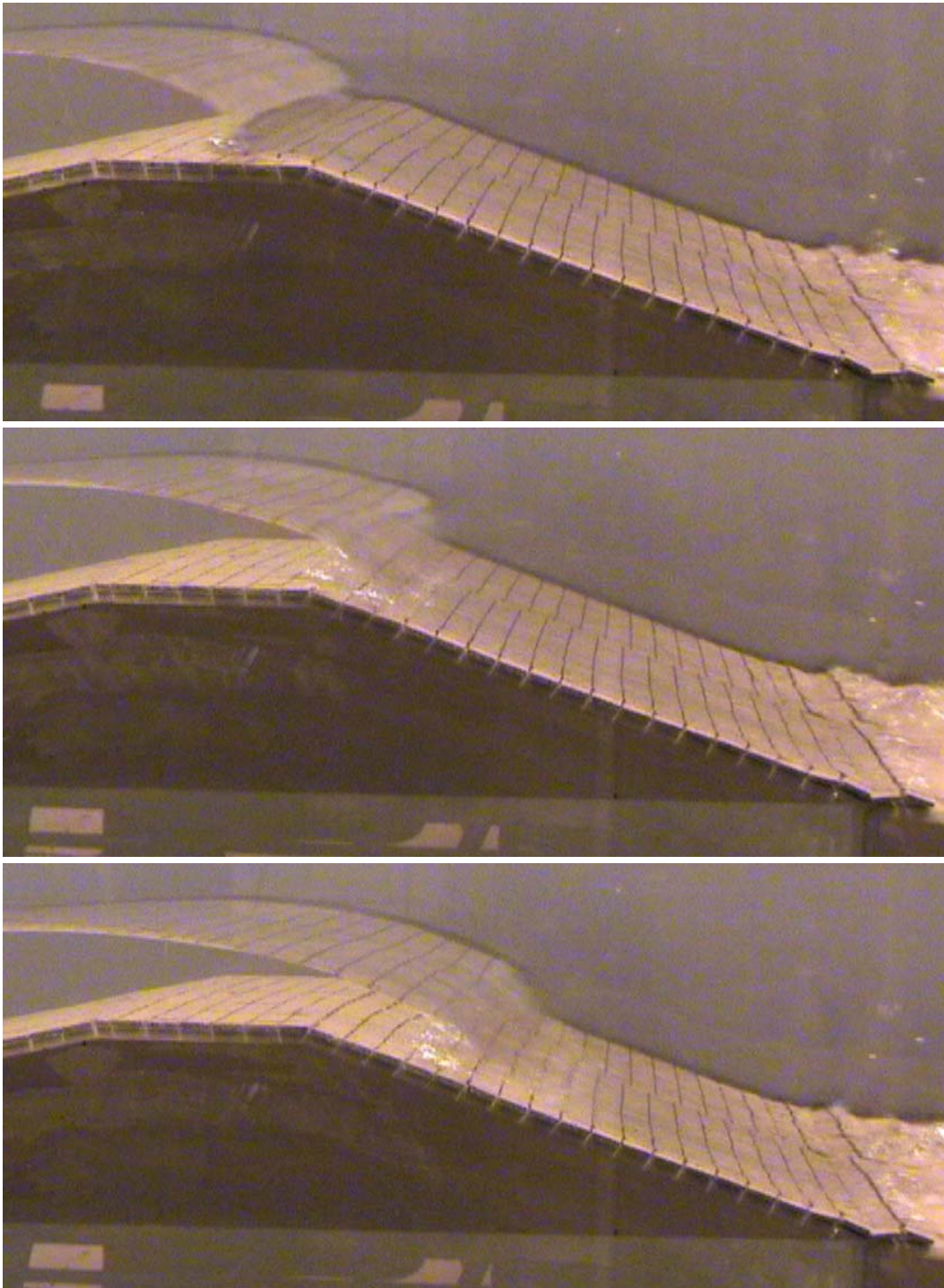


Figure 29. Video capture sequence showing wave overtopping (1 of 2).

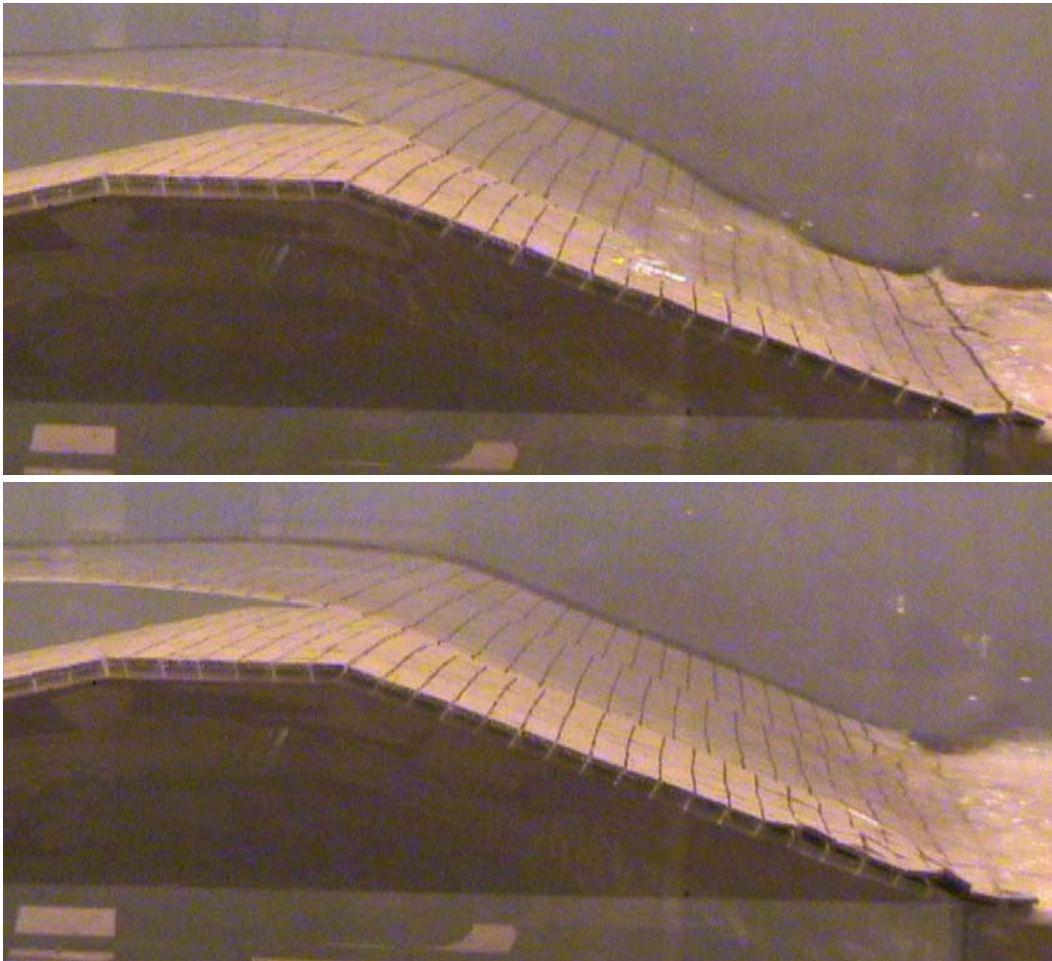


Figure 30. Video capture sequence showing wave overtopping (2 of 2).

Test with 3-ft surge, 6-ft waves

Test NOLAS3H6To6Ro10 increased the nominal wave height to 6 ft ($H_{mo} = 4.8$ ft and $T_p = 5.9$ sec) while maintaining the 3-ft steady surge overflow level. The additional wave energy, while not as high as planned, was enough to immediately start moving the mat landward by sliding. Eventually, the mat was swept from the levee. This test was not altogether realistic because in actual mat deployments the mats would be properly anchored. Nevertheless, the test illustrated that mat self-weight does not provide any stability factor of safety when subjected to combined wave and surge overtopping.

At this point ACM stability testing was terminated because the remaining wave and surge conditions in the test matrix were all more severe than those that had already been run. Thus, mat instability was assured for all remaining test conditions.

Summary of ACM stability testing

Testing results

Stability of ACMs was examined in nine tests with combined steady surge and wave overtopping. The physical model most closely replicated the prototype case where the mats would be placed on top of a gravel filter layer. Even during the mildest condition with a 0.75-ft steady surge and a 3-ft, 6-sec (nominal) irregular wave condition, the mats experienced a slight uplift near the toe of the protected-side slope where the levee transitioned between the 1:3 levee slope and 1:25 berm slope. Mat uplift continued in a similar manner when the wave period was increased to 10 and 14 sec.

As flow transitions from the steeper to milder slopes, there will be an increase in pressure at the transition with a corresponding increase in force on the levee surface. This increased pressure beneath the mat may be the main contributing factor to uplift of the mats at the transition. The other factor is flow separation at the end of the mattress that may contribute to initiating uplift. A possible remedy might be to somehow prevent water from getting underneath the ACMs on the lower portion of the protected-side slope and through the transition at the berm.

Increasing the wave height to a nominal 6 ft produced mat roll-up instability at the toe of the flood-side levee 1:4.25 slope. Uplift was also observed for that portion of the mat on the flood-side slope near the levee crest. The entire mat was swept off the levee when the wave period was increased for this wave height.

Tests with a steady surge level 3 ft above the levee crest indicated mat instability with just steady overflow. When even relatively mild waves were added, mat uplift instability became pronounced.

If the failure criterion is no movement or uplift of the blocks, it can be concluded that ACMs simulated in the physical model will not be sufficient for armoring earthen levees subjected to combined storm surge overflow and wave overtopping. Mats placed directly on the levee soil without filter cloth or a filter layer might resist higher levels of overtopping flow for a while because it will take some time for water to seep under the blocks. However, once erosion begins, the high-velocity flow will cause rapid loss of soil. Stability testing of ACMs placed directly on soil cannot be

accomplished reliably at reduced scale; tests must be conducted at full scale. Unfortunately, no laboratory facilities presently exist that can conduct these tests using combined wave and surge overtopping.

The stability testing illustrated the important need to anchor the mats at both ends. This could be done by burial of the mats in a trench or with some type of anchoring system. The burial option could include large stones placed atop the mats prior to burial.

If these particular mats have an economic advantage over other options, the mat stability could be improved by installing with intermittent anchoring, particularly lower on the protected-side slope where flow velocities reach maximum values. Another option would be to achieve stability by placing a double layer of mats, effectively doubling the armoring self-weight, along with doubling the cost. Even in this deployment, the two mat layers would have to be lashed together. Otherwise, the top layer would experience uplift, and many of the blocks would be broken by impact with the lower mat.

Finally, it is recognized that even with substantial movement of the mats, a reasonable degree of levee protection is provided by the tested ACM system. A severe hurricane event might produce damaging surge overflow and wave overtopping, and there may be substantial erosion of soil underlying the mats, but the erosion will be less than would be expected on an unprotected earthen levee. Therefore, even with extensive damage, breaching of a levee over the time span of the storm is less likely because the mats hinder formation of headcuts and retard erosion of the levee soil. Of course, it would be necessary to undertake expensive repairs after the storm, but for rare events this might be a tolerable compromise to the costs of armoring with a totally stable solution that will be able to withstand frequent events with only minimal post-storm repair.

Suggestions

If the particular ACMs tested in this study remain a viable armoring option, several additional tests could be conducted. Using the small-scale facility at ERDC it would be possible to investigate the benefits of both end and intermittent mat anchoring, and it may even be feasible to determine the uplift forces that would be exerted on the anchors for different combinations of overtopping waves and surge overflow. Also, the two existing model mats could be doubled and lashed together to examine whether this

option gains enough stability to meet the no-movement criterion for different wave and surge flow combinations.

As mentioned, one option under consideration was to place the ACMs directly on the groomed levee soil. Examination of stability and potential erosion of underlying soil can be tested reliably only at prototype scale. Present testing capability at full scale includes only steady overflow, but it may be possible to estimate steady flow parameters that produce similar shear stresses as unsteady flow overtopping. A less accurate alternative would be to test at smaller scale with model mats lying on a compacted clay levee. Even with incorrect similitude, the tests could give a qualitative indication of the ACM's capability to prevent or delay levee breaching.

7 Hydrodynamics of Combined Wave and Surge Overtopping

The second principal goal of the levee overtopping model was to investigate the flow characteristics associated with combined wave and surge overtopping of the MRGO levee cross section. The purpose of this investigation was to develop a preliminary capability to predict parameters of the unsteady flow overtopping that can be used to assess maximum flows that will occur on the protected-side slopes of levees. This chapter describes the hydrodynamic experiment results measured in the small-scale physical model and presents a prediction method for estimating the combined wave and surge overtopping average discharge and the unsteady discharge distribution in terms of incident wave parameters and surge elevation above the levee crest.

Summary of experiments

Testing began with the steady surge elevation set at +1 ft (prototype scale) above the levee crest. The nine unique wave conditions for this surge level were run beginning with the mildest condition and finishing with the largest wave condition. The surge elevation was then raised to successive heights (+3 ft and then +5 ft), and the wave conditions were repeated. Subsequent data analysis revealed that the LDV measurements for a few of the early experiments contained errors, and those experiments were repeated and results verified. Test setup and operating procedures are detailed in Chapter 5.

Table 6 summarizes the 27 experiments conducted for this phase of the study. The first column contains the run number associated with the data files and logs. Prototype-scale equivalents of the target significant wave height H_{mo} and peak spectral wave period T_p are given in columns 2 and 3, respectively. The measured wave parameters determined by applying the reflection analysis to the three-gauge wave array are shown in columns 4 through 8. Included are both model-scale and prototype-scale values along with the bulk reflection coefficient for each experiment. In the majority of cases the measured significant wave heights fell below the target higher values. The measured values were used in all subsequent data analyses, but plots are labeled with nominal target wave parameters.

Table 6. Summary of experiments and hydrodynamic forcing.

Exp. No.	Target Waves		Measured Wave Parameters					Steady Overflow	
	Prototype		Model		Prototype			Model	Proto
	H_{m0} (ft)	T_p (sec)	H_{m0} (cm)	T_p (sec)	H_{m0} (ft)	T_p (sec)	Reflec. Coef.	q_s (gpm/ft)	q_s (ft ² /sec)
Surge Level = +1 ft above Levee Crown									
R128	3.0	6.0	3.28	1.21	2.69	6.07	0.112	10.27	2.86
R129	6.0	6.0	6.67	1.19	5.47	5.94	0.129	11.91	3.32
R130	9.0	6.0	10.15	1.19	8.33	5.94	0.179	11.09	3.09
R104	3.0	10.0	4.01	2.10	3.29	10.51	0.174	10.01	2.79
R105	6.0	10.0	7.56	2.10	6.20	10.51	0.184	9.33	2.60
R131	9.0	10.0	11.30	2.10	9.27	10.51	0.248	9.29	2.59
R107	3.0	14.0	3.15	2.73	2.58	13.66	0.294	9.55	2.66
R108	6.0	14.0	6.73	2.73	5.52	13.66	0.298	10.00	2.78
R109	9.0	14.0	9.93	2.73	8.15	13.66	0.344	10.08	2.81
Surge Level = +3 ft above Levee Crown									
R110	3.0	6.0	3.08	1.14	2.53	5.69	0.095	44.64	12.43
R111	6.0	6.0	5.85	1.19	4.80	5.94	0.117	46.89	13.06
R112	9.0	6.0	9.62	1.19	7.89	5.94	0.169	45.62	12.71
R113	3.0	10.0	3.52	2.02	2.88	10.12	0.127	43.50	12.11
R132	6.0	10.0	7.65	2.02	6.27	10.12	0.134	61.88	17.23
R115	9.0	10.0	10.65	2.10	8.74	10.51	0.200	48.24	13.44
R116	3.0	14.0	3.00	2.87	2.46	14.37	0.223	45.33	12.62
R117	6.0	14.0	6.53	2.28	5.36	11.38	0.256	48.31	13.45
R118	9.0	14.0	9.66	2.87	7.92	14.37	0.280	47.81	13.32
Surge Level = +5 ft above Levee Crown									
R119	3.0	6.0	2.56	1.21	2.10	6.07	0.127	94.82	26.41
R120	6.0	6.0	4.68	1.21	3.84	6.07	0.136	97.58	27.18
R121	9.0	6.0	9.21	1.21	7.55	6.07	0.157	98.40	27.41
R122	3.0	10.0	3.45	2.02	2.83	10.12	0.127	101.62	28.30
R123	6.0	10.0	7.15	2.02	5.86	10.12	0.151	97.76	27.23
R124	9.0	10.0	10.96	2.02	8.99	10.12	0.186	100.01	27.85
R125	3.0	14.0	2.96	2.87	2.43	14.37	0.179	93.40	26.01
R126	6.0	14.0	6.00	2.87	4.92	14.37	0.192	95.67	26.64
R127	9.0	14.0	9.25	2.87	7.59	14.37	0.219	98.08	27.31

Finally, columns 9 and 10 list the steady surge overflow discharge per unit levee width in both model- and prototype-scale units. These values were estimated from the time series of discharge calculated as the product of water depth and flow velocity measured near the landward side of the levee crest (location P2 on Figure 23) before the first wave arrived at the levee.

Typical measured results

Time series measurements

Results from two of the experiments are presented in the following plots to give a sense of the significant increase in flow velocity and discharge magnitudes caused by waves overtopping the levee.

Low surge, low wave height

Figure 31 shows results from run 104 with a +1 ft surge with nominal 3-ft, 10-sec irregular waves (actual wave height 3.3 ft). The upper plot is water depth at pressure gauge P2. The steady overtopping depth was about 0.54 ft (see left edge of plot), but the wave overtopping depths were as much as three times larger. Velocities (middle plot) were sometimes twice as large as the steady overtopping flow velocity of about 5.1 ft/sec. Flow discharge (bottom plot) temporarily exceeded 3-4 times the steady surge discharge of 2.8 ft³/sec per ft.

Note the discharge was computed at each time-step as the product of flow depth and velocity at pressure gauge location P2. This calculation assumed that the velocity throughout the flow over pressure gauge P2 was uniform over the depth at that instant and can be represented by the measurement at a single point. The discharge calculation can be performed only when the water depth was above the vertical location of the LDV beams. During wave troughs, particularly for the +1-ft surge condition, the flow level over the crest fell beneath the laser beam elevation, and often the crest was momentarily dry. Velocities were not recorded in this situation, and no meaningful discharge can be estimated. However, the flow depths on the levee are still accurately recorded during wave troughs. Thus, the lower values on the discharge time series plot represent the last level of discharge before the water level fell beneath the LDV beams. Figure 32 is an enlarged extract from the time series shown in Figure 31.

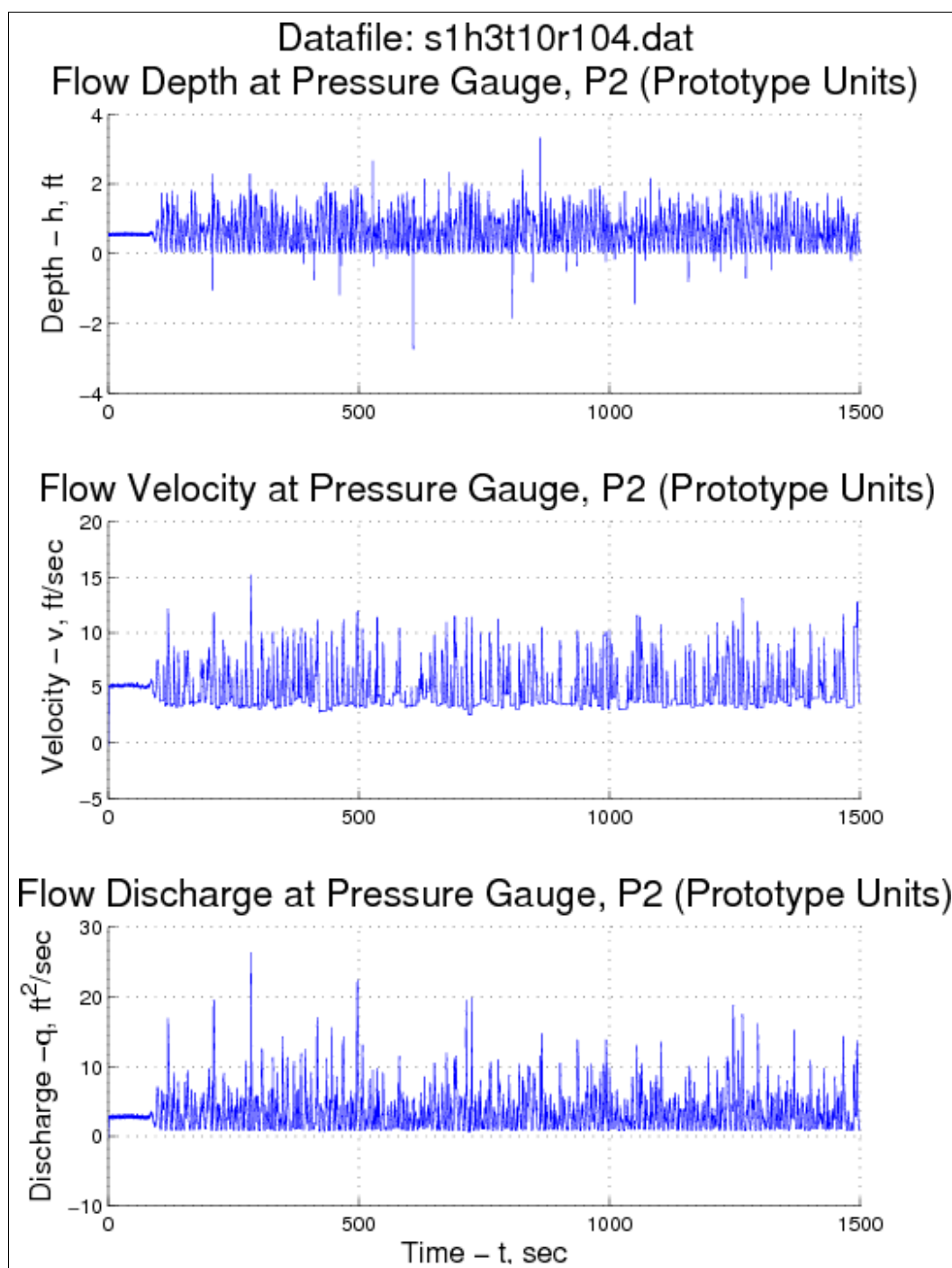


Figure 31. Test R104: Surge = +1 ft, H_{m0} = 3.3 ft, T_p = 10.5 sec.

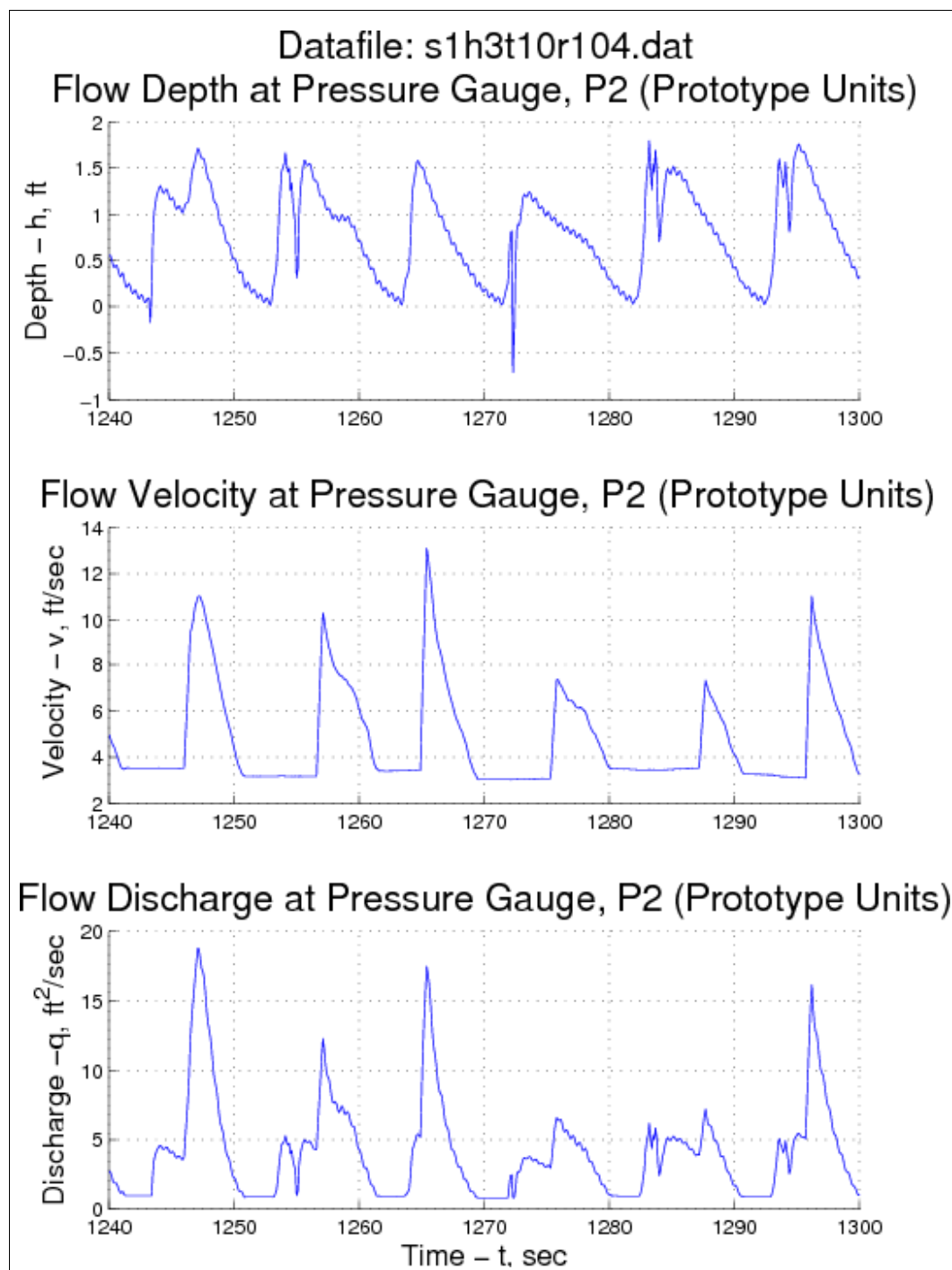


Figure 32. Test R104 (extract): Surge = +1 ft, H_{m0} = 3.3 ft, T_p = 10.5 sec.

On Figure 32 an occasional “dropout” is evident in the flow depth data (top plot). The horizontal portions on the velocity data (middle plot) indicate times when the water level was below the LDV position and data could not be obtained. The combination of the upper two plots produced the lower plot of discharge. Horizontal lines indicate time spans for which no estimates can be made.

The data peaks shown on Figure 32 indicate a rapid increase in velocity and water depth with the arrival of each wave, and a slower decrease as the wave passes over the P2 location. This may be an important aspect because the rapid rise in discharge is accompanied by a fairly large (but short duration) flow acceleration that may have consequences for potential armoring solutions.

High surge, high wave height

Figure 33 presents measured data for a test (run 115) conducted with a steady surge elevation of +3 ft above the levee crest combined with a nominal 9-ft, 10-sec irregular wave condition (actual wave height was 8.7 ft). As seen in the lower plot, the instantaneous discharge was often above 40 ft³/sec per ft, and this level is nearly three times the steady flow discharge of about 13 ft³/sec per ft. Flow velocities exceeded 15 ft/sec near the rearward edge of the levee crown, and faster flows occurred on the protected-side levee slope.

Figure 34 shows an extracted portion of the data displayed in Figure 33. When looking at the magnitudes on the water depth, velocity, and discharge, keep in mind that the surge-only values for these parameters are 1.5 ft, 9 ft/sec, and 13.4 ft³/sec per ft, respectively. For the peak located at $t = 410$ sec, the maximum velocity on the protected-side slope was estimated to be around 23 ft/sec. Time series plots similar to Figures 31 and 33 are given in the appendix for all experiments.

Water surface profile measurements

Figure 35 shows a time series record of the vertical variation of water level over pressure gauge P4 during combined surge and wave overtopping of monochromatic waves having a nominal wave height of 3 ft and a period of 14 sec (prototype-scale values).

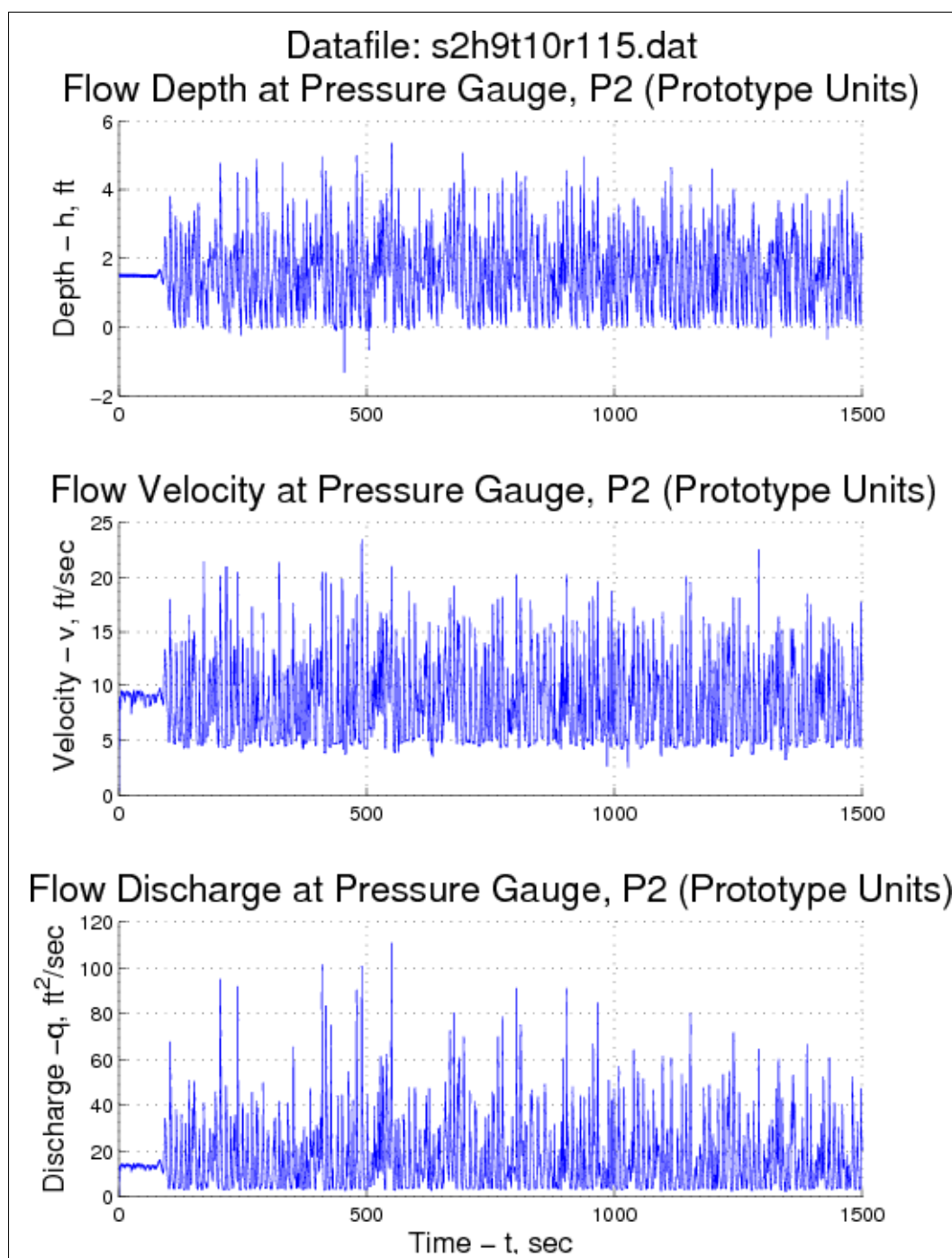


Figure 33. Test R115: Surge = +3 ft, $H_{m0} = 8.7$ ft, $T_p = 10.5$ sec.

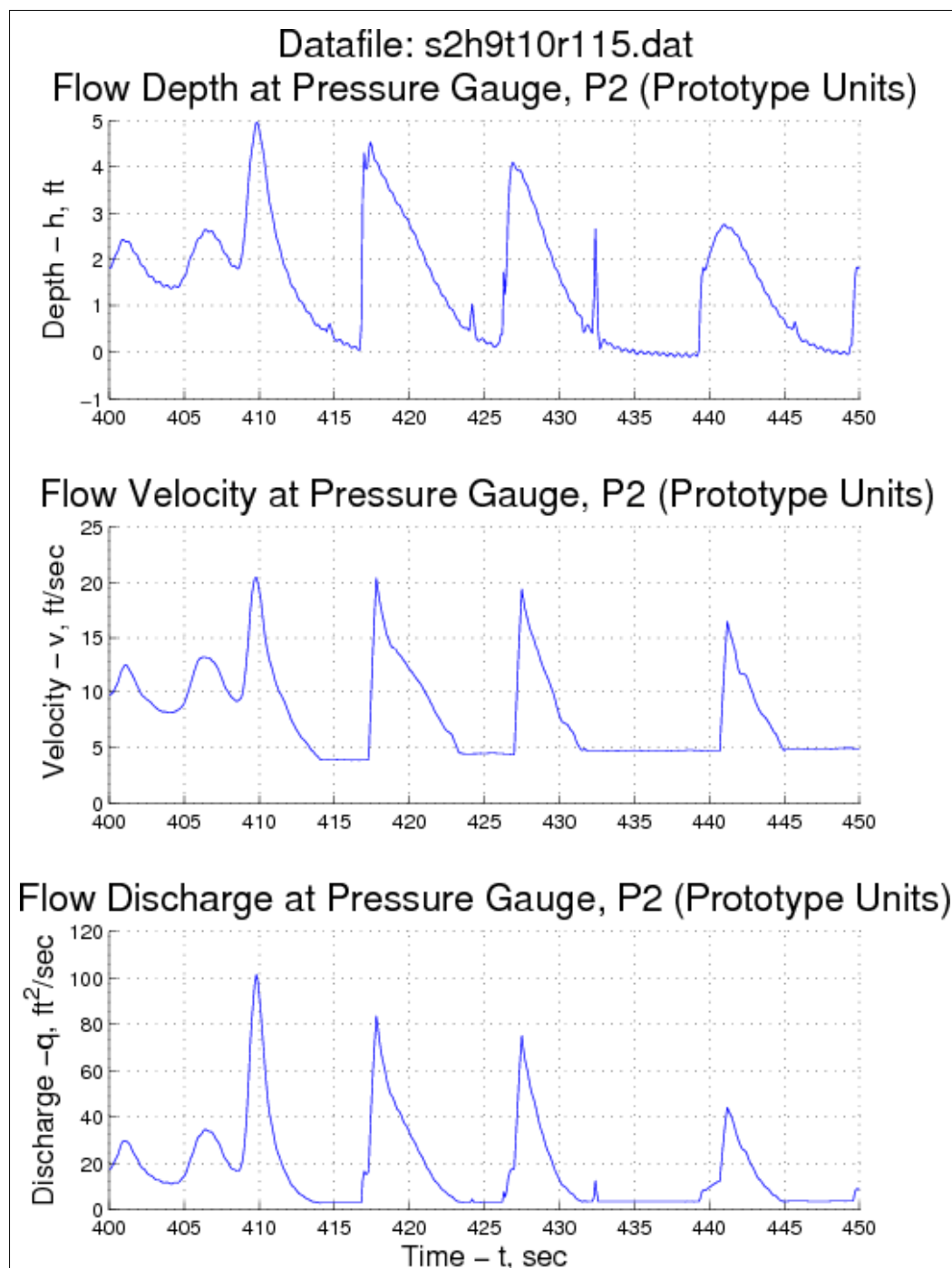


Figure 34. Test R115 (extract): Surge = +3 ft, H_{m0} = 8.7 ft, T_p = 10.5 sec.

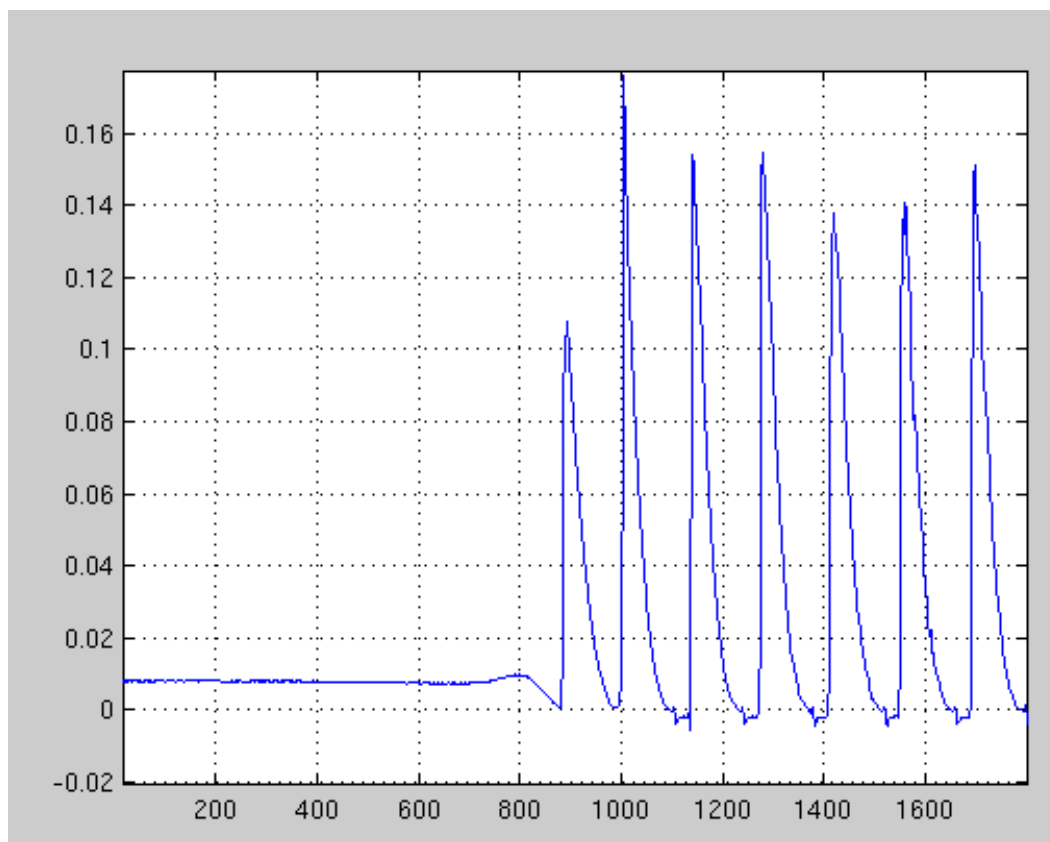


Figure 35. Pressure head (model feet) output from gauge P4.

The first 700+ data points correspond to only steady flow overtopping associated with a 1-ft surge. From previous point gauge measurements, this elevation was known, and the pressure time series has been shifted vertically to match the correct steady flow elevation. Note that this 3-ft wave produced water elevations on the levee backside slope that were as much as 3.75 ft (prototype scale), which is 15 times the depth of steady overflow from a 1-ft surge.

To better understand the physical process of waves overtopping a levee, a single wave was selected at random from the pressure time-history of Figure 35 and examined in detail. Figure 36 shows the time-history of pressure gauge measurements expressed in feet of water over the gauge for a period of about 3.4 sec in the model (17 sec at full scale). The X-axis is data point number. The data were collected at a 50-Hz rate (50 points per sec), so the grid lines are spaced at 0.4-sec intervals (2 sec at full scale). As the wave overtops the levee, there is a rapid rise in water level, followed by a slower decrease in water level as the discharge flows off the backside slope.

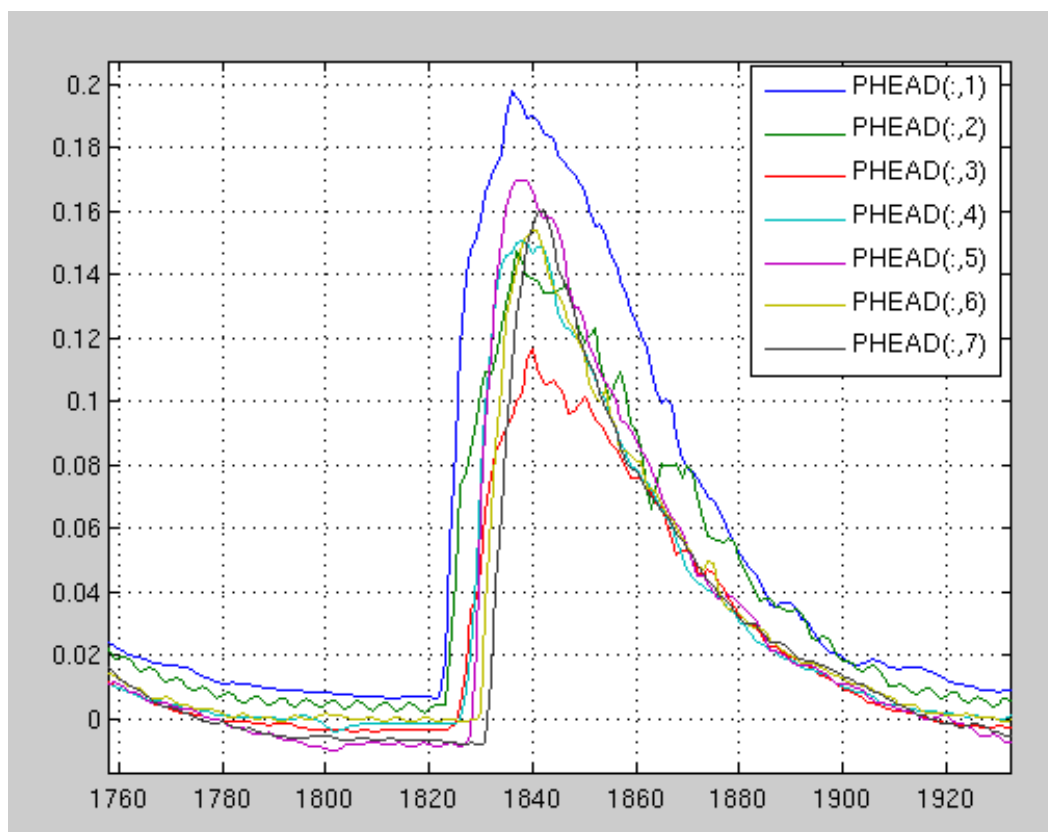


Figure 36. Single wave overtopping time-history.

Figure 37 shows the water surface profile change over the levee during the interval between data points 1830 and 1837 shown in Figure 36. This interval equates to 0.14 sec in the model or 0.7 sec at full scale. This transient flow has significant downslope acceleration. A rough estimate of the forward velocity of the wave leading edge is around 30-40 ft/sec based on the forward progress from profile 1830 to 1831.

Figure 38 shows the water surface profiles for the data interval 1840-1845 shown on the pressure data plots of Figure 36. Notice that these five profiles are nearly constant, and this occurs at about the maximum water depth of the overtopping wave.

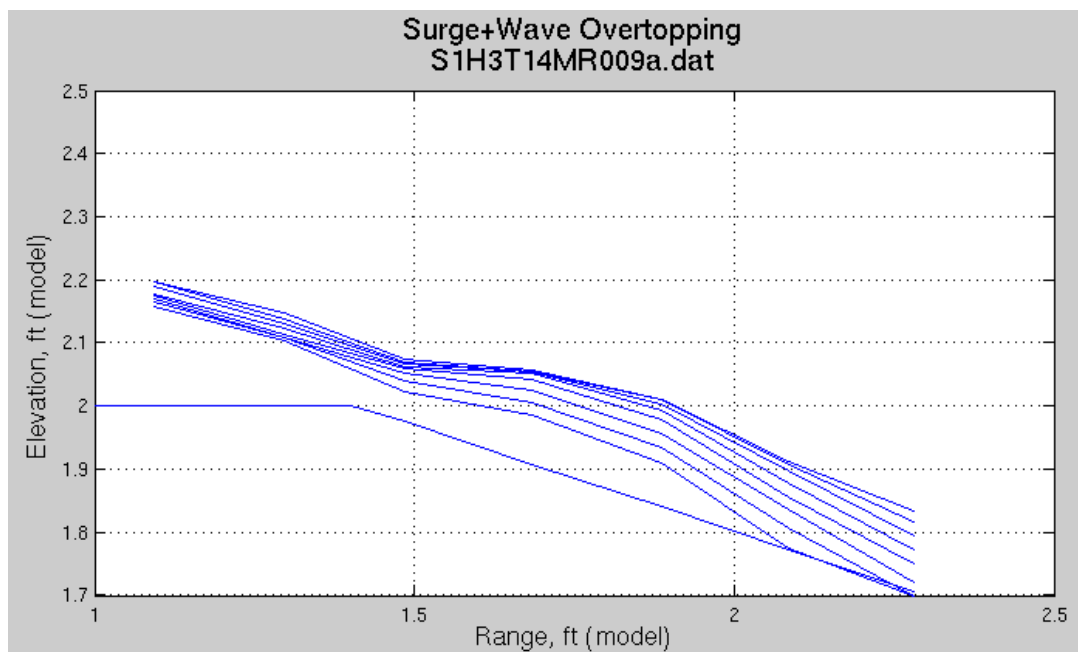


Figure 37. Water surface profiles for 1830-1837 data interval.

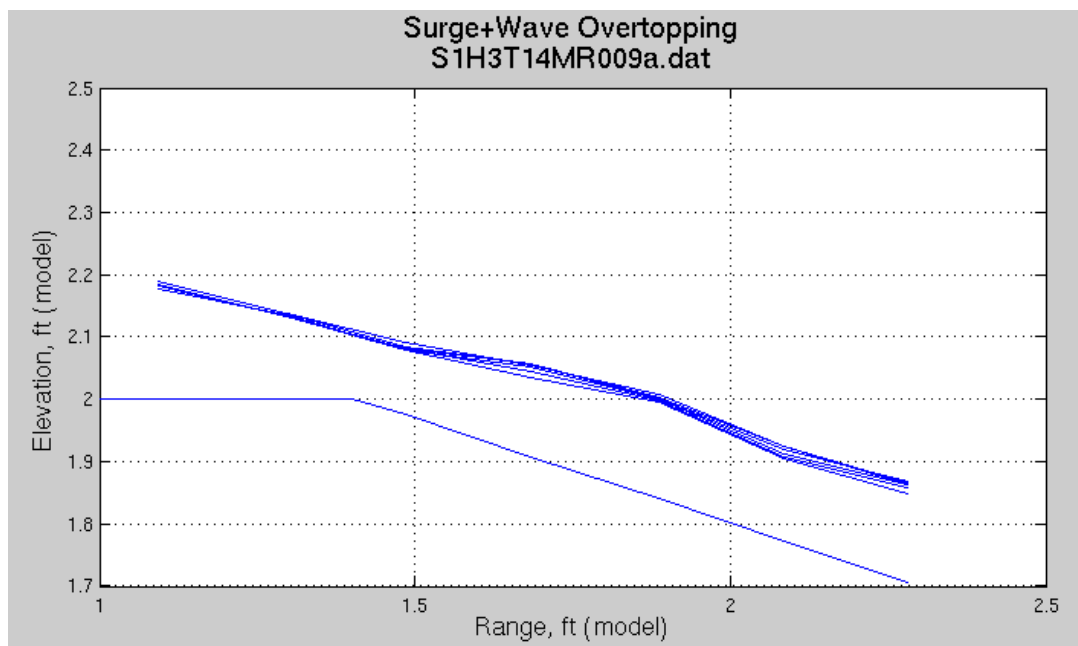


Figure 38. Water surface profiles for 1840-1845 data interval.

This is an interesting and potentially important observation for two reasons. First, during this short interval (0.1 sec in the model, 0.5 sec in the prototype), the flow might be similar to the steady flow overtopping situation, and this could greatly simplify estimating flow velocity or shear stress on the slope. Terms in the unsteady flow equation of motion associated with variation of velocity with time and distance downstream,

and the term associated with downstream variation of water depth are small during this short interval compared to the discharge and shear stress. Thus, at first approximation it may be appropriate to analyze this stage of the unsteady overtopping as steady flow with a balance between the flow momentum and bottom shear stress. Therefore, combining the pressure measurements with flow velocity measured at a single location on the slope during this time interval would allow an estimate of the shear stress on the levee.

Second, this brief period of quasi-steady overtopping occurs around the maximum water depth over the levee backside slope, and this produces near maximum shear stresses. However, there may be very brief times during the unsteady portion of the initial wave overtopping where higher shear stresses occur, and this also needs to be investigated in the future. Examination of the unsteady portion of the flow requires at least two point measurements of flow velocity at locations of two adjacent pressure cells, and a second velocity meter was not available during these experiments.

Average overtopping discharge

The time series of instantaneous discharge determined at the location of pressure gauge P2 near the landward edge of the levee crest was used to estimate the average overtopping discharge q_{ws} for each experiment. Averages were calculated for data points 1,000 to 15,000 (280 seconds at 50-Hz rate). This range did not include any data from the initial steady overflow portion at the start of the experiment before waves arrived at the levee.

As mentioned in the previous section, discharge estimates were held at a constant value when the water level fell beneath the elevation of the laser beams. This resulted in values of discharge during these periods that were higher than actual. Consequently, the calculated average overtopping discharges were higher than actual. The degree of overestimation was evaluated by a second calculation in which the instantaneous discharge was set to zero whenever the water level was lower than the LDV laser beams. This calculation underestimated actual discharge, and the two values effectively bracket the true value of the measurement.

Comparison between the high and low estimates revealed the maximum difference was about 13 percent for experiment R130, and the average difference was only 4 percent for all experiments. There was barely any

difference at the highest surge elevation because the laser beams remain submerged most of the time. The true average overtopping discharge is somewhere between the two estimates, so the mean value of q_{ws} was assumed to be a reasonable value to adopt, and it was used in subsequent analyses. The difference between q_{ws} and the steady surge overflow q_s decreased as surge elevation increased, indicating that net overtopping due to the wave contribution approaches zero as negative freeboard increases.

Figure 39 plots the dimensionless combined wave/surge average overtopping discharge versus the relative (negative) freeboard for all 27 experiments. The indicated surge levels in the plot legend are the average of the negative freeboards determined for all nine experiments at that nominal surge level. As seen, the measurements gave a distinct trend with increasing relative freeboard, and the solid line is a best-fit empirical equation given by the formula

$$Q_{ws} = \frac{q_{ws}}{\sqrt{g} H_{m0}^3} = 0.0336 + 0.53 \left(\frac{-R_c}{H_{m0}} \right)^{1.58} ; \quad R_c < 0 \quad (42)$$

where q_{ws} is the average combined wave and surge overtopping discharge, H_{m0} is the energy-based significant wave height, and R_c is the freeboard which will be less than zero for this formula. This best-fit equation had a correlation coefficient of 0.9987 and a root-mean-square (RMS) percent error of 0.12. Note that R_c must be entered as a negative number so the ratio in brackets will be positive. Peak spectral wave period had negligible influence in the determination of Q_{ws} for the range of periods tested in the model. Like any other empirical equation, application of Equation 42 should be limited to the range of tested parameters. In particular, seaward-side levee slopes different than 1:4.25 could influence the wave overtopping, but seaward-side slope effects should decrease as surge level increases.

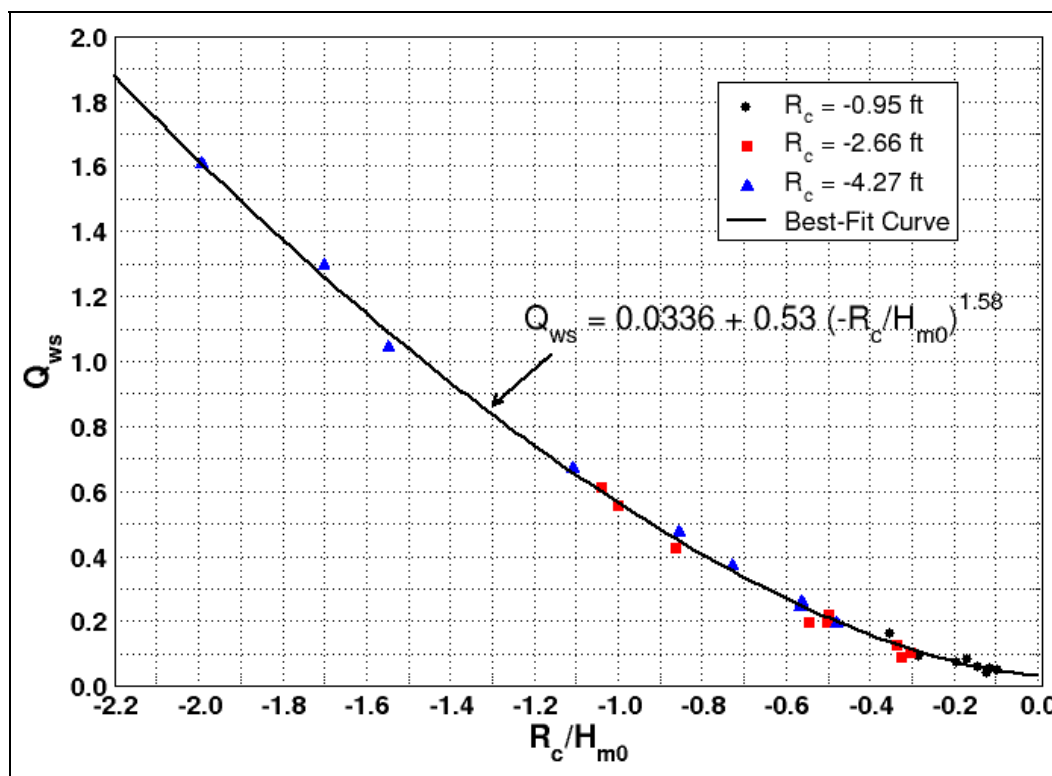


Figure 39. Dimensionless combined average discharge versus relative freeboard.

Overtopping flow discharge distributions

The time series measurements of overtopping flow discharge acquired at the location of pressure gauge P2 near the landward edge of the levee crest were analyzed to determine the cumulative distribution of instantaneous discharge over the levee crest. After discarding the first 1,000 discharge time series data points corresponding to only steady flow discharge, the remaining 14,000 values of instantaneous discharge were rank ordered and plotted as discharge distributions. Figure 40 presents the distribution results for a typical test with the surge level at +1 ft.

The upper plot (Figure 40) is the cumulative probability of discharge. The curve gives the probability that the overtopping discharge will be below a given value, i.e., $\text{prob}(q < q_{\text{specified}})$. For example, in Figure 40 the probability that a discharge will be below $q = 10$ ft³/sec per ft is about 0.85. The lower end of the discharge curve is not entirely accurate because any discharge below the water depth of the LDV beams was recorded as if the discharge had remained steady at the last valid measurement. This is not a severe shortcoming because this end of the curve holds less importance for design. The extreme discharges are more relevant to slope protection design.

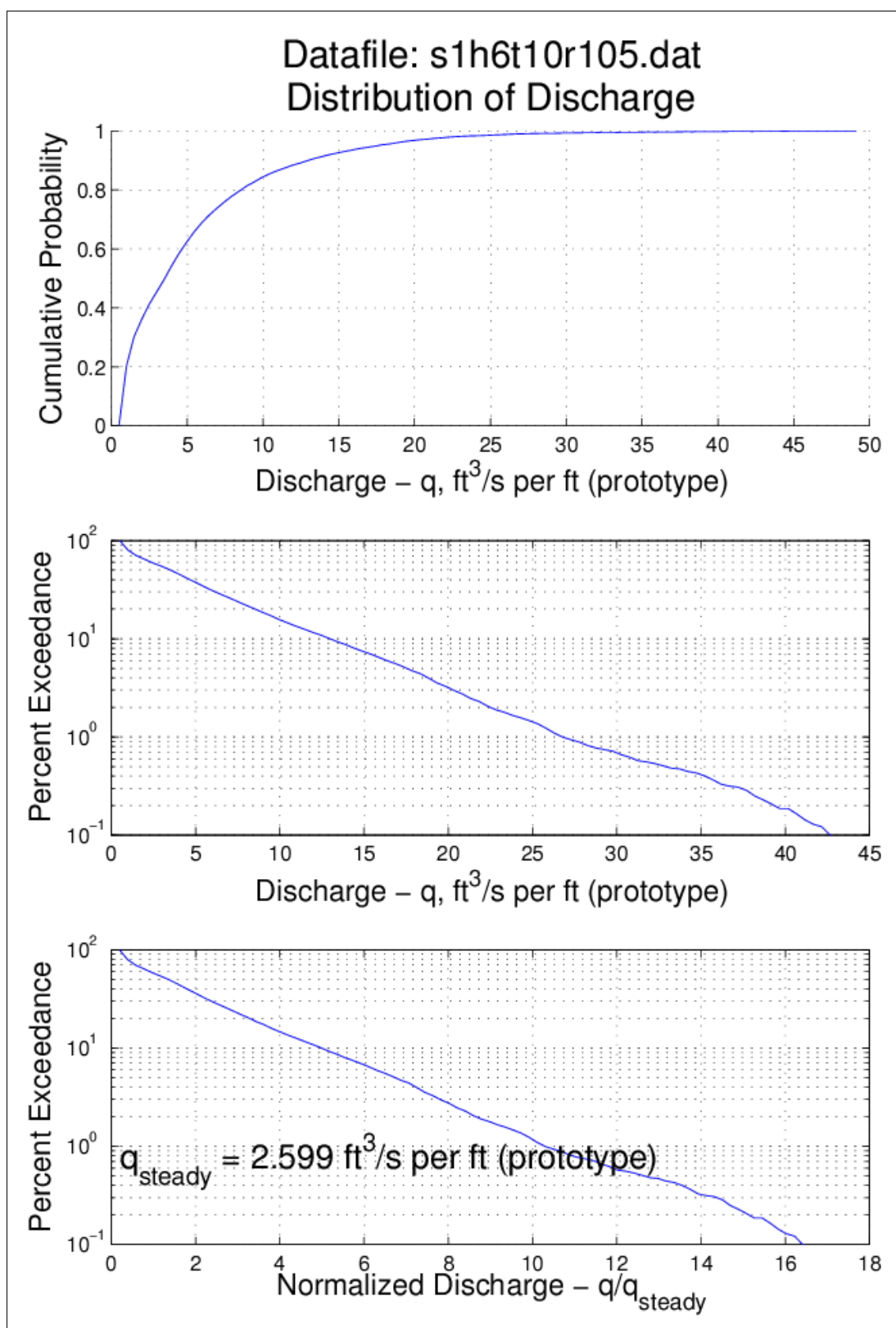


Figure 40. Discharge distribution for surge = +1 ft, $H_{m0} = 6.2$ ft, $T_p = 10.5$ sec.

The middle plot in Figure 40 shows the percent exceedance for a given value of discharge. Percent exceedance is simply given as

$$P\%(q > q_{\text{specified}}) = [1 - \text{prob}(q < q_{\text{specified}})] \times 100\% \quad (43)$$

The curve is plotted with a semilog ordinate to better present the extreme end of the exceedance probability. For example, from Figure 40, it is seen that 1 percent of the overtopping discharge exceeds about $q = 26 \text{ ft}^3/\text{sec}$ per ft.

The lower plot in Figure 40 uses the same data as given in the middle plot, but the discharge has been normalized by the value of the steady surge overflow that would occur in the absence of waves for that surge level. Figure 40 shows that the discharge exceeds twice the steady surge discharge about 35 percent of the time, and 10 times the steady discharge just over 1 percent of the time. Plots showing the calculated distributions for all tests are given in the appendix.

Overtopping distribution variation with wave and surge parameters

Figures 41-46 show the variation in overtopping discharge distribution with the surge elevation, wave height, and wave period for selected experiments. Wave parameter values shown in the figures are the nominal target values. Actual resolved wave parameters are given in Table 6.

As expected, surge elevation had a substantial influence on the discharge distribution as seen in Figures 41 (medium waves) and 42 (large waves). Each increase in surge elevation allowed much more water to overtop the levee, and the percent exceedance curves are very different over the entire distribution.

Figure 43 shows the effect on exceedance probability of varying wave height when the short wave period and storm surge level are kept constant at +1 ft above the levee crest. Figure 44 shows the variation for a +5 ft surge elevation with a longer wave period. For the shorter wave period and lower surge level (Figure 43) wave height increase affects mostly the discharge levels exceeded about 10 percent of the time. For the two higher wave heights, there is very little difference over 99 percent of the distribution. This may be caused by wave breaking on the levee crest with the lower surge level.

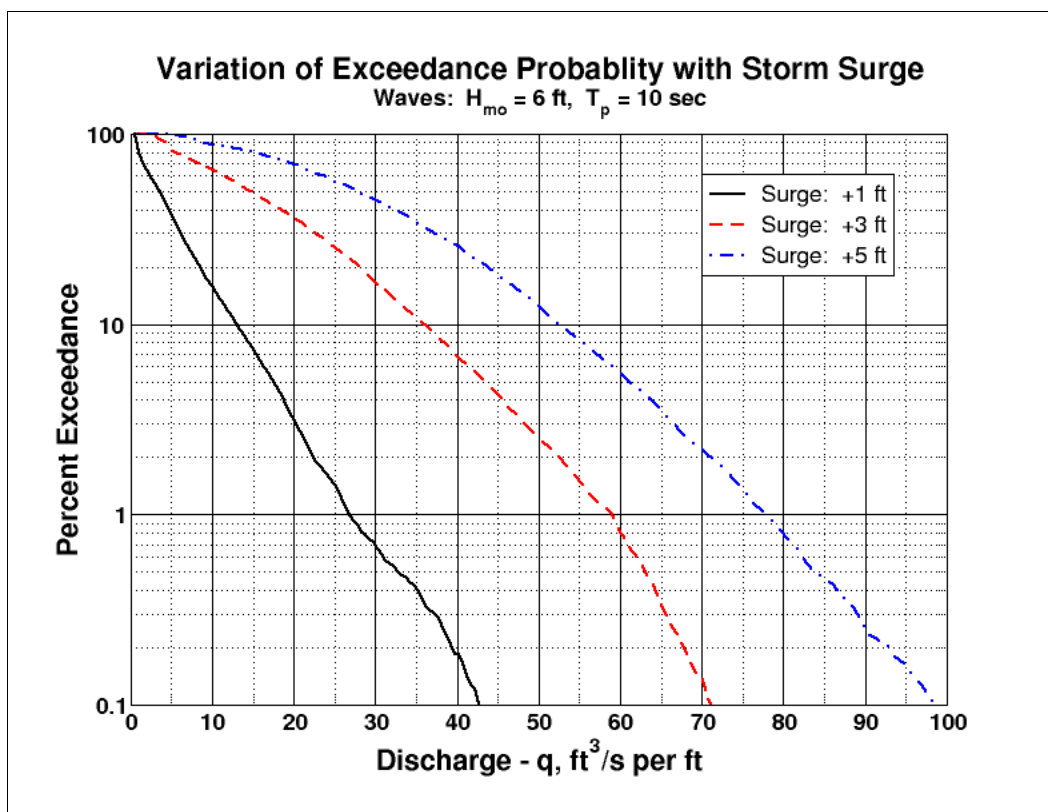


Figure 41. Exceedance probability variation with storm surge (medium waves).

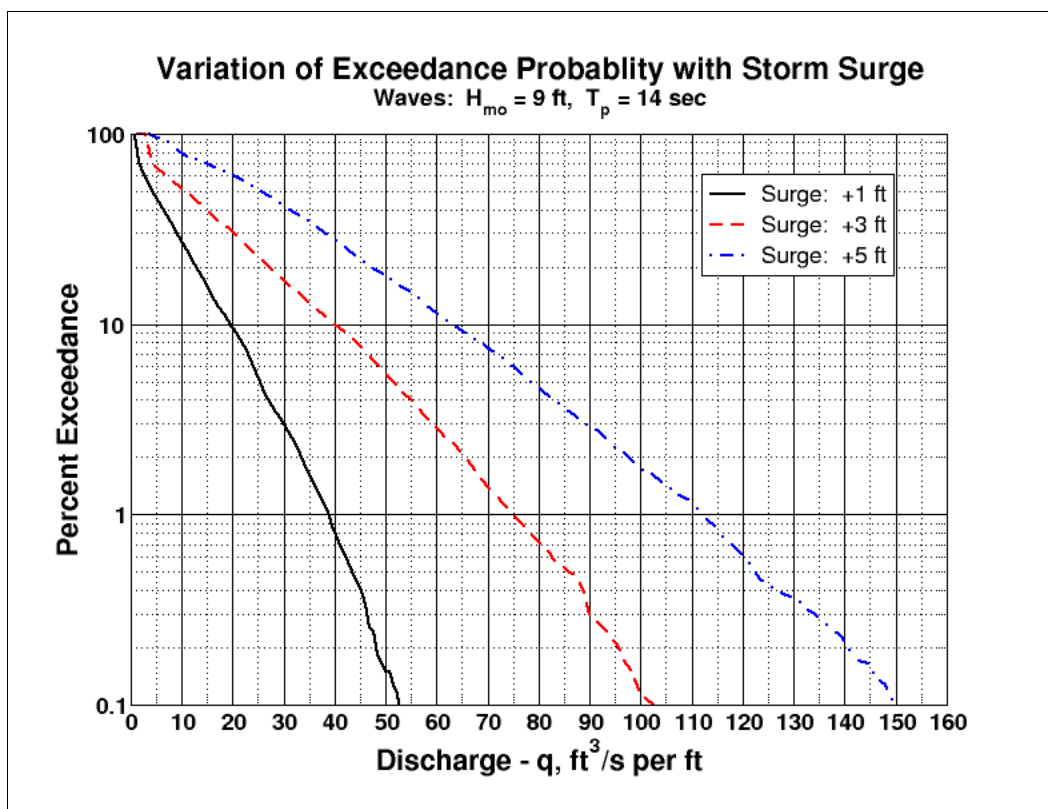


Figure 42. Exceedance probability variation with storm surge (large waves).

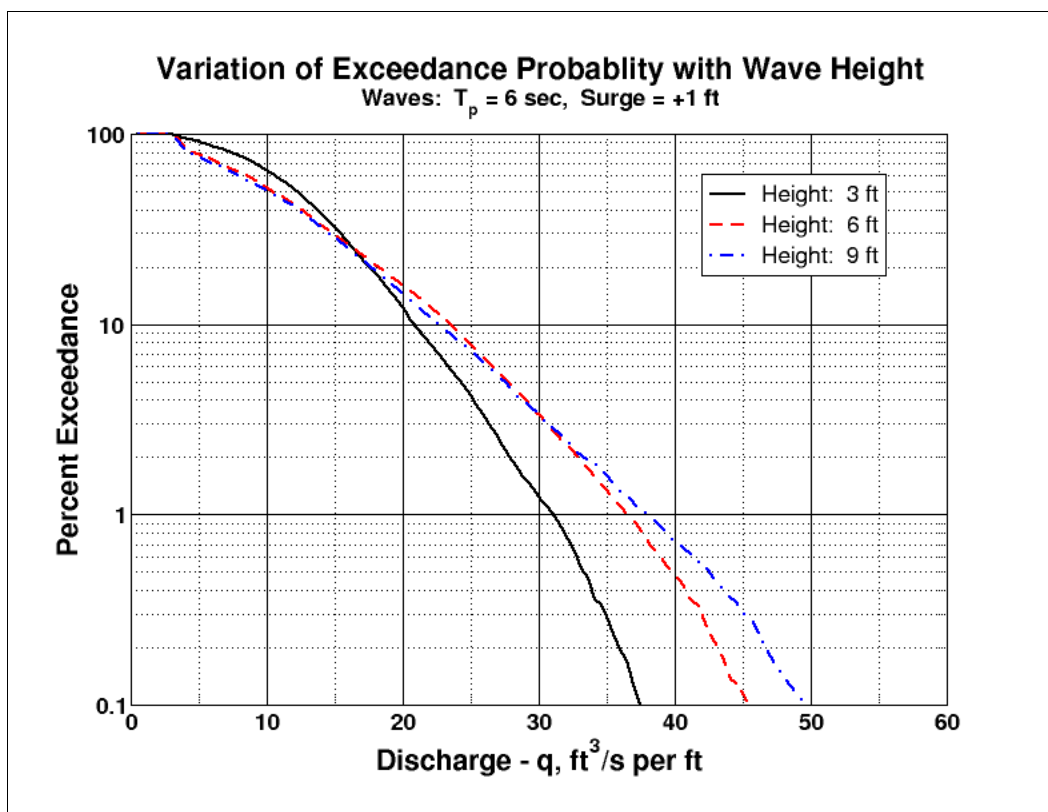


Figure 43. Exceedance probability variation with wave height (+1-ft surge).

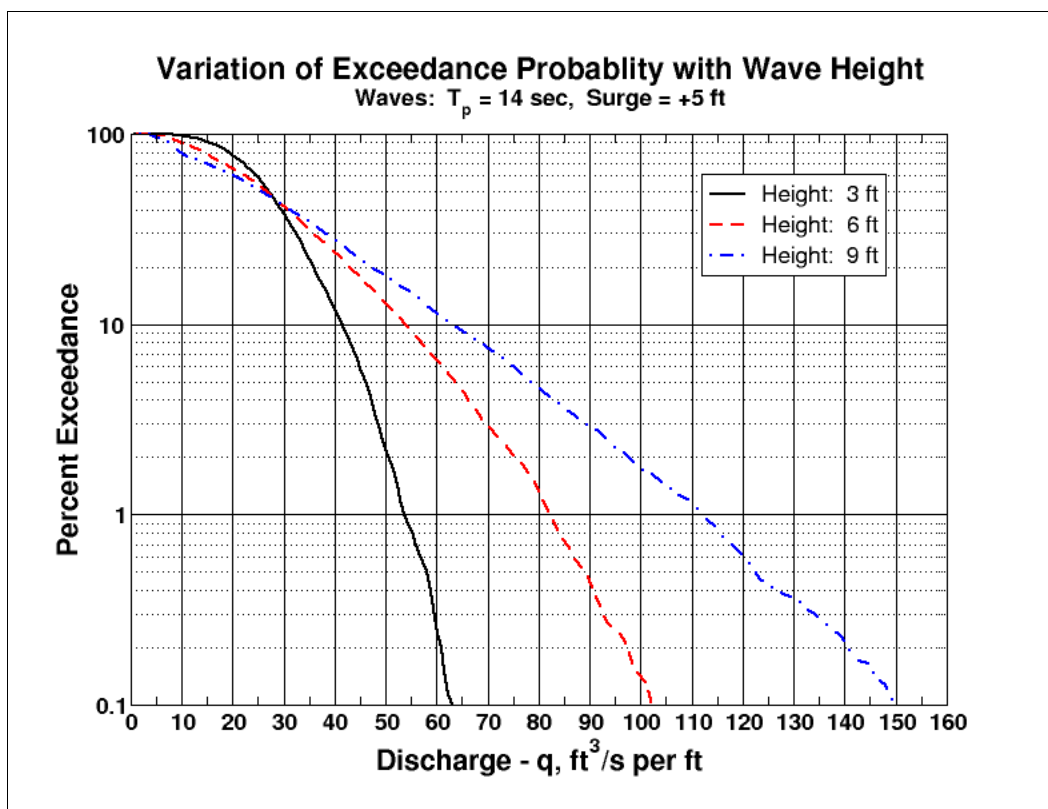


Figure 44. Exceedance probability variation with wave height (+5-ft surge).

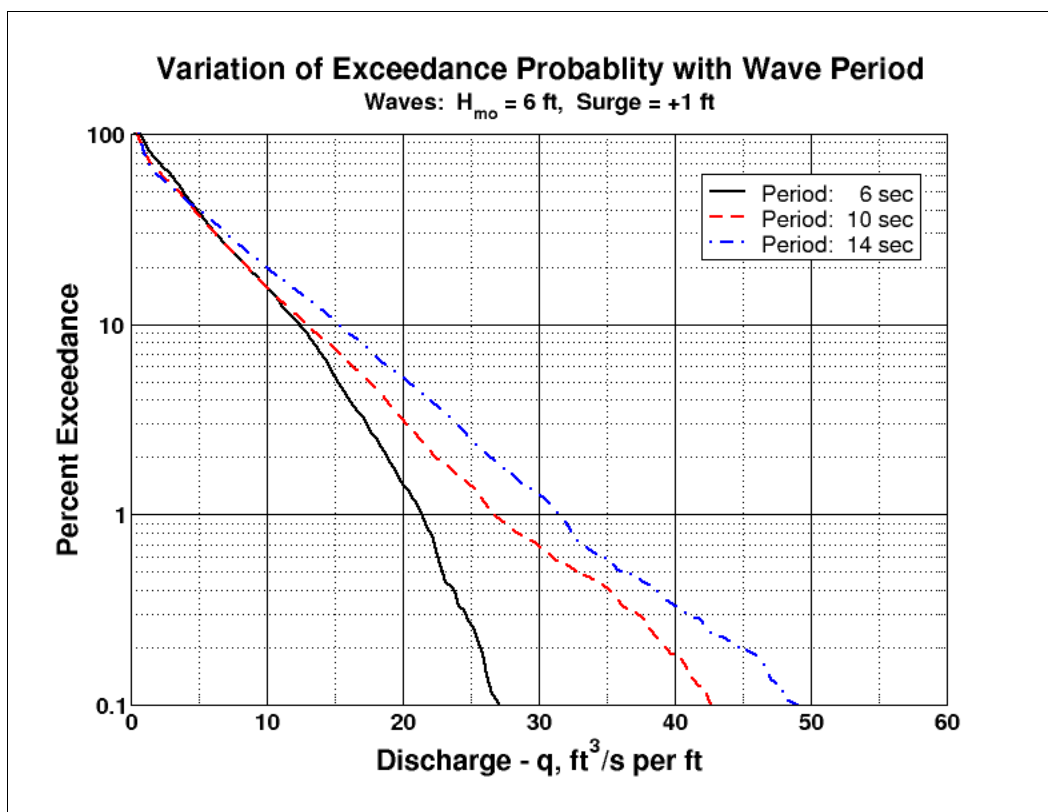


Figure 45. Exceedance probability variation with wave period (+1-ft surge).

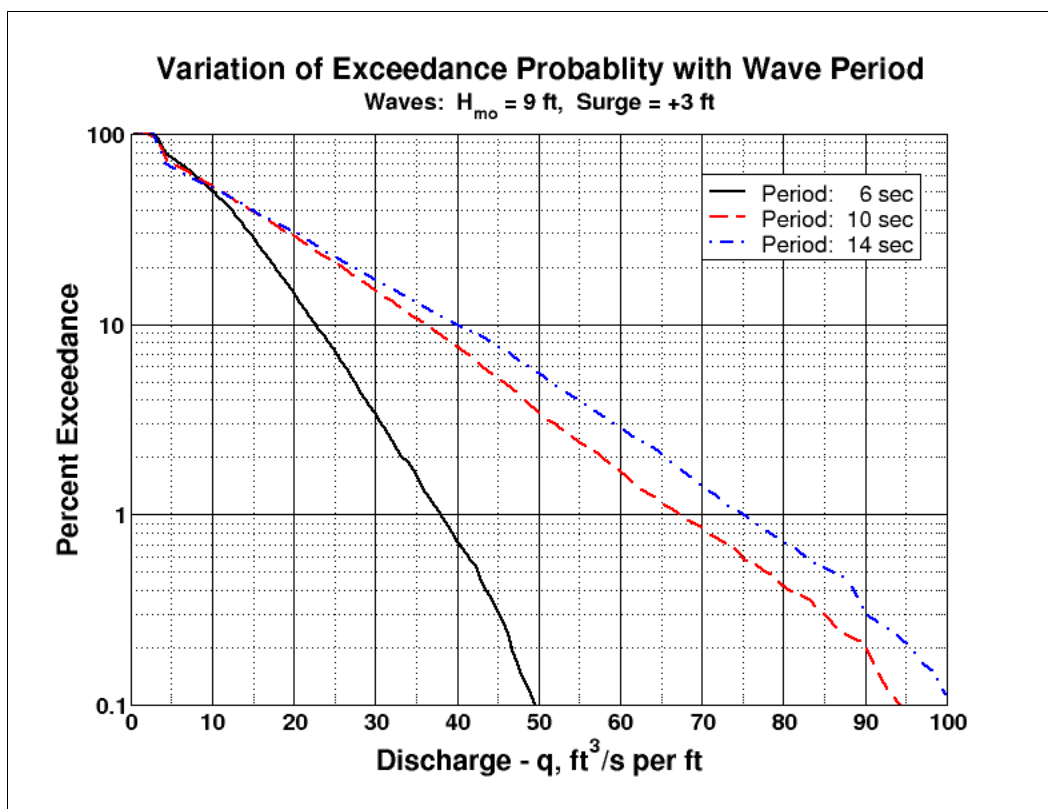


Figure 46. Exceedance probability variation with wave period (+3-ft surge).

Greater variation in exceedance probability is seen for the higher surge elevation and longer wave period shown on Figure 44. Most waves pass over the levee with less breaking, and the variation is particularly pronounced for the extreme values of discharge beyond the 20-percent occurrence level. This indicates that wave height is an important parameter related to the shape of the distribution extreme tail.

Figures 45 and 46 show the variation in percent exceedance probability as a function of wave period for conditions having the same surge level and wave height. At the lower surge level (Figure 45) there appears to be little difference between the curves for periods of 10 and 14 sec. However, the shorter period 6-sec wave had less extreme overtopping values. A similar trend is seen in Figure 46 with a higher wave height and higher surge level. The difference might be related to the wave steepness and wave transformation on the flood-side levee slope, but this hypothesis is unproven.

In summary, the surge elevation above the levee crest, as manifested by the steady overflow discharge, is the most important hydrodynamic parameter, and it most closely controls the scale of the exceedance probability distribution. Wave height appears to influence the shape of the distribution extreme tail, whereas the wave period seems to have the least influence except for short waves.

The next steps were to fit an appropriate mathematical probability distribution to the measured distribution, and then relate the distribution fitting parameters to the steady flow discharge and wave characteristics. The following sections describe this development.

Weibull probability distribution

After testing several candidate probability distributions, the most appropriate probability distribution was found to be the Weibull cumulative probability distribution given by the equation

$$P(q < q_{\text{specified}}) = 1 - \exp \left[- \left(\frac{q_{\text{specified}}}{c} \right)^b \right] \quad (44)$$

where c is the scale factor and b is the shape factor of the distribution. The scale factor c has units of discharge per unit length, whereas the shape

factor b is dimensionless. The corresponding distribution of percent exceedance is given by

$$P\%(q > q_{\text{specified}}) = 100 \cdot \exp \left[- \left(\frac{q_{\text{specified}}}{c} \right)^b \right] \quad (45)$$

Figure 47 shows the best fit of the Weibull cumulative probability distribution and the percent exceedance distribution to the measured instantaneous overtopping distribution from one of the experiments. The RMS error for this fit was 0.0095.

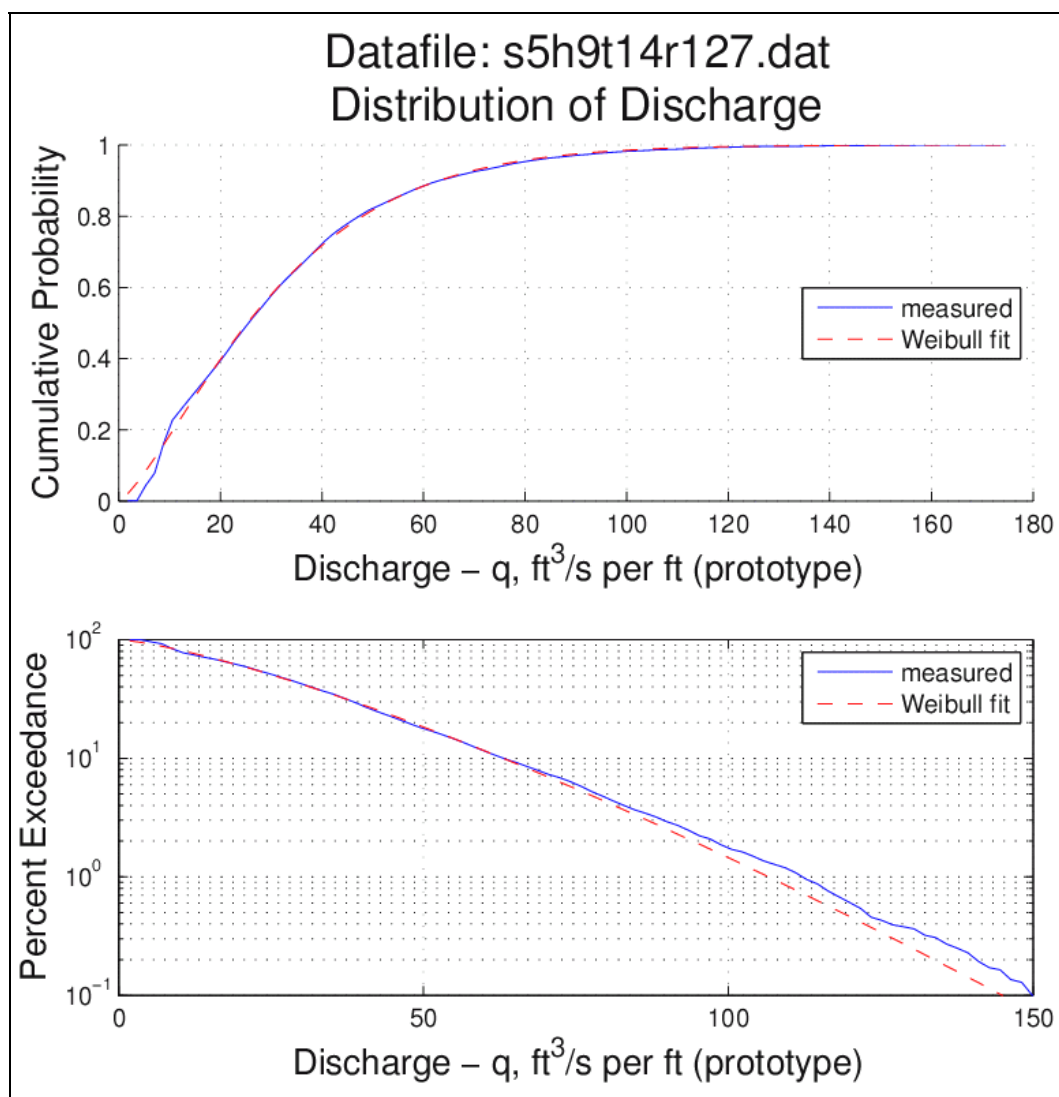


Figure 47. Example best fit of Weibull distribution to measured data.

A little better understanding of the Weibull distribution is obtained by taking the natural logarithm of both sides of Equation 45, i.e.,

$$\ln P = \ln (100) - \left(\frac{q_{\text{specified}}}{c} \right)^b \quad (46)$$

or

$$\ln P = \ln (100) - a \left(q_{\text{specified}} \right)^b \quad (47)$$

where $a = (1/c)^b$. Equation 47 indicates the Weibull probability of exceedance curve (lower plot in Figure 47) has the shape of a power curve with intercept $q = 0$ at $\ln 100$ when the distributions are plotted with semilog percent exceedance axis. Note that values of shape factor $b = 1.0$ would be straight lines with slopes equal to a on semilog plots.

Figure 48 shows a relatively good fit of the Weibull distribution to data with an RMS error of 0.0149. The fit is judged to be good through the 1-percent exceedance level. A somewhat poorer fit of the extreme tail is shown in Figure 49 with an RMS error of 0.0137. Even though the RMS error is similar to the fit found for Figure 48, the best-fit fails to describe adequately the extreme tail of the distribution at exceedance levels less than about 5 percent. Nevertheless, the Weibull distribution did a fairly good job of representing the distribution of instantaneous overtopping due to combined waves and surge. Because all the data points are equally weighted, variations at the extreme tail do not have much influence on the best fit. Best-fit results for all the experiments are shown along with plots of the measured distributions in the appendix. Table 7 summarizes the hydrodynamic surge and wave parameters along with the obtained best-fit scale factors and shape factors for the Weibull probability distribution.

Prediction of combined wave and surge overtopping probability

A predictive capability for estimating the probability distribution of instantaneous overtopping discharge resulting from combined wave overtopping and surge overflow was developed in this study. This required relating the best-fit values of parameters b and c in Equation 44 to parameters of the overtopping surge and incident waves. The process was subjective and several different approaches were tried before arriving at a

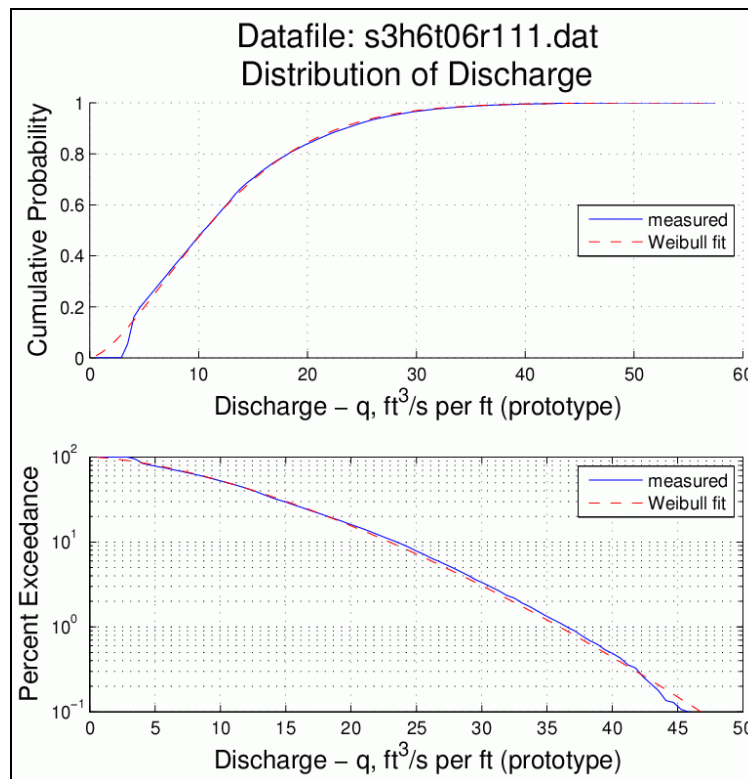


Figure 48. A good fit of Weibull distribution to measured data.

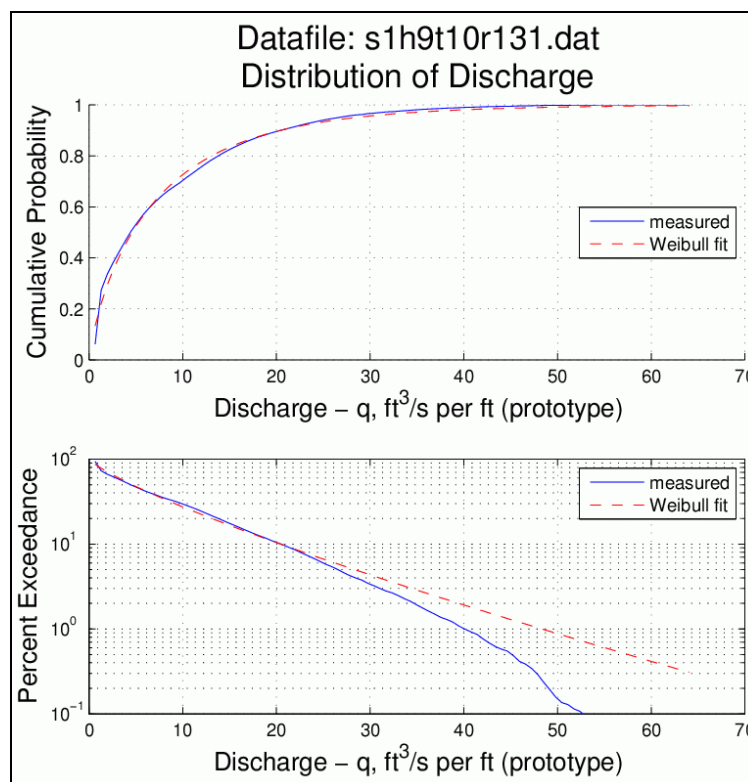


Figure 49. A mediocre fit of Weibull distribution to measured data distribution tail.

Table 7. Parameters from best fit of Weibull probability distribution.

Exp. No.	Hydrodynamic Parameters (Prototype)			Weibull Probability Parameters		
	H_{m0} (ft)	T_p (sec)	q_s (ft ² /sec)	c	b	RMS Error
Surge Level = +1 ft above Levee Crown						
R128	2.69	6.07	2.86	4.371	1.165	0.0154
R129	5.47	5.94	3.32	5.505	1.101	0.0138
R130	8.33	5.94	3.09	6.088	1.079	0.0091
R104	3.29	10.51	2.79	3.459	1.245	0.0202
R105	6.20	10.51	2.60	5.131	0.921	0.0118
R131	9.27	10.51	2.59	7.250	0.805	0.0137
R107	2.58	13.66	2.66	3.873	1.039	0.0205
R108	5.52	13.66	2.78	5.495	0.829	0.0169
R109	8.15	13.66	2.81	7.064	0.837	0.0162
Surge Level = +3 ft above Levee Crown						
R110	2.53	5.69	12.43	14.332	2.236	0.0068
R111	4.80	5.94	13.06	13.328	1.541	0.0149
R112	7.89	5.94	12.71	12.891	1.489	0.0159
R113	2.88	10.12	12.11	13.416	1.934	0.0097
R132	6.27	10.12	17.23	19.342	1.324	0.0125
R115	8.74	10.51	13.44	16.080	1.056	0.0192
R116	2.46	14.37	12.62	15.223	1.904	0.0087
R117	5.36	11.38	13.45	16.682	1.128	0.0197
R118	7.92	14.37	13.32	16.391	0.963	0.0210
Surge Level = +5 ft above Levee Crown						
R119	2.10	6.07	26.41	30.312	4.179	0.0079
R120	3.84	6.07	27.18	31.860	2.661	0.0070
R121	7.55	6.07	27.41	32.374	1.652	0.0075
R122	2.83	10.12	28.30	30.965	3.373	0.0070
R123	5.86	10.12	27.23	33.215	1.856	0.0050
R124	8.99	10.12	27.85	32.954	1.364	0.0124
R125	2.43	14.37	26.01	30.817	3.070	0.0099
R126	4.92	14.37	26.64	33.311	1.759	0.0076
R127	7.59	14.37	27.31	33.428	1.318	0.0095

useful formulation. It must be stressed the resulting empirical parameterizations were not based on physical arguments, but instead they were formulated through trial and error.

Scale factor, c

The scale factor c has units of discharge per length of levee. A visual inspection of the best-fit values obtained for the scale factor immediately revealed a strong correspondence with the magnitude of the average combined wave and surge overtopping. The mean and standard deviation of the Weibull cumulative distribution are given in terms of the b and c parameters as (e.g., Goda 2000)

$$\mu = q_{ws} = c \cdot \Gamma\left(1 + \frac{1}{b}\right) \quad (48)$$

and

$$\sigma = c \cdot \left[\Gamma\left(1 + \frac{2}{b}\right) - \Gamma^2\left(1 + \frac{1}{b}\right) \right]^{1/b} \quad (49)$$

respectively, where Γ is the gamma function. Equation 48 was used to estimate q_{ws} using the best-fit values of the Weibull b and c parameters from Table 7 for all experiments. Comparison with values q_{ws} determined directly from the discharge time series showed excellent agreement as illustrated on Figure 50.

Because Equation 42 provides a reasonable estimate of q_{ws} , Equation 48 can be rearranged to give an expression for the scale factor c , i.e.,

$$c = \frac{q_{ws}}{\Gamma\left(1 + \frac{1}{b}\right)} \quad (50)$$

Therefore, if the shape factor b can be expressed in terms of the hydrodynamic parameters; the cumulative probability distribution of instantaneous wave/surge overtopping discharge can be estimated as a function of q_{ws} . The gamma function can be accurately calculated over the range of shape factor b found for these experiments ($0.5 < b < 4$) by the best-fit of a cubic equation given by

$$\Gamma(x) = 1.3 - 0.368 \cdot x - 0.072 \cdot x^2 + 0.09 \cdot x^3 \quad \text{valid for: } (1.25 < x < 3) \quad (51)$$

This approximation had a residual sum of the squares of error equal to 0.00348 over this range.

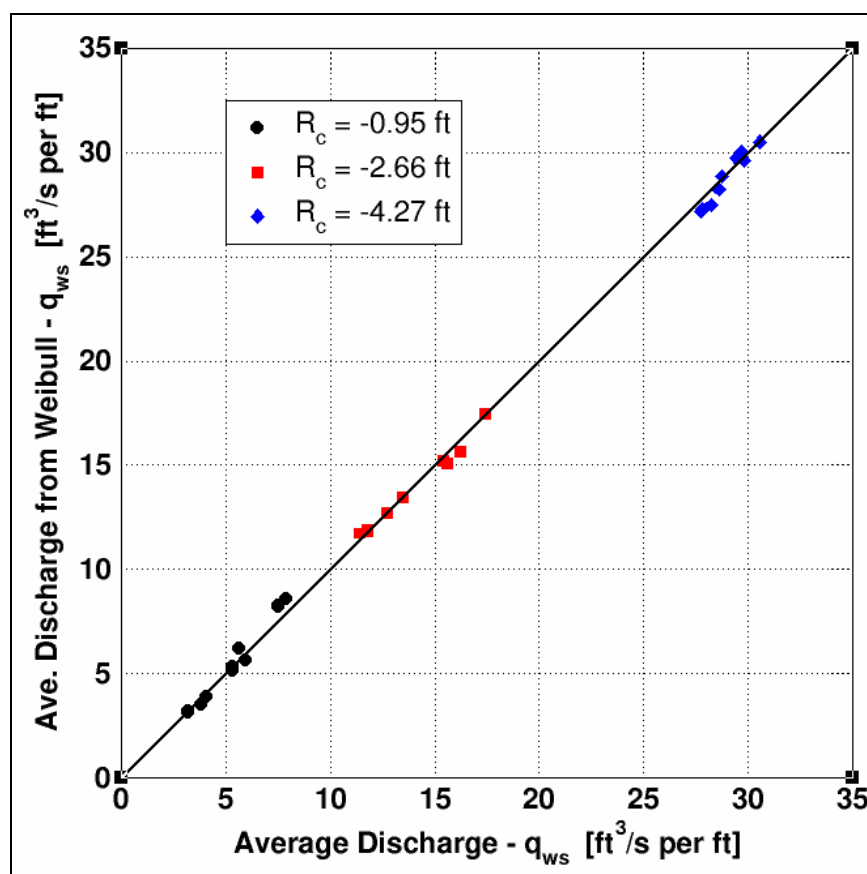


Figure 50. Measured average discharge versus discharge from Weibull distribution.

Shape factor, b

The dimensionless shape factor b exerts control over the extreme tail of the distribution, and the tail is sensitive to small differences in the shape factor. Through inspection, and after several attempts using non-dimensional combinations of the wave height, wave period, and steady surge discharge, the best empirical expression found for the shape factor was the relationship

$$b = 8.10 \left(\frac{q_s}{g H_{m0} T_p} \right)^{0.343} \quad (52)$$

where g is acceleration of gravity. Figure 51 shows the best-fit curve for the shape factor given by Equation 52 along with the plotted values of b obtained from the measured data (Table 7). The correlation coefficient for the best fit of Equation 52 was 0.922.

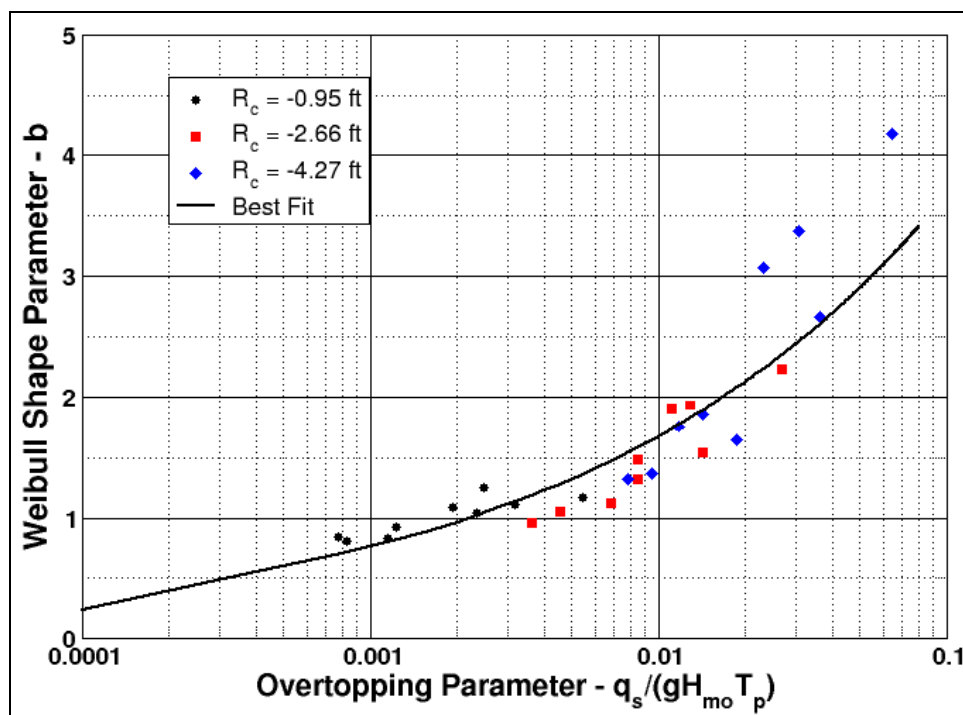


Figure 51. Correlation of shape factor b with wave and surge parameters.

The three data points in Figure 51 with values of b greater than 3 deviated significantly from the data trend. These points came from experiments with the surge level at +5 ft and nominal wave heights around 3 ft. A possible explanation for the observed deviation might be the effect of wave deformation by the strong steady overtopping flow as waves reach the levee. The nonlinear interaction between the waves and the coincident current at the levee crest is more pronounced at the higher surge level, and smaller waves would be more affected than larger waves. The resulting smaller wave heights would reduce the extreme overtopping discharge, and this gives higher values for the shape factor b .

As mentioned, little theoretical reasoning went into development of the empirical relationship given by Equation 52. However, in retrospect a little insight can be gained by examining the characteristics of the dimensionless parameter used in the correlation. Splitting the dimensionless parameter into two dimensionless numbers and multiplying the numerator and denominator by the specific weight of water yields

$$\frac{q_s}{g H_{m0} T_p} = \left(\frac{H_{m0}}{g T_p^2} \right) \cdot \left[\frac{(\rho g q_s) \cdot T_p}{\rho g H_{m0}^2} \right] \quad (53)$$

The first dimensionless term on the right-hand side of Equation 53 is the spectral wave steepness parameter. The $(\rho g q_s)$ portion of the numerator of the term in square brackets has units of surge overflow power per unit surface area, and multiplying by the wave period yields average flow work (or energy) per surface unit area for the mean wave. The denominator in the square-bracketed term is recognized as being proportional to the average wave energy per unit surface area. Thus, the dimensionless number in Equation 52 is the product spectral wave steepness and the ratio of steady overflow energy density to average wave energy density. Higher values of this dimensionless number give higher values of the shape parameter b , which in turn decreases the extreme tail of the exceedance probability distribution. Therefore, as the overtopping surge elevation increases (or alternately wave height and period decrease), the ratio of the extreme peak instantaneous discharge to the average surge-only overtopping will decrease.

Equations 50 and 52 were used to predict scale factors c and shape factors b , respectively, using the measured overtopping steady discharge and incident wave parameters given in Table 7. These parameters were then substituted into the percent exceedance probability distribution given by Equation 45, and the predicted distributions were compared to the measured distributions for all tests. Figure 52 shows the comparison for the mildest wave condition at the three different surge levels. The measured distributions are given by non-solid lines, and the predictions are shown as solid lines. The plot ordinate is semilog, and that accentuates the extreme tail of the distributions. Generally, the comparison between data and prediction appears to be useful.

Figures 53-60 show the rest of the comparisons between predicted and actual distributions. Some predictions are not as good as those shown in Figure 52, and some miss the 10-percent exceedance region by a substantial amount. Nevertheless, the estimation procedure developed during this study is the first method available for estimating the distribution of instantaneous discharge due to combined wave overtopping and storm surge overflow.

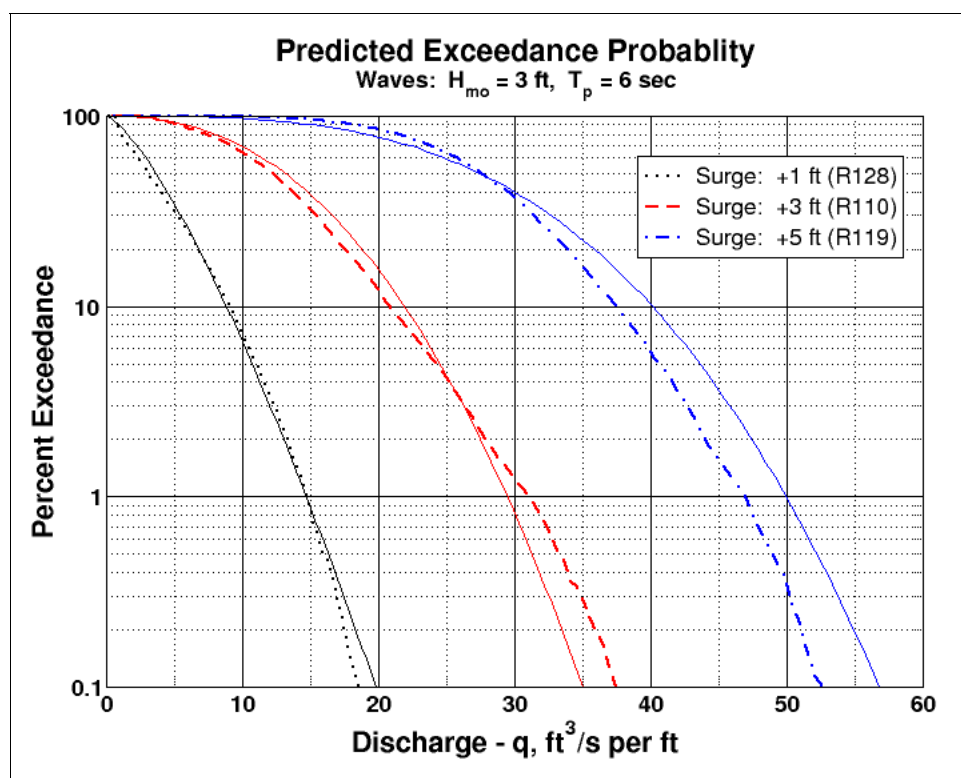


Figure 52. Predicted versus actual exceedance probability ($H_{m0} = 3$ ft, $T_p = 6$ sec).

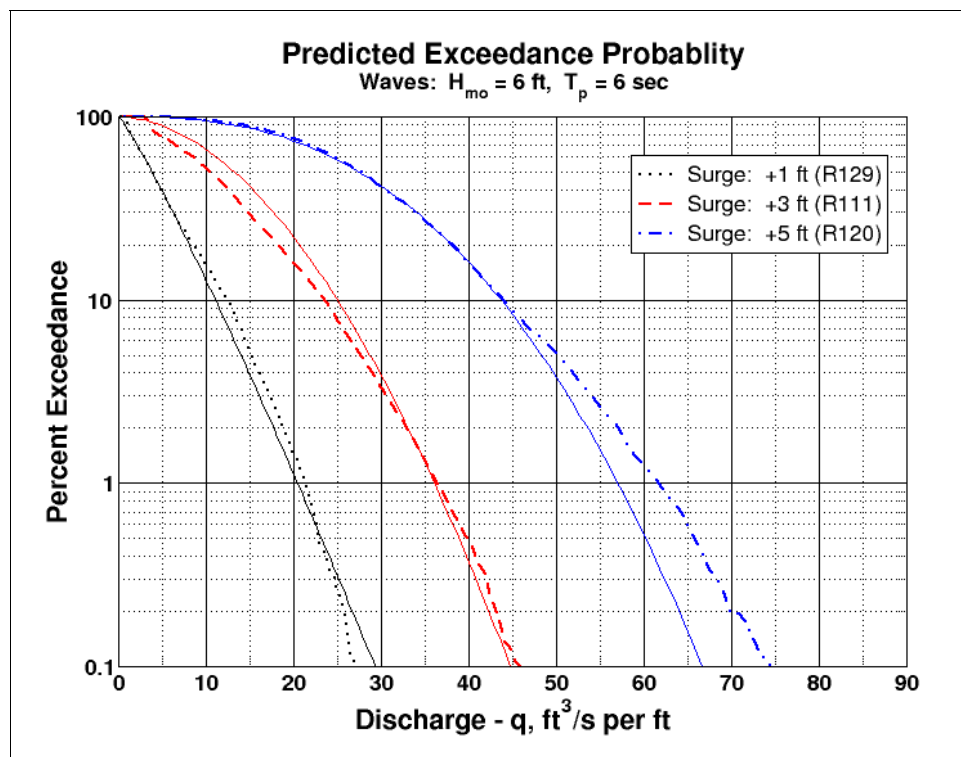


Figure 53. Predicted versus actual exceedance probability ($H_{m0} = 6$ ft, $T_p = 6$ sec).

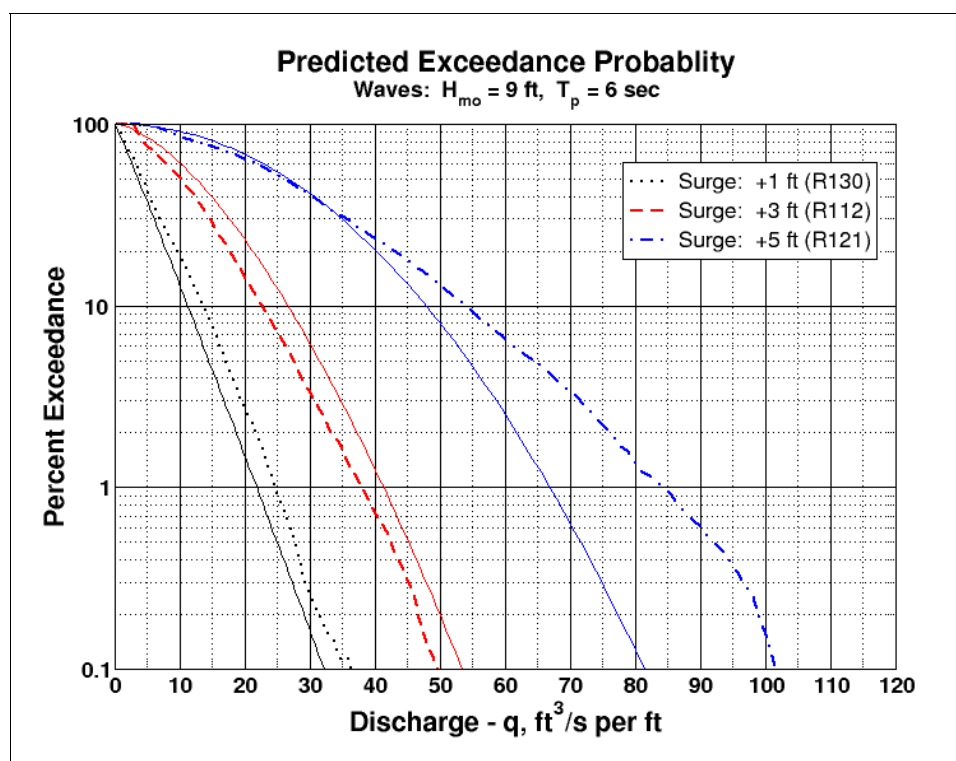


Figure 54. Predicted versus actual exceedance probability ($H_{m0} = 9$ ft, $T_p = 6$ sec).

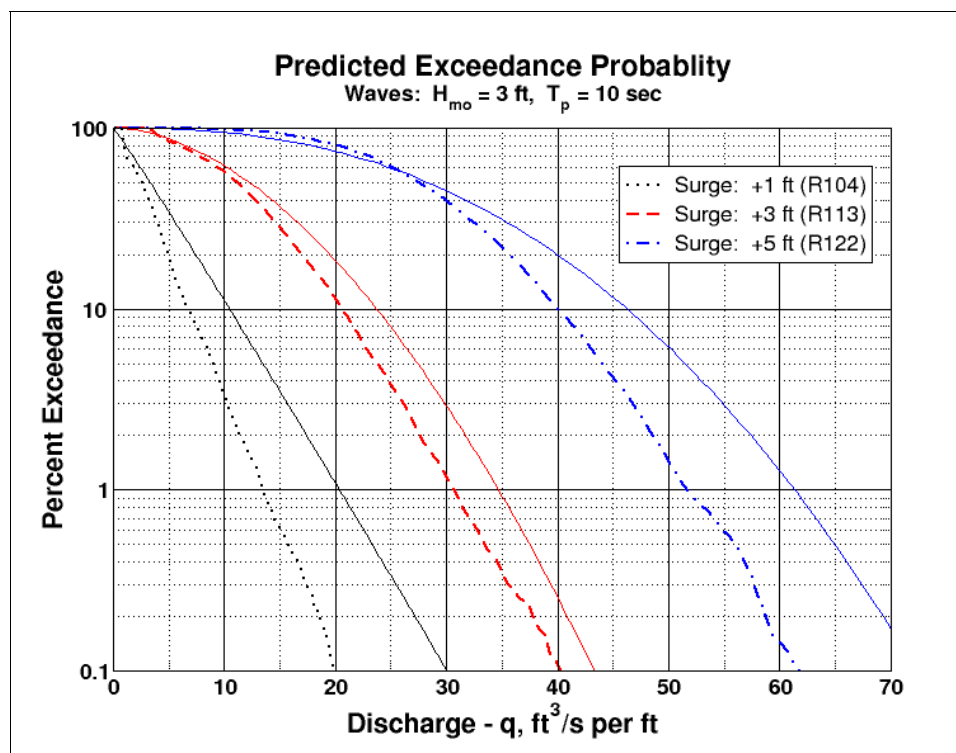


Figure 55. Predicted versus actual exceedance probability ($H_{m0} = 3$ ft, $T_p = 10$ sec).

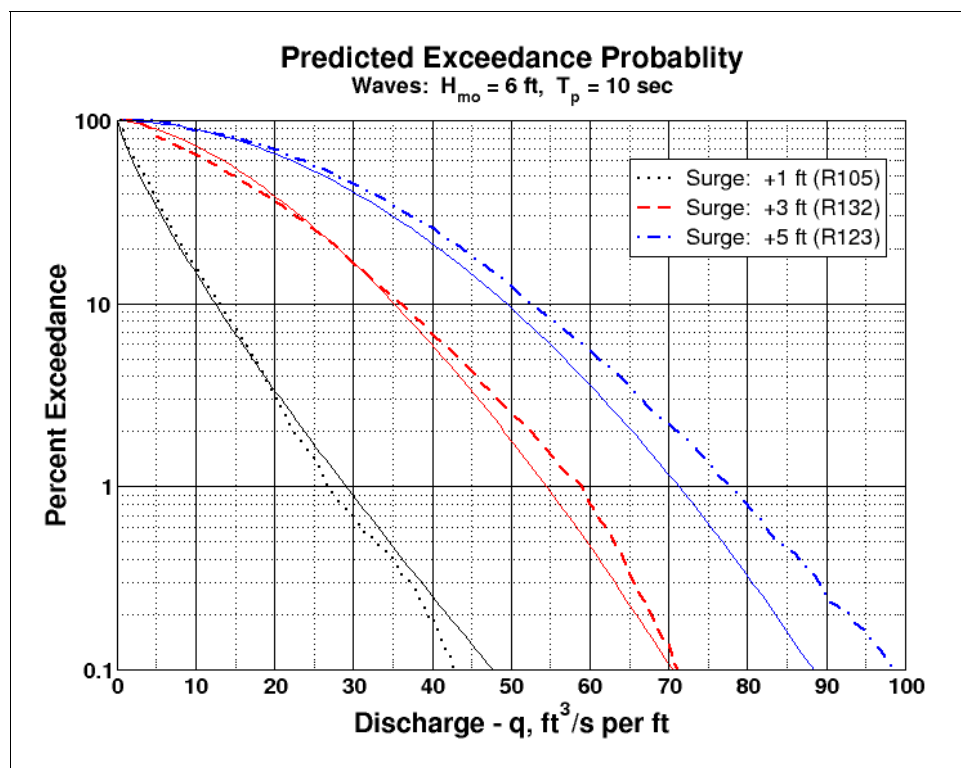


Figure 56. Predicted versus actual exceedance probability ($H_{m0} = 6$ ft, $T_p = 10$ sec).

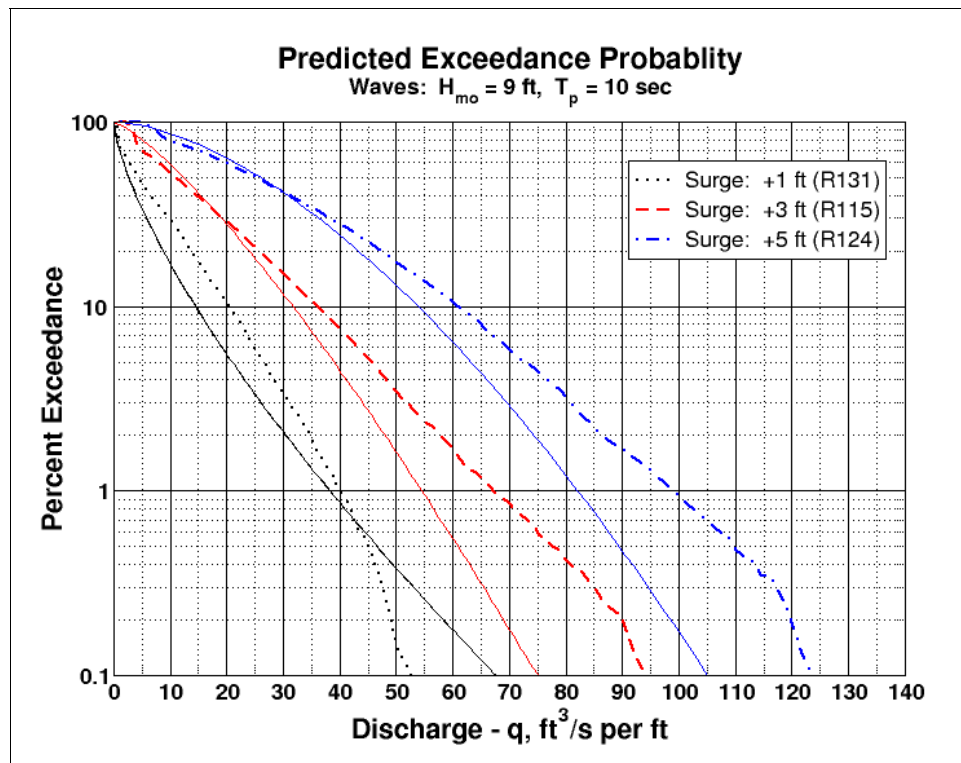


Figure 57. Predicted versus actual exceedance probability ($H_{m0} = 9$ ft, $T_p = 10$ sec).

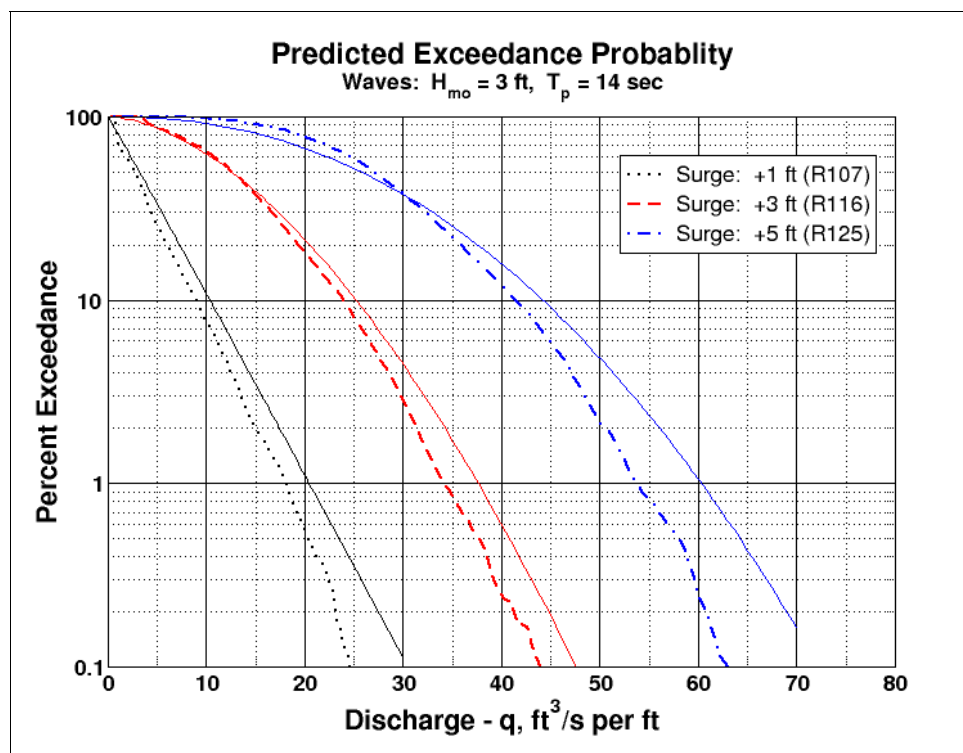


Figure 58. Predicted versus actual exceedance probability ($H_{m0} = 3$ ft, $T_p = 14$ sec).

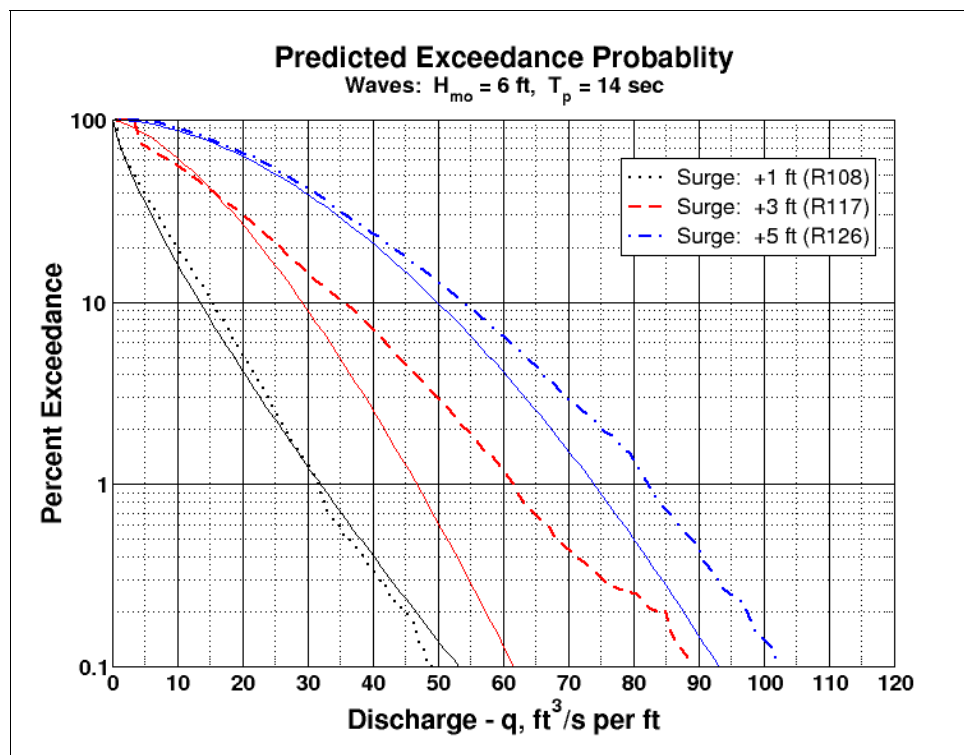


Figure 59. Predicted versus actual exceedance probability ($H_{m0} = 6$ ft, $T_p = 14$ sec).

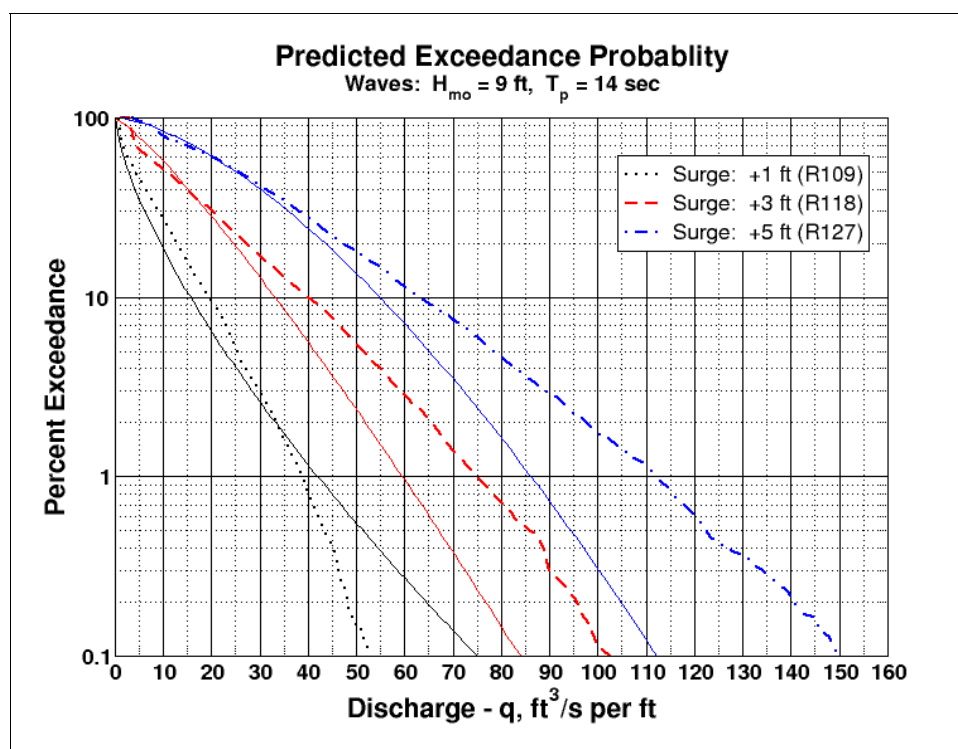


Figure 60. Predicted versus actual exceedance probability ($H_{m0} = 9$ ft, $T_p = 14$ sec).

Summary of combined wave and surge overtopping hydrodynamics

A total of 27 experiments were conducted covering a range of three storm surge elevations exceeding the levee crest and nine irregular wave conditions. Pressure measurements of instantaneous water depth were obtained at two locations on the levee crest and at five equally spaced positions on the levee protected-side slope. Flow-parallel velocities were measured near the landward edge of the levee crown at the same location as a pressure gauge. All data were collected at a 50-Hz rate.

The synoptic time series of water depth and flow velocity were multiplied together to create time series of instantaneous discharge per unit length over the levee. This calculation assumed the flow velocity was uniform over the water column during the unsteady overtopping flow. For experiments with large waves and/or lower surge levels, the water level dropped below the laser beams of the LDV during wave troughs, and velocity data were not valid for these time periods. A predictive empirical equation for the average overtopping discharge was developed (Equation 42), and the relationship exhibited little scatter.

The cumulative probability distributions and the related percent exceedance probability distributions were calculated from the instantaneous discharge time series. These distributions were well represented by the Weibull probability distribution (Equations 44 and 45), and subsequent best fits of the mathematical distribution produced a table of distribution parameters associated with each experiment. The distribution scale factor c (Equation 50) was given as a function of q_{ws} and the shape factor b . An empirical expression for b (Equation 52) was developed in terms of the incident wave parameters and the steady surge discharge. Substitution of estimated factors c and b into the Weibull cumulative distribution (Equation 44) or percent exceedance distribution (Equation 45) yields an estimate of the instantaneous overtopping distribution for the case of combined wave and surge overtopping of a levee.

This development was strictly for waves shoaling on a 1:4.25 levee flood-side slope, and different results should be expected for milder or steeper flood-side slopes because seaward slope affects the waves that go over the levee crest. Future development should include measurements for different levee flood-side slopes so this slope parameter can be incorporated into the empirical formulations presented in this report.

8 Summary and Conclusions

Summary

This study was commissioned by the New Orleans District of the Corps of Engineers. The District was interested in investigating the use of articulated concrete mats (ACMs) to armor the backside (protected side) slopes along selected reaches of the Mississippi River Gulf Outlet (MRGO). With the levees at present design crest elevations, portions of the MRGO levee will be overtopped by both waves and storm surge associated with hurricanes comparable to Hurricane Katrina. Whereas it might be possible to transfer full-scale stability results from propriety ACM tests to the Corps' design as a first approximation, this would cover only the case of steady surge overflow, and not the more problematic situation where overtopping waves create additional stress on the levee backside-slope protection. Chapter 2 of this report presents a summary of existing methodologies for estimating overtopping flow velocities on the protected-side slope for steady surge overflow and for wave-only overtopping.

Physical model

A 1-to-25 scale physical model of a typical cross section of MRGO was constructed and installed in a 3-ft-wide flume at the U.S. Army Engineer Research and Development Center's Coastal and Hydraulics Laboratory in Vicksburg, MS. The purpose of the physical model was to obtain hydrodynamic measurements of unsteady flow conditions caused by combined wave overtopping and surge overflow of the levee, and to examine the feasibility of using ACMs for levee protection during this type of overtopping event. Specifically, the New Orleans District was interested in determining whether the same ACMs used by the Corps' Mat Sinking Unit to protect riverbanks could be used to protect the MRGO levee against surge and wave overtopping.

The physical model featured fixed-bed bathymetry seaward of the levee, and the levee cross section was fabricated out of high-density foam. Because of scaling effects, no attempt was made to construct the levee using erodible soil. Thus, aspects related to erodibility of the underlying soil were not simulated in these tests. In addition to the wave generation capacity, a recirculation system was installed to simulate steady surge

overflow of the levee combined with wave propagation and overtopping. Thus, the physical model was capable of simulating steady storm surge overflow, wave overtopping when the surge level was lower than the levee crest elevation, and wave overtopping when the surge elevation exceeded the levee crest elevation. After the model was fully calibrated and operational, tests were conducted following established operating procedures with appropriate measurements and documentation.

Stability of articulated concrete mats

Stability of ACMs was examined in nine tests with combined steady surge overflow and wave overtopping. The physical model most closely replicated the prototype case where the mats would be placed on top of a gravel filter layer. Even during the mildest condition with a 0.75-ft steady surge above the levee crest and a 3-ft, 6-sec (nominal) irregular wave condition, the mats experienced a slight uplift near the toe of the protected-side slope where the levee transitioned between the 1:3 levee slope and 1:25 berm slope. Mat uplift continued in a similar manner when the wave period was increased to 10 and 14 sec.

Increasing the wave height to a nominal 6 ft produced mat roll-up instability at the toe of the flood-side levee 1:4.25 slope. Uplift was also observed for that portion of the mat on the flood-side slope near the levee crest. The entire mat was swept off the levee when the wave period was increased for this wave height.

Tests with a steady surge level 3 ft above the levee crest indicated mat instability with just steady overflow. When even relatively mild waves were added, mat uplift instability became pronounced. This is a clear indication of the need to bury or anchor the leading and trailing edges of the mats. Mat stability could be increased with additional anchoring or increasing mat thickness.

Hydrodynamics of combined wave and surge overtopping

A total of 27 experiments were conducted covering a range of three storm surge elevations exceeding the levee crest and nine irregular wave conditions. Pressure measurements of instantaneous water depth were obtained at two locations on the levee crest and at five equally spaced positions on the levee protected-side slope. Flow-parallel velocities were measured near

the landward edge of the levee crown at the same location as a pressure gauge. All data were collected at a 50-Hz rate.

Synoptic time series of water depth and flow velocity were multiplied together to create time series of instantaneous discharge over the levee. This calculation assumed the flow velocity was uniform over the water column during the unsteady overtopping flow. Maximum instantaneous overtopping discharges were many times the steady surge discharge level, and this indicates the severity of erosional risk that accompanies combined wave and surge overtopping. An empirical equation (Equation 42) was developed for the average overtopping discharge for combined wave and surge overtopping.

The cumulative probability distributions and the related percent exceedance probability distributions were calculated from the instantaneous discharge time series. These distributions were well represented by the Weibull probability distribution (Equations 44 and 45). Subsequent analysis provided an estimation technique for the instantaneous overtopping distribution for the case of combined wave and surge overtopping of a levee as a function of the steady surge overflow discharge per unit length, incident significant wave height, and spectral peak wave period.

Conclusions

Stability of articulated concrete mats

If the failure criterion for articulated concrete mats is no movement or uplift of the blocks, it can be concluded that the particular articulated concrete mats simulated in the physical model will not be sufficient for armoring earthen levees subjected to combined storm surge overflow and wave overtopping. Mats placed directly on the levee soil without filter cloth or a filter layer might resist higher levels of overtopping flow for a while because it will take some time for water to seep under the blocks. Once erosion begins, however, the high-velocity flow will cause rapid loss of soil. Stability testing of ACMs placed directly on soil cannot be accomplished reliably at reduced scale; tests must be conducted at full scale. Unfortunately, no laboratory facilities presently exist that can conduct these tests using combined wave and surge overtopping.

The stability testing illustrated the important need to anchor the mats at both ends. This could be done by burial of the mats in a trench or with

some type of anchoring system. The burial option could include large stones placed atop the mats prior to burial.

If these particular mats have an economic advantage over other options, the mat stability could be improved by installing with intermittent anchoring. This is particularly important lower on the protected-side slope where unsteady flow velocities reach maximum values, and near the transition between the levee slope and berm where water pressure beneath the mats is higher. Another option would be to achieve stability by placing a double layer of mats, effectively doubling the armoring self-weight, along with doubling the cost. Even in this deployment, the two mat layers would have to be lashed together. Otherwise, the top layer would experience uplift, and many of the blocks would be broken by impact with the lower mat.

Finally, it is recognized that, even with substantial movement of the mats, a reasonable degree of levee protection is provided by the tested ACM system. A severe hurricane event might produce damaging surge and wave overtopping, and there may be substantial erosion of soil underlying the mats, but the erosion will be less than would be expected on an unprotected earthen levee. Therefore, even with extensive damage, breaching of a levee over the time span of the storm is less likely because the mats hinder formation of headcuts and retard erosion of the levee soil. Of course, it would be necessary to undertake expensive repairs after the storm, but for rare events this might be a tolerable compromise to the costs of armoring with a totally stable solution that will be able to withstand frequent events with only minimal post-storm repair.

Hydrodynamics of combined wave and surge overtopping

The hydrodynamics associated with levee overtopping by storm surge combined with irregular waves have been measured, and the instantaneous overtopping discharge per unit length has been quantified in terms of an average overtopping rate and by the Weibull probability distribution. Analysis based on the measured data produced empirical expressions (Equations 50 and 52) for the distribution scale and shape factors, respectively. This development allows a reasonable estimate of the overtopping probability distribution in terms of the steady surge discharge and incident wave characteristics. The next step is using these overtopping estimates to predict maximum shear stresses experienced on the protected-side slope during this type of levee overtopping condition.

Development of the overtopping discharge estimation technique was strictly for waves shoaling on a 1:4.25 levee flood-side slope, and different results should be expected for milder or steeper flood-side slopes because this affects the waves that go over the levee crest. However, the influence of the flood-side slope should decrease as the surge level above the levee crest increases.

Finally, the research and findings described in this report are applicable at any location in the levee system that could be exposed to surge and wave overtopping, provided the levee cross section does not differ significantly from that of the representative MRGO levee used in this physical model study.

Suggestions for future research

If the particular ACMs tested in this study remain a viable armoring option, several additional tests could be conducted. Using the small-scale facility at ERDC, it would be possible to investigate the benefits of both end and intermittent mat anchoring, and it may even be feasible to determine the uplift forces that would be exerted on the anchors for different combinations of overtopping waves and surge. Also, the two existing model mats could be doubled and lashed together to examine whether this option gains enough stability to meet the no-movement criterion for different wave and surge flow combinations.

One option under consideration for the ACMs was to place the ACMs directly on the groomed levee soil. Examination of stability and potential erosion of underlying soil can be tested reliably only at prototype scale. Present testing capability at full scale includes only steady flow overtopping, but it may be possible to estimate steady flow parameters that produce similar shear stresses as unsteady flow overtopping. A less accurate alternative would be to test at smaller scale with model mats lying on a compacted clay levee. Even with incorrect similitude, the tests could give an indication of the ACMs capability to prevent or delay levee breaching.

The time series of water elevation on the protected-side slope need to be further analyzed in an attempt to extract estimates of shear stress. This feat is complicated because no direct velocity measurements were acquired on the protected-side slope. Additional experiments with velocity and water depth measured at two adjacent locations on the protected-side slope would provide all information necessary to characterize the unsteady

flow shear stresses, and this could be directly related to existing stability results for armoring systems subjected to steady flow overtopping.

Future development of the overtopping discharge distribution predictive technique should include measurements for different levee flood-side slopes so this slope parameter can be incorporated into the empirical formulations presented in this report.

References

- Chen, Y. H., and B. A. Anderson. 1987. *Development of a methodology for estimating embankment damage due to flood overtopping*. Turner-Fairbank Highway Research Center Report No. FHWA/RD-86/126. Washington, DC: Federal Highway Administration.
- Cornett, A. M., and E. Mansard. 1994. Wave stresses on rubble mound armour. In *Proceedings, 24th International Coastal Engineering Conference* Vol. 1, ASCE, 986-1,000.
- de Waal, J. P., and J. W. van der Meer. 1992. Wave run-up and overtopping on coastal structures. In *Proceedings of the 23rd International Coastal Engineering Conference* Vol. 2, ASCE, 1,758-1,771.
- Goda, Y. 2000. *Random seas and design of maritime structures*. 2nd ed. Singapore: World Scientific Publishing Co., Singapore.
- Goda, Y., and Y. Suzuki. 1976. Estimation of incident and reflected waves in random wave experiments. In *Proceedings 15th International Coastal Engineering Conference* Vol. 1, ASCE, 828-845.
- Hartung, F., and H. Scheuerlein. 1970. Design of overflow rockfill dams. In *Proceedings International Commission on Large Dams, Tenth International Congress on Large Dams* Q36, R.35. Montreal, Canada, 587-598.
- Henderson, F. M. 1966. *Open channel flow*. New York, NY: MacMillan Publishing Co., Inc.
- Hudson, R. Y., F. A. Herrmann, R. A. Sager, R. W. Whalin, G. H. Keulegan, C. E. Chatham, and L. Z. Hales. 1979. *Coastal hydraulic models*. Special Report No. 5. Vicksburg, MS: U.S. Army Engineer Waterways Experiment Station.
- Hughes, S. A. 1993. Physical models and laboratory techniques in coastal engineering. In *Advanced series on ocean engineering* 7. Singapore: World Scientific.
- _____. 2003. Physical modeling considerations for coastal structures. In *Advances in coastal structure design*, ed., R. Mohan, ASCE, 97-115.
- _____. 2004. Estimation of wave run-up on smooth, impermeable slopes using the wave momentum flux parameter. *Coastal Engineering* 51(11):1,085-1,104, Elsevier.
- Kamphuis, J. W. 1991. Physical modeling. In *Handbook of coastal and ocean engineering* 2, ed., J. B. Herbich. Houston, TX: Gulf Publishing Company.
- Kindsvater, C. E. 1964. *Discharge characteristics of embankment-shaped weirs*. Water-Supply Paper 1617-A. Washington, DC: U.S. Geological Survey.
- Le Méhauté, B. 1976. Similitude in coastal engineering. *Journal of the Waterways, Harbors and Coastal Engineering Division* 102(WW3):317-335, ASCE.

- Mansard, E., and E. Funke. 1980. The measurement of incident and reflected spectra using a least square method. In *Proceedings, 17th International Coastal Engineering Conference* Vol. 1, World Scientific, 154-172.
- Schüttrumpf, H. 2006. Personal communication via email, 5 April 2006.
- Schüttrumpf, H., and H. Oumeraci. 2005. Layer thicknesses and velocities of wave overtopping flow at seadikes. *Coastal Engineering* 52:473-495, Elsevier.
- Schüttrumpf, H., and M. R. van Gent. 2003. Wave overtopping at seadikes. In *Proceedings, Coastal Structures '03*, ASCE, 431-443.
- Schüttrumpf, H., J. Möller, and H. Oumeraci. 2002. Overtopping flow parameters on the inner slope of seadikes. In *Proceedings, 28th International Coastal Engineering Conference* Vol. 2, World Scientific, 2,116-2,127.
- van der Meer, J. W., P. Bernardini, W. Snijders, and E. Regeling. 2006. The wave overtopping simulator. In *Proceedings, 30th International Conference on Coastal Engineering*.
- van Gent, M. R. 2001. Wave run-up on dikes with shallow foreshores. *Journal of Waterway, Port, Coastal and Ocean Engineering* 127(5):2,203-2,215. ASCE.
- _____. 2002. Wave overtopping events at dikes. In *Proceedings, 28th International Coastal Engineering Conference* Vol.2, World Scientific, 2,203-2,215.
- Warnock, J. E. 1950. Hydraulic similitude. In *Engineering Hydraulics*, ed., H. Rouse, 136-176. New York: John Wiley & Sons.

Appendix A: Data Plots

Time series plots

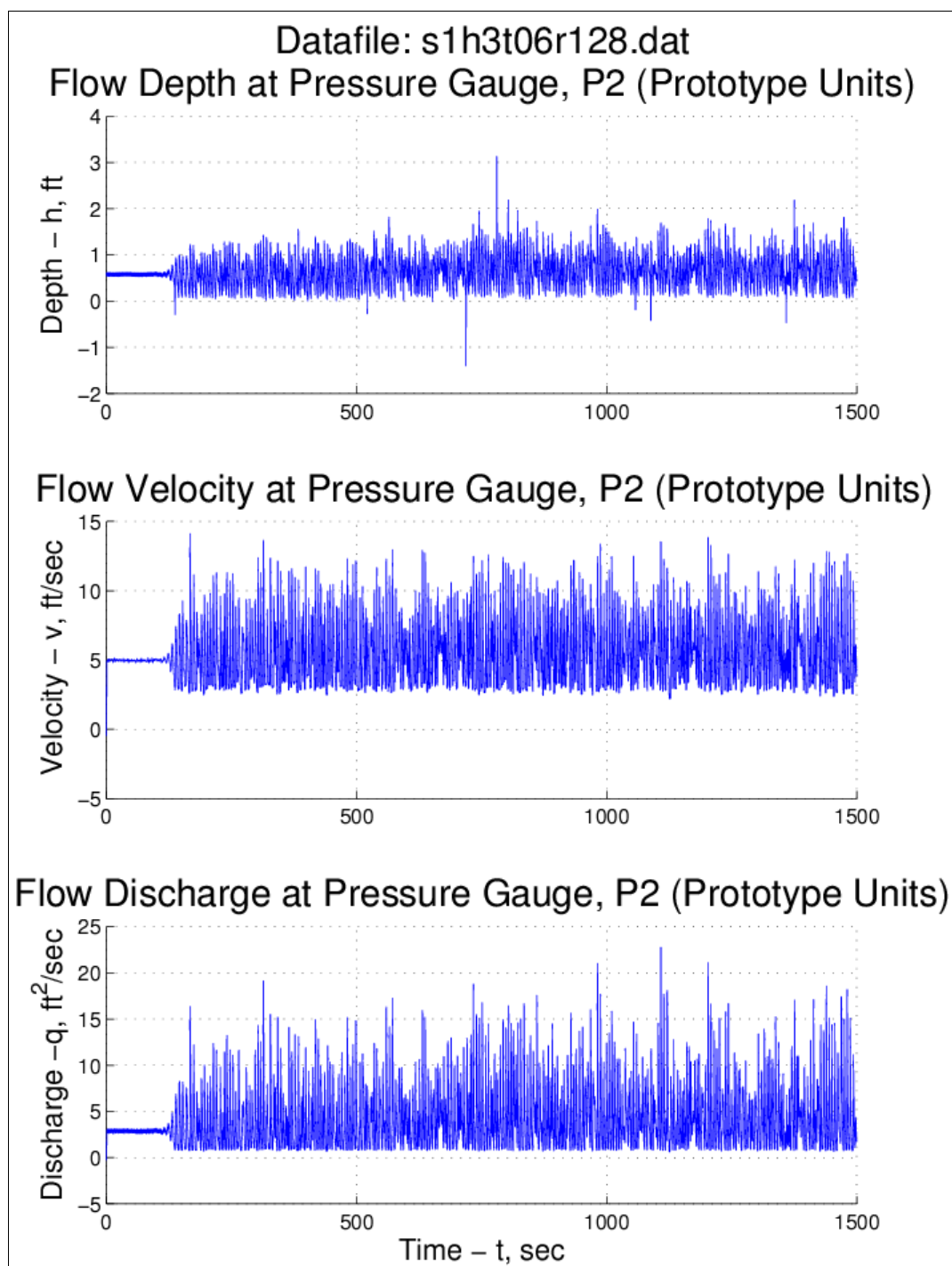


Figure A1. Run 128 time series plots (surge = +1 ft, $H_{m0} = 3$ ft, $T_p = 6$ sec).

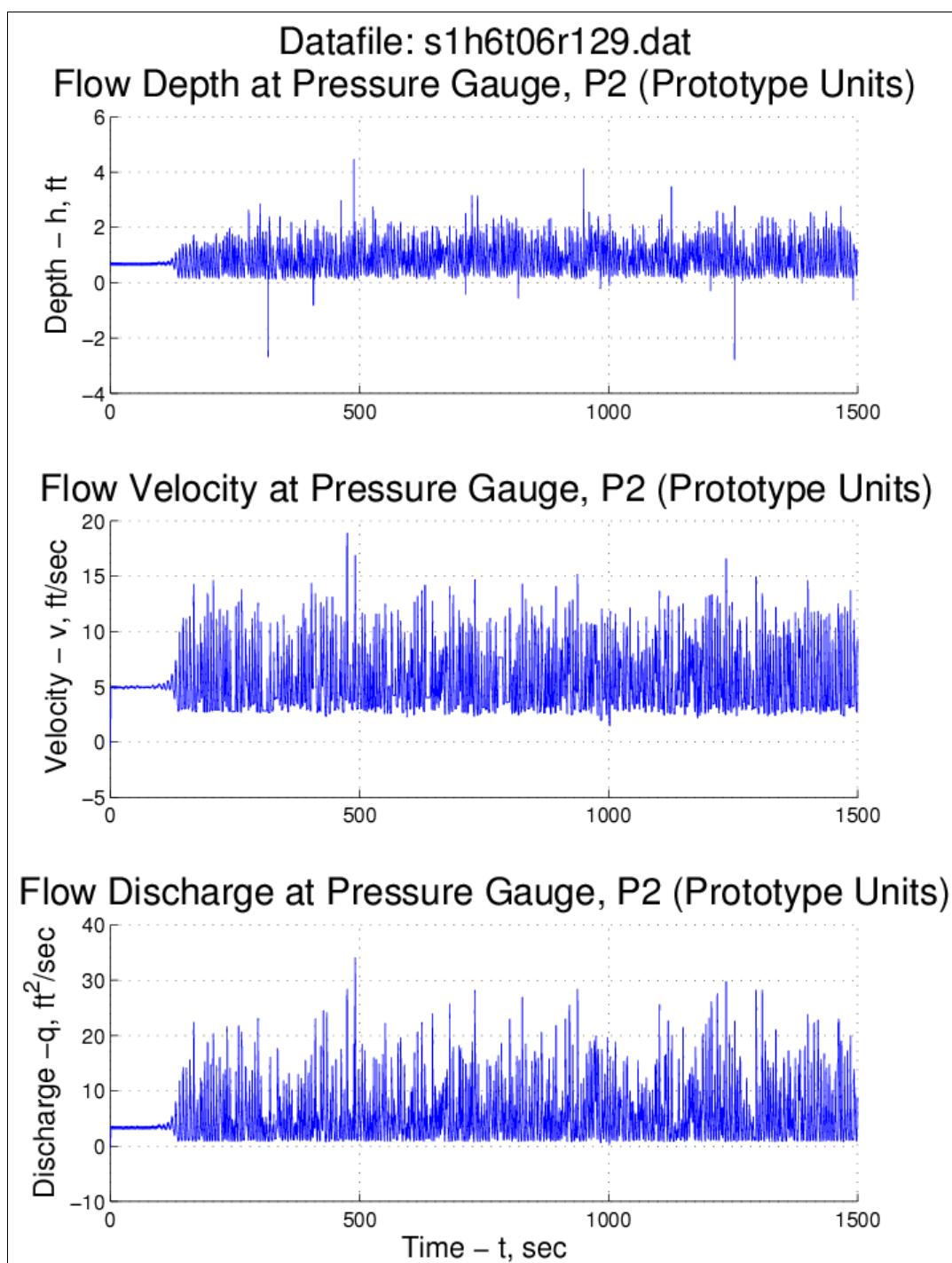


Figure A2. Run 129 time series plots (surge = +1 ft, $H_{m0} = 6$ ft, $T_p = 6$ sec).

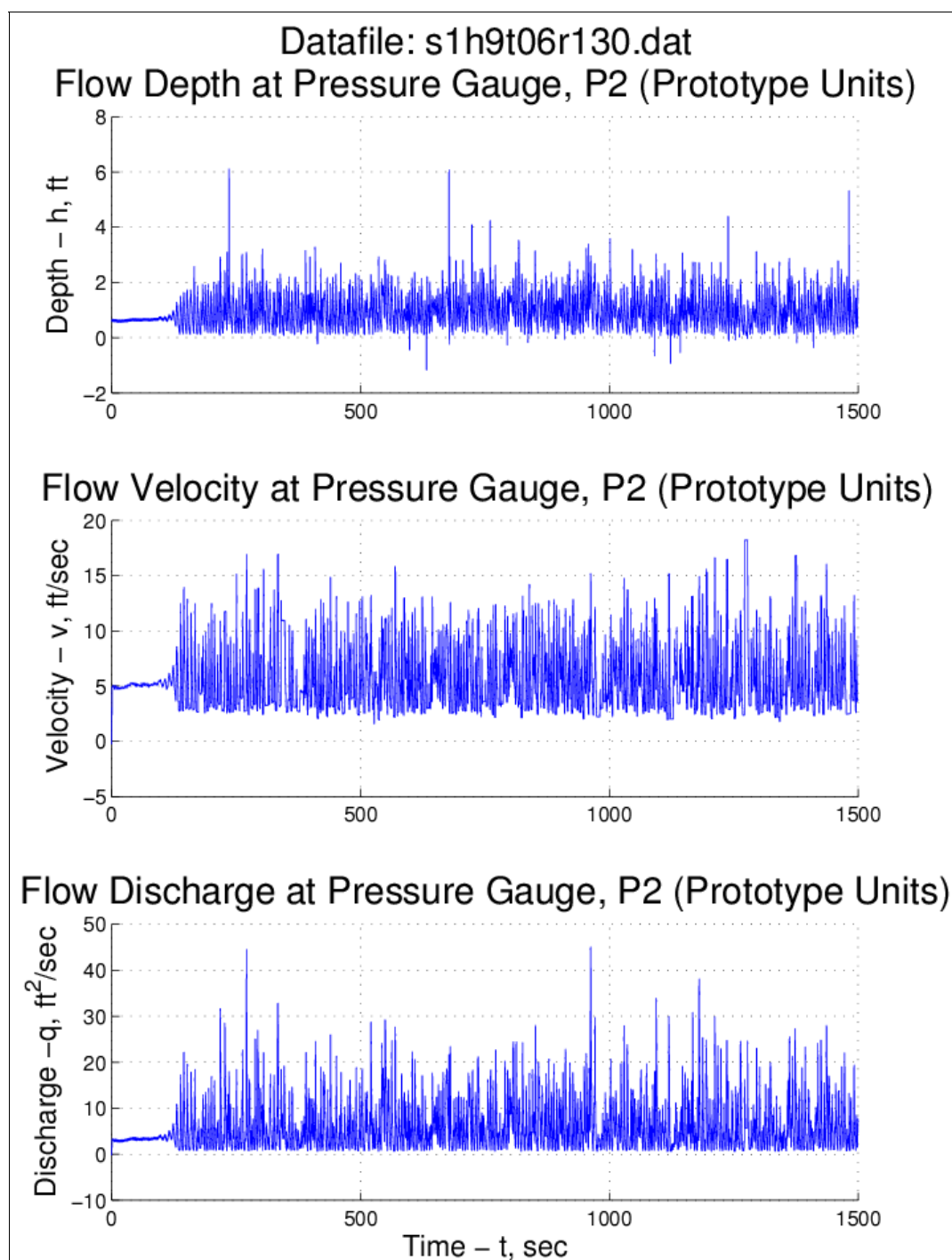


Figure A3. Run 130 time series plots (surge = +1 ft, $H_{m0} = 9$ ft, $T_p = 6$ sec).

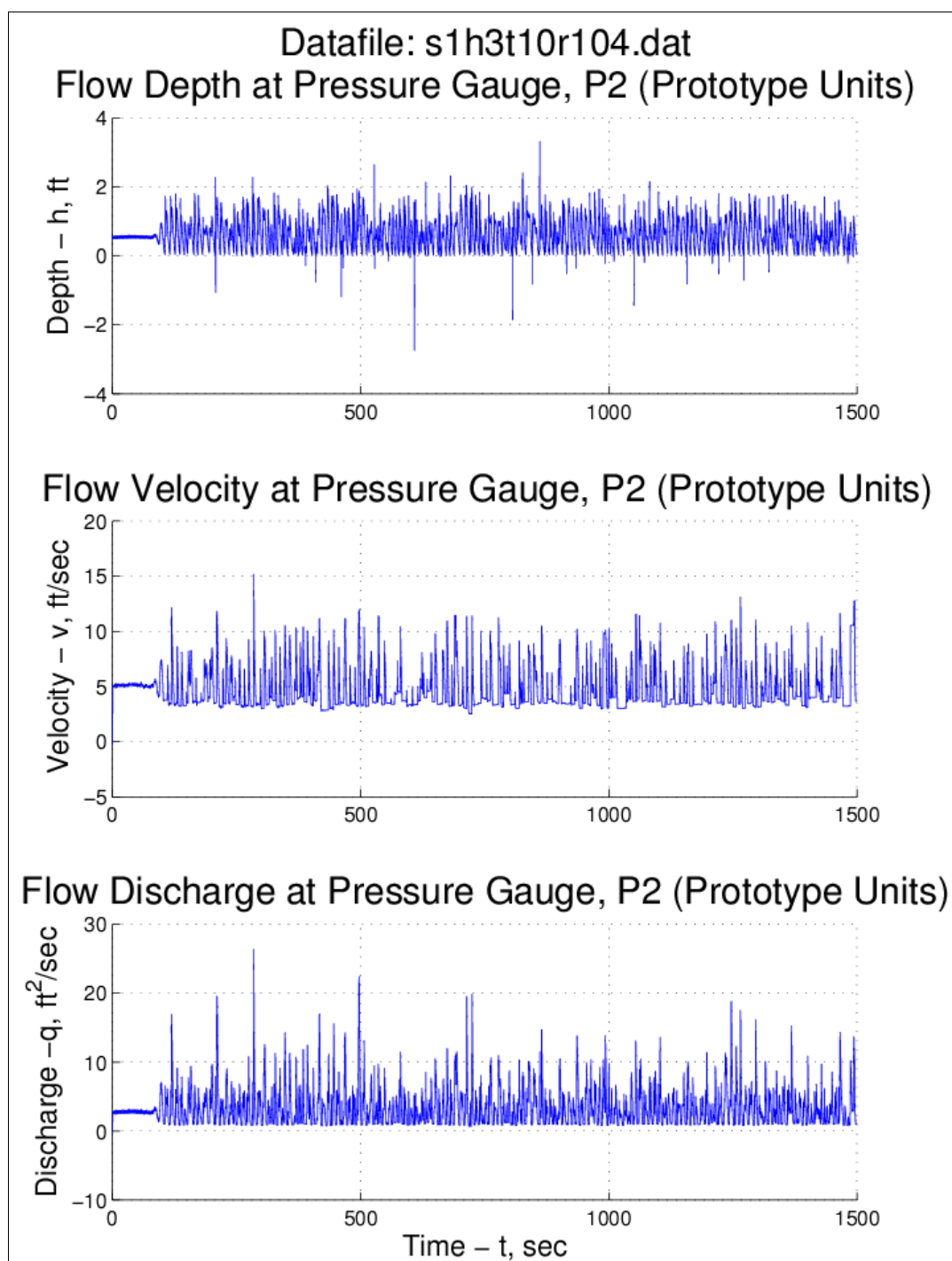


Figure A4. Run 104 time series plots (surge = +1 ft, $H_{mo} = 3$ ft, $T_p = 10$ sec).

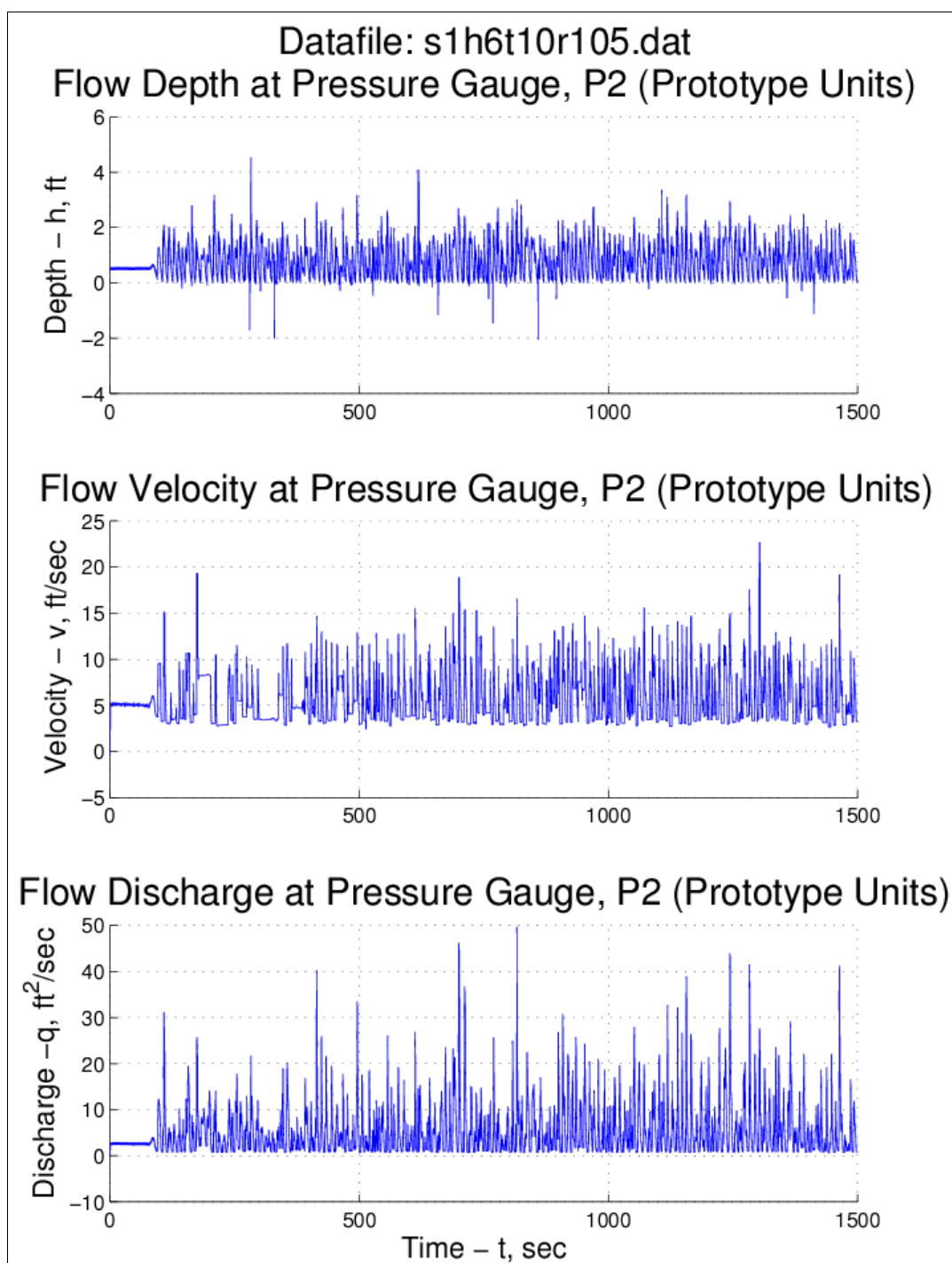


Figure A5. Run 105 time series plots (surge = +1 ft, H_{m0} = 6 ft, T_p = 10 sec).

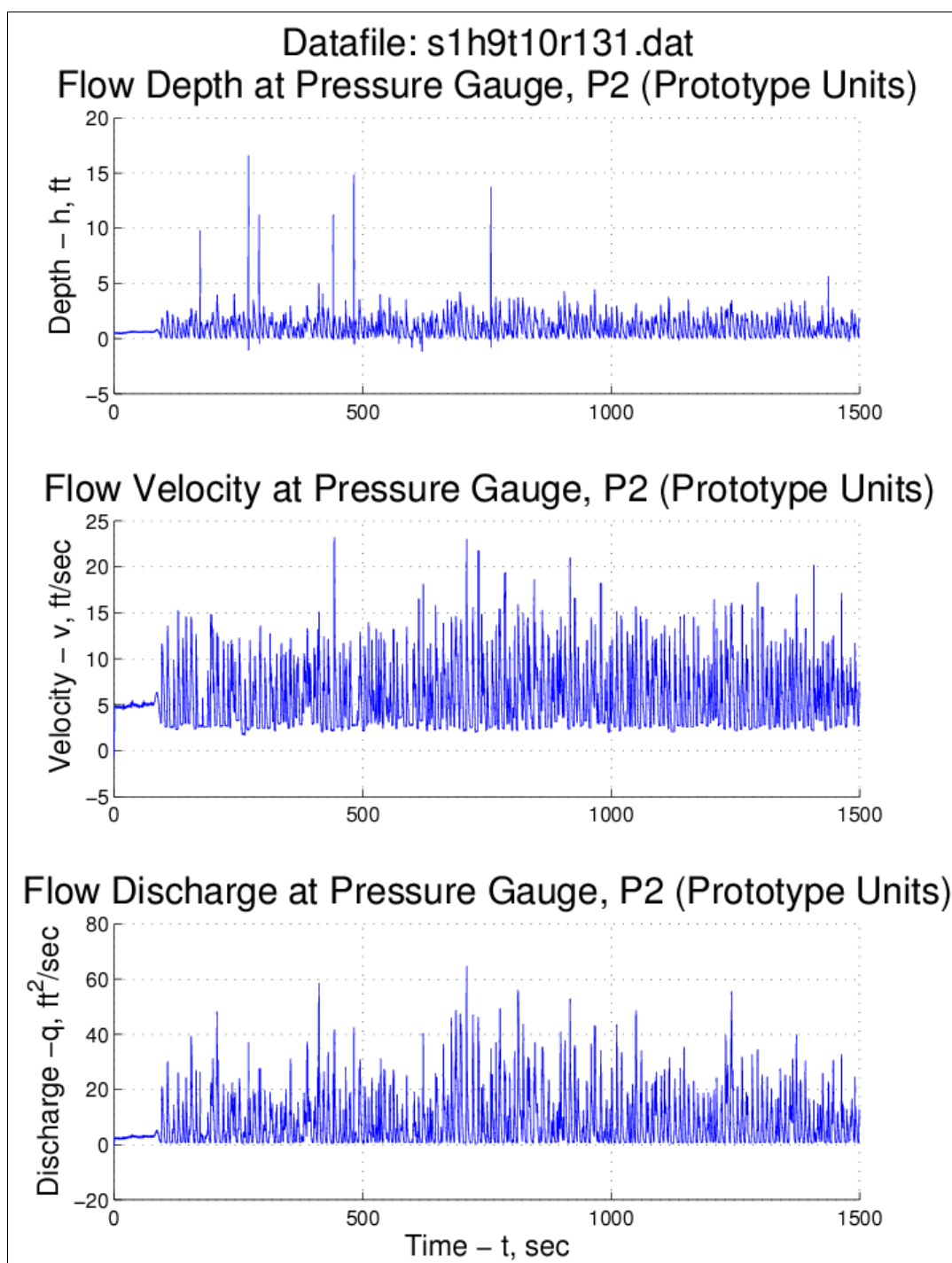


Figure A6. Run 131 time series plots (surge = +1 ft, $H_{m0} = 9$ ft, $T_p = 10$ sec).

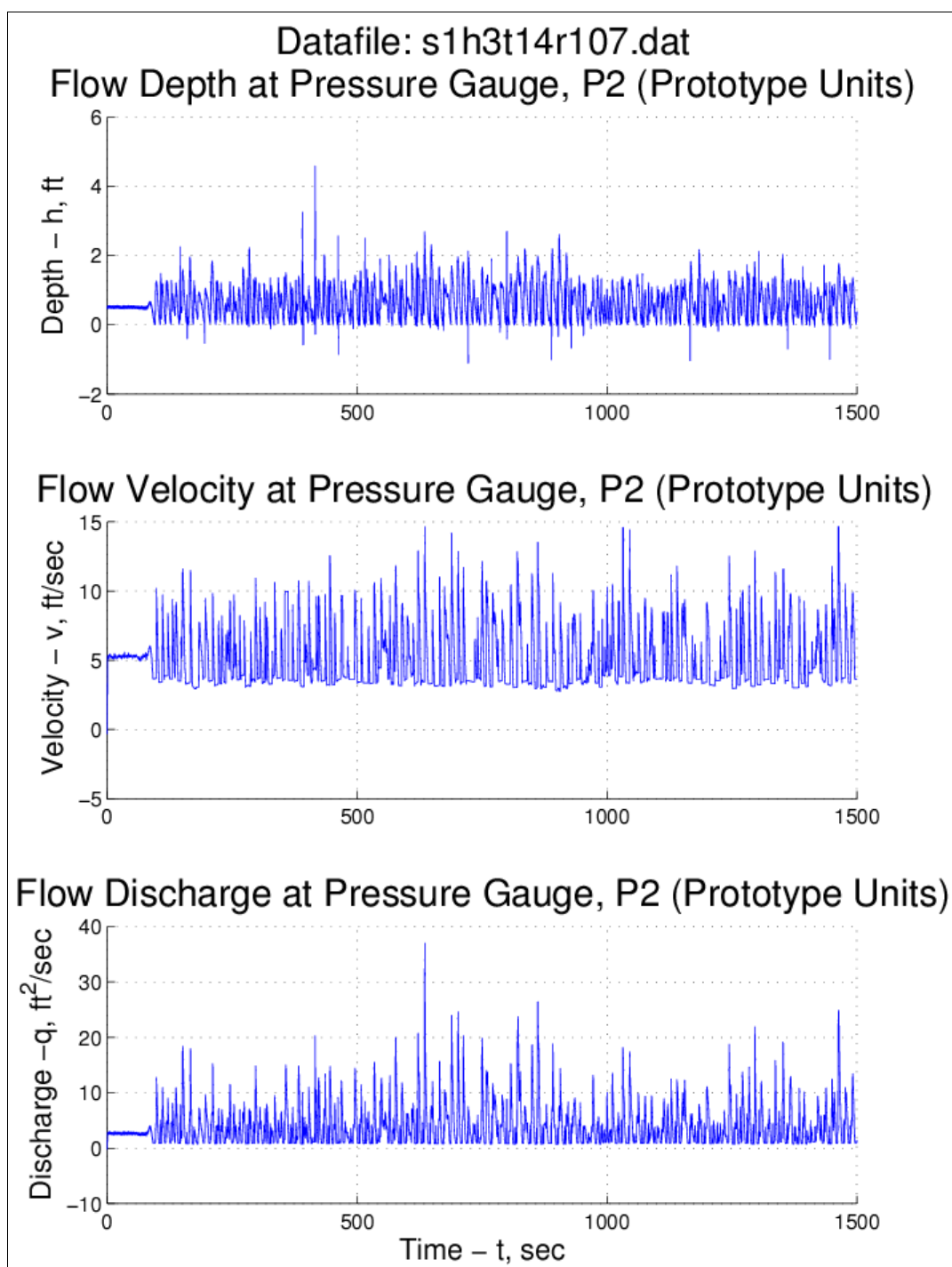


Figure A7. Run 107 time series plots (surge = +1 ft, $H_{m0} = 3$ ft, $T_p = 14$ sec).

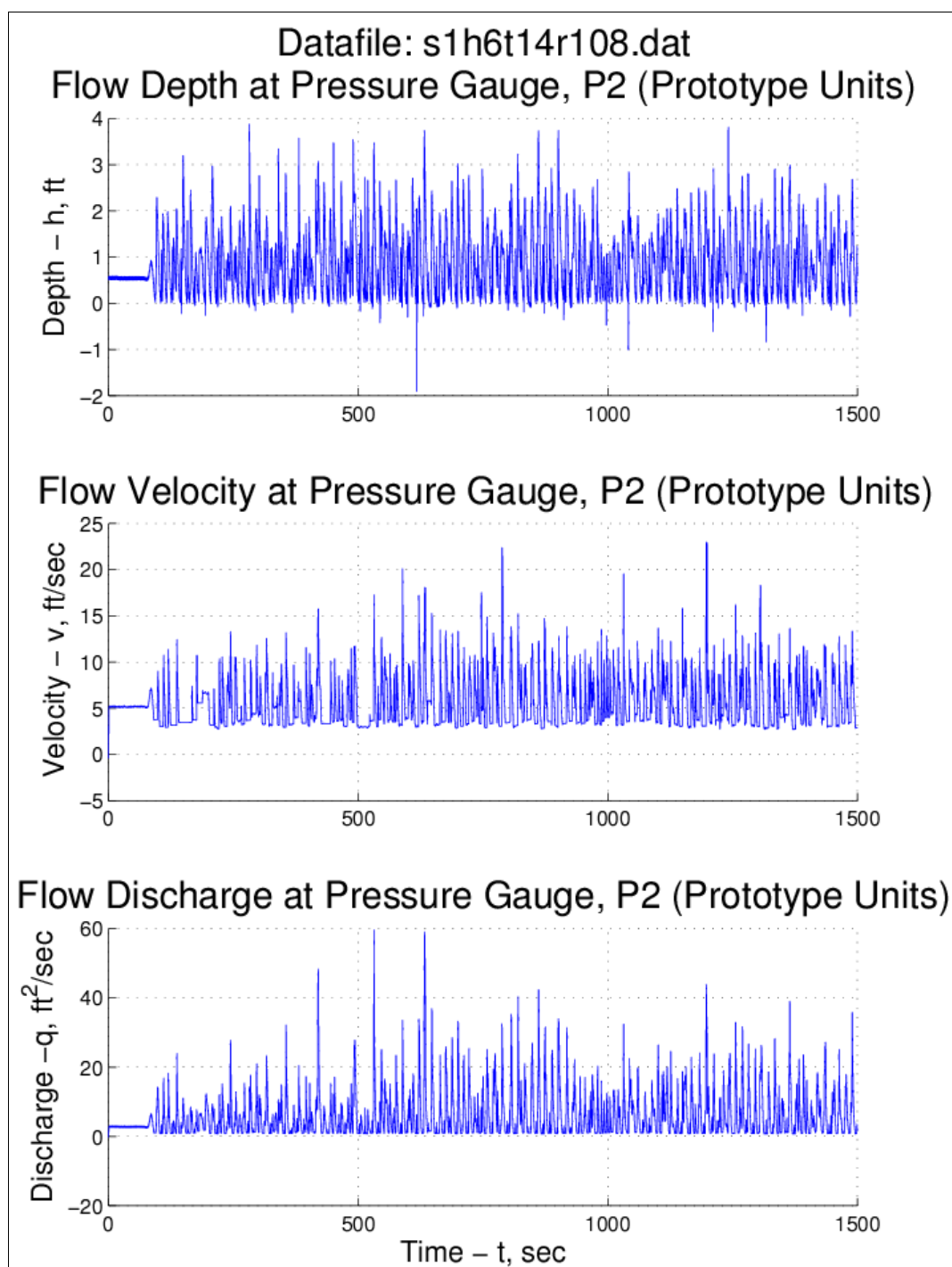


Figure A8. Run 108 time series plots (surge = +1 ft, $H_{m0} = 6$ ft, $T_p = 14$ sec).

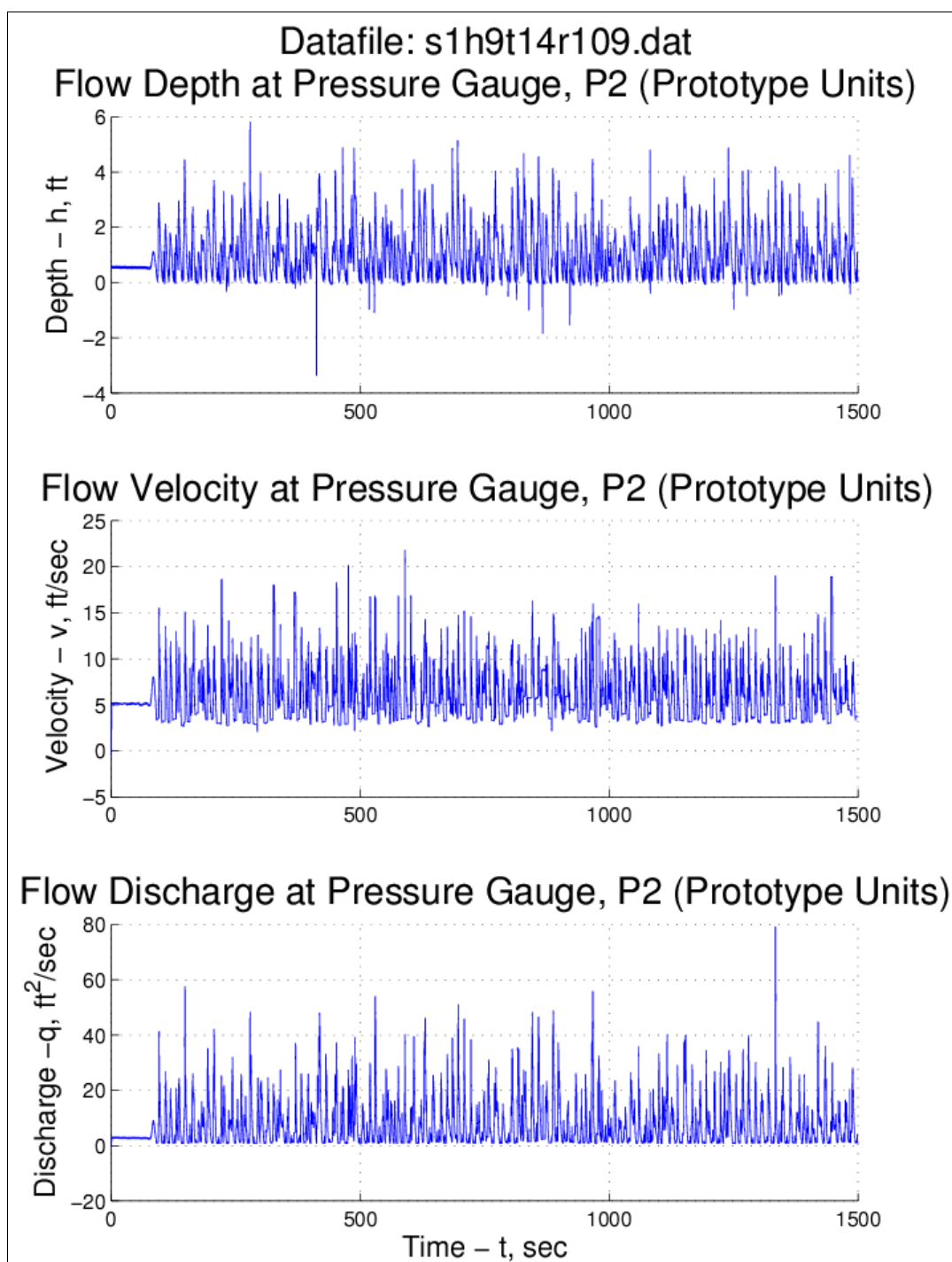


Figure A9. Run 109 time series plots (surge = +1 ft, $H_{m0} = 9$ ft, $T_p = 14$ sec).

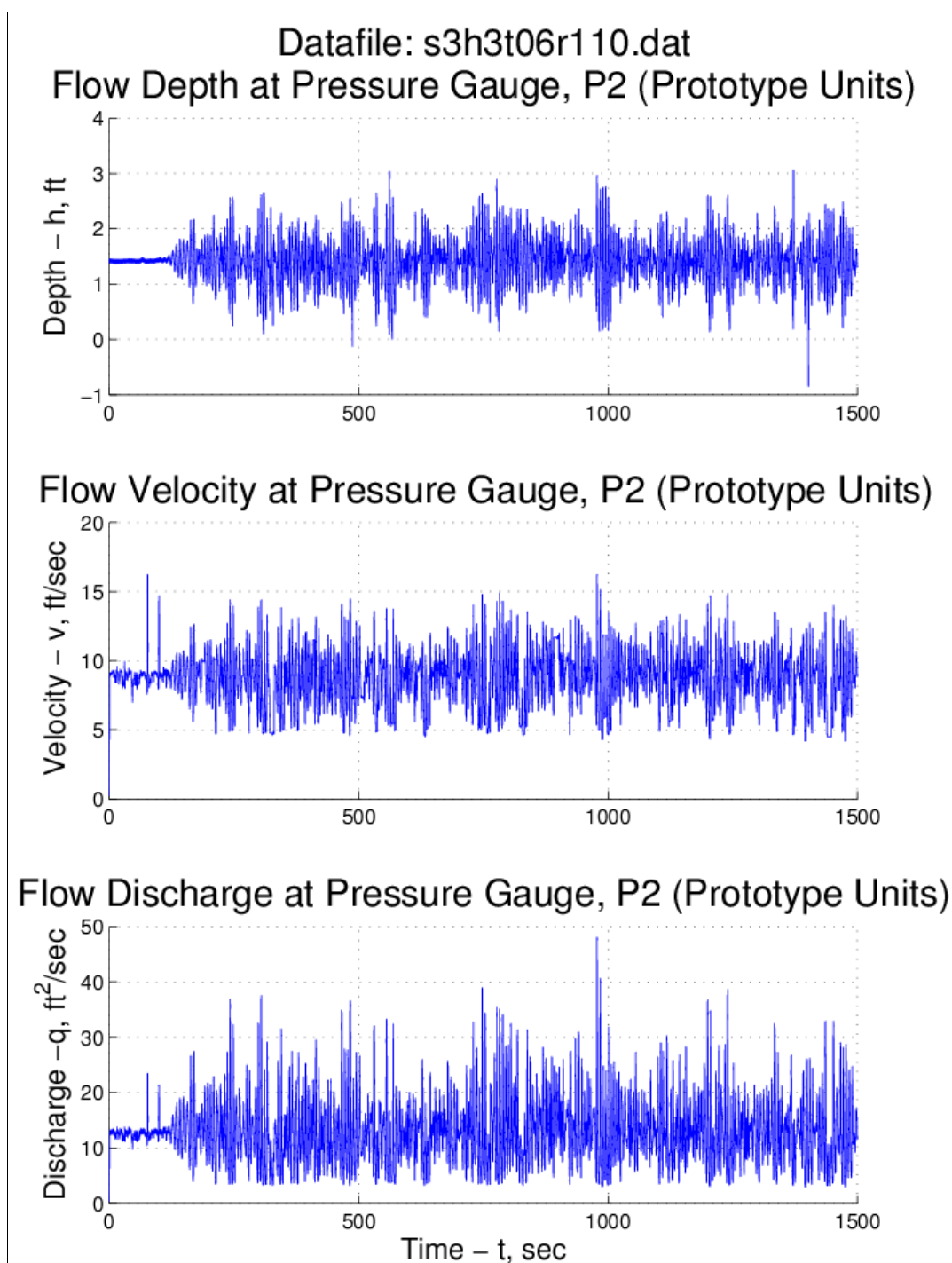


Figure A10. Run 110 time series plots (surge = +3 ft, $H_{m0} = 3$ ft, $T_p = 6$ sec).

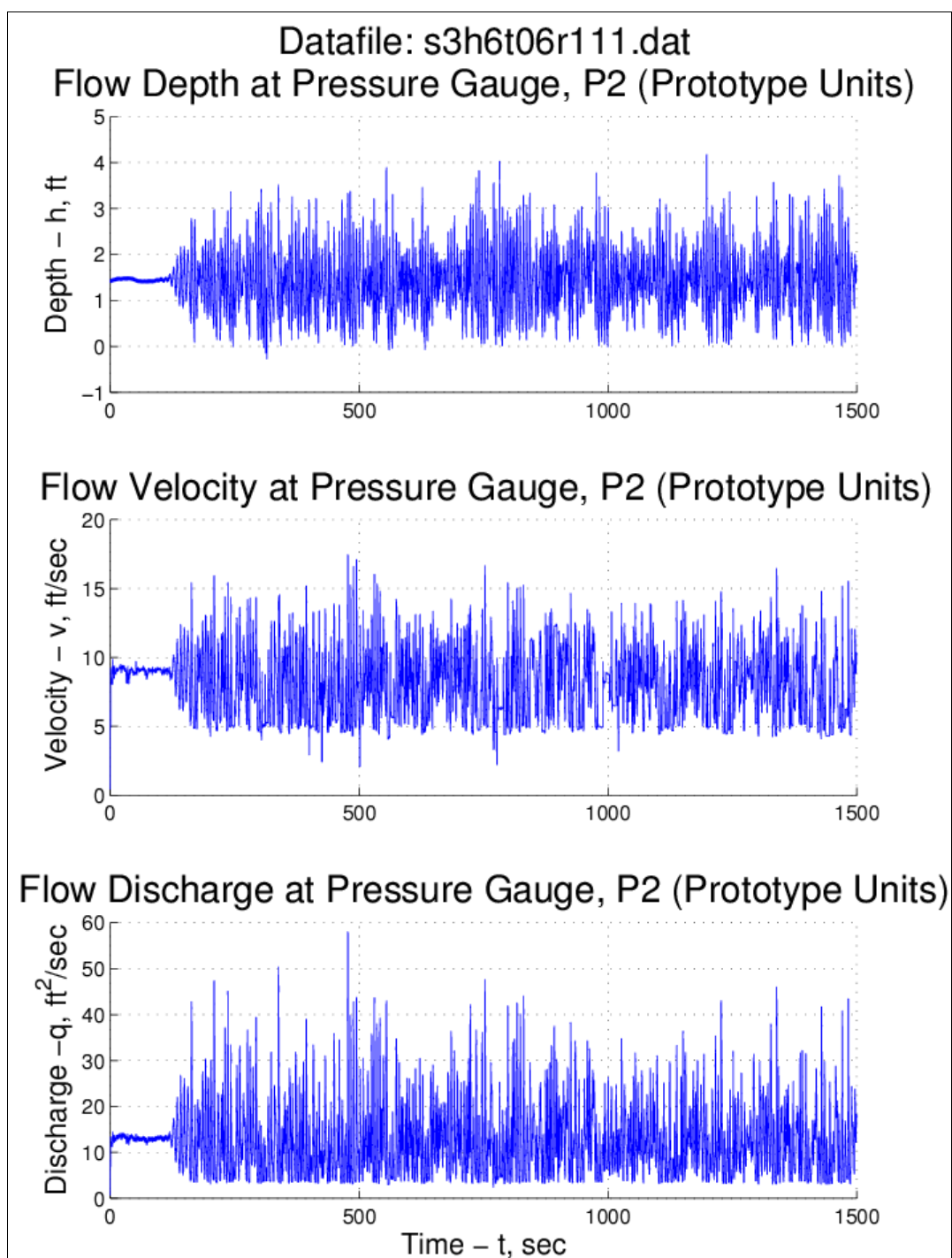


Figure A11. Run 111 time series plots (surge = +3 ft, $H_{m0} = 6$ ft, $T_p = 6$ sec).

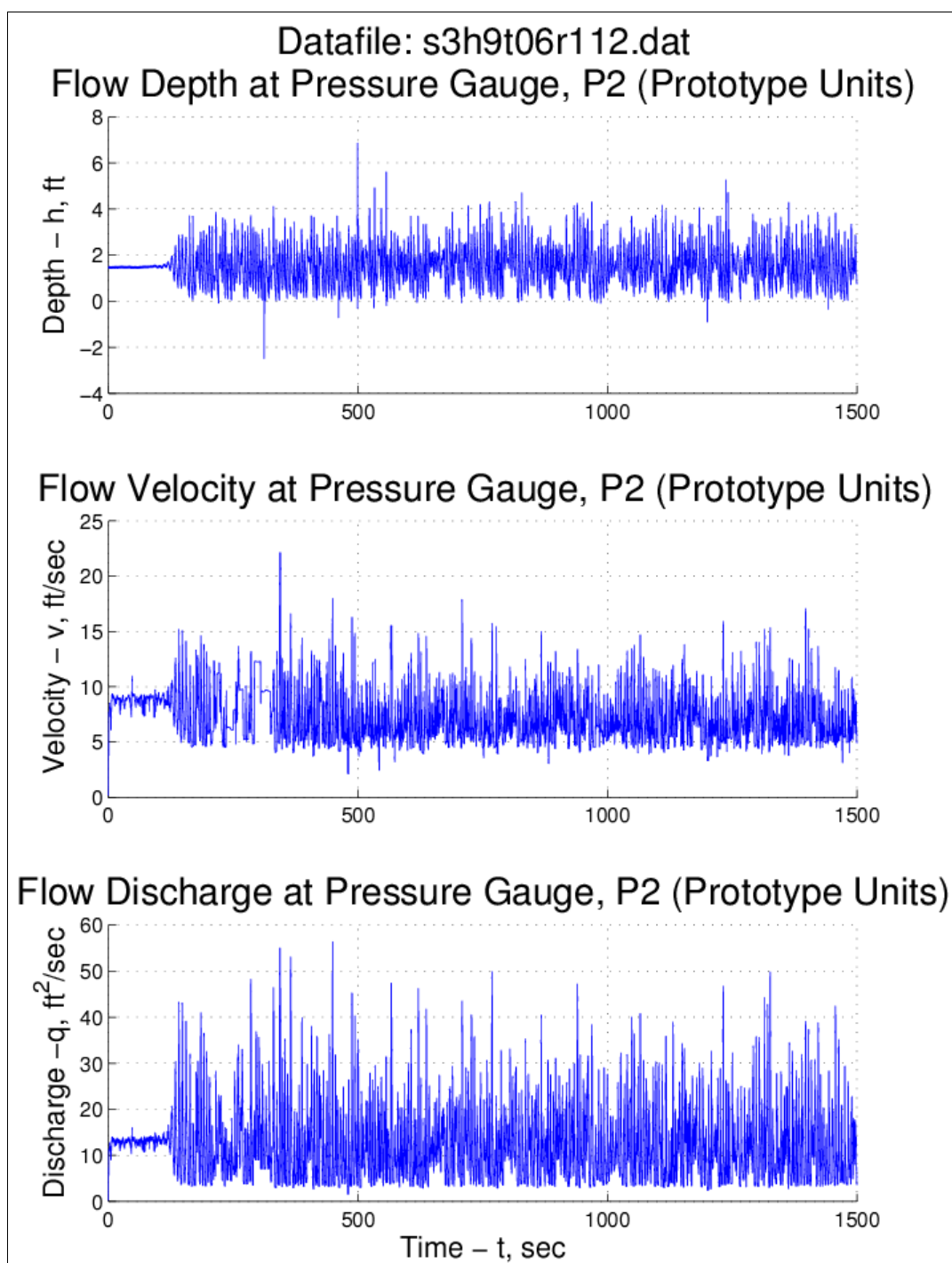


Figure A12. Run 112 time series plots (surge = +3 ft, H_{m0} = 9 ft, T_p = 6 sec).

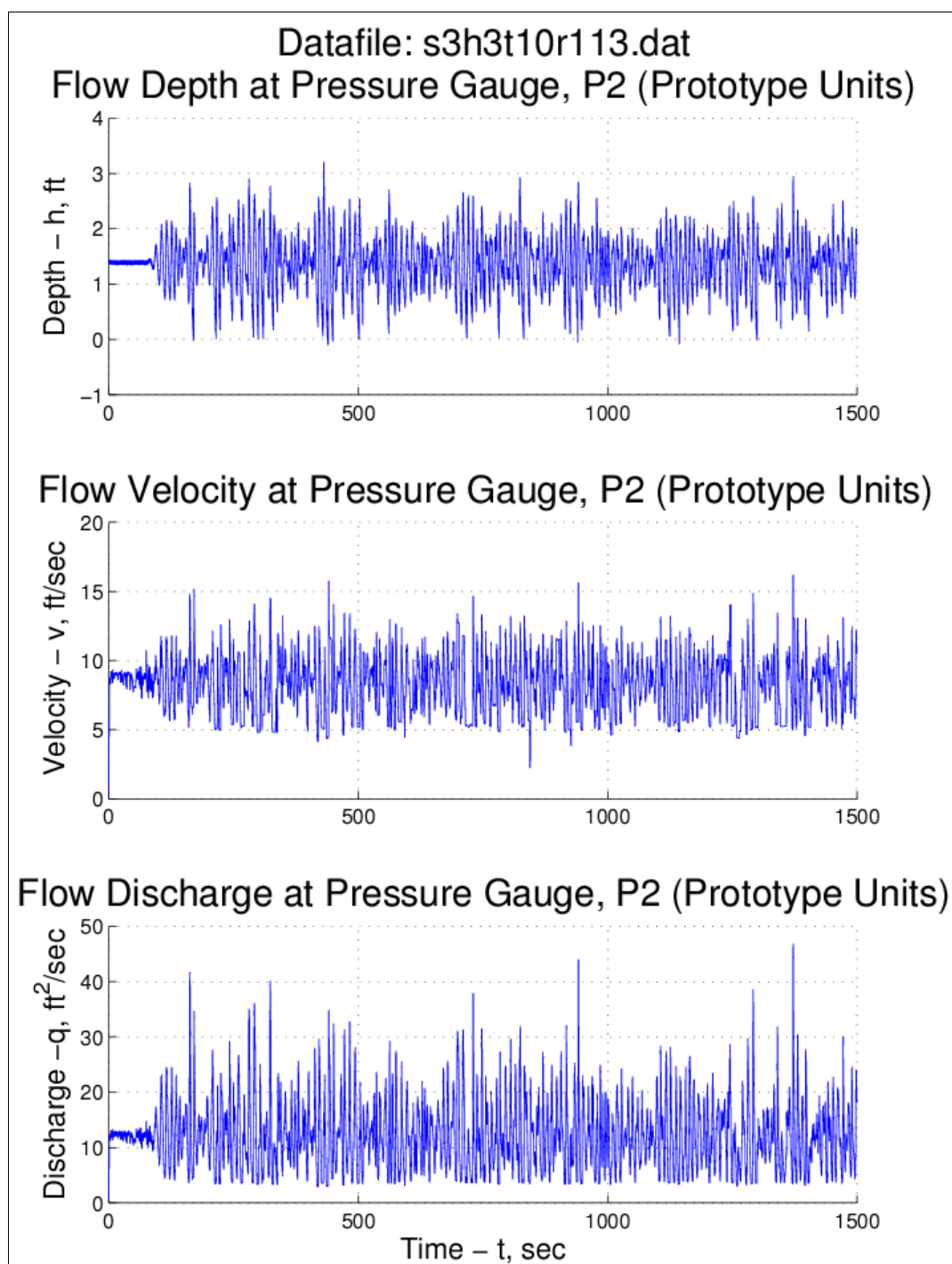


Figure A13. Run 113 time series plots (surge = +3 ft, H_{m0} = 3 ft, T_p = 10 sec).

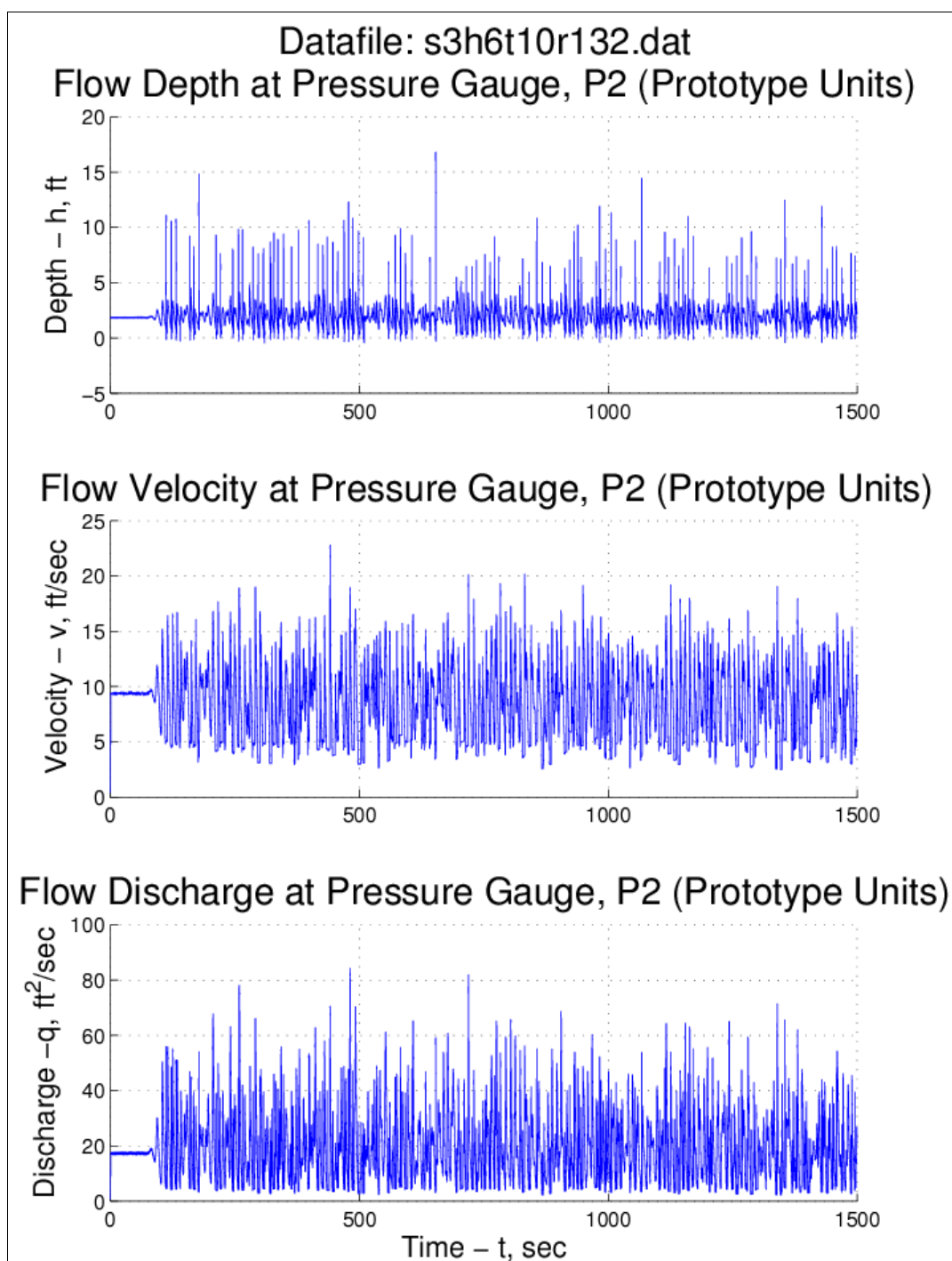


Figure A14. Run 132 time series plots (surge = +3 ft, $H_{m0} = 6$ ft, $T_p = 10$ sec).

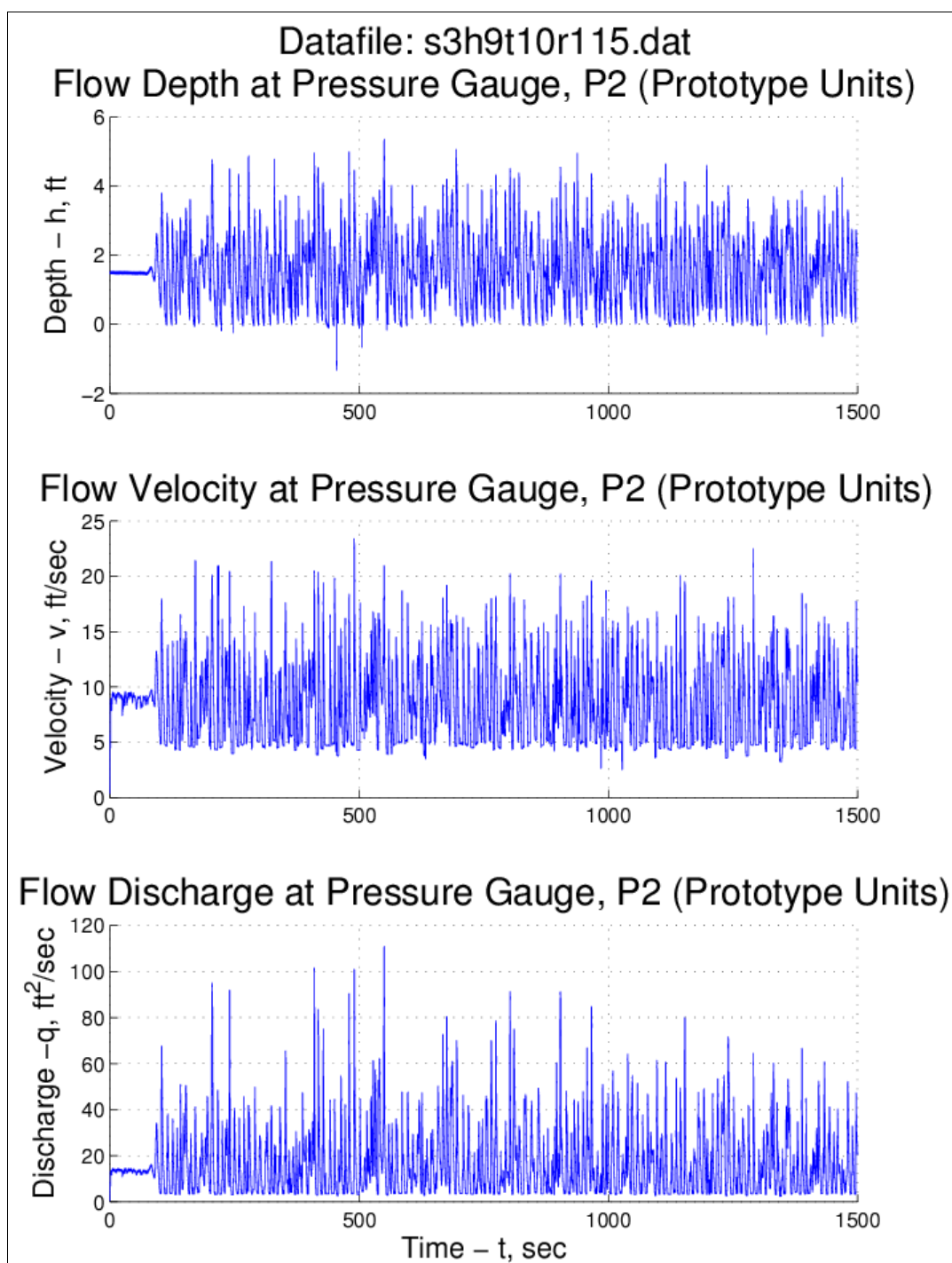


Figure A15. Run 115 time series plots (surge = +3 ft, H_{m0} = 9 ft, T_p = 10 sec).

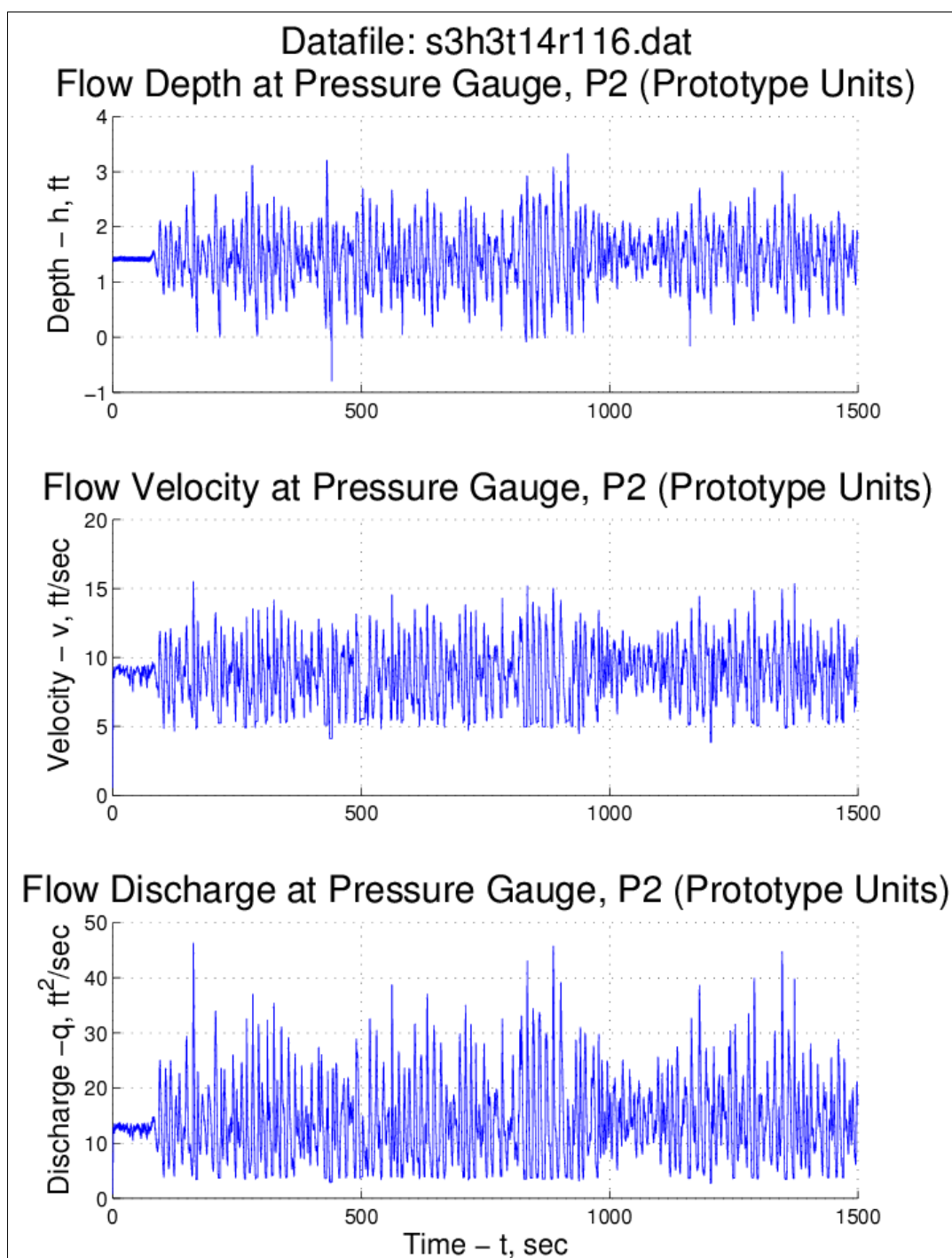


Figure A16. Run 116 time series plots (surge = +3 ft, $H_{m0} = 3$ ft, $T_p = 14$ sec).

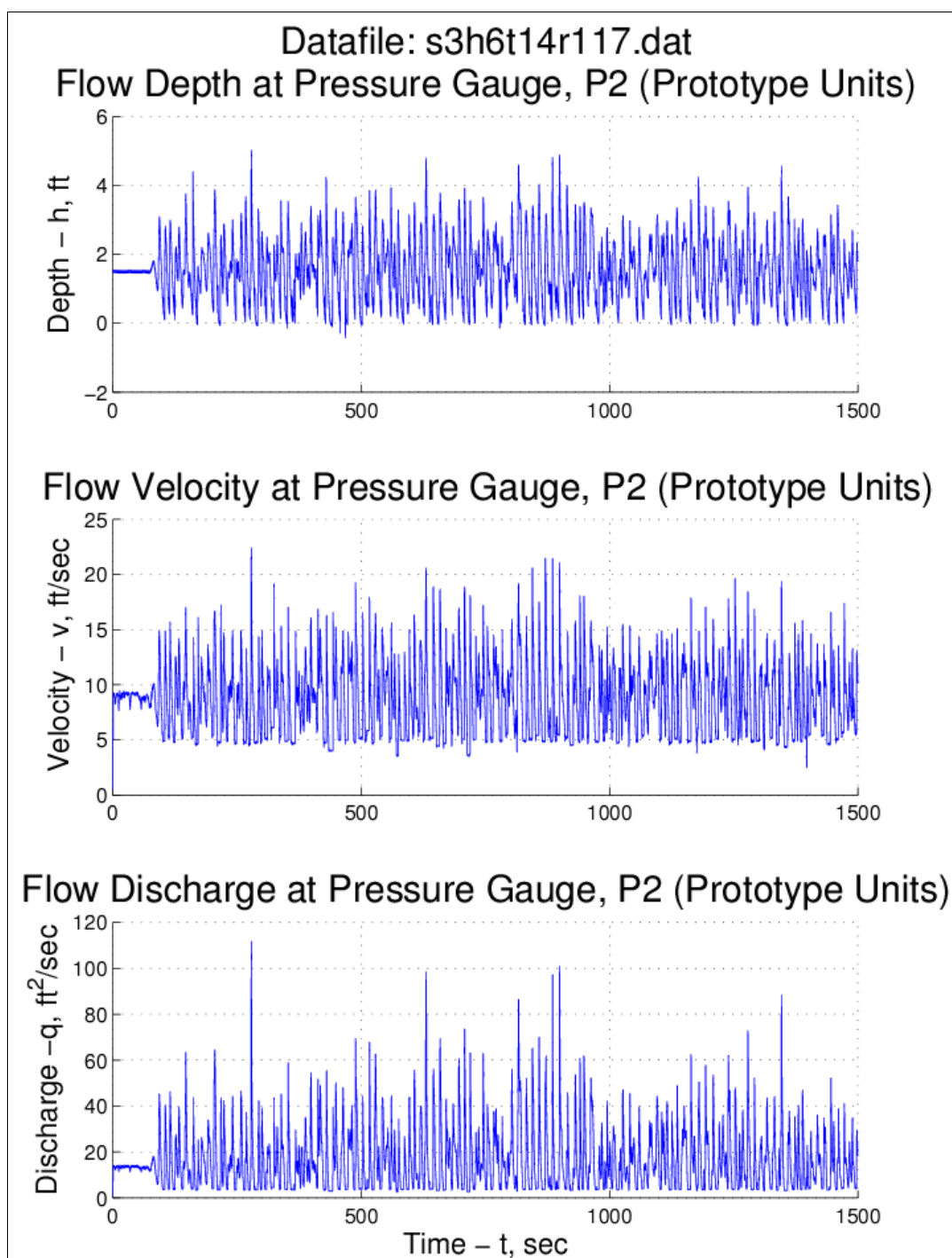


Figure A17. Run 117 time series plots (surge = +3 ft, $H_{m0} = 6$ ft, $T_p = 14$ sec).

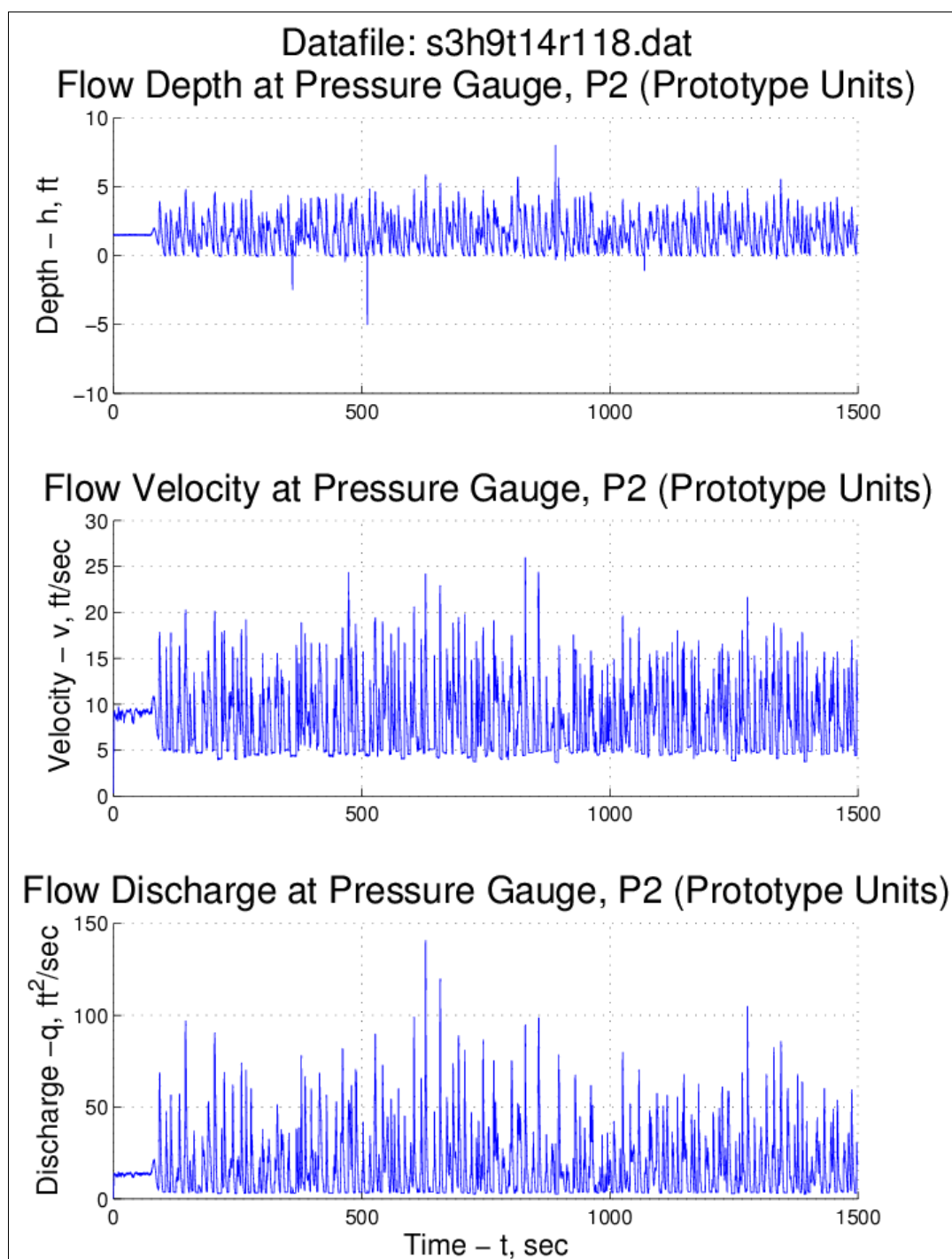


Figure A18. Run 118 time series plots (surge = +3 ft, $H_{m0} = 9$ ft, $T_p = 14$ sec).

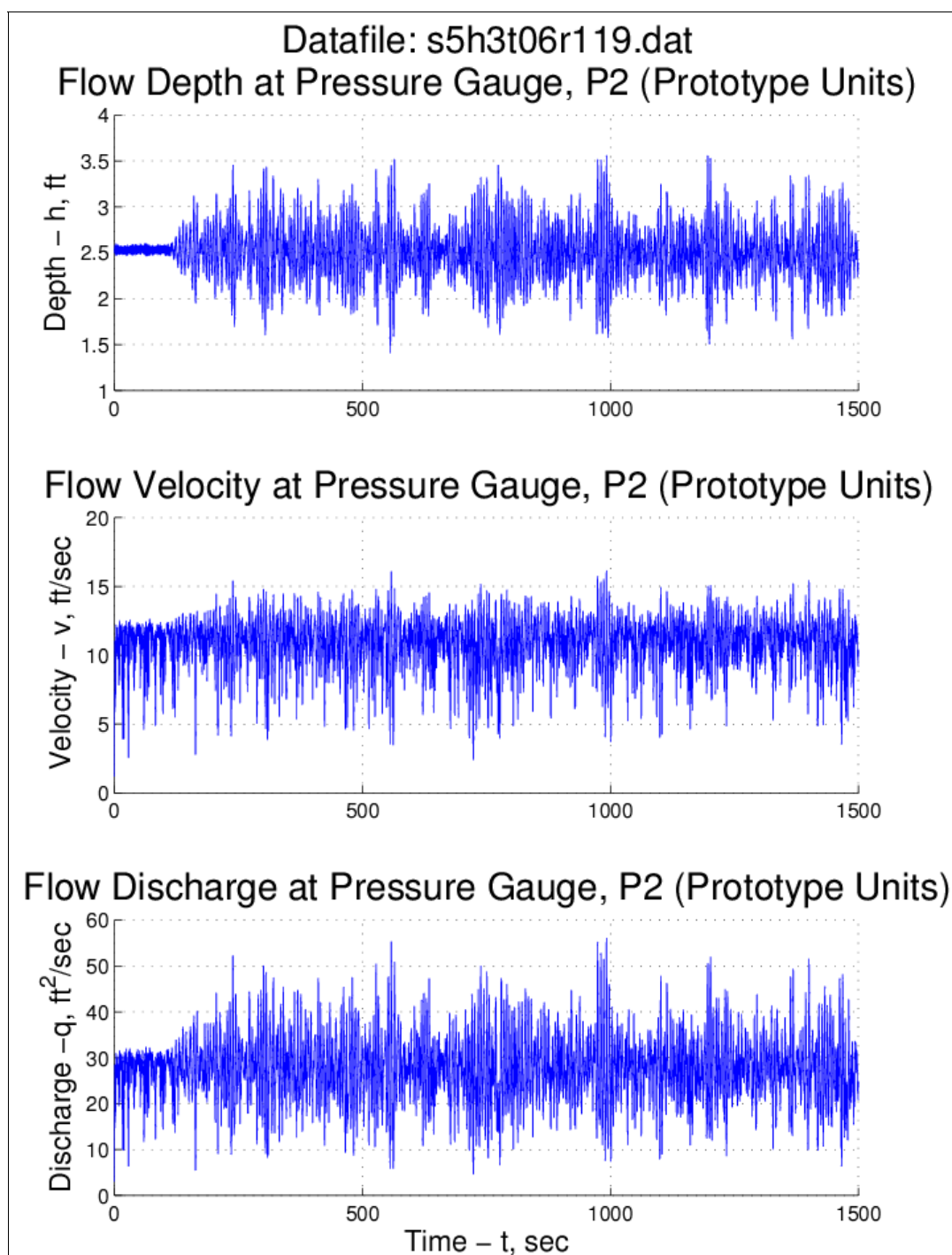


Figure A19. Run 119 time series plots (surge = +5 ft, $H_{m0} = 3$ ft, $T_p = 6$ sec).

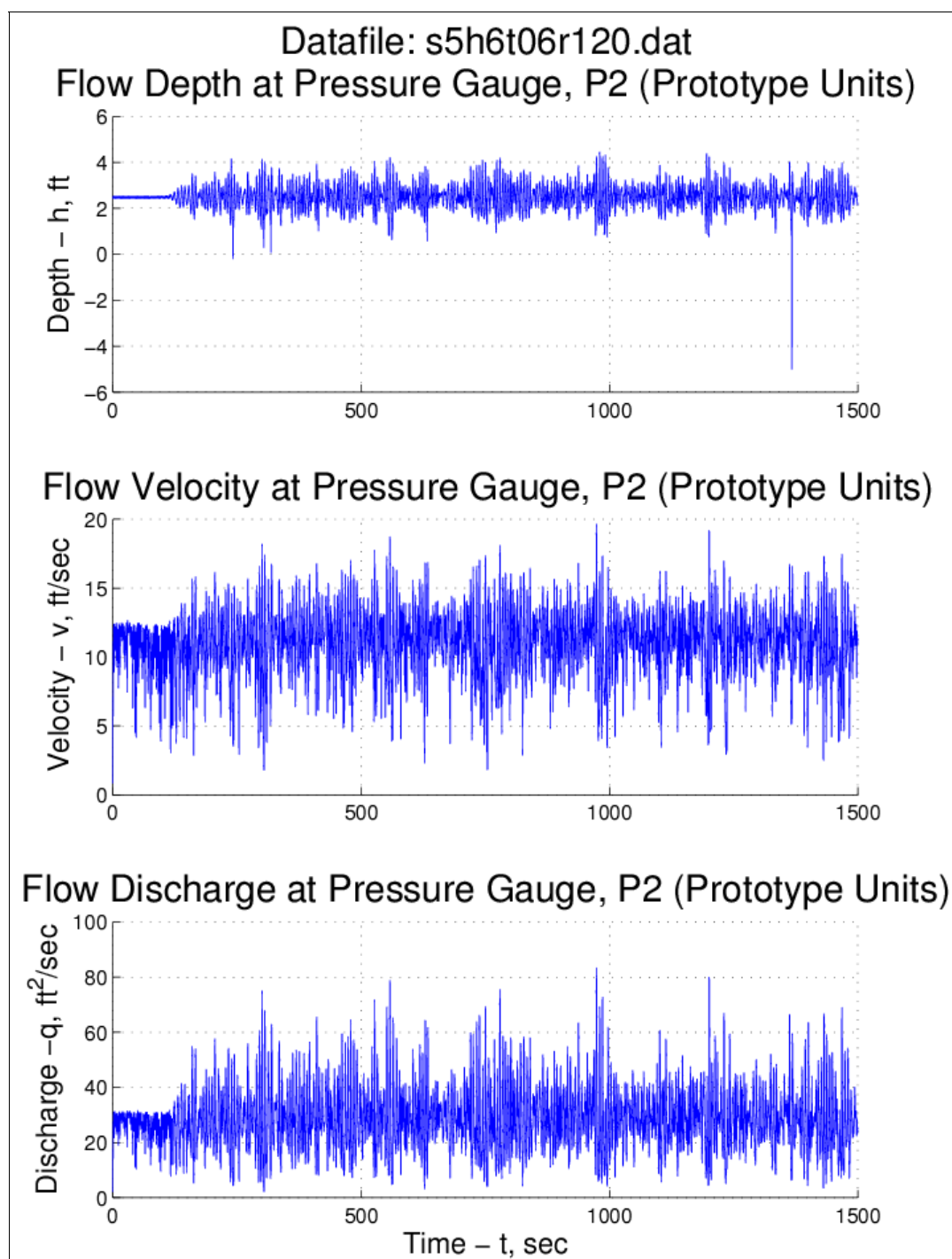


Figure A20. Run 120 time series plots (surge = +5 ft, H_{m0} = 6 ft, T_p = 6 sec).

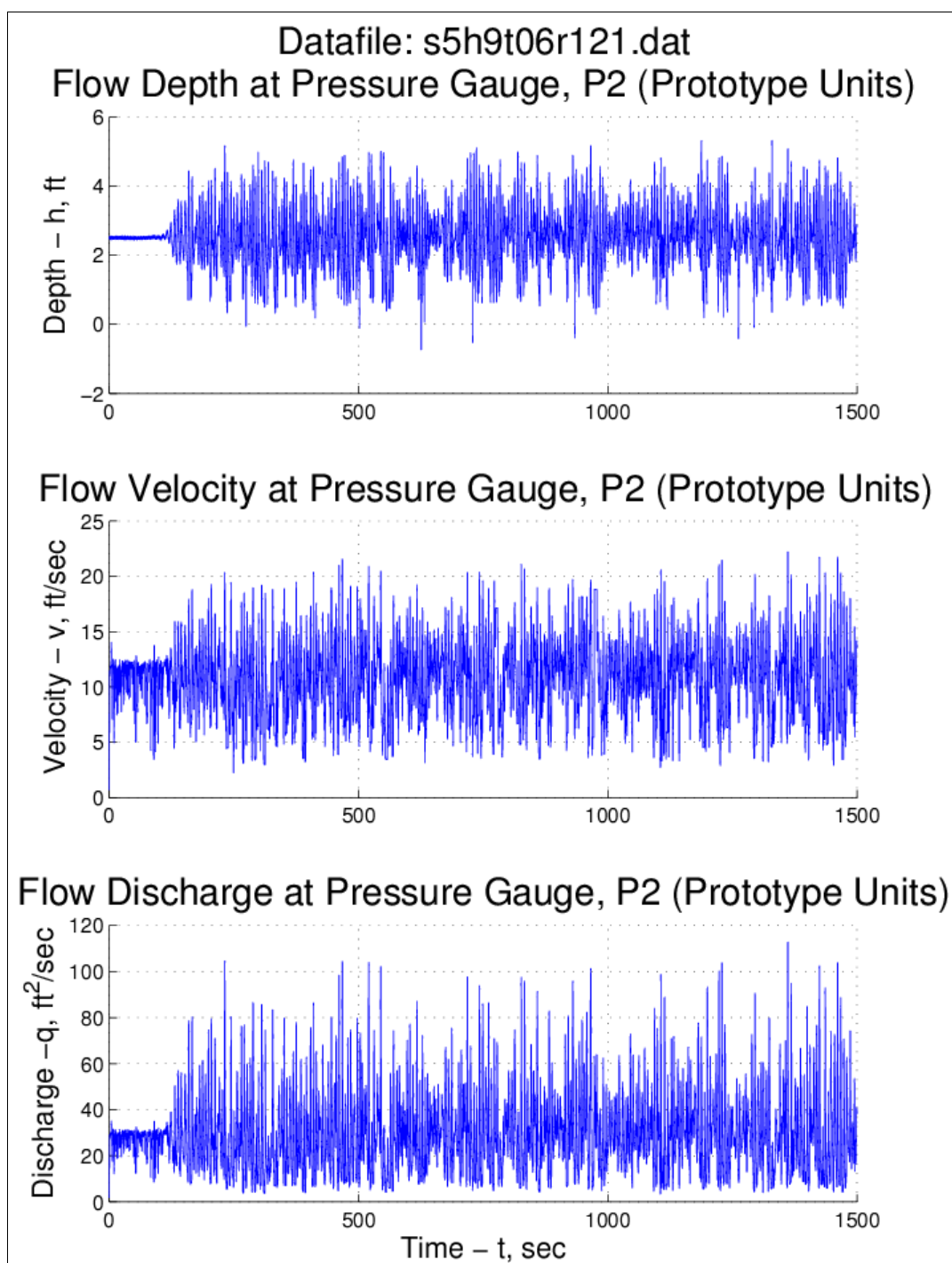


Figure A21. Run 121 time series plots (surge = +5 ft, $H_{m0} = 9$ ft, $T_p = 6$ sec).

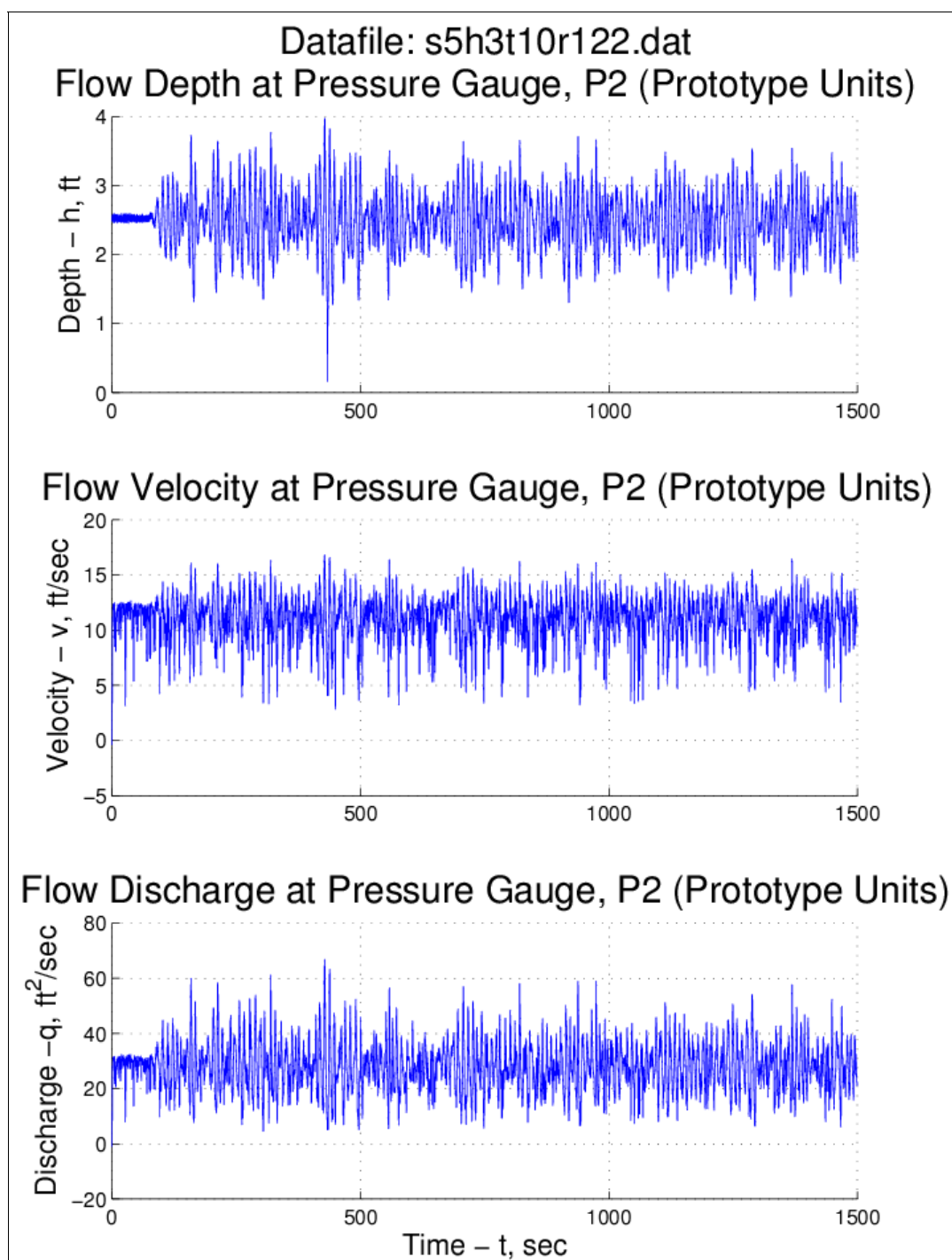


Figure A22. Run 122 time series plots (surge = +5 ft, $H_{m0} = 3$ ft, $T_p = 10$ sec).

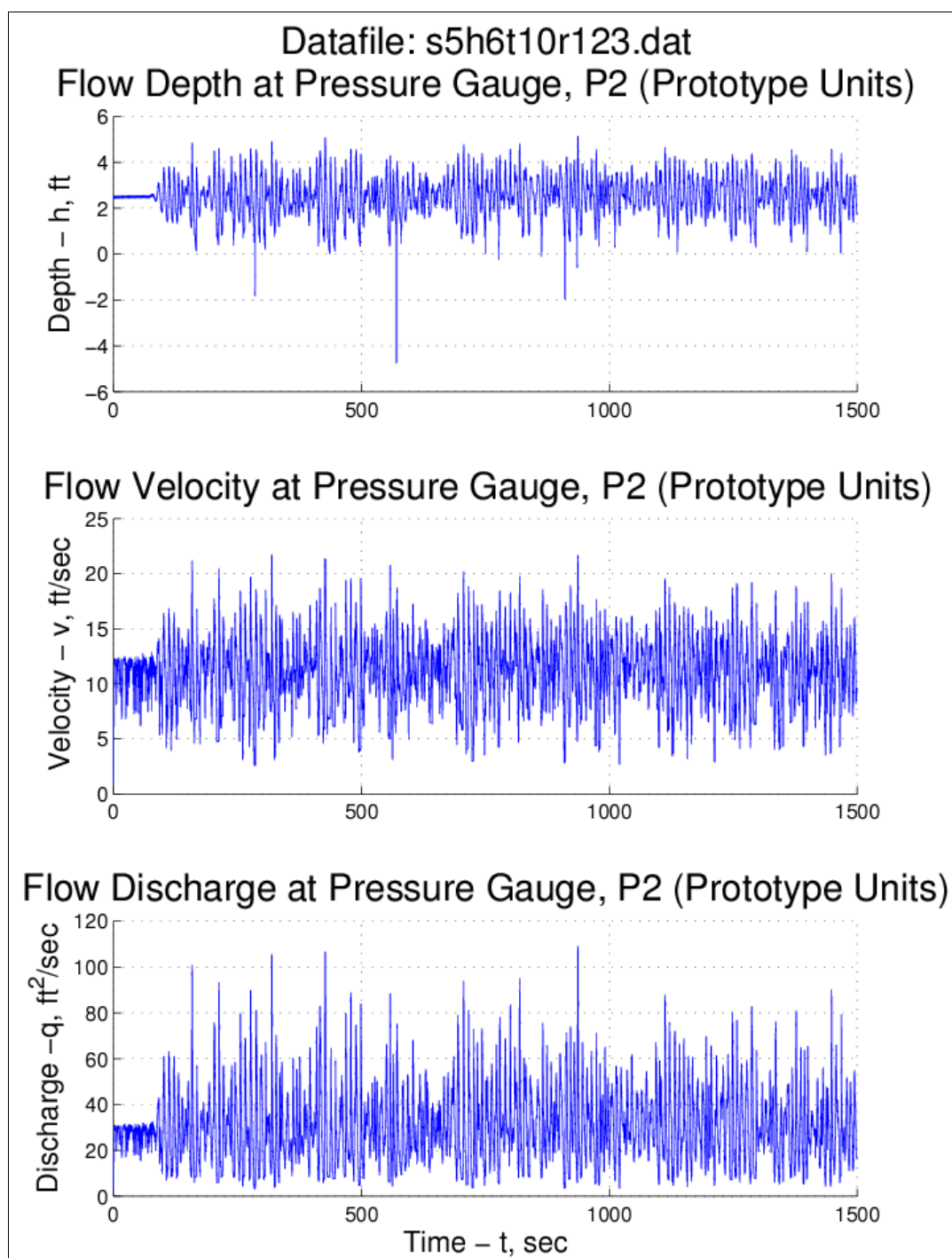


Figure A23. Run 123 time series plots (surge = +5 ft, H_{m0} = 6 ft, T_p = 10 sec).

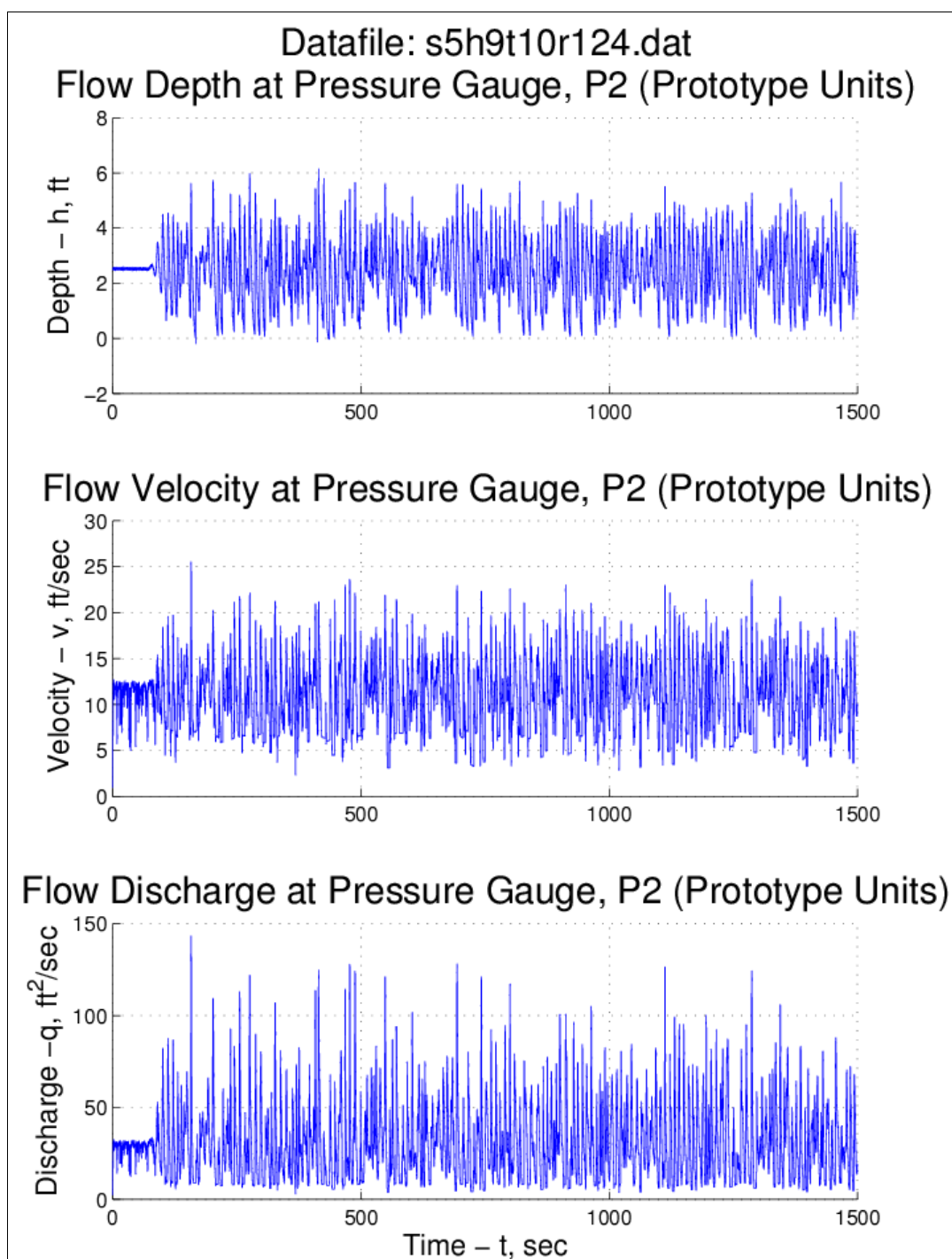


Figure A24. Run 124 time series plots (surge = +5 ft, $H_{m0} = 9$ ft, $T_p = 10$ sec).

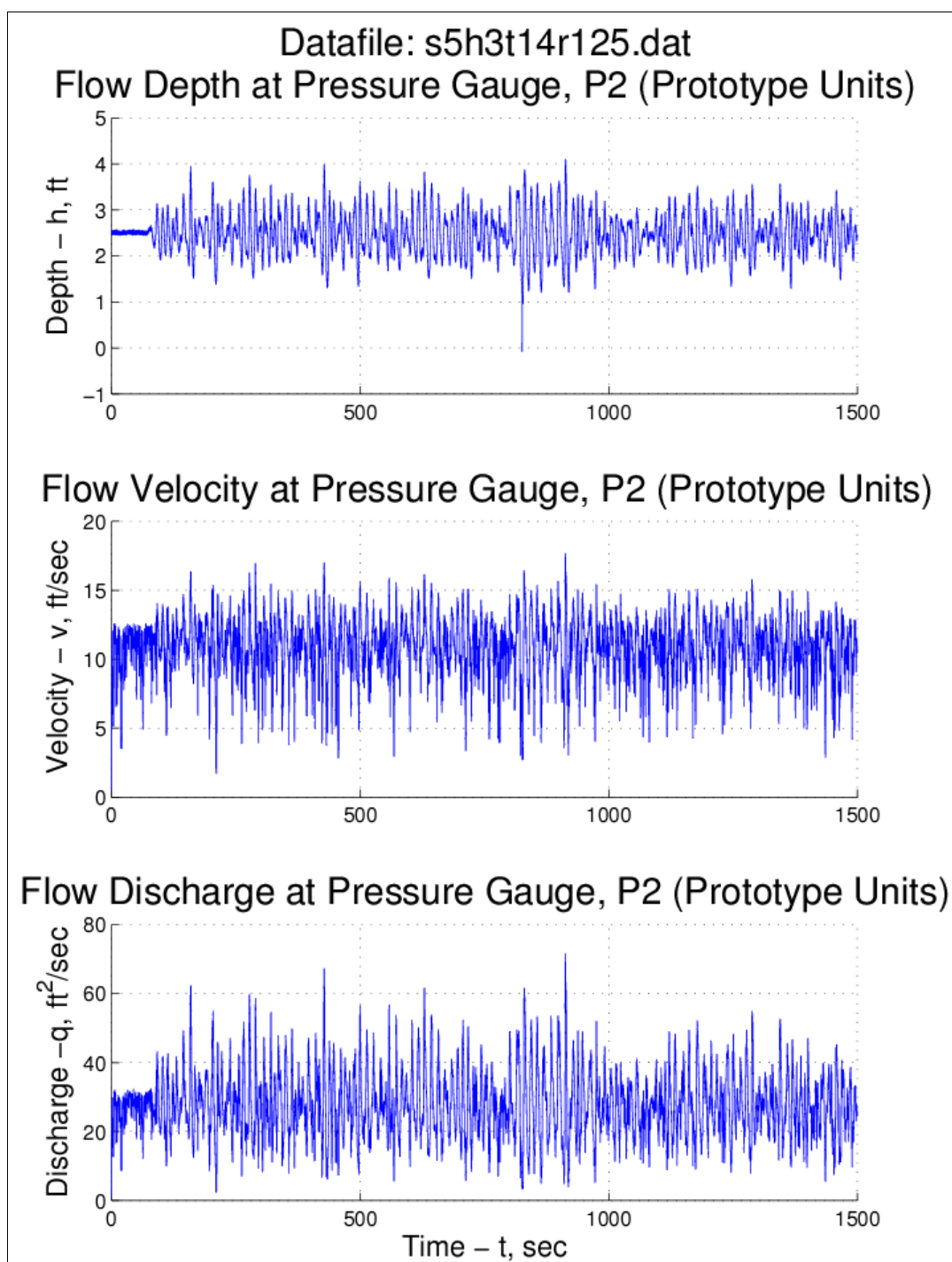


Figure A25. Run 125 time series plots (surge = +5 ft, H_{m0} = 3 ft, T_p = 14 sec).

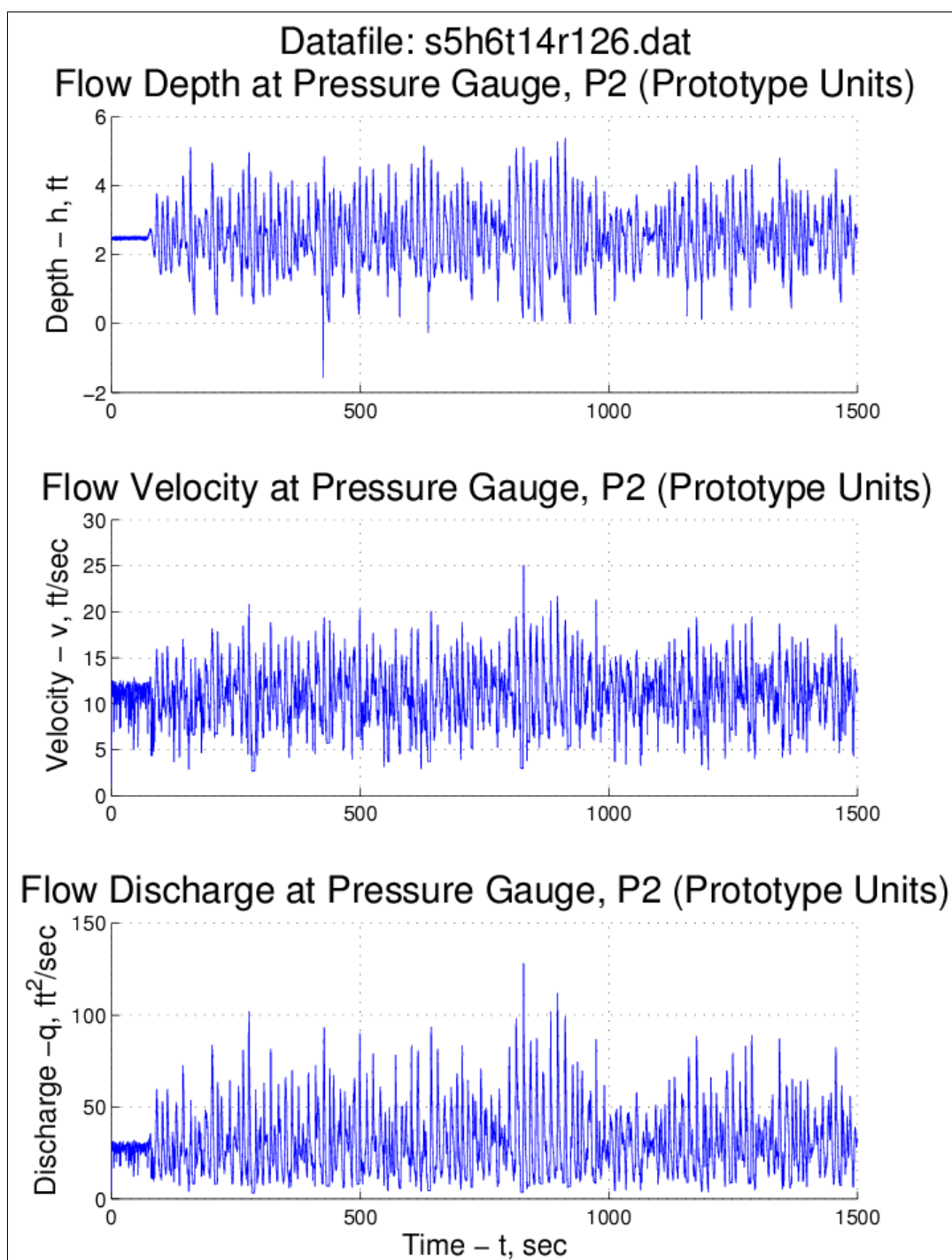


Figure A26. Run 126 time series plots (surge = +5 ft, H_{m0} = 6 ft, T_p = 14 sec).

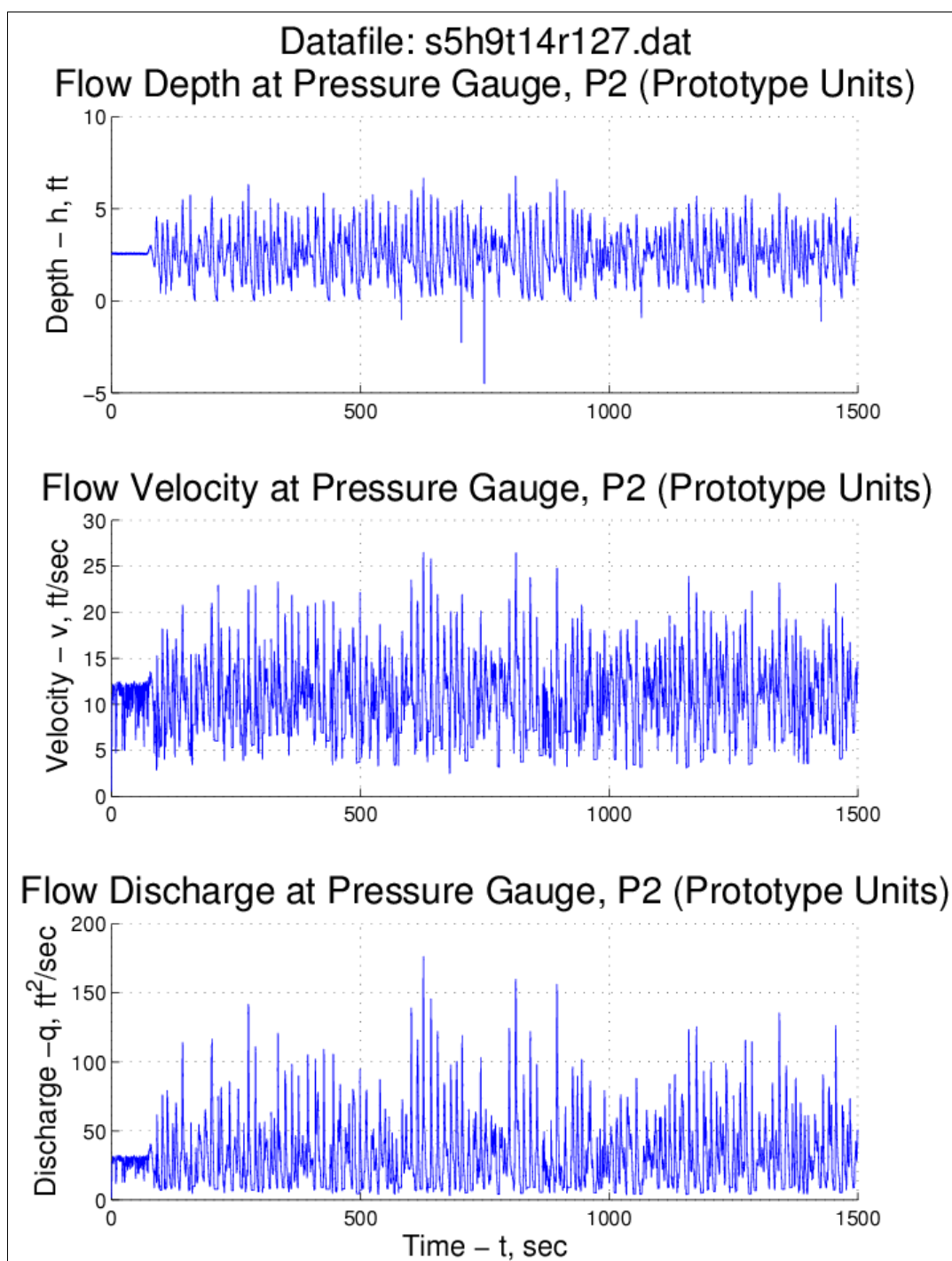


Figure A27. Run 127 time series plots (surge = +5 ft, $H_{m0} = 9$ ft, $T_p = 14$ sec).

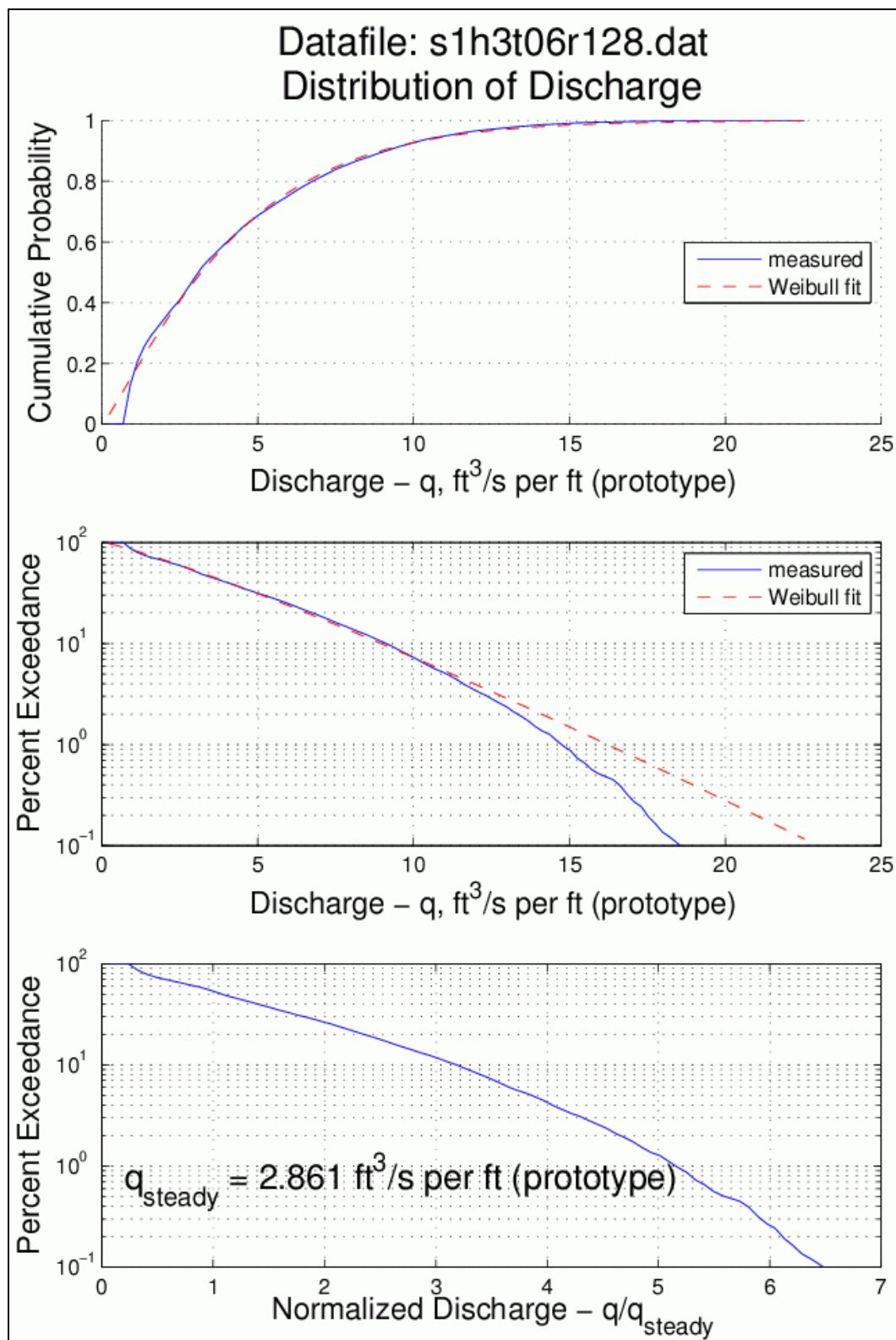
Overtopping probability distributions

Figure A28. Run 128 overtopping distribution plots (surge = +1 ft, $H_{m0} = 3$ ft, $T_p = 6$ sec).

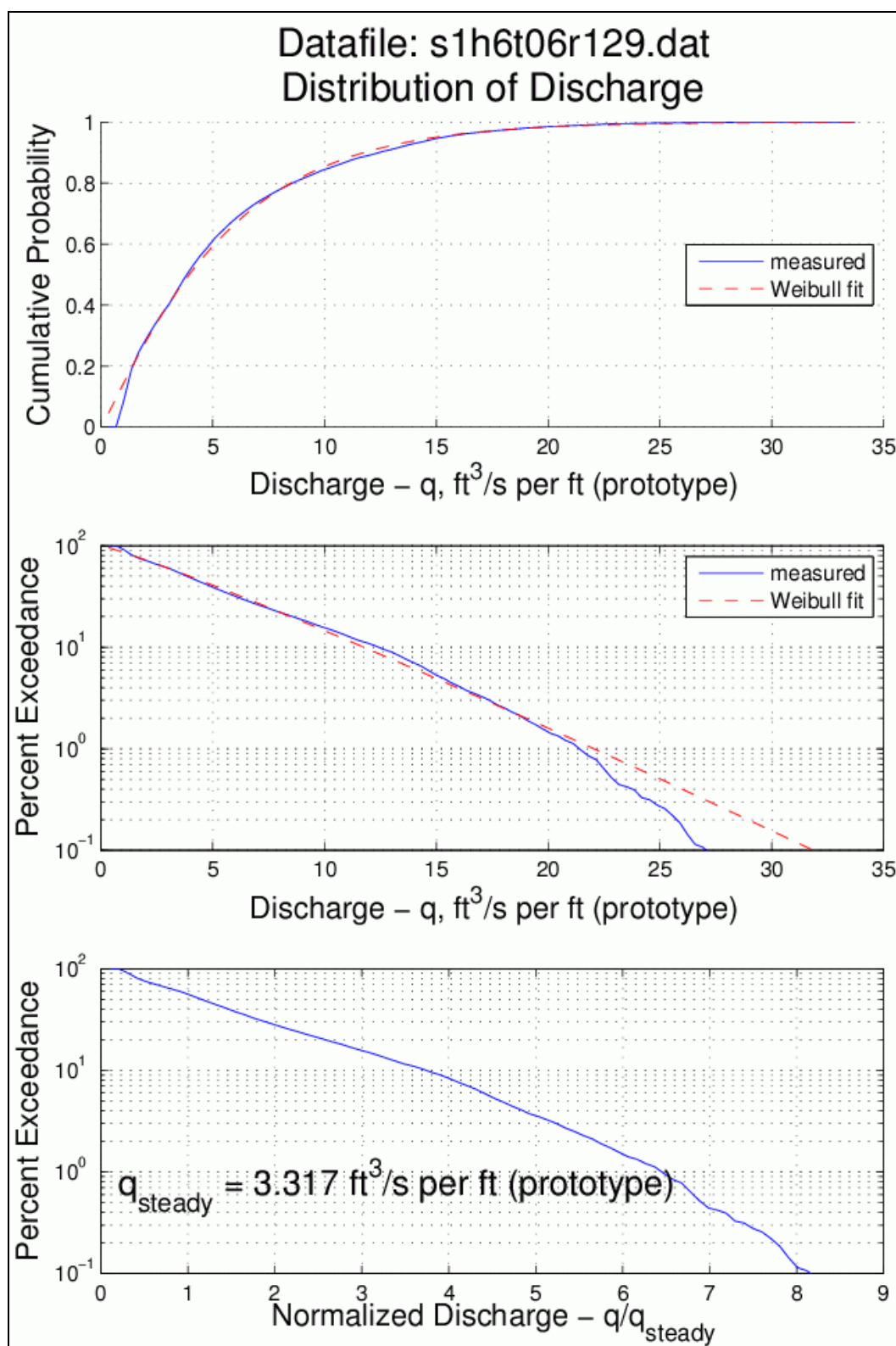


Figure A29. Run 129 overtopping distribution plots (surge = +1 ft, $H_{m0} = 6$ ft, $T_p = 6$ sec).

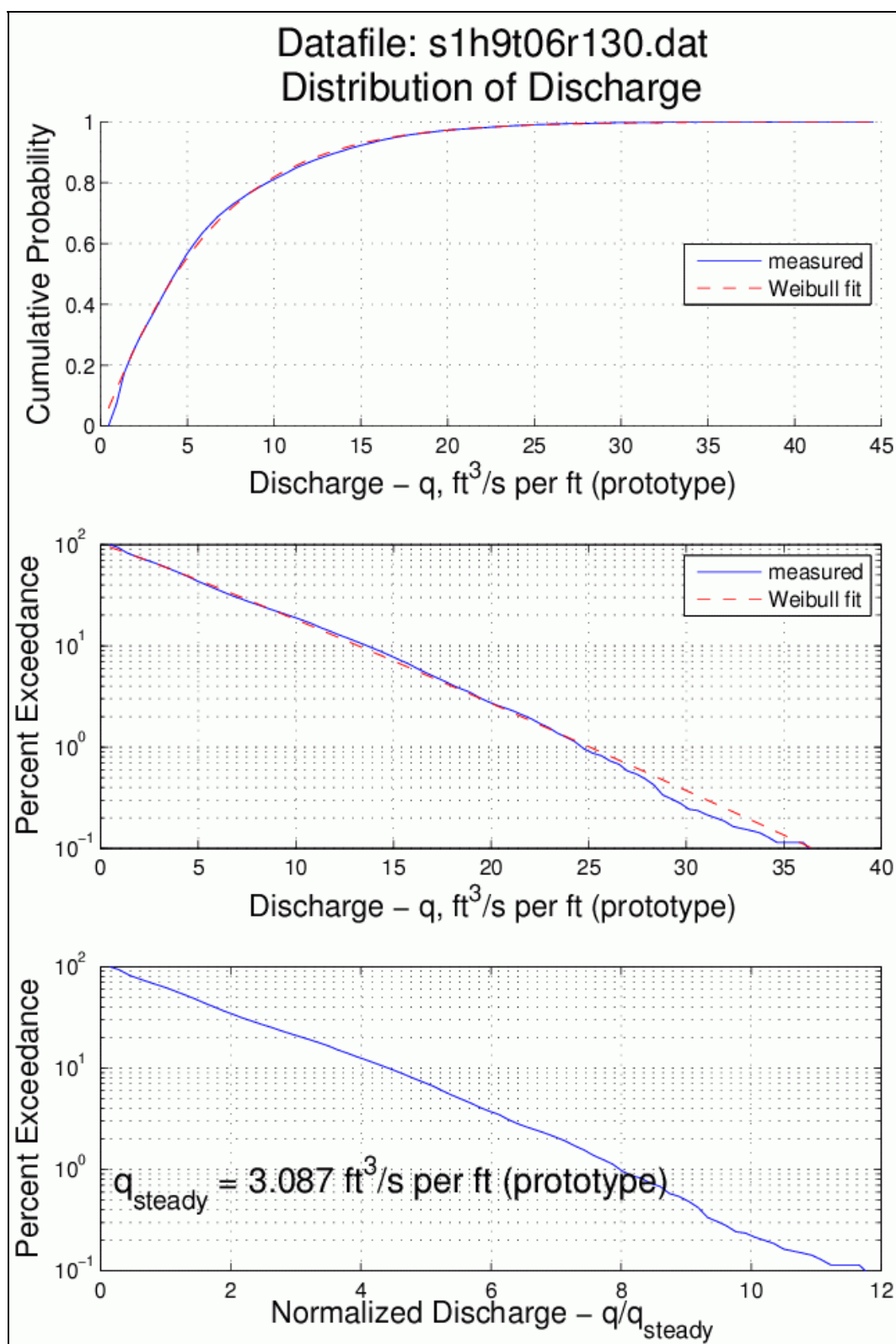


Figure A30. Run 130 overtopping distribution plots (surge = +1 ft, $H_{m0} = 9$ ft, $T_p = 6$ sec).

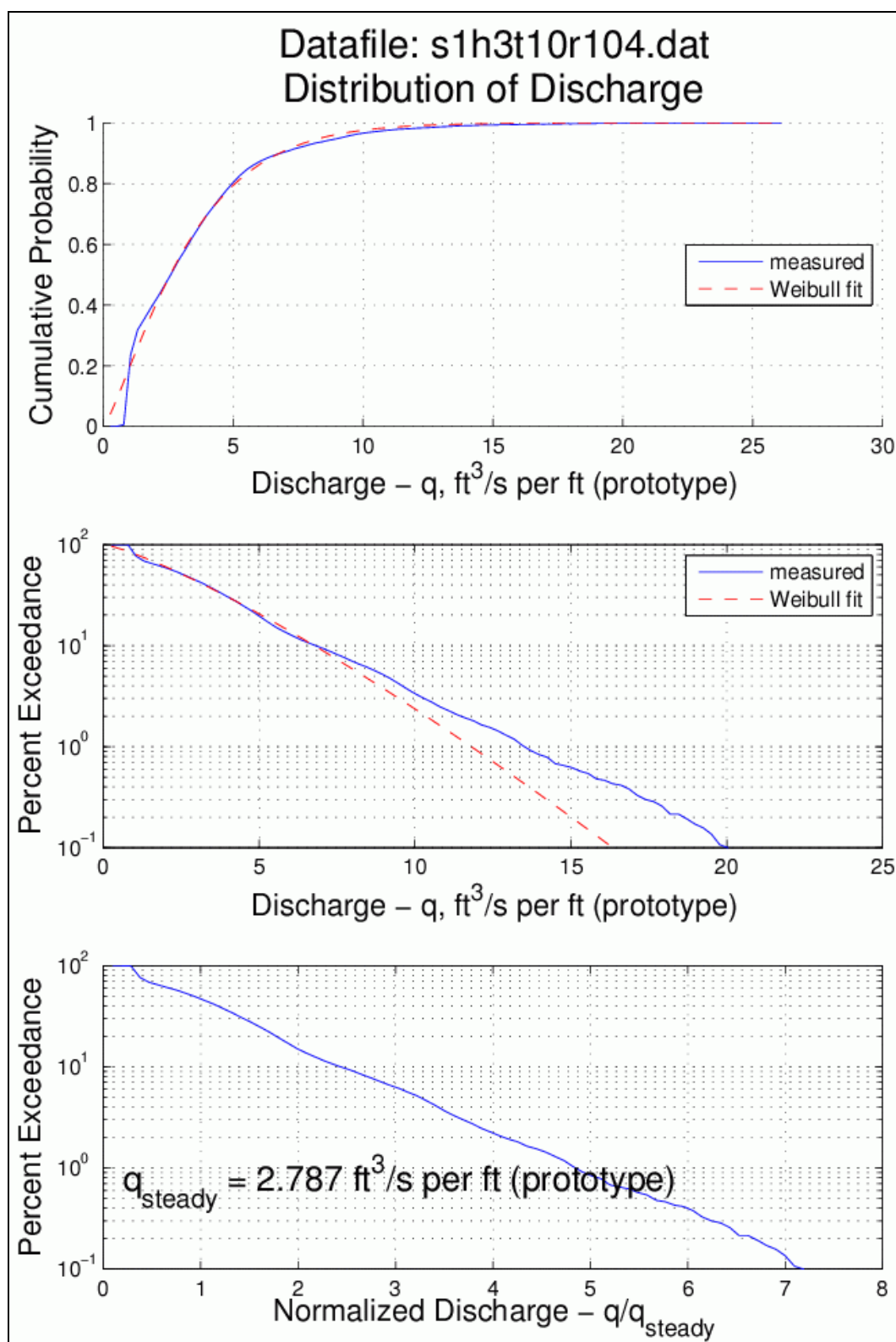


Figure A31. Run 104 overtopping distribution plots (surge = +1 ft, $H_{mo} = 3$ ft, $T_p = 10$ sec).

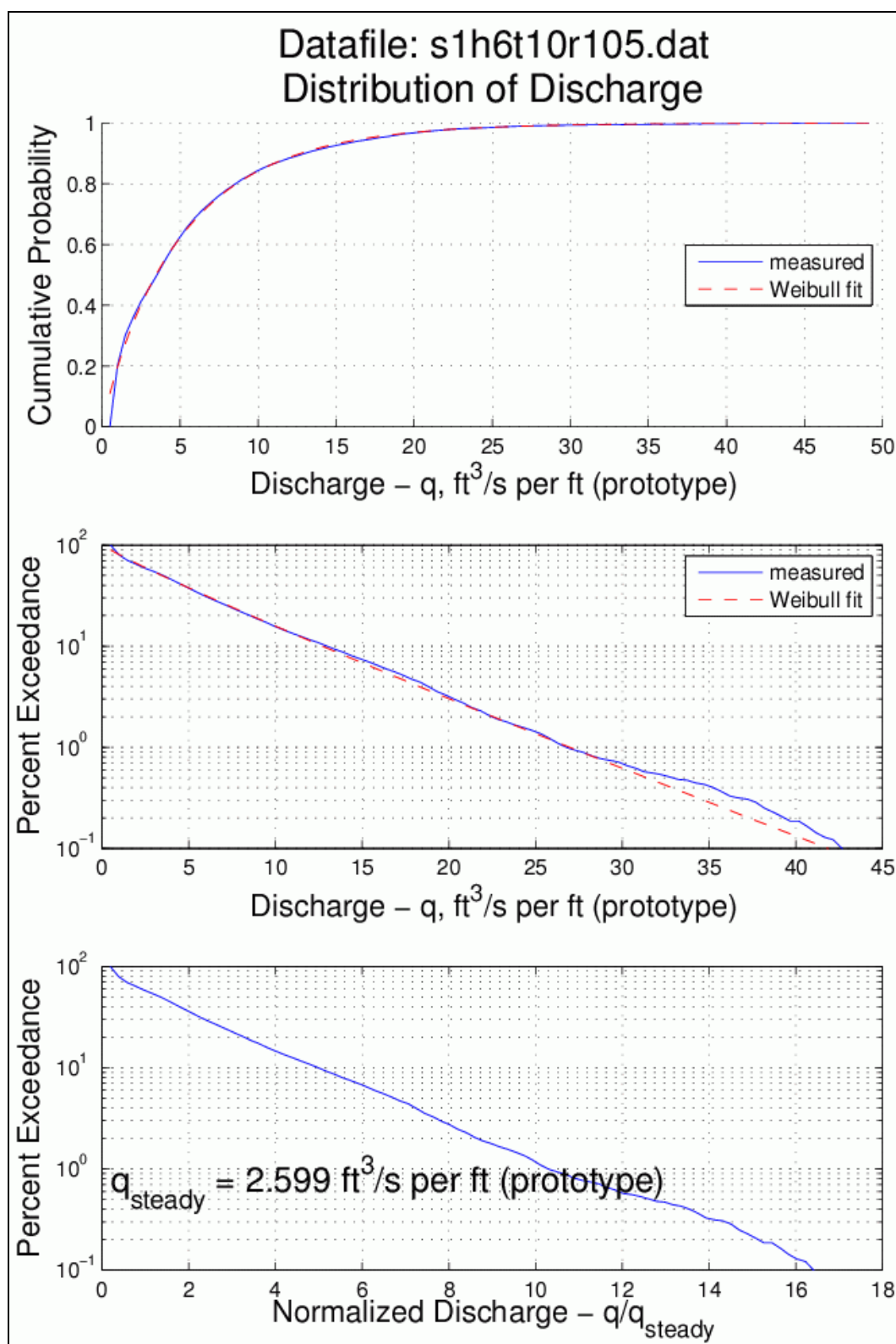


Figure A32. Run 105 overtopping distribution plots (surge = +1 ft, $H_{m0} = 6$ ft, $T_p = 10$ sec).

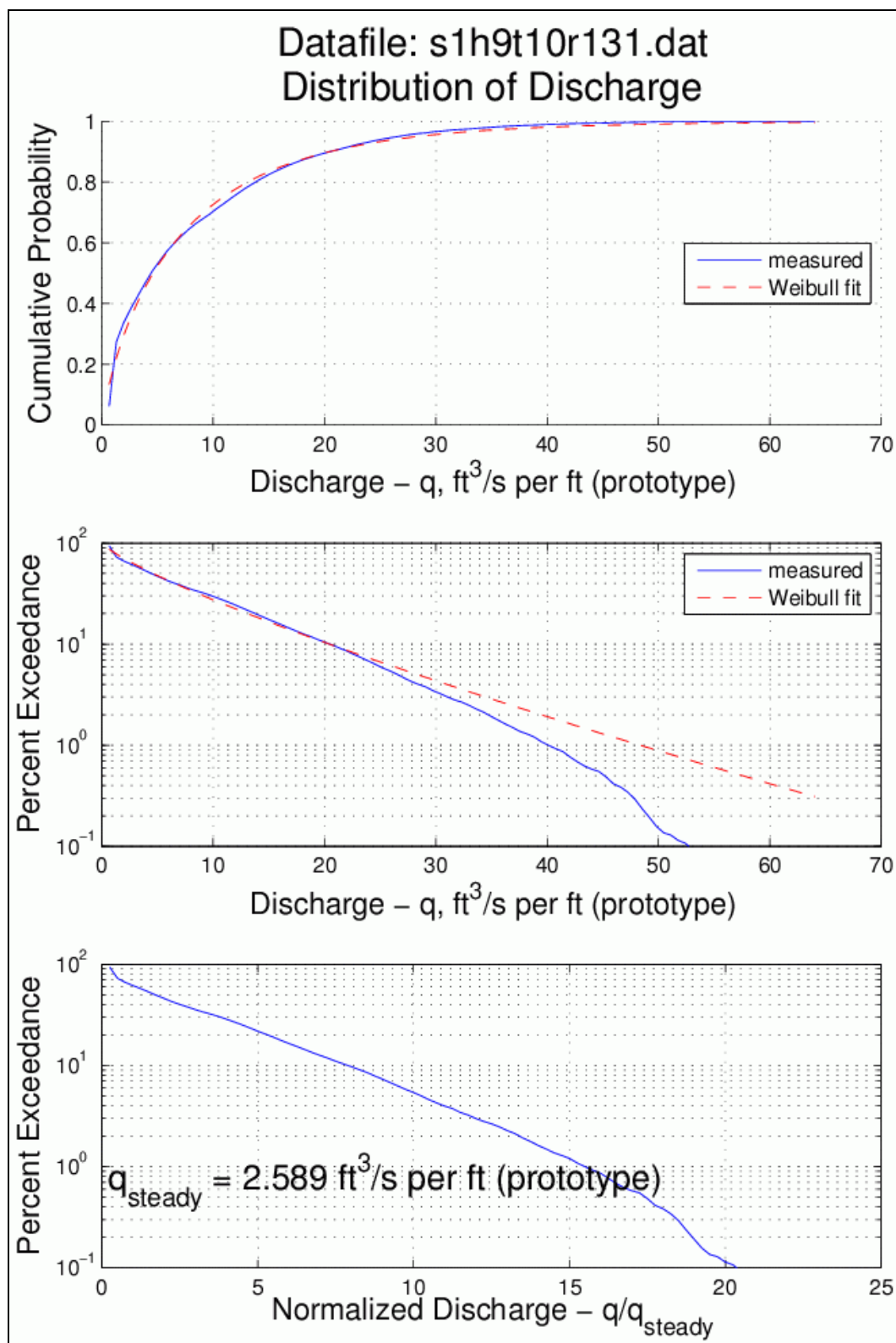


Figure A33. Run 131 overtopping distribution plots (surge = +1 ft, $H_{m0} = 9$ ft, $T_p = 10$ sec).

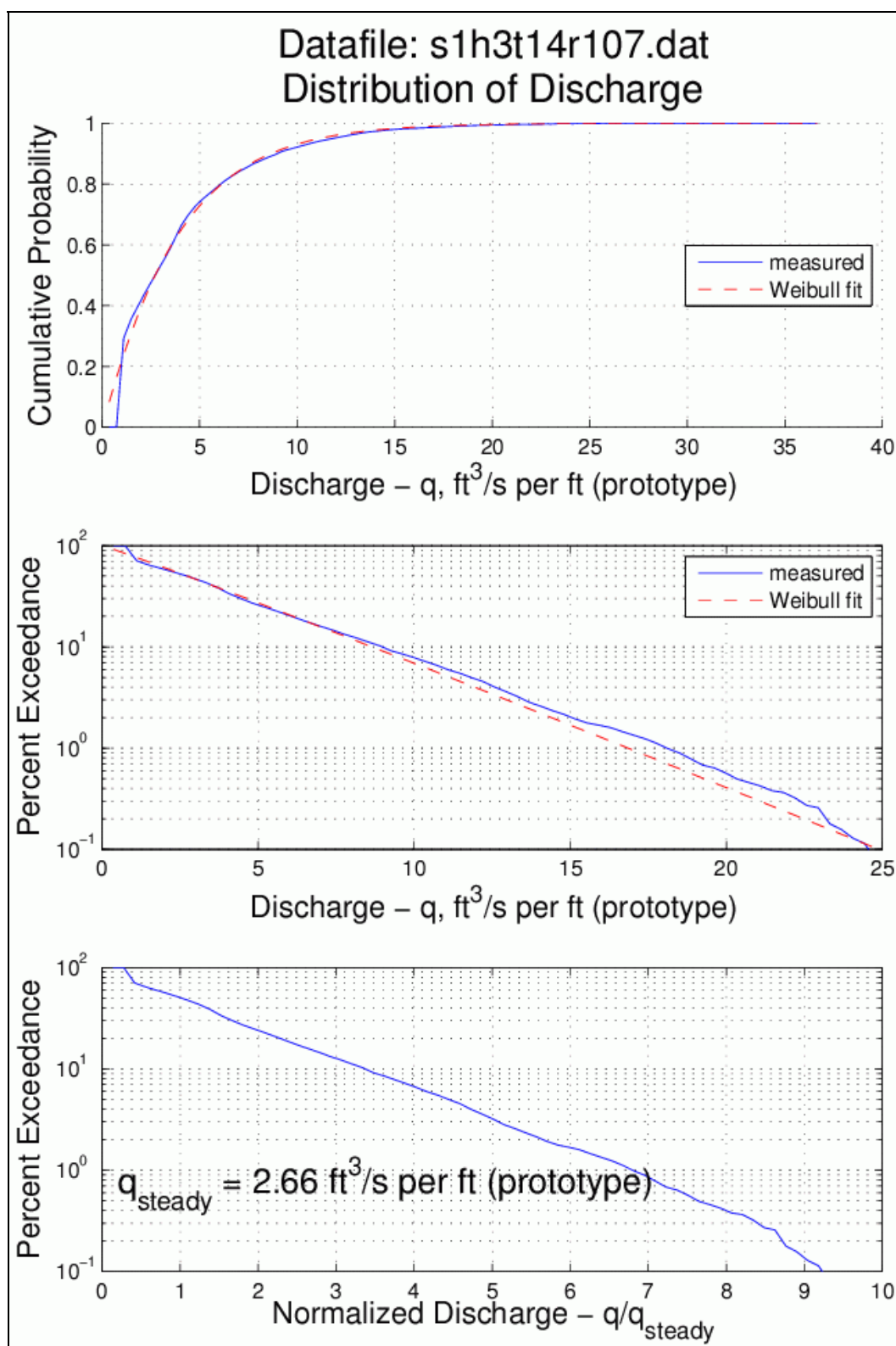


Figure A34. Run 107 overtopping distribution plots (surge = +1 ft, $H_{mo} = 3$ ft, $T_p = 14$ sec).

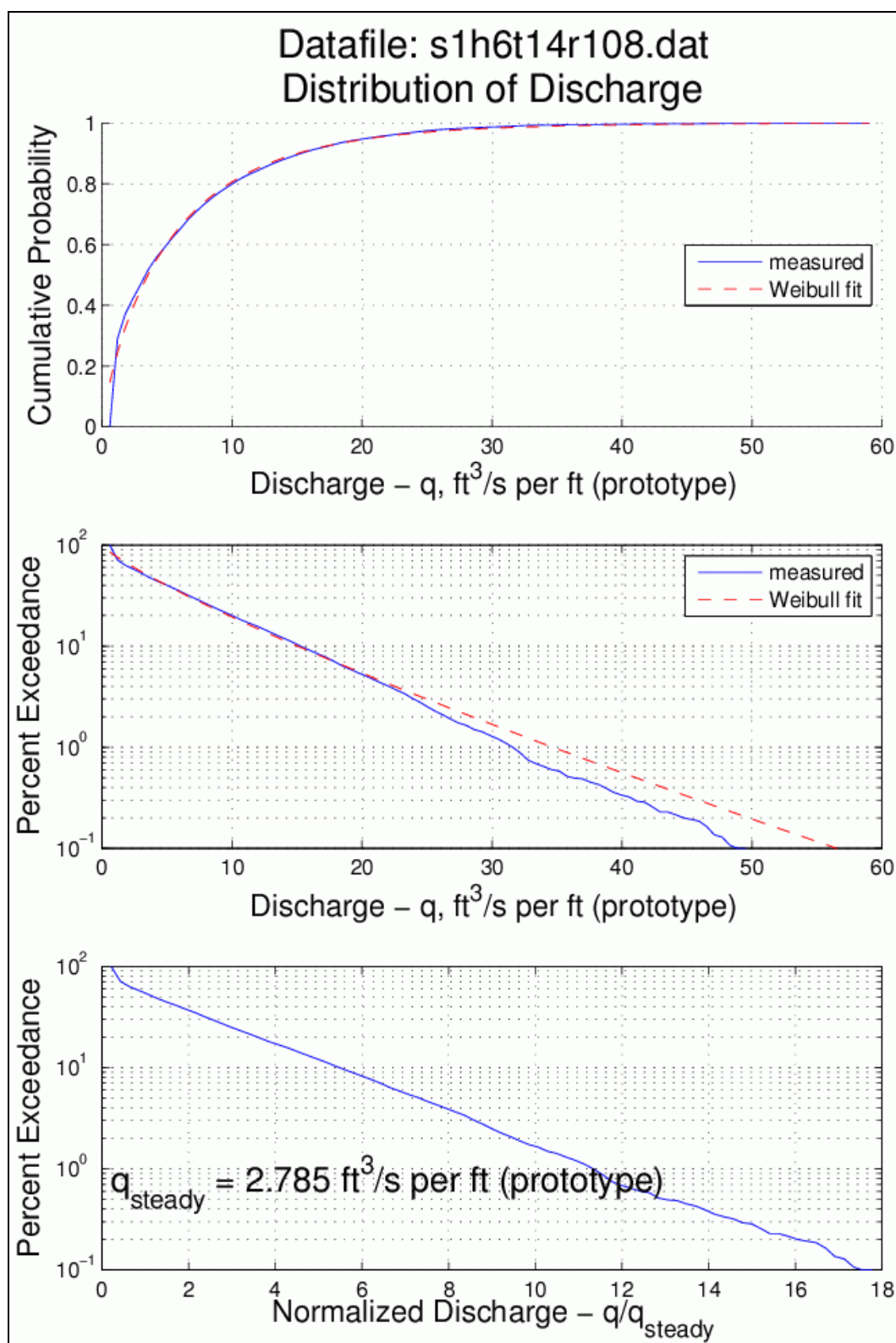


Figure A35. Run 108 overtopping distribution plots (surge = +1 ft, $H_{mo} = 6$ ft, $T_p = 14$ sec).

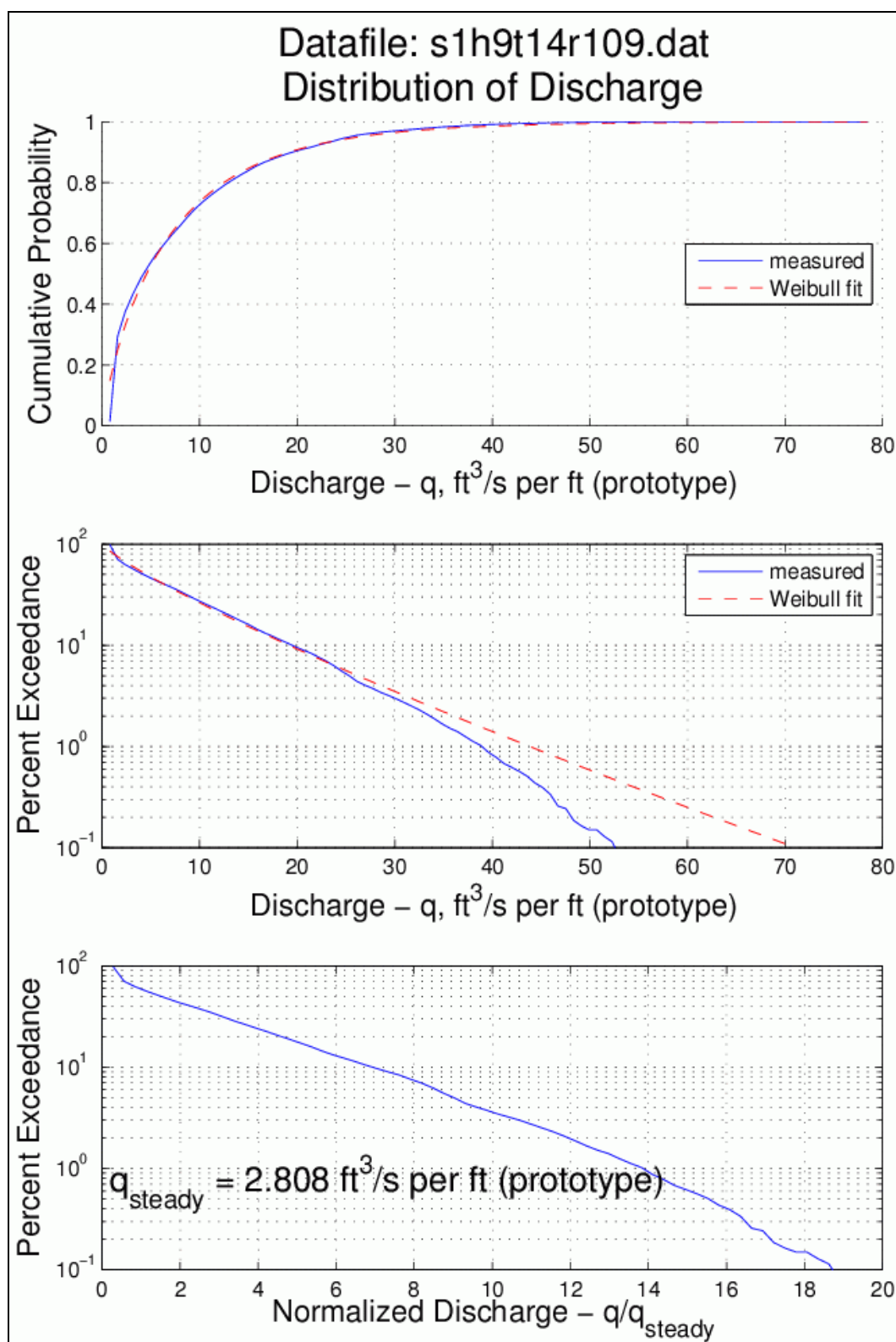


Figure A36. Run 109 overtopping distribution plots (surge = +1 ft, $H_{m0} = 9$ ft, $T_p = 14$ sec).

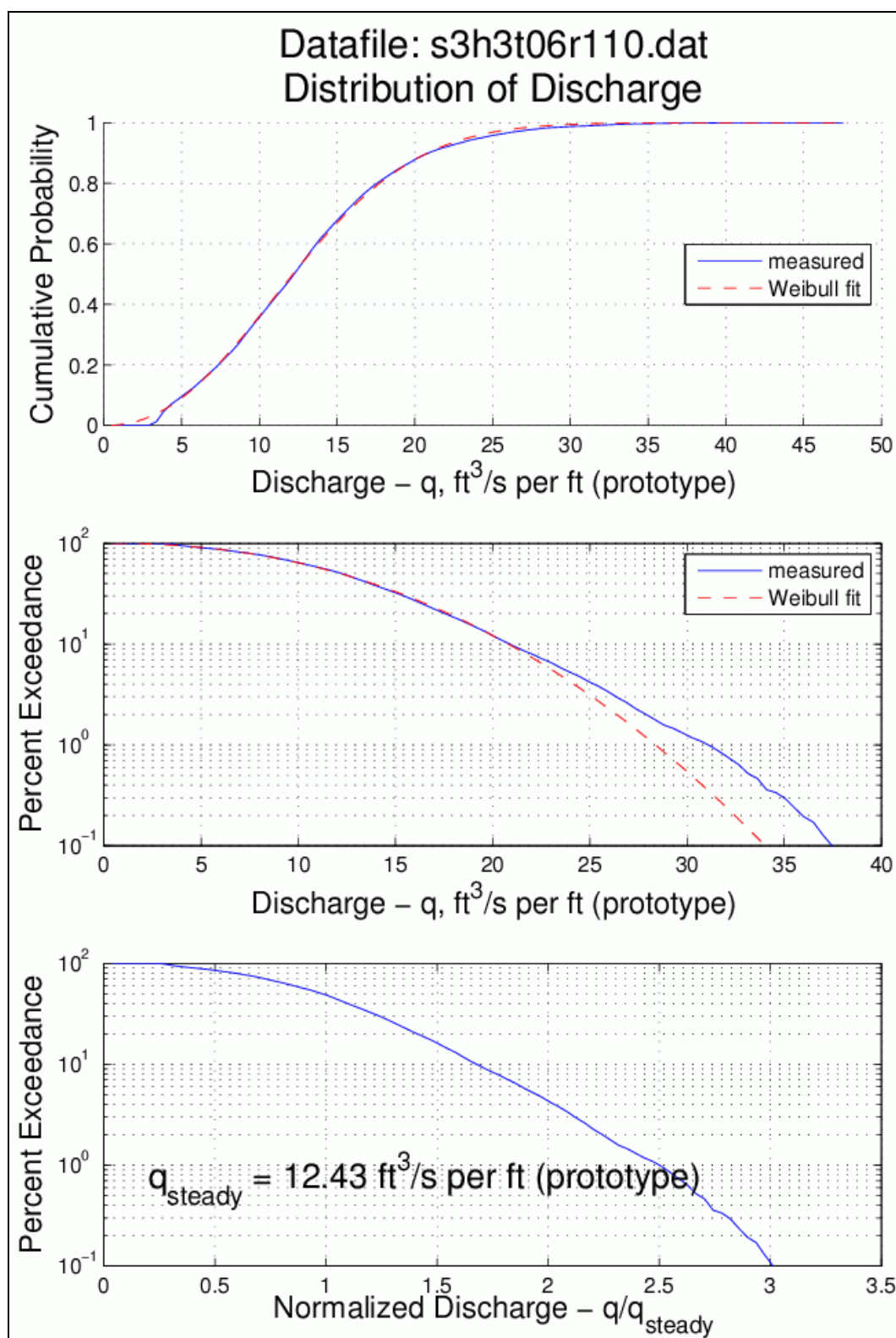


Figure A37. Run 110 overtopping distribution plots (surge = +3 ft, $H_{m0} = 3$ ft, $T_p = 6$ sec).

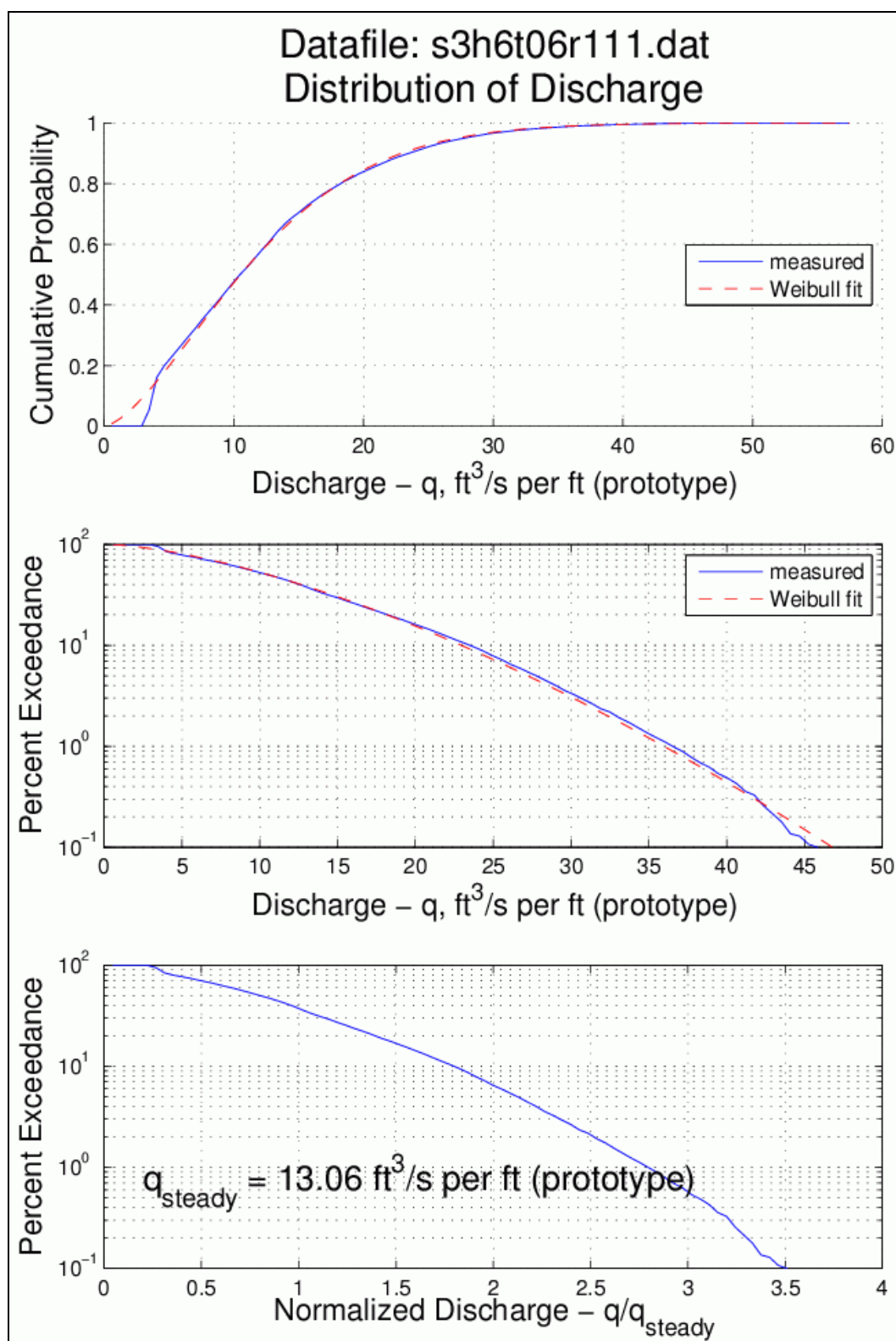


Figure A38. Run 111 overtopping distribution plots (surge = +3 ft, H_{m0} = 6 ft, T_p = 6 sec).

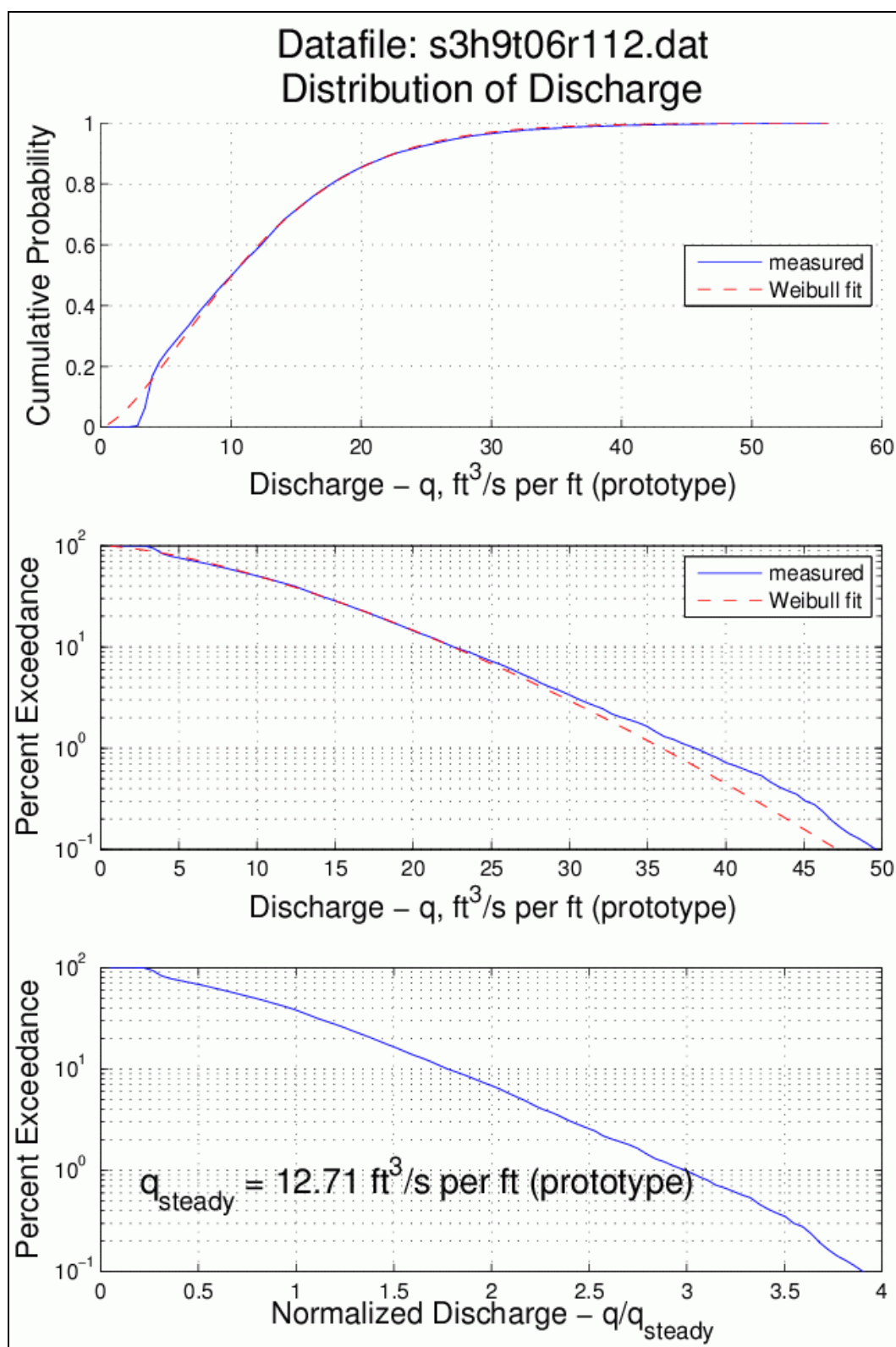


Figure A39. Run 112 overtopping distribution plots (surge = +3 ft, $H_{m0} = 9$ ft, $T_p = 6$ sec).

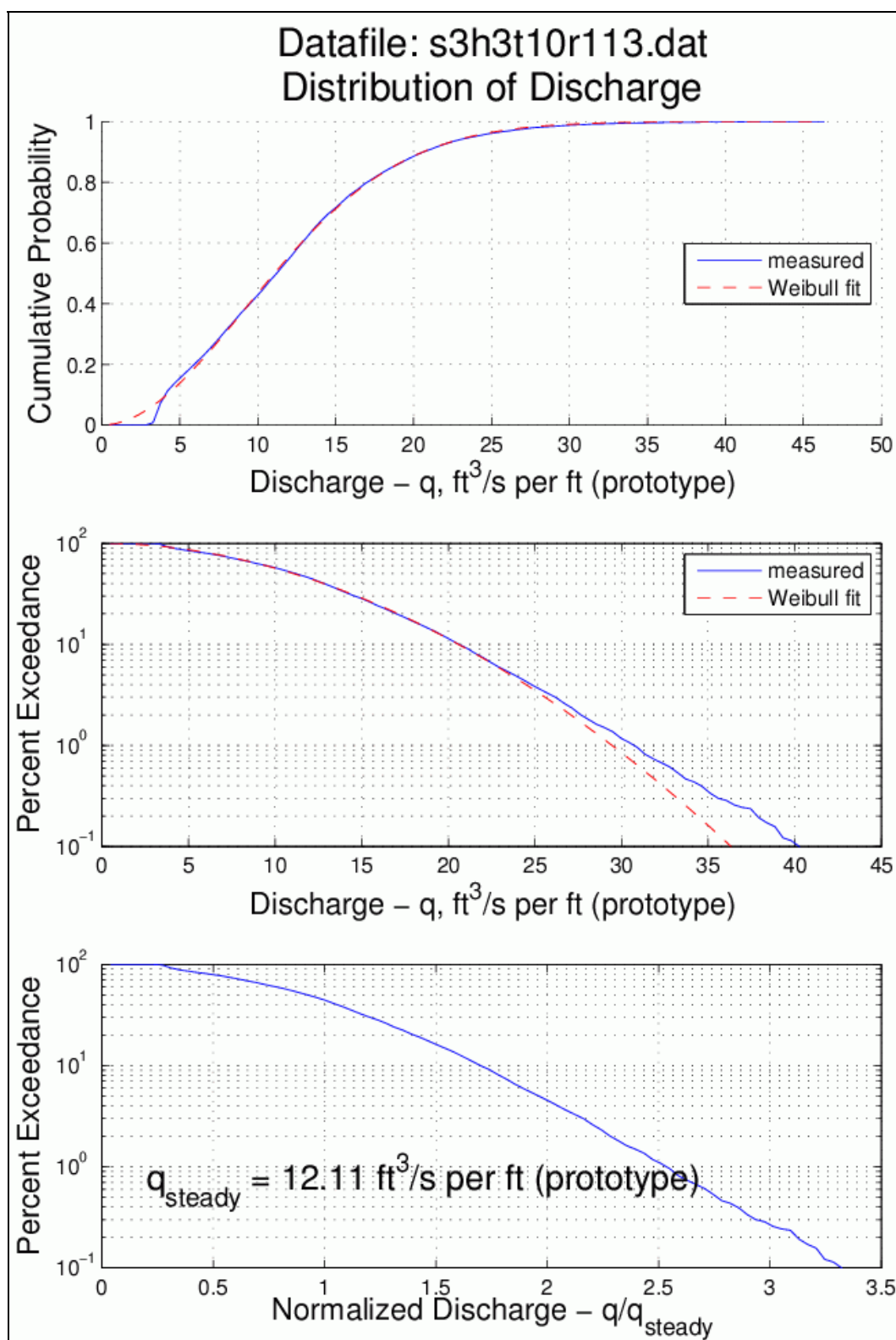


Figure A40. Run 113 overtopping distribution plots (surge = +3 ft, $H_{m0} = 3$ ft, $T_p = 10$ sec).

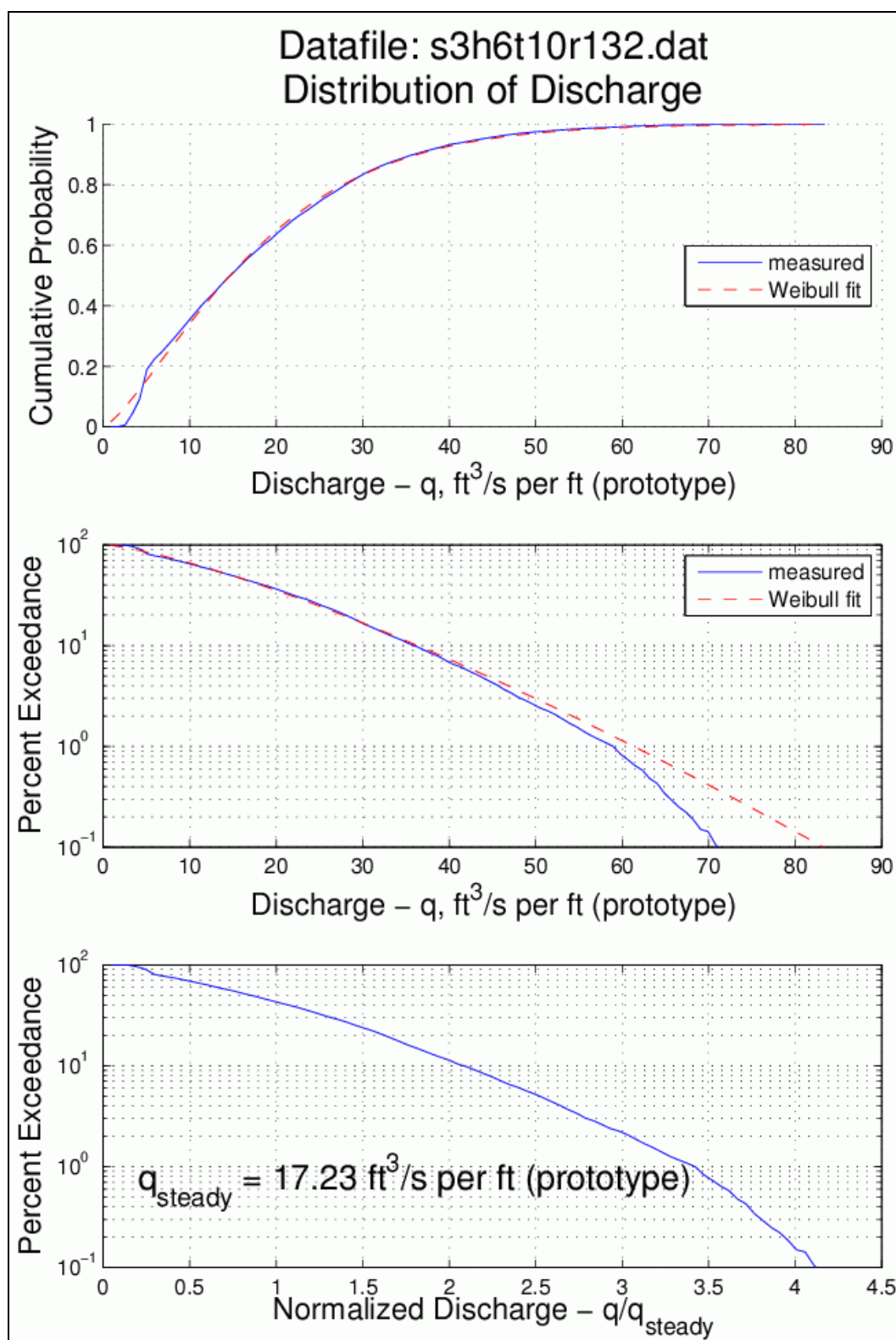


Figure A41. Run 132 overtopping distribution plots (surge = +3 ft, $H_{m0} = 6$ ft, $T_p = 10$ sec).

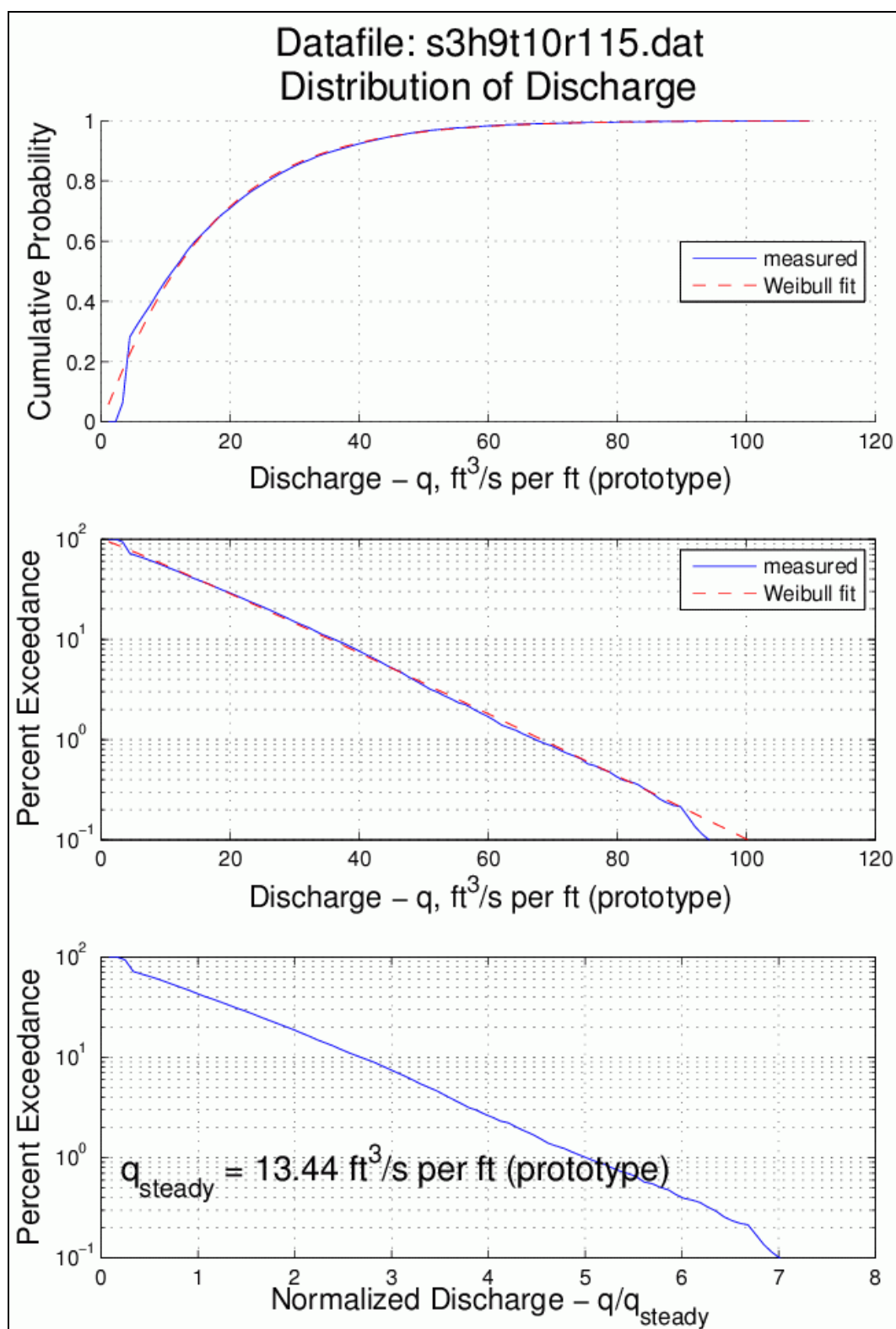


Figure A42. Run 115 overtopping distribution plots (surge = +3 ft, $H_{m0} = 9$ ft, $T_p = 10$ sec).

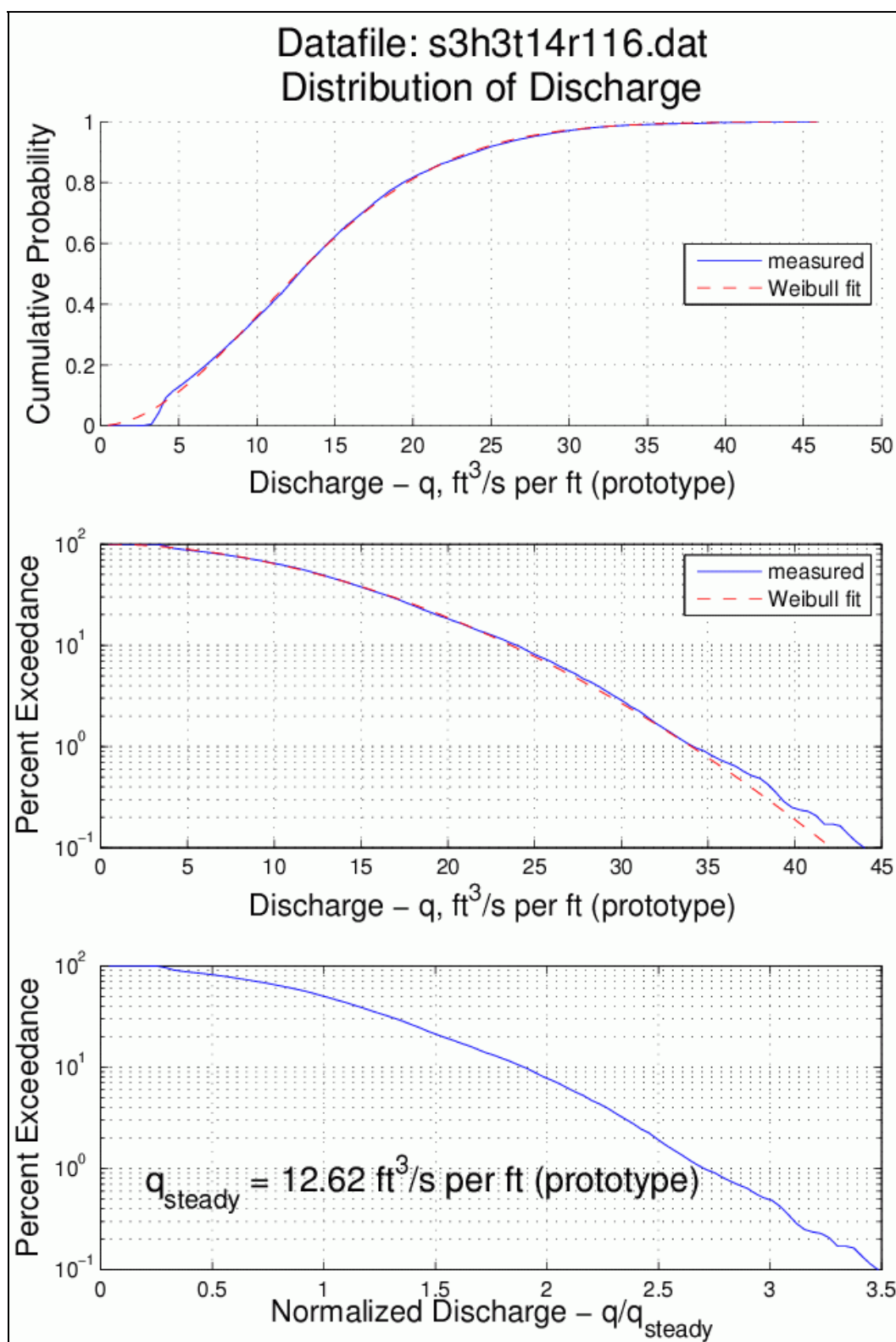


Figure A43. Run 116 overtopping distribution plots (surge = +3 ft, $H_{m0} = 3$ ft, $T_p = 14$ sec).

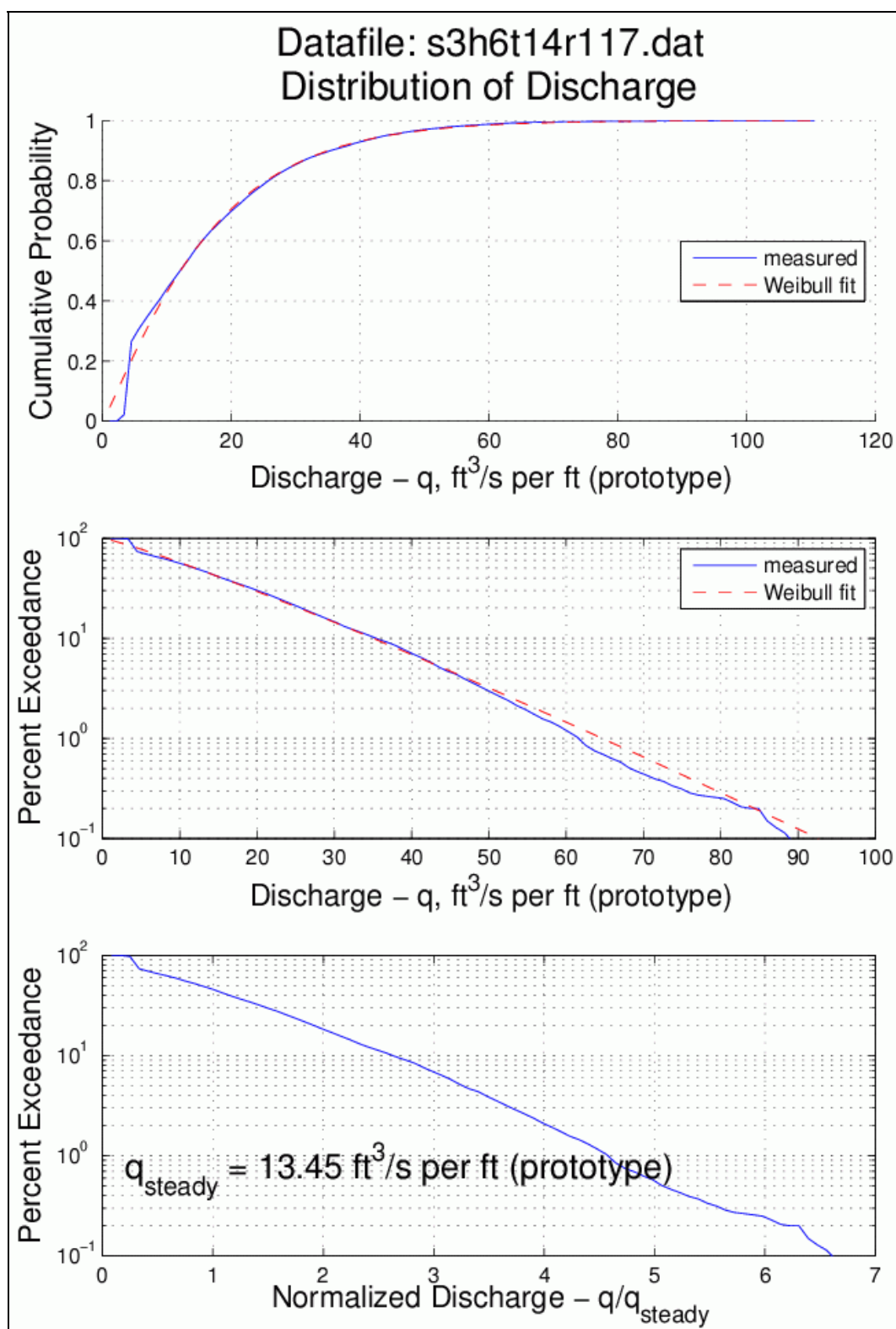


Figure A44. Run 117 overtopping distribution plots (surge = +3 ft, $H_{m0} = 6$ ft, $T_p = 14$ sec).

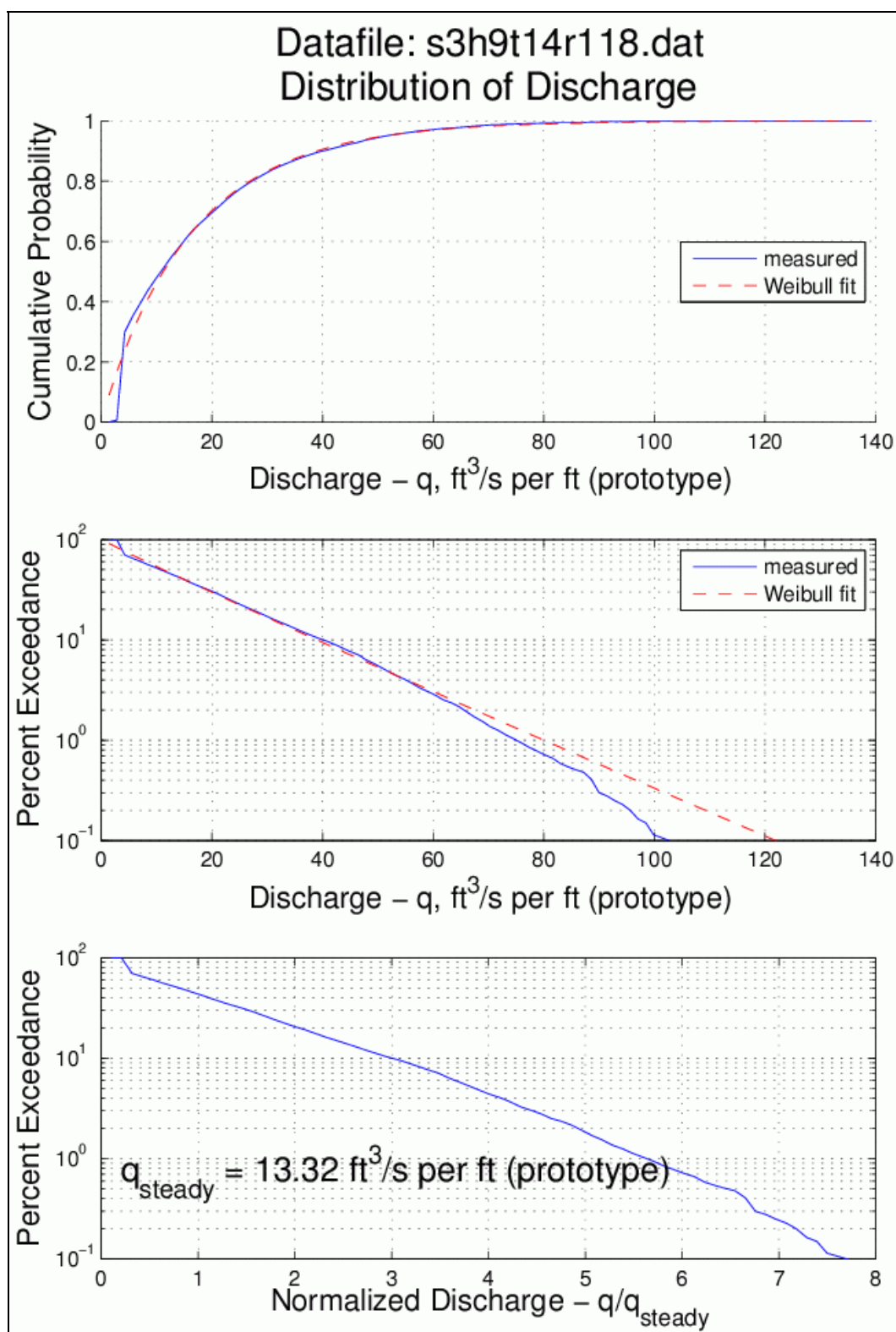


Figure A45. Run 118 overtopping distribution plots (surge = +3 ft, $H_{m0} = 9$ ft, $T_p = 14$ sec).

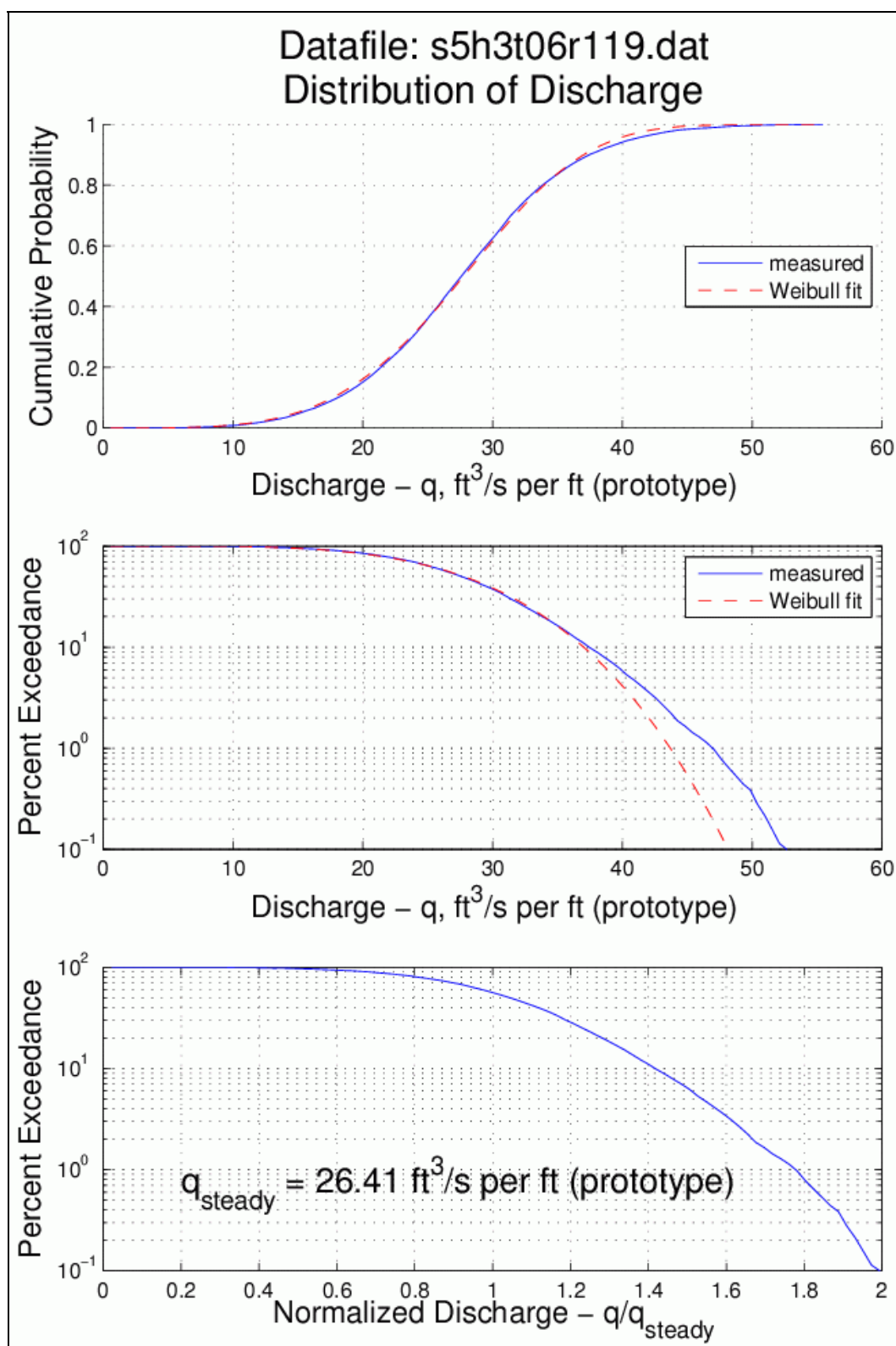


Figure A46. Run 119 overtopping distribution plots (surge = +5 ft, $H_{m0} = 3$ ft, $T_p = 6$ sec).

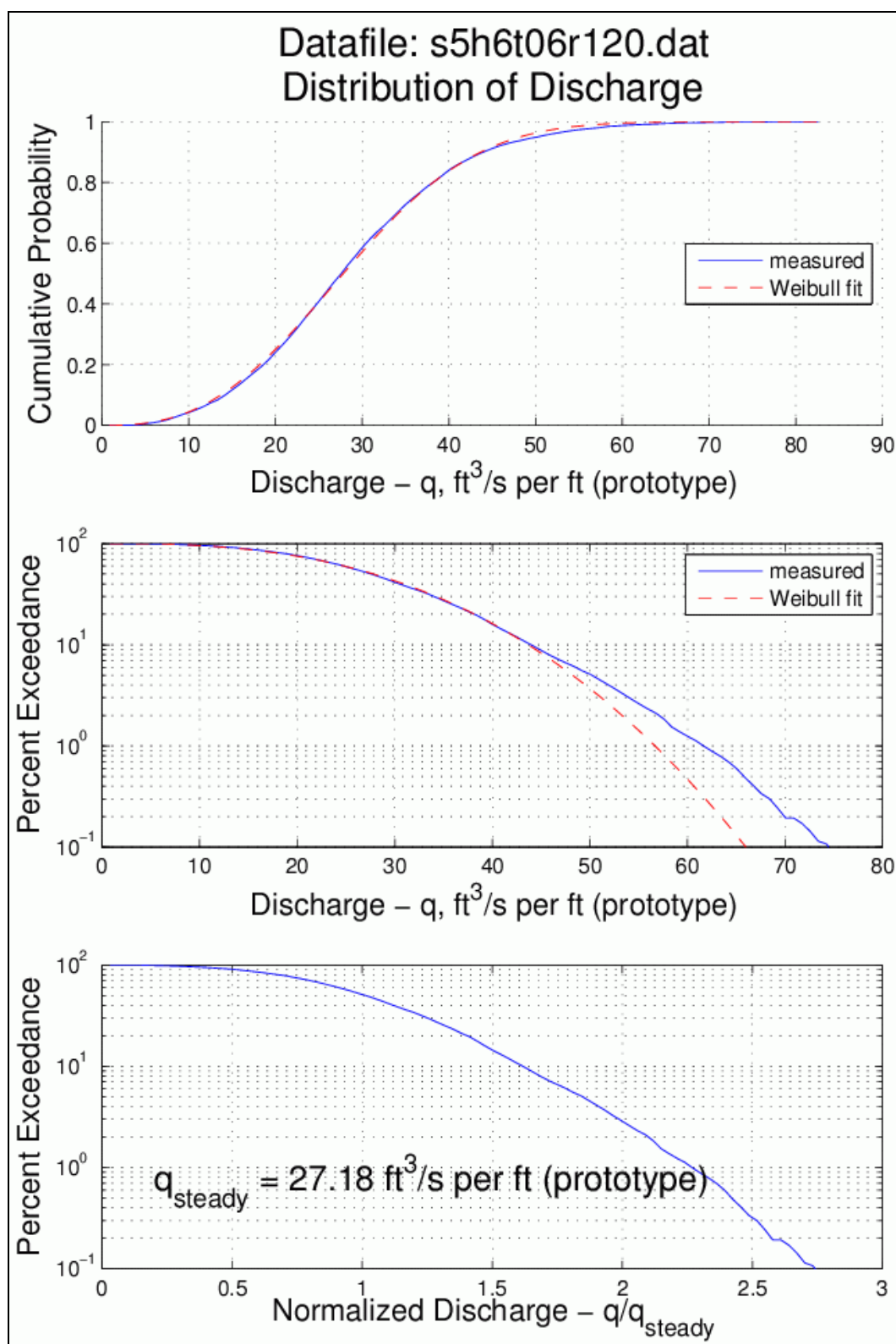


Figure A47. Run 120 overtopping distribution plots (surge = +5 ft, H_{m0} = 6 ft, T_p = 6 sec).

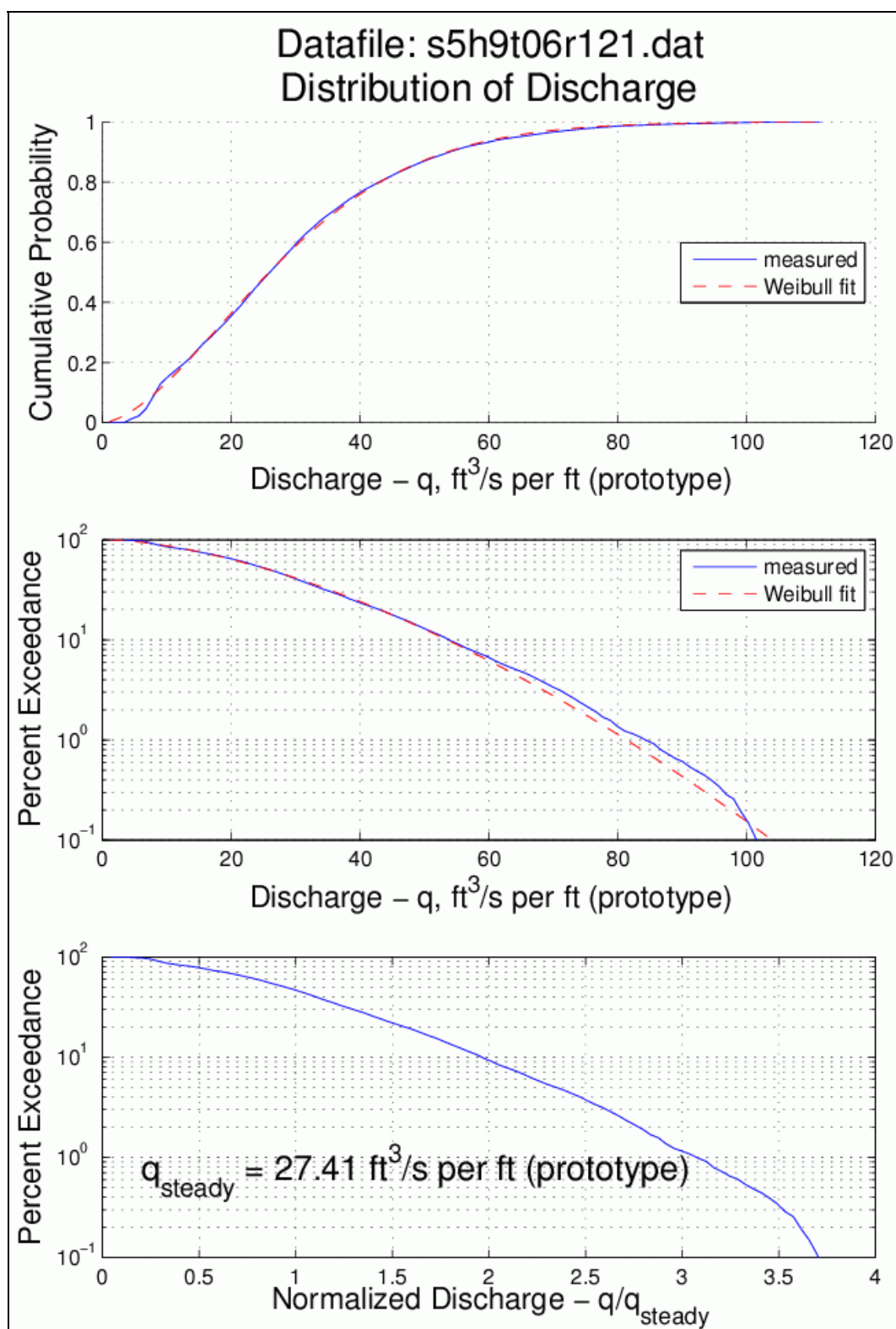


Figure A48. Run 121 overtopping distribution plots (surge = +5 ft, $H_{m0} = 9$ ft, $T_p = 6$ sec).

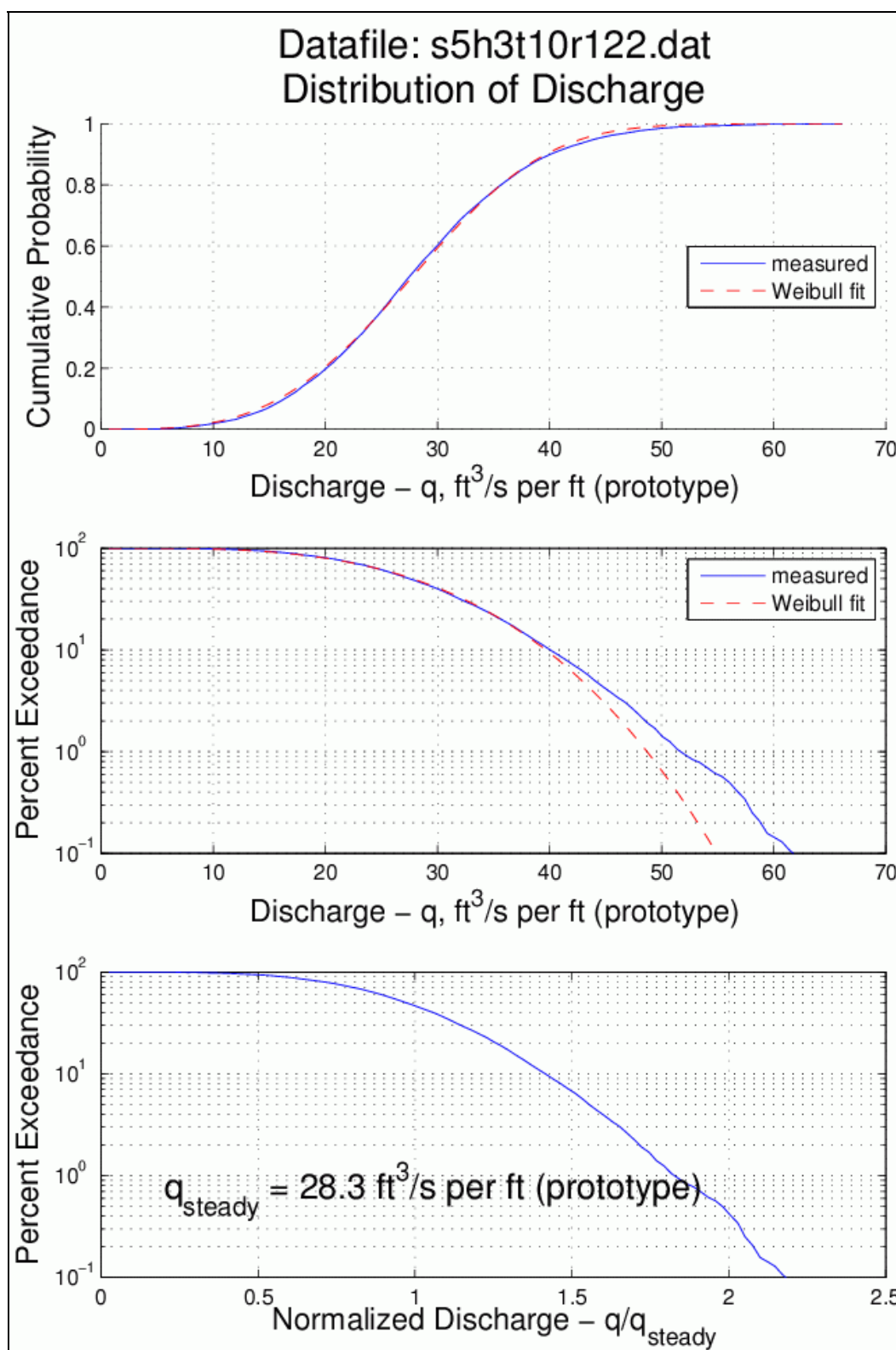


Figure A49. Run 122 overtopping distribution plots (surge = +5 ft, $H_{m0} = 3$ ft, $T_p = 10$ sec).

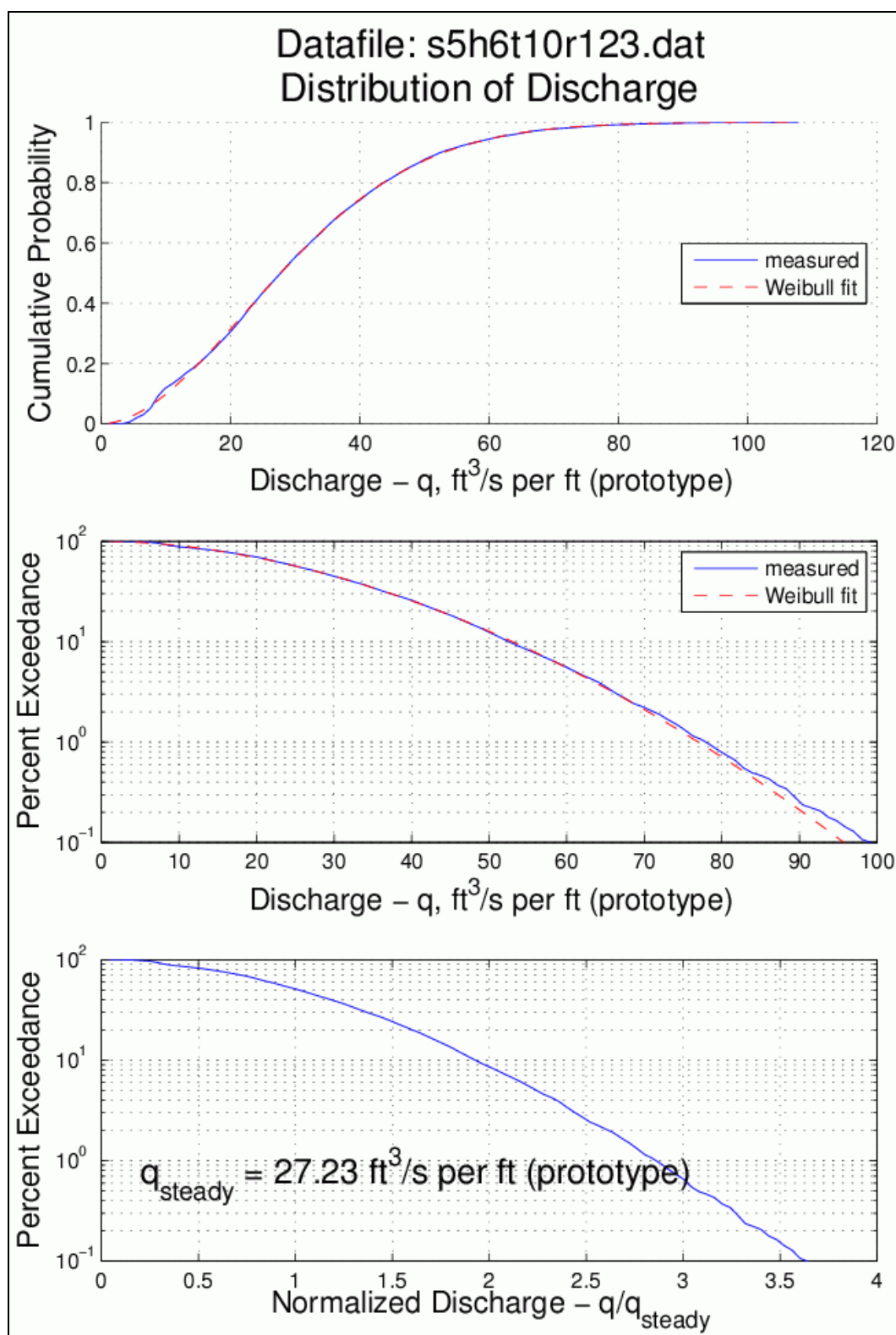


Figure A50. Run 123 overtopping distribution plots (surge = +5 ft, $H_{m0} = 6$ ft, $T_p = 10$ sec).

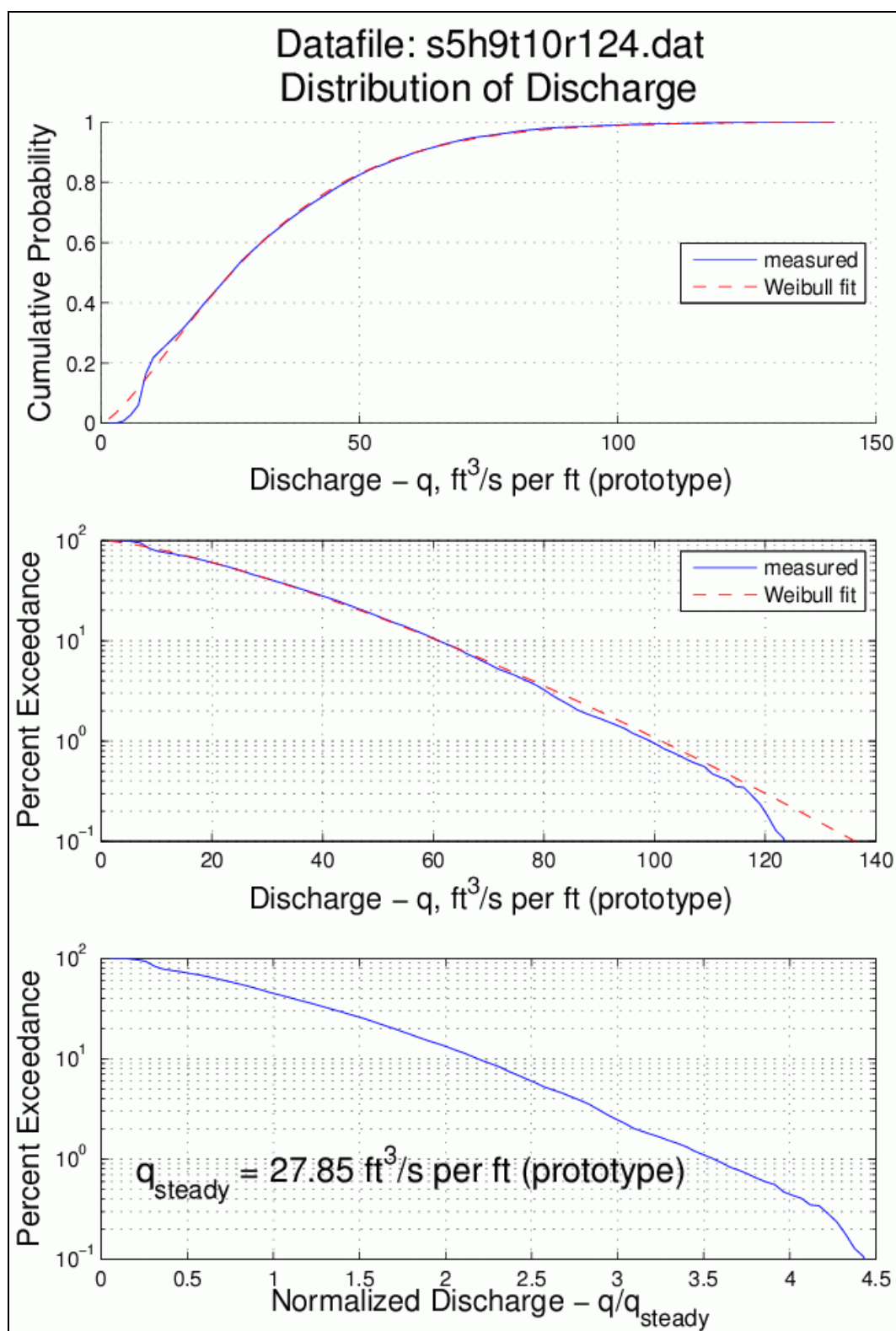


Figure A51. Run 124 overtopping distribution plots (surge = +5 ft, $H_{m0} = 9$ ft, $T_p = 10$ sec).

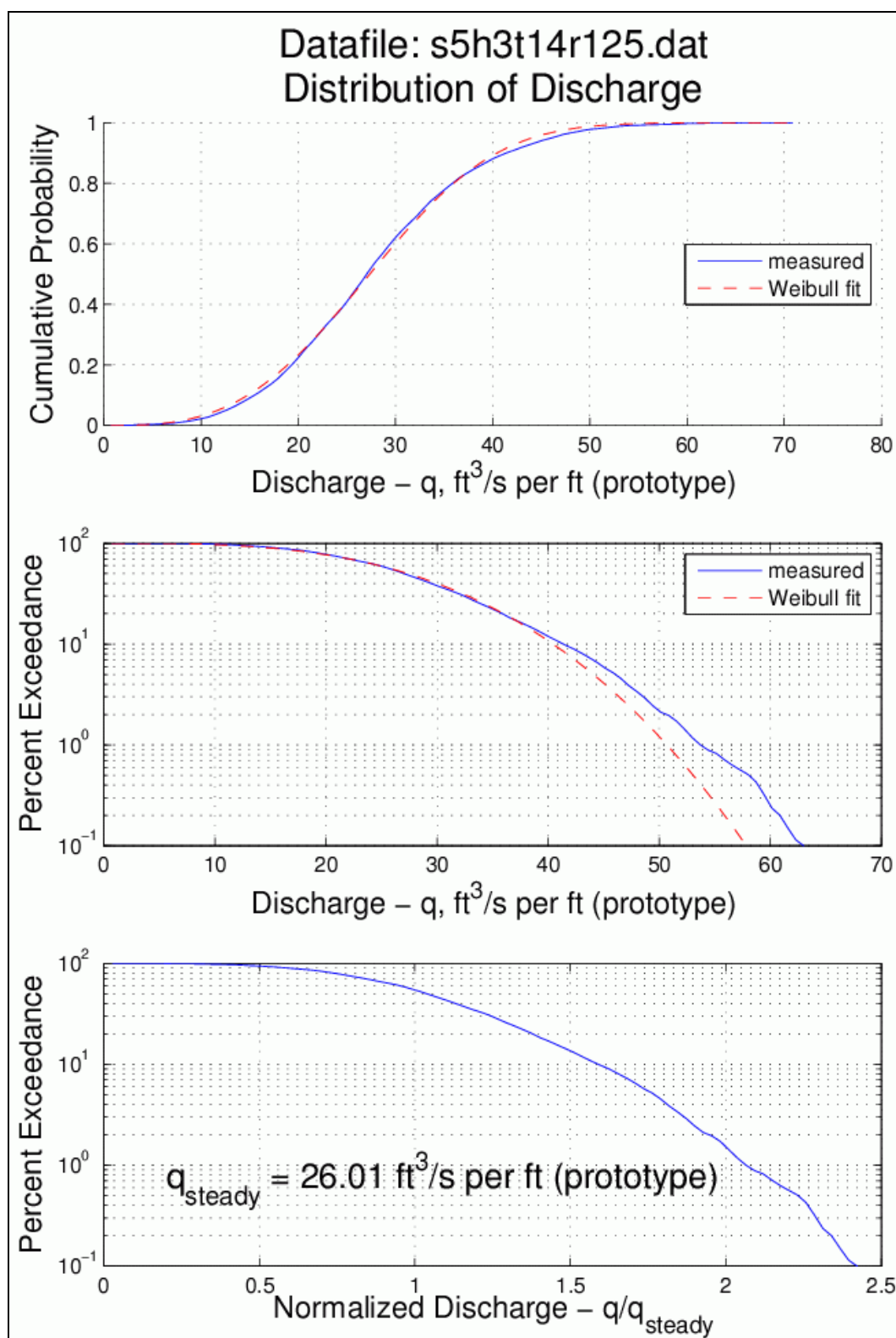


Figure A52. Run 125 overtopping distribution plots (surge = +5 ft, $H_{m0} = 3$ ft, $T_p = 14$ sec).

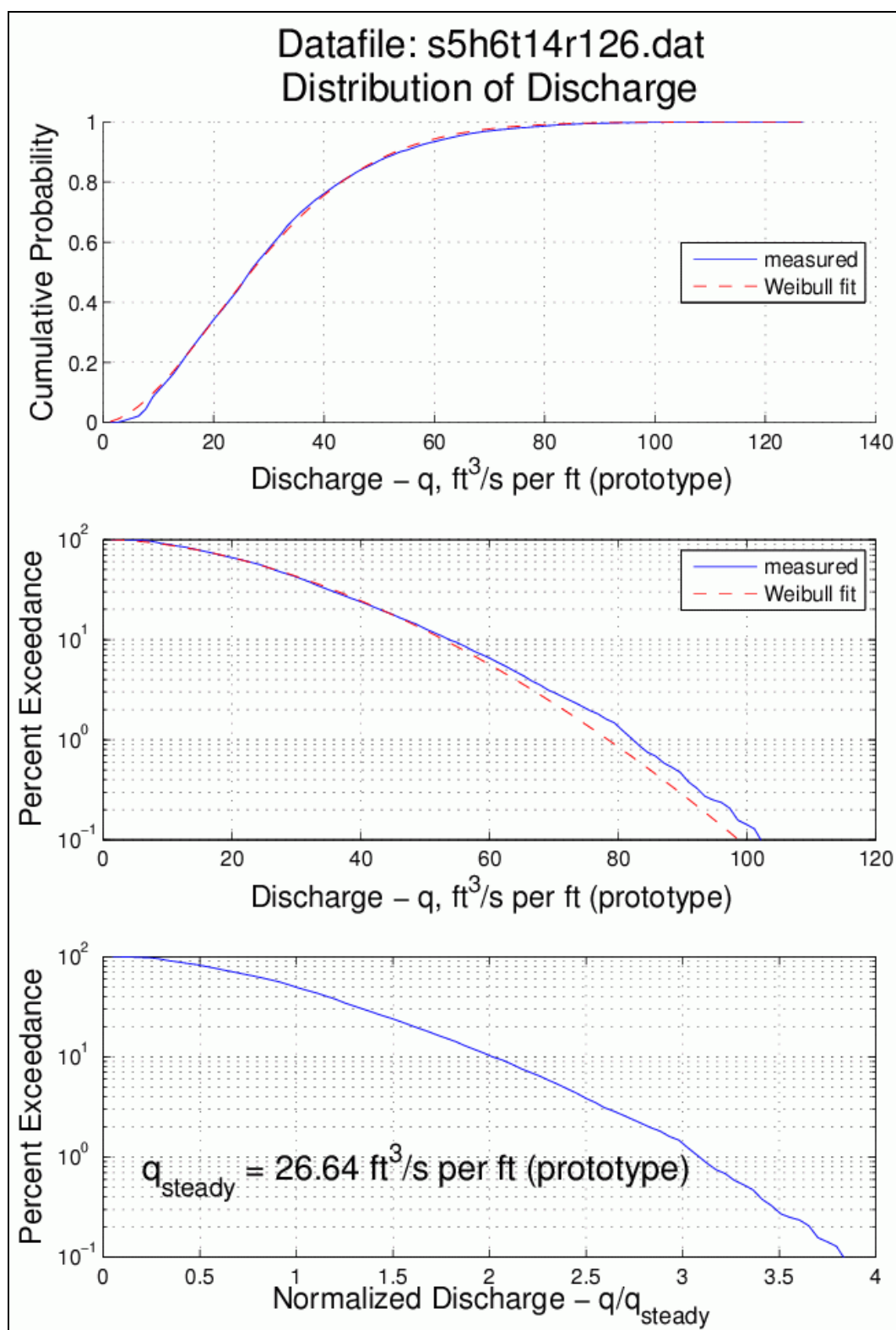


Figure A53. Run 126 overtopping distribution plots (surge = +5 ft, $H_{m0} = 6$ ft, $T_p = 14$ sec).

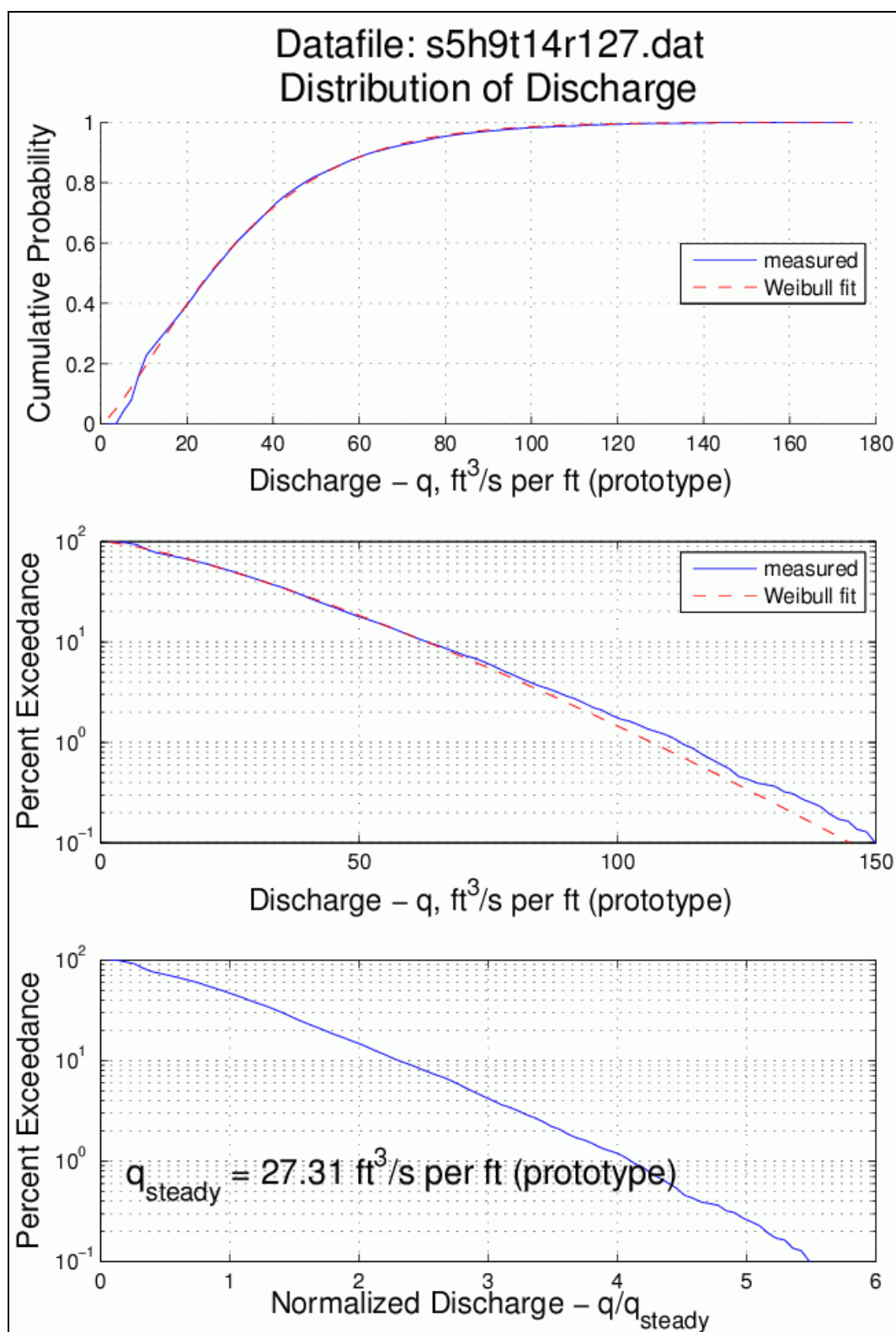


Figure A54. Run 127 overtopping distribution plots (surge = +5 ft, $H_{m0} = 9$ ft, $T_p = 14$ sec).

REPORT DOCUMENTATION PAGE						Form Approved OMB No. 0704-0188	
Public reporting burden for this collection of information is estimated to average 1 hour per response, including the time for reviewing instructions, searching existing data sources, gathering and maintaining the data needed, and completing and reviewing this collection of information. Send comments regarding this burden estimate or any other aspect of this collection of information, including suggestions for reducing this burden to Department of Defense, Washington Headquarters Services, Directorate for Information Operations and Reports (0704-0188), 1215 Jefferson Davis Highway, Suite 1204, Arlington, VA 22202-4302. Respondents should be aware that notwithstanding any other provision of law, no person shall be subject to any penalty for failing to comply with a collection of information if it does not display a currently valid OMB control number. PLEASE DO NOT RETURN YOUR FORM TO THE ABOVE ADDRESS.							
1. REPORT DATE (DD-MM-YYYY) August 2008		2. REPORT TYPE Final report			3. DATES COVERED (From - To)		
4. TITLE AND SUBTITLE Combined Wave and Surge Overtopping of Levees: Flow Hydrodynamics and Articulated Concrete Mat Stability					5a. CONTRACT NUMBER		
					5b. GRANT NUMBER		
					5c. PROGRAM ELEMENT NUMBER		
6. AUTHOR(S) Steven A. Hughes					5d. PROJECT NUMBER		
					5e. TASK NUMBER		
					5f. WORK UNIT NUMBER		
7. PERFORMING ORGANIZATION NAME(S) AND ADDRESS(ES) U.S. Army Engineer Research and Development Center Coastal and Hydraulics Laboratory 3909 Halls Ferry Road Vicksburg, MS 39180-6199					8. PERFORMING ORGANIZATION REPORT NUMBER ERDC/CHL TR-08-10		
9. SPONSORING / MONITORING AGENCY NAME(S) AND ADDRESS(ES) U.S. Army Engineer District, New Orleans P.O. Box 60267 New Orleans, LA 70160-0267					10. SPONSOR/MONITOR'S ACRONYM(S)		
					11. SPONSOR/MONITOR'S REPORT NUMBER(S)		
12. DISTRIBUTION / AVAILABILITY STATEMENT Approved for public release; distribution is unlimited.							
13. SUPPLEMENTARY NOTES							
14. ABSTRACT A 1-to-25 scale physical model of a typical cross section of the levee along the Mississippi River Gulf Outlet (MRGO) was constructed at the U.S. Army Engineer Research and Development Center's Coastal and Hydraulics Laboratory in Vicksburg, MS. The purpose of the physical model was to obtain hydrodynamic measurements of unsteady flow conditions caused by combined wave and surge overtopping of the levee, and to examine the feasibility of using articulated concrete mats (ACMs) for levee protection during this type of overtopping event. Specifically, the U.S. Army Engineer District, New Orleans, was interested in determining whether the same ACMs used by the Corps' Mat Sinking Unit to protect river banks could be used to protect the MRGO levee against surge and wave overtopping. When the storm surge elevation was 0.75 ft above the levee crest, the stability tests indicated the ACMs were prone to uplift on the lower portion of the levee protected-side slope for even relatively mild wave overtopping. An increase in wave height created mat roll-up instability at the toe of the flood-side levee slope, indicating the need to bury or anchor the leading and tailing edges of the mats. Mat stability could be increased with additional anchoring or increasing mat thickness. <div style="text-align: right;">(Continued)</div>							
15. SUBJECT TERMS Concrete mats Levees Soil stabilization Erosion control Simulation modeling							
16. SECURITY CLASSIFICATION OF:				17. LIMITATION OF ABSTRACT	18. NUMBER OF PAGES 183	19a. NAME OF RESPONSIBLE PERSON	
a. REPORT UNCLASSIFIED	b. ABSTRACT UNCLASSIFIED	c. THIS PAGE UNCLASSIFIED	19b. TELEPHONE NUMBER (include area code)				

14. ABSTRACT (Concluded)

Tests were also conducted to document the hydrodynamics associated with combined wave and surge overtopping. The primary parameters were three overtopping surge levels (+1, +3, and +5 ft); three significant wave heights (3, 6, and 9 ft); and three peak wave periods (6, 10, and 14 sec) for a total of 27 unique conditions. Measurements included the incident irregular waves and time series of water elevations at seven locations on the crest and protected-side slope of the levee. Horizontal flow velocity was recorded near the leeward levee crest shoulder, and the velocity was then combined with water elevation to estimate the unsteady instantaneous discharge over the levee. Discharge cumulative probability distributions were determined using the Weibull probability distribution, and a predictive equation was developed for the distribution of overtopping discharge as a function of wave and surge parameters.